THE DEVELOPMENT AND UTILIZATION OF THE PERIODIC FOCUSING ION FUNNEL

A Dissertation

by

KYLE FORT

Submitted to the Office of Graduate and Professional Studies of
Texas A&M University
in partial fulfillment of the requirements for the degree of

DOCTOR OF PHILOSOPHY

Chair of Committee,	David H. Russell
Committee Members,	Simon W. North
	Emile A. Schweikert
	Renyi Zhang
Head of Department,	Francois Gabbai

December 2014

Major Subject: Chemistry

ABSTRACT

Ion mobility-mass spectrometry (IM-MS) provides gas phase, size-based separation, on an ultrafast timescale (μs-ms). With the incorporation of electrospray ionization, IM-MS is a valuable tool to investigate conformations of biological molecule ions that can be representative of their solution-phase structure. In some cases, evaporative cooling during ESI can kinetically trap these solution-phase structures in local minima along the potential energy surface. However, if the internal energy of the ion is increased via collisional activation, these solution-phase structures can be readily converted to an energetically preferred, gas-phase structure. Radio frequency (RF) confining devices, such as the RF ion funnel, are typically used to increase ion transmission in IM-MS measurements; however, these devices can lead to collisional activation and structural rearrangement due to high voltage oscillation amplitudes (V_{p-p}). Recently, periodic focusing ion mobility spectrometry (PF IMS) has been shown to provide comparable radial confinement, while utilizing reduced radial electric fields V_{p-p} as compared to the RF ion funnel. Work presented herein describes the development and characterization of a periodic focusing ion funnel (PF IF) that is capable of increasing ion transmission while being able to preserve nascent conformer distributions and subsequently inducing structural rearrangement.

The utility of the PF IF is demonstrated with the neuropeptide Substance P (SP), as it provides a model for studying the structural effects of collisional activation due to the presence of both a kinetically trapped and gas-phase conformer, denoted $\mathbf{A}_{SP}$ and

$\mathbf{B}_{SP}$, respectively. By increasing the internal energy of $[SP + 3H]^{3+}$ ions, $\mathbf{A}_{SP}$ is quantitatively converted to $\mathbf{B}_{SP}$, which is consistent with $\mathbf{A}_{SP}$ being a kinetically trapped conformer and $\mathbf{B}_{SP}$ being a gas-phase conformer. The collision cross section and mobility resolution of the $\mathbf{A}_{SP}$ suggests that it is comprised of a broad distribution of compact globular conformations. Intramolecular solvation appears to stabilize the compacted structure of $\mathbf{A}_{SP}$ in the gas-phase; however, as the ion's internal energy increases, these noncovalent interactions are disrupted and the peptide converts into the gas-phase conformation. Mutations of various amino acid residues of SP provide a means of identifying these interactions and their effect on the stability of the kinetically trapped conformers.

For my parents

ACKNOWLEDGEMENTS

I would first like to acknowledge my advisor, Dr. David H. Russell for his support, encouragement, and for allowing me to join his research group. He has allowed me the freedom to explore my own ideas and provided advice and wisdom when tasks seemed insurmountable. For all that he has done, and for all that he continues to do, I am deeply grateful.

I would also like to acknowledge my committee members: Dr. Simon W. North, Dr. Emile A. Schweikert, and Dr. Renyi Zhang for their advice and supervision of my scientific progress during my time here at Texas A&M.

I would like to acknowledge and thank the members, both current and past, of the Russell Research Group for their help and advice. I am indebted to my first student mentor in the RRG, Dr. Stephanie Cologna. She has been a wonderful friend, a pillar of constant support, and mentor through the entirety of my graduate school career. She also is the person who convinced me the RRG was the place for me and for that, I am forever grateful. A special thank you to the group members who helped shape my research along the way: Joshua Silveira, Kelly Servage, Chris Barlow, Kevin Kmiec, Roberto Gamez, Kim May, Greg Matthijetz, Peggy Pai, Junho Jeon, and Ryan Blase; I couldn't ask for better lab mates and friends.

I have learned that an instrument builder is only as good as the machinist making the parts and I have had the great fortune of working with three of the best: Carl Johnson, Ron Page, and Will Seward; they have been invaluable to the progression of

my research. I would especially like to thank Will for his countless hours of help and his years of friendship.

Finally, I would like to thank all the friends I have made in College Station; they have made this place my home and constantly supported me; I am very fortunate to have them in my life and for that, I am grateful.

TABLE OF CONTENTS

Page

LIST OF FIGURES

LIST OF TABLES

1.INTRODUCTION

1.1 Ion Mobility Spectrometry

Ion mobility spectrometry (IMS) is a gas phase, electrophoretic technique that separates ions owing to differences in their collision cross sections (CCS) with a neutral gas, known as the drift gas, on an ultrafast timescale (μs-ms).[1-8] There are two main types of IMS: scanning and dispersive. In scanning IMS, ions of a certain mobility selection are constantly exiting the mobility analyzer. The constant output of mobility-selected ions allows for increased instrument duty cycle, however, the parameters of the separation must be scanned in order to obtain a complete mobility separation. The most common example of a scanning IMS analyzer is the differential ion mobility spectrometer (DMS), where ions are separated owing to the differences in their mobility under high and low electric fields. Because DMS facilitates separation by a difference in mobility, these devices are unable to provide CCS information. Thus, DMS and other scanning techniques are typically utilized for analytical separations where duty cycle is critical and CCS information is not needed.[9-13] In dispersive IMS, an ion packet, which typically contains all ionized analytes present in a sample, is injected into a mobility analyzer.[14-19] These ions then undergo mobility separation owing to the CCS differences and are subsequently detected. During the time it takes for one ion packet to traverse the mobility analyzer, any ions being produced by the source must be deflected or prevented from entering device, which, in turn, limits the overall duty cycle of the instrument. However, unlike DMS and other scanning techniques, dispersive IMS allows for an

entire mobility separation to occur with one ion packet. Additionally, because ions are separated solely based on their CCS, these values can be directly determined. Dispersive IMS techniques are typically utilized for CCS measurements and structural investigations. Drift tube or drift cell IMS (DT IMS), shown in Figure 1, is the most traditional example of a dispersive IMS instrument and operates by establishing an axial electric field (E_z) in the presence of the drift gas, which can range in pressure from mTorr to several hundred Torr.

Ions are injected into the drift cell and experience two opposing forces, namely the acceleration owing to E_z and a drag force owing to collisions with the neutral drift gas molecule. Upon several collisions, the ions adopt an average velocity, known as a drift velocity (V_d), which is the equilibrium between collisional dampening and reacceleration. The apparent V_d is defined by equation (1):[1]

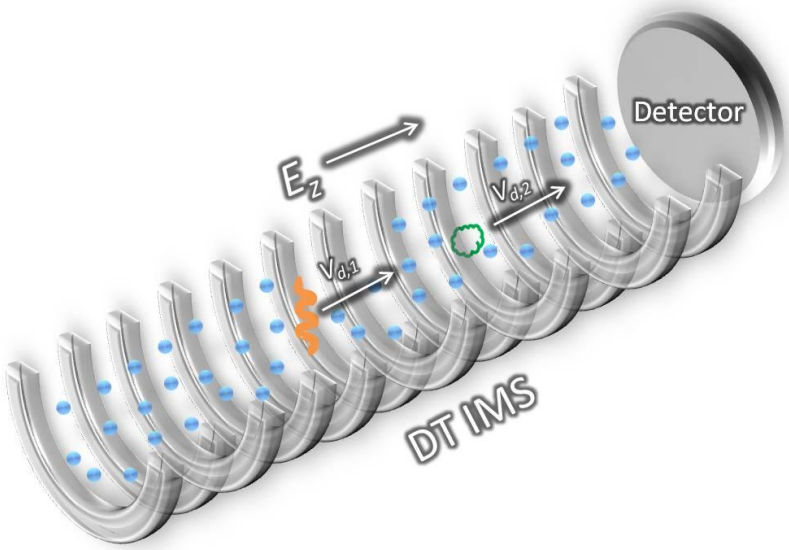

Figure 1: A representation of a DT IMS instrument. A voltage gradient is applied across a resistor string (not shown) that connects each electrode and establishes the E_z. Ions are introduced to the drift cell and are transported with a certain drift velocity, which is CCS dependent, through the drift gas (blue spheres). Upon traversing the drift cell, ions collide with a detector plate and are registered as an ion count. If two ions are introduced and have the same *m/z*, but differing conformations, the more elongated ion (orange) will drift at a slower velocity as compared to the more compact ion (green).

$$V_d = \mathrm{K}E_z \tag{1}$$

where K is the analyte specific mobility constant. In order to determine V_d, the drift time (t_d), or time it takes an ion to traverse the entire axial length (L) of the drift cell, can be determined by knowing the injection time and the detection time for an ion. This is related to V_d by equation (2):

$$V_d = \frac{L}{t_d} = KE_z \tag{2}$$

In order to compare K values that are taken at variable temperature and pressure regimes, the mobility constant is often expressed in terms of a normalized constant called the reduced mobility constant (K_0)[1], which is defined by equation (3):

$$K_0 = K\left(\frac{P}{P_0}\right)\left(\frac{T_0}{T}\right) \tag{3}$$

where P is the pressure (Torr) of the drift gas, P_0 is the standard pressure, T_0 is the standard temperature, and T is the temperature of the drift gas. The analyte dependent reduced mobility constant can then be expressed in terms of CCS by equation (4)[1, 20] :

$$K_0 = \frac{3ze}{16N_0}\left(\frac{2\pi}{\mu k_b T}\right)^{\frac{1}{2}}\frac{1}{\Omega} \tag{4}$$

where z is the charge of the ion, e is the elementary charge, N_0 is the standard particle number density of the buffer gas, μ is the reduced mass of the ion and drift gas, T is the temperature, and Ω is the CCS. By combining equations (1), (2), (3), and (4), the expression of CCS in terms of t_d is shown by equation (5):

$$\Omega = \left(\frac{3ze}{16N_0}\right)\left(\frac{2\pi}{\mu k_b T}\right)^{\frac{1}{2}}\left(\frac{t_d E_z}{L}\right)\left(\frac{P_o}{P}\right)\left(\frac{T}{T_0}\right) \tag{5}$$

Equation (5) shows that as the CCS increases, the t_d increases proportionally. Thus, if two ions with the same mass-to-charge (*m/z*) but differing sizes or conformations (i.e. different CCS) enter the drift cell, the ion with the larger size or more extended conformation would undergo more dampening collisions with the drift gas and thus would have a slower drift velocity as compared to the smaller, more compact ion. This conformational separation is the basis of the use of IMS as an analytical tool. While the application of IMS as a standalone separation is well suited for the separation of mixtures with large differences in mobility constants[21], as mixtures become more complex and more chemically similar, an added dimension of separation is needed to identify ions.

1.2 Ion Mobility-Mass Spectrometry

Incorporation of IMS with mass spectrometry (MS) allows for the direct determination of *m/z* and CCS for a specific ion.[22-29] There are a variety of mass analyzers that can be coupled to IMS; however, the choices that are compatible with DT IMS are often limited owing to the time scale of the IMS separation, which is typically on the order of hundreds to thousands of μs. Because of the fast time scale of IMS, the use of long acquisition mass analyzers, such as, Fourier transform ion cyclotron resonance mass spectrometers (FT ICR) and orbitraps have been limited with dispersive IMS techniques owing to a further reduction in instrument duty cycle.[30] Traditionally, dispersive IMS devices have been coupled to time-of-flight (TOF) and quadrupole mass

analyzers owing to the reduced timescale of the mass analysis, which allows for increased duty cycle.

With the development of the ion mobility-mass spectrometer (IM-MS), the analytically utility of the technique is most aptly shown with the separation of increasingly complex mixtures owing to the increased peak capacity relative to IMS or MS alone. The separation of ions by their CCS followed by the mass analysis, to obtain *m/z* information, allows for these data to be plotted in two-dimensional space with the arrival time distribution (ATD) or CCS being on the y-axis and *m/z* on the x-axis. Given that chemically similar compounds or classes, such as peptides, proteins, or hydrocarbons, have comparable atomic densities, these various classes result in distinct trendlines in two-dimensional space when analyzing several analytes from each chemical class.[2, 31-32] These trendlines may be selected and analyzed individually, which allows for a deconvolution of the mass spectra and an increase in the signal to noise ratio for the selected trendline. Moreover, in samples that contain large amounts of background, such as detergent or buffer, which dominate the spectra in a MS only mode, these interferences can often be removed with the selection of various trendlines in mobility space.[33]

1.3 Application of IM-MS to Structural Biology

While IM-MS presents an analytical tool capable of ultra fast size separations and aids in the analysis of complex biomolecule mixtures[31, 34-36], polymers[37-38], and peteroleum molecules[32, 39-40], IM-MS is also advantageous in the field of structural

biology. Traditionally, techniques such as x-ray diffraction (XRD) and nuclear magnetic resonance (NMR) spectroscopy are used to characterize the structure of peptide, proteins, and protein assemblies in a crystal or solution, respectively. While these techniques demonstrate excellent selectivity, they also have inherent limitations with regard to sample preparation, concentration requirements, and temporal resolution. The sample preparation for XRD analysis can be rigorous as the technique requires that the sample of interest be in a crystallized form.[41] Furthermore, NMR requires large sample concentrations and measures a conformational average of the structures present in solution.[42] While IM-MS analysis does not have the selectivity of either XRD or NMR, its dispersive nature allows for the analysis of multiple conformations and charge states of peptides, proteins, and protein complexes simultaneously. Additionally, with the incorporation of electrospray ionization (ESI) as a means to generate ions for IM-MS experiments, biological molecules can be sampled directly from their solution environments.[43]

ESI coupled to IM-MS has allowed investigators to analyze the gas-phase structure of analytes ranging from peptides to protein complexes.[44-58] While there is ongoing debate in regard to the correlation of the conformations measured with IM-MS and those present in solution, there have been several studies that have shown that ions can demonstrate solution memory effects.[48, 52, 54, 59-67] Furthermore, for several biomolecule ions, particularly ions of large proteins and protein assemblies, it has been demonstrated that the CCS measured via IM-MS is consistent with the calculated CCS for XRD determined structures.[57, 62, 68-69] These data indicate that the conformations

being measured by IM-MS can be consistent with the biologically relevant structure. While this growing body of evidence demonstrates the application of IM-MS to structural studies, there are several limitations to the use of it as a structural probe, namely IM resolution, sensitivity, and collisional activation.

The ability to separate various conformations of a charge state of an ion is directly tied to the resolution of the IM separation. When IM analysis is performed within the low field limit, i.e. ions do not obtain significant energy from the electric field, the resolution (FWHM) of the separation is limited by the diffusion of the ion swarm. The diffusion limited resolution (R_d) is defined by equation 6:[70-71]

$$R_d = \frac{1}{4}\left(\frac{qEL}{k_b T \ln(2)}\right)^{\frac{1}{2}} \tag{6}$$

where q is the ion's charge. Equation 6 only takes into account the resolution due to isotropic diffusion; however, during actual IM analysis there are other variables that can affect the observed resolution, including columbic repulsion, temporal width of the initial ion packet that is injected into the IM analyzer, and ion-neutral interactions. These effects can be minimized through optimization of sample concentration, IM gate width, and through the use of helium as a drift gas, respectively. Equation 6 shows that there are four variables that affect R_d: q, E, L, and T. Modifying these variables to enhance IM-MS studies has previously been shown[17, 72-79]; however, these modifications present difficulty owing to engineering limitations.

The use of ESI allows for the production of multiply charged analyte ions. Additionally, recent reports have demonstrated that the average charge state distribution can be increased through the use of supercharging reagents.[80-84] However, owing to the atmospheric nature of ESI, this ionization method increases the gas load within the instrument and subsequently increases the pumping requirements. Typical IM-MS CCS measurements are performed with a helium drift gas and thus gas poisoning from the ESI source (e.g., nitrogen) is a concern. Increasing *E* in IM-MS presents multiple challenges in regard to the engineering of the instrument, as well as considerations for, the analysis of biological analytes. As the voltage applied across the drift cell is increased, the potential for electrical breakdown is also increased.[85] While helium reduces complications associated with ion–neutral interactions during IM-MS analysis, it is also has the lowest breakdown potential for the pressure regime used in IM. Electrical break can be mitigated through the use of seeded gases such as SF_6;[86] however, the addition of these gases can alter the CCS measurements. Furthermore, increasing *E* increases the kinetic energy of the ion as it traverses the drift cell. An increase in kinetic energy can lead to collisional activation and conformational rearrangement, as well as, dissociation of covalent bonds.[57, 87-88] Decreasing *T* allows for decreased diffusion of the ion packet; however, presents challenges associated with thermal expansion and contraction.[89] Additionally, at reduced temperatures the effects of long range ion-neutral interaction potentials become more pronounced.[90] The variable that presents to fewest engineering challenges is an increase in the length of the drift cell; however, ion transmission decreases owing to an increase in radial diffusion with increased length.[15]

Thus, while mobility resolution will increase, the acquisition times and sample concentrations required to obtain an ATD may limit the use of a longer drift cell.

There have been several modifications performed to the traditional drift cell, termed a uniform field (UF) drift cell, which are able to increase overall ion transmission while preserving increased mobility resolution. Almost exclusively these modifications include the application of RF confinement.[17, 56, 91] Typically an RF ion funnel (RF IF) is placed in the drift cell to radial focus a diffuse ion packet[92] (Figure 2); however, examples of application of RF potentials to the electrodes throughout the drift cell to increase ion transmission have been reported.[56] While the use of such devices increases the transmission of ions through the drift cell, the application of RF potentials can potentially alter the conformational distribution of the ion population.[91, 93-94] Recently, an electrostatic alternative, termed Periodic Focusing (PF), has been shown to increase ion transmission while decreasing the radial electrical potentials required to confine ions.[15, 72, 95-97]

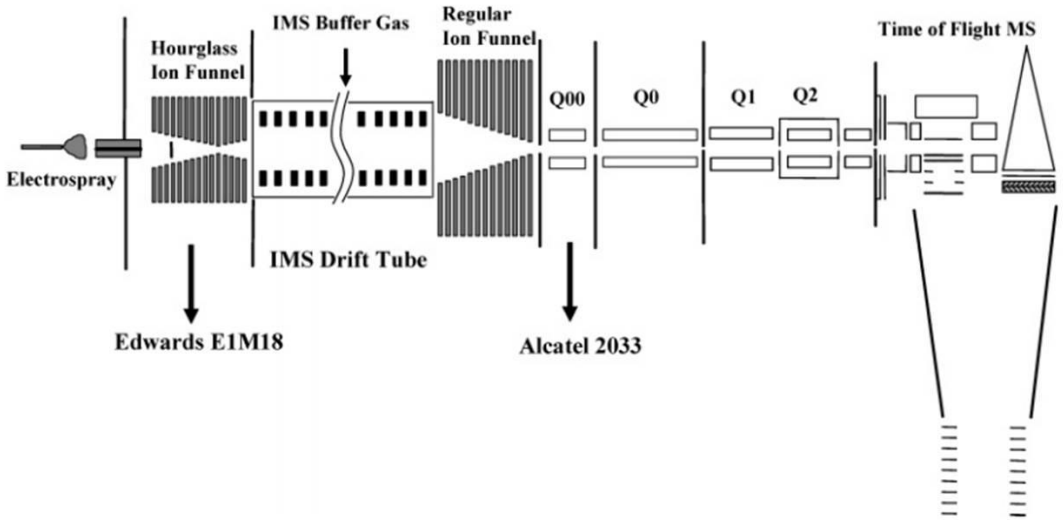

Figure 2: Schematic of an IM-MS instrument that utilizes an RF ion funnel to increase ion transmission through the IMS drift tube. Figure adapted from reference 92.

1.4 Periodic Focusing Ion Mobility Spectrometry

Periodic focusing ion mobility spectrometry (PF IMS) utilizes an electrostatic voltage, which establishes E_z, across the drift cell and operates at comparable pressures to that of UF IMS. However, while UF drift cells use large inner diameter electrodes, PF IMS uses smaller inner diameter electrodes that also have an increased width. This unique electrode geometry allows for the basis of the radial confinement mechanism present in PF IMS owing to fringing fields that penetrate the inner diameter of the electrodes (Figure 3). These fringing fields give rise to a radial component to the electric field, E_r. Additionally, both E_z and E_r oscillate 90 degrees out of phase, as shown by equations 7 and 8:[95-96]

$$\mathrm{E}_z\left(z\right) = \mathrm{E}_{0,z}\mathrm{COS}\left(\frac{2\pi z}{\lambda}\right) + \mathrm{E}_\mathrm{C} \tag{7}$$

where $E_{0,z}$ is the amplitude of the axial oscillation, λ is the wavelength as defined by the sum of the width and spacing of the electrodes, and E_c is the central axial electric field as defined by the voltage applied divided by L.

$$E_r(z) = E_{0,r} \sin\left(\frac{2\pi z}{\lambda}\right) \tag{8}$$

where $E_{0,r}$ is the amplitude of radial oscillation. Both $E_{0,z}$ and $E_{o,r}$ increase in magnitude at increasing radial distances as shown by figure 4:

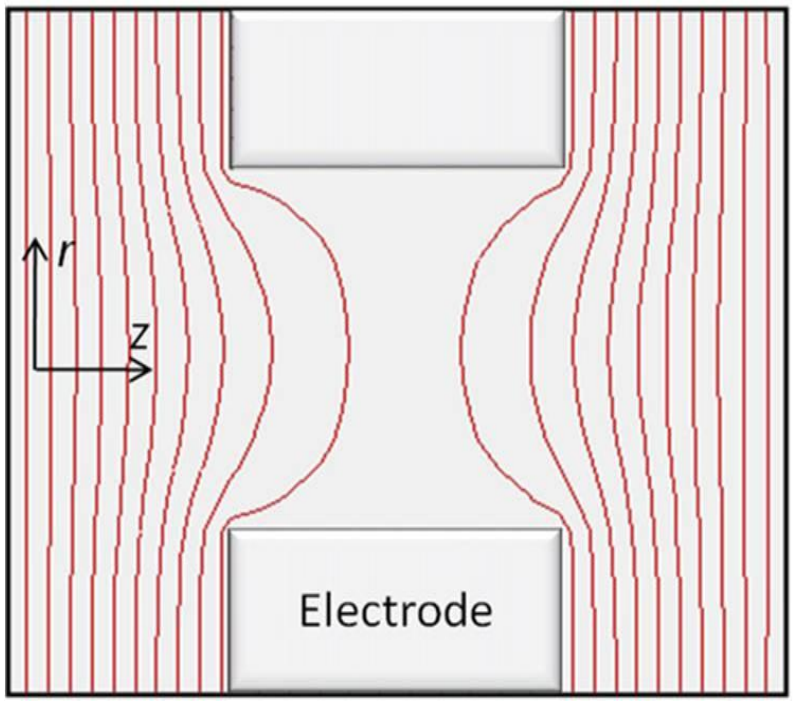

Figure 3: The equipotential lines established in the inner diameter of a PF IMS electrode. Owing to the penetrating electric fields, the lines are concave to the center of the electrode and provide for radial motion of the ion. Figure is adapted from reference 95.

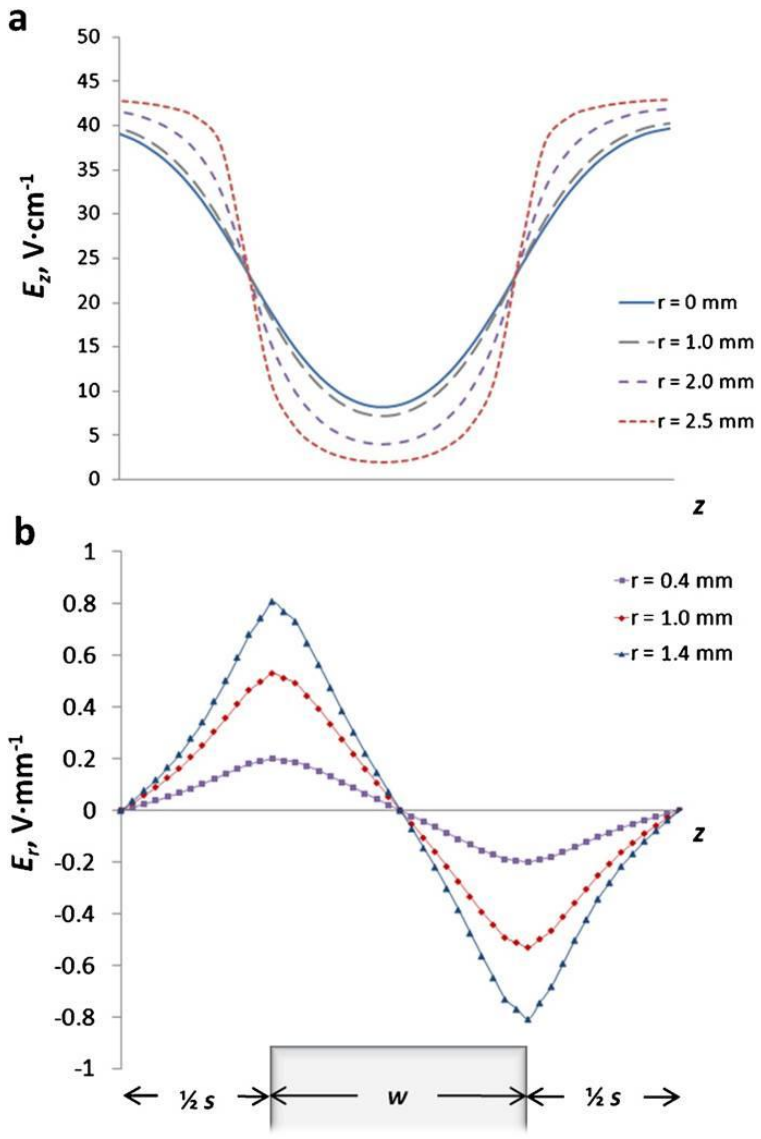

Figure 4: E_z (a) and E_r (b) of a PF IMS drift cell as a function of radial displacement. As an ion increases in radial displacement, the amplitude of the field oscillation for both the axial and radial components is increased. This leads to increased radial motion and collisional dampening at larger radial displacements. Figure is adapted from reference 96.

These oscillations give rise to the radial confinement mechanism, which can be defined by three discrete transport modes: (1) axial drift, (2) radial ripple, (3) central drift, which are depicted in Figure 5.[95-96]

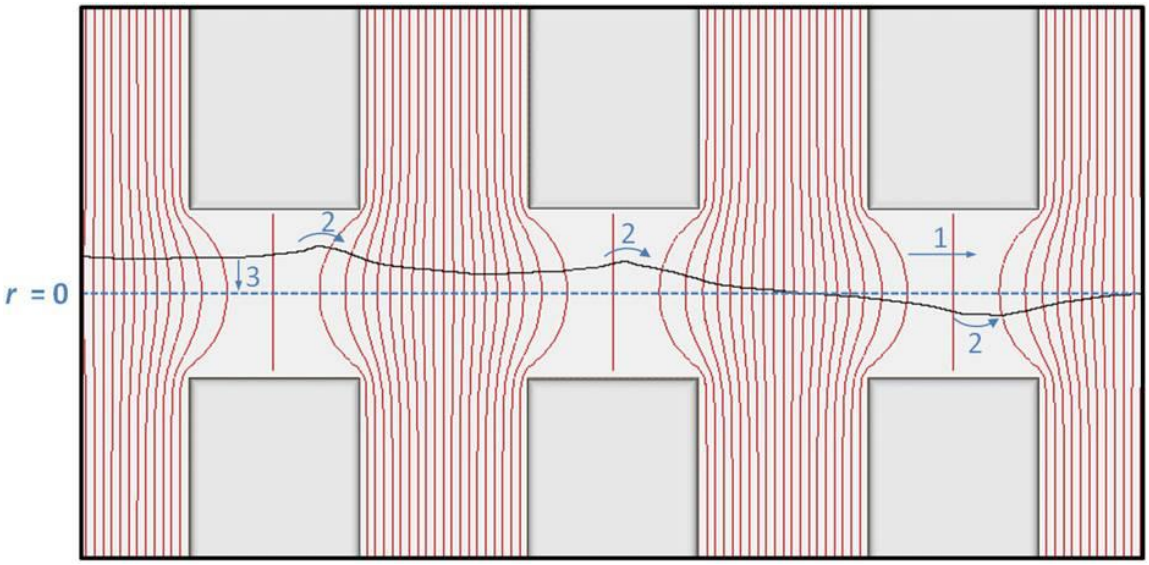

Figure 5: A SIMION depiction of a typical ion trajectory in a PF IMS drift cell. The three transport modes are denoted. Axial drift (1) describes the motion of the ion as it traverses the drift cell. The radial ripple (2) describes the radial variation that occurs as the ion enters and leaves an electrode. The central drift (3) describes the overall radial correction that occurs as the ion traverses multiple electrodes. Notice that the initial ion (black line) is displaced from the central drift axis (r = 0, dashed line). Upon traversing three electrodes, the ion has been radial focused on to the central drift axis owing to the three transport modes. Figure is adapted from reference 96.

Axial drift arises from the ion experiencing E_z as it traverses the drift cell; this is the transportation mode that gives rise to mobility separation. Owing to the oscillation of E_z, the ion's axial velocity, V_z, is dampened as the ions enter the inner diameter of the electrode and are subsequently reaccelerated toward the tailing edge of the electrode.

This collisional dampening and reacceleration is critical to the performance of a PF IMS drift cell as the ion must undergo momentum conservation to successfully traverse the drift cell, as well as, undergo collisional dampening in order to experience the subsequent transport modes. The radial ripple motion is due to the ion being subjected to the oscillations of E_r; as an ion enters the electrode, it undergoes radial displacement from the central axis of the drift cell (r =0); however, owing to the oscillation of E_r, the ion experiences radial correction, i.e. the ion is directed toward the central axis, at the tail end of the electrode. Finally, the last transport mode, the central drift, is a convolution of the first two transport modes and demonstrates the importance of collisional cooling as described by the effective potential, V^*, which is defined by equation 9:[98]

$$V^* = \frac{q^2 E_{0,r}(r)^2}{4m\Omega_{eff}^{\ 2}} \tag{9}$$

where Ω_{eff} is the effective RF experience by an ion traversing the device as defined by equation 10:[95-96]

$$\Omega_{eff} = \frac{2\pi V_z}{\lambda} \tag{10}$$

By combining equation 9 and 10 and removing constants, the dependence of V^* on the axial velocity can be determined (Equation 11).

$$V^* \propto \frac{E_{0,r}(r)^2}{V_z^{\ 2}} \tag{11}$$

While E_r oscillates symmetrically about E_r = 0 V cm^{-1} and thus does not affect the magnitude of V^*, Equation 11 shows that V^* is inversely proportional to the square of V_z

and as such, the magnitude of these potentials is increased at the back of the electrode owing to the collisional dampening. Thus, over several λ values, i.e. after an ion traverses several electrodes, an overall radial correction is observed. Collectively, these three transport modes allow for overall radial confinement and axial transport of an ion in the PF IMS drift cell. This leads to an increase in the overall transmission of the device as compared to a traditional UF IMS drift cell as shown by Figure 6.

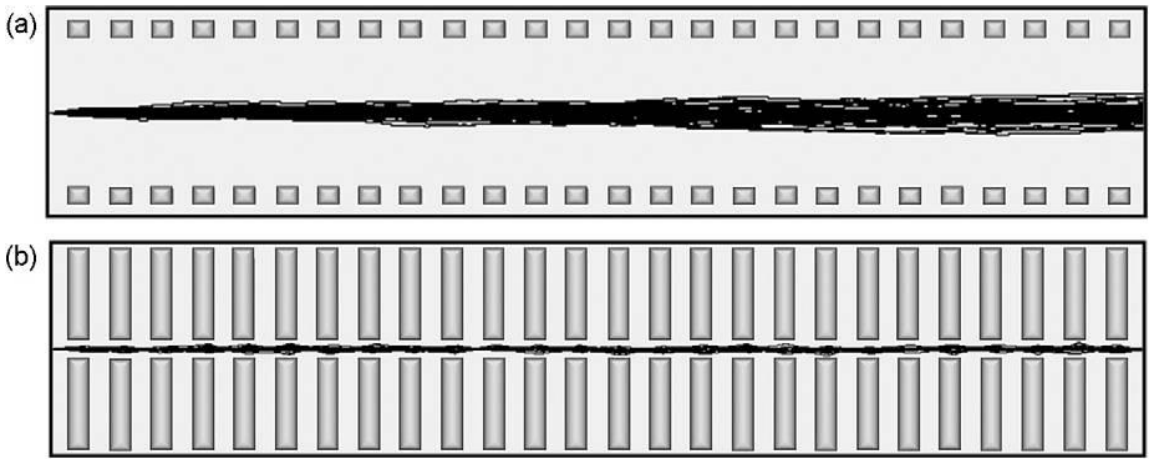

Figure 6: A comparison of UF IMS (a) ion trajectories (black lines) versus ion trajectories present in PF IMS (b). Because UF IMS does not possess any radial confinement mechanism, ions undergo radial diffusion, which limits transmission through the conductance limiting aperture located at the back of the drift cell. Conversely, PF IMS shows radial confinement and a decrease in the radial diffusion of the ion swarm owing to the three transport modes. Figure is adapted from reference 95.

Additionally, it has been empirically demonstrated that PF IMS allows for the determination of CCS similarly to UF IMS[97]; however, owing to the radial motion of the ion, a dampening factor, α, must be incorporated into equation 5, which gives:

$$\Omega = \left(\frac{3ze}{16\mathrm{N}_0}\right)\left(\frac{2\pi}{\mu k_b T}\right)^{\frac{1}{2}}\left(\frac{t_d \alpha E_z}{L}\right)\left(\frac{\mathrm{P}_0}{P}\right)\left(\frac{T}{\mathrm{T}_0}\right) \tag{12}$$

Alpha originates owing to the axial dampening that occurs within the electrode of the PF IMS drift cell. This leads to an increased number of collisions per unit axial distance, n_z. Thus, α can be represented by equation 13:[97]

$$\alpha = \frac{\mathrm{K}_{0,\,\mathrm{PF\ IMS}}}{\mathrm{K}_{0,\,\mathrm{UF\ IMS}}} = \frac{1/n_{z,\,\mathrm{PF\ IMS}}}{1/n_{z,\,\mathrm{UF\ IMS}}} \tag{13}$$

Computational and empirical determination of α as a function of charge state has recently been reported and has shown excellent agreement (≤4% difference) between CCS values determined by UF IMS versus PF IMS.

Collectively, these results demonstrate that PF is capable of providing radial focusing with electrostatic potentials. Moreover, the amplitude of the radial electric field is reduced as compared to that of traditional RF devices and may indicate that the collisional activation that an ion experience within the PF device may be less than that experienced in RF devices. While the PF IMS drift cell has eliminated the need for RF ion funnels within the drift cell, these devices are commonly used in combination with ESI sources prior to IMS separation.[99-101] The collective results of the PF IMS drift cell suggest that a device analogous to the RF ion funnel may be possible. Work presented herein describes the development and characterization of a PF ion funnel.

2. DEVELOPMENT OF THE PERIODIC FOCUSING ION FUNNEL: THE 8-4 FUNNEL

2.1 Introduction

Mass spectrometry (MS) is an analytical technique that is capable of the rapid analysis (ns-ms) of analyte ions.[102-105] However, the application of this technique to the analysis of biological molecules was limited until the development of modern ionization techniques, such as, matrix-assisted laser desorption ionization (MALDI)[106-108] and electrospray ionization (ESI)[43, 109]. ESI allows for the direct sampling of biological analytes from solution environments. The ionization is facilitated by directing infusing an analyte solution into an emitter that is biased a high (+/- 2-4 kV) electric potential with respect to a counter electrode. Typically, the counter electrode is a heated inlet and serves two functions. The first is to enhance the desolvation of the solution droplets, while the second is to act a pressure differential region. ESI is typically performed at atmospheric pressure (760 Torr) and the ions are transported into a vacuum region of the instrument. Upon entering this vacuum region, ions and neutrals undergo expansion owing to the pressure differential and thus ions become radial diffuse, which leads to low ion transmission at conductance limiting apertures.

A similar problem exists with UF IMS separations; where conductance-limiting apertures are used owing to the pressure differential of the drift cell (1-5 Torr) and the mass analyzer region (10^{-4}-10^{-7} Torr). As the ion swarm traverses the UF IMS drift cell, the ions undergoes axial and radial diffusion.[15] While axial diffusion will reduce the

resolution of the measurement, radial diffusion limits ion transmission through the terminal aperture, reducing the sensitivity.

RF focusing devices, namely the RF ion funnel (IF)[99-101, 110-112] are typically utilized to increase the sensitivity of mass spectrometers and UF IMS drift cells by providing radial focusing of the ion packet. Schematically, the RF IF consists of a series of thin ring electrodes. Across the entire device, the inner diameter of the electrodes is tapered and a DC potential and RF waveform is applied. When axial momentum is conserved, a pseudo potential (V*) is generated and provides radial confinement and increased ion transmission. Additionally, ions may be accumulated within the RF IF to increase ion density and duty cycle of gated experiments. However, the use of RF devices has been shown to induce collisional activation of biological moles and thus may be detrimental to the preservation of native-like conformations.[91, 93-94]

Previously our lab has demonstrated that radial confinement can be achieved through the use of a DC only drift cell, that has been termed the PF IMS drift cell.[15, 72, 95-97] Through the reduction of the inner diameter of the electrodes, as well as, the presence of momentum dampening collisions, ions experience an effective RF. However, the effective RF voltage, peak-to-peak (V_{p-p}), is less than 1 V, whereas, traditional RF devices typically utilize higher electric potentials such as Vp-p values typically ranging from 50-300V. The ability of the PF IMS drift cell to increase ion transmission without the use of RF lead to the investigation of a DC device analogous to the RF IF. Herein the development of the first generation periodic focusing ion funnel (PF IF) and ion trap (PF IT) is described.

2.2 Experimental

The optimal electrode geometry of the PF IF was determined through simulation of $[C_{60}]^{\cdot+}$ ion trajectories using the *collision_hs1.lua* that is provided with SIMION 8.1 (Scientific Instrument Services, Ringoes, NJ). The simulated pressure was 1 Torr and the ions were given a CCS of 124 $Å^2$. Transmission was studied by creating a Gaussian distribution of the ion in front of E1 and recording the number of ions that successfully traverse the device. Modeling of the trapping capabilities of the PF IT was performed by varying simulated electric potential on each electrode. Initial kinetic energies are denoted for individual experiments. Optimization of the turning optic design utilized pressures of 0.75, 1.00, 1.25 Torr and were modeled using the bradykinin $[M+2H]^{2+}$ ion.

Solutions of bradykinin and cytochrome C were prepared to a concentration of 0.5 mg mL^{-1} in 50:49:1% methanol:water:acetic acid, v:v. These solutions was infused into a pulled silica ESI emitter at 500 nL min^{-1}, where the emitter was biased at +1.7-2.0 kV with respect to the heated capillary. Ion current measurements were performed on various electrodes in the source and drift cell assembly in order to determine optimal transmission tuning voltages.

2.3 Results and Discussion

2.3.1 Simulation of the PF IF

In order to maximize ion transmission, three different geometries for the PF IF were investigated using ion trajectory simulations. The three models varied by the width of the electrode elements, which were 4 mm, 6 mm, and 8 mm for model 1, 2, and 3,

respectively. Each model consisted of 5 electrode elements. The electrodes were spaced 6 mm apart in each model. The simulated ion transmission for each model was 51%, 93%, and 91%, respectively (Table 1).

Electrode Width	Ion Transmission, %
2mm	51 ± 6
4 mm	93 ± 2
6 mm	91 ± 3

Table 1: Simulated ion transmission for the three models that have various electrode widths that comprise the PF IF.

The simulated ion trajectories for each model are shown in Figure 7. Model 1 has reduced ion transmission owning to a reduction in the radial correction efficiency. Similar to the PF IMS drift cells, the radial focusing properties of the PF IF are dependent on the dampening of the axial momentum within the electrode in order for radial motion to occur; however, owing to the reduced electrode width of model 1, the momentum is not dampened efficiently enough to facilitate this motion. The ion trajectories shown for model 1 (Figure 7a) are predominately straight when the ion is in the electrode and shows no sign of the radial ripple or central drift motion described for the PF IMS drift cell. Ion trajectories for model 2 and 3 (Figure 7b,c) both show the radial ripple and central drift motion owing to the increase width of the electrodes allowing for sufficient dampening of the axial momentum of the ion. Thus, the simulated ion transmission for these two models is >90%. The ion transmission for

model 2 does appear to be slightly higher than model 3. Just as was the case with reduced ion transmission of model 1, the amount of momentum dampening is dependent on the width of the electrode. While model 1 shows reduced ion transmission from a lack of dampening, the slight reduction in ion transmission of model 3 as compared to model 2 may originate from an increased percentage of ions losing all axial momentum within the wider 8 mm electrodes. Because model 2, termed the PF $IF_{8\text{-}4}$, has the highest simulated ion transmission, it will be the basis for future development of the ESI source.

2.3.2 Simulation of the PF IT

The periodic focusing ion trap (PF IT) is designed similarly to the PF $IF_{8\text{-}4}$. It consists of 7 electrode elements (Figure 8). The width and spacing of these elements are 4 mm and 6 mm, respectively. The inner diameter of each electrode is listed in Table 2. The trap is designed to allow for ions to accumulate within this region during the time between gating events for ion mobility measurements. In order to facilitate this trapping, the electric field of the PF IT must be alternated so that ions will oscillate axially within the device.

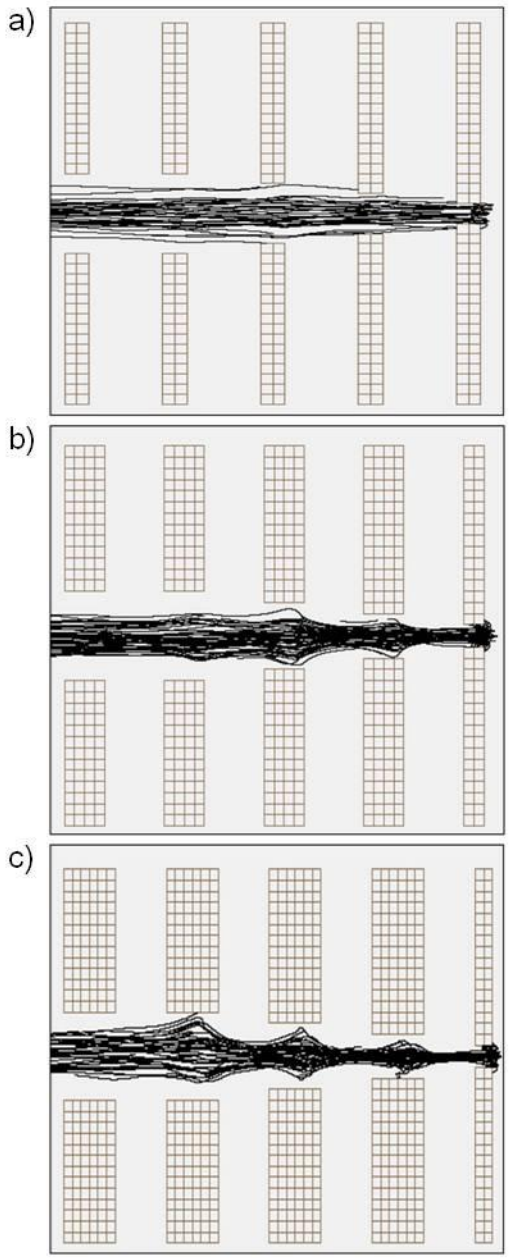

Figure 7: Simulated ion trajectories are shown for PF IF model 1 (a), 2 (b), and 3 (c). The simulated ion was representative of the $[C_{60}]^{-+}$ ion. The initially starting conditions for the ion packet were 4 mm before the opening of the PF IF with a Gaussian radial distribution centered on the central drift axis ($r = 0$) with a standard deviation of 1 mm. The initial kinetic energy was 2000 eV. Ions were considered successfully transmitted upon breaking the plane defined by the last electrode.

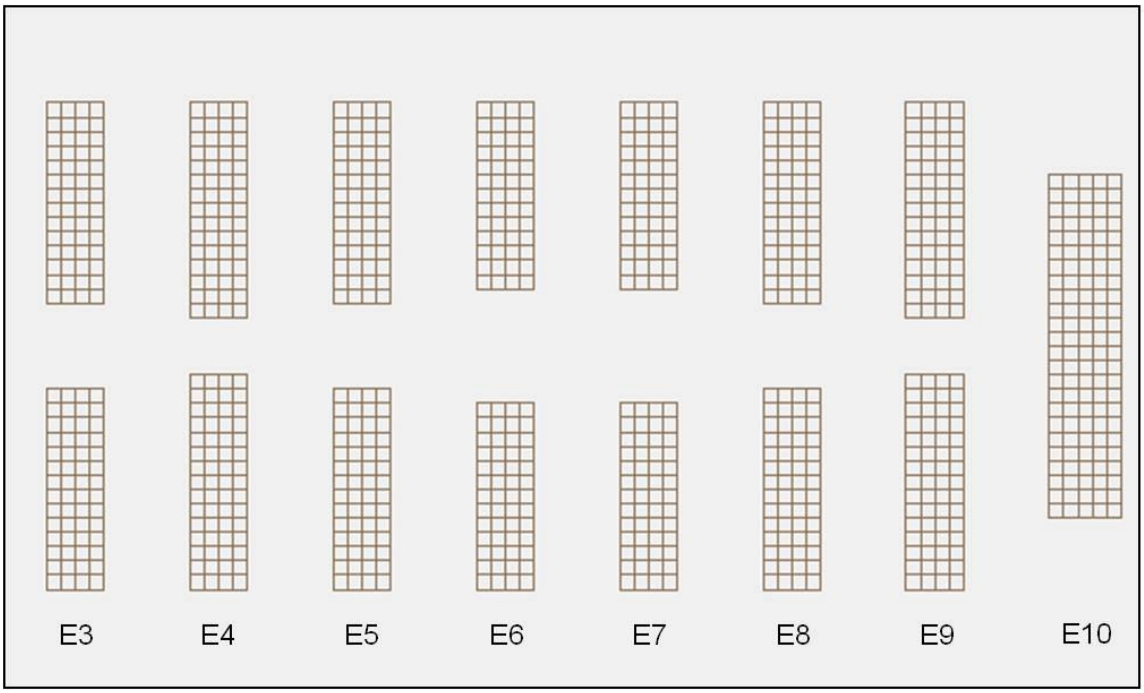

Figure 8: Depiction of the SIMION model of the PF IT. The electrodes are numbered E3-E10. The width of the electrodes is 4 mm and they are spaced 6 mm apart.

Electrode	Inner diameter, mm
E3	6
E4	4
E5	6
E6	8
E7	8
E8	6
E9	4
E10	0

Table 2: The inner diameter of each electrode used in the initial PF IT simulation.

Several simulation experiments were carried out to further characterize the PF IT. The peptide bradykinin, BK, was used as a model ion. The axial position $[BK + 2H]^{2+}$ and $[BK+H]^{+}$ ions were determined using ion trajectories simulations. In order to determine the frequency at which the electric field must be switched, the time-of-flight (TOF) required to traverse the device for each species was calculated. The TOF of $[BK + 2H]^{2+}$ and $[BK +H]^{+}$ was 81 ± 4 μs and 168 ± 17 μs, respectively. Owing to the increased charge, the $[BK + 2H]^{2+}$ ions have the shortest TOF and thus dictates the frequency of the electric field oscillations. The electric field for was alternated at 14.3 kHz, which corresponds to electric field oscillating every 70 μs. The axial position of the $[BK + H]^{+}$ and $[BK + 2H]^{2+}$ ions as a function of time shows that the ions oscillate within the PF IT (Figure 9).

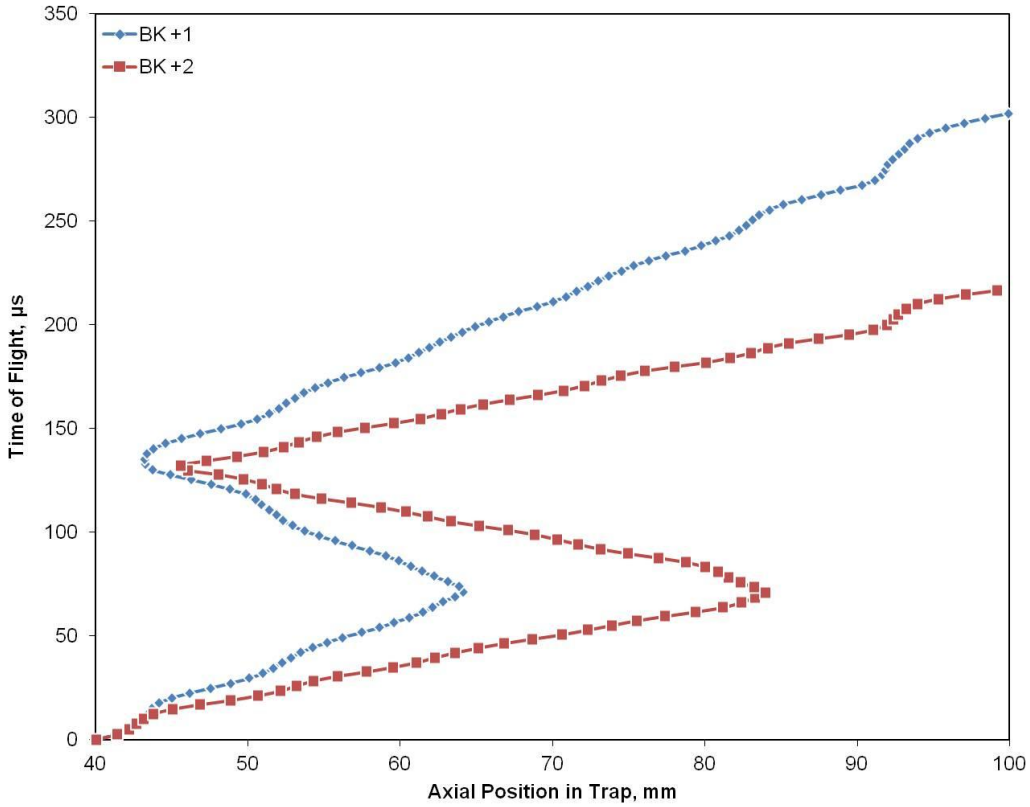

Figure 9: The axial position of $[BK + H]^+$ and $[BK + 2H]^{2+}$ within the trap during a single trapping cycle. Axial position is plotted on the x-axis for clarity. The initial ion parameters were 2 eV of kinetic energy and a 37 mm axial position with a Gaussian radial distribution centered on the central drift axis with a standard deviation of 0.5 mm.

One pulse cycle of the PF IT shows that ion losses are ~5-10%. These losses are primarily due to ions that are axial thermalized upon the switching of the electric field, which can occur when an ion is located within the inner diameter of the electrodes. Nevertheless, these data suggest that the PF IT is capable of trapping ions axially and successfully transmitting them through the final electrode. Moreover, the ion density will increase with each pulse cycle, as ions will enter the trap when the electric field is

not switched and thus the total ion population with increase in spite of the <10% loss upon electric field switching.

2.3.3 Combining the PF IF and PF IT

Ion simulations of various models of the PF IF and PF IT combined were preformed in order to determine the optimal number of electrodes and electrode inner diameter. The three models are depicted in Figure 10 and the inner diameter of each electrode element is listed in Table 3. Ions were considered transmitted upon crossing the plane defined by the last electrode element.

Simulated ion transmission for various charge states of C_{60} ion are shown in Table 4. Model 1 shows a reduction in ion transmission the $[M]^+$ species as compared to model 2 and model 3. The reduced ion transmission originates from the reduced inner diameter of the electrodes E5 and E12. Because of the reduced inner diameter, the dampening of the electric field within this electrode is increased and thus ions are thermalized and collide with the electrode wall. Model 2 eliminates the first 2mm electrode from the assembly and thus a 10% increase in ion transmission for the singly charged ion is observed; however, ion transmission is not optimal owing to the remaining 2 mm inner diameter electrode (E10). Model 3 eliminates all 2mm inner diameter electrodes and thus has the highest ion transmission for a singly charged ion, 93%. By eliminating these 2 mm inner diameter electrodes, the ion transmission is similar to that calculated for the PF $IF_{8\text{-}4}$, which demonstrates the transfer to the PF IT does not produce significant ion losses for the $[M]^+$ species.

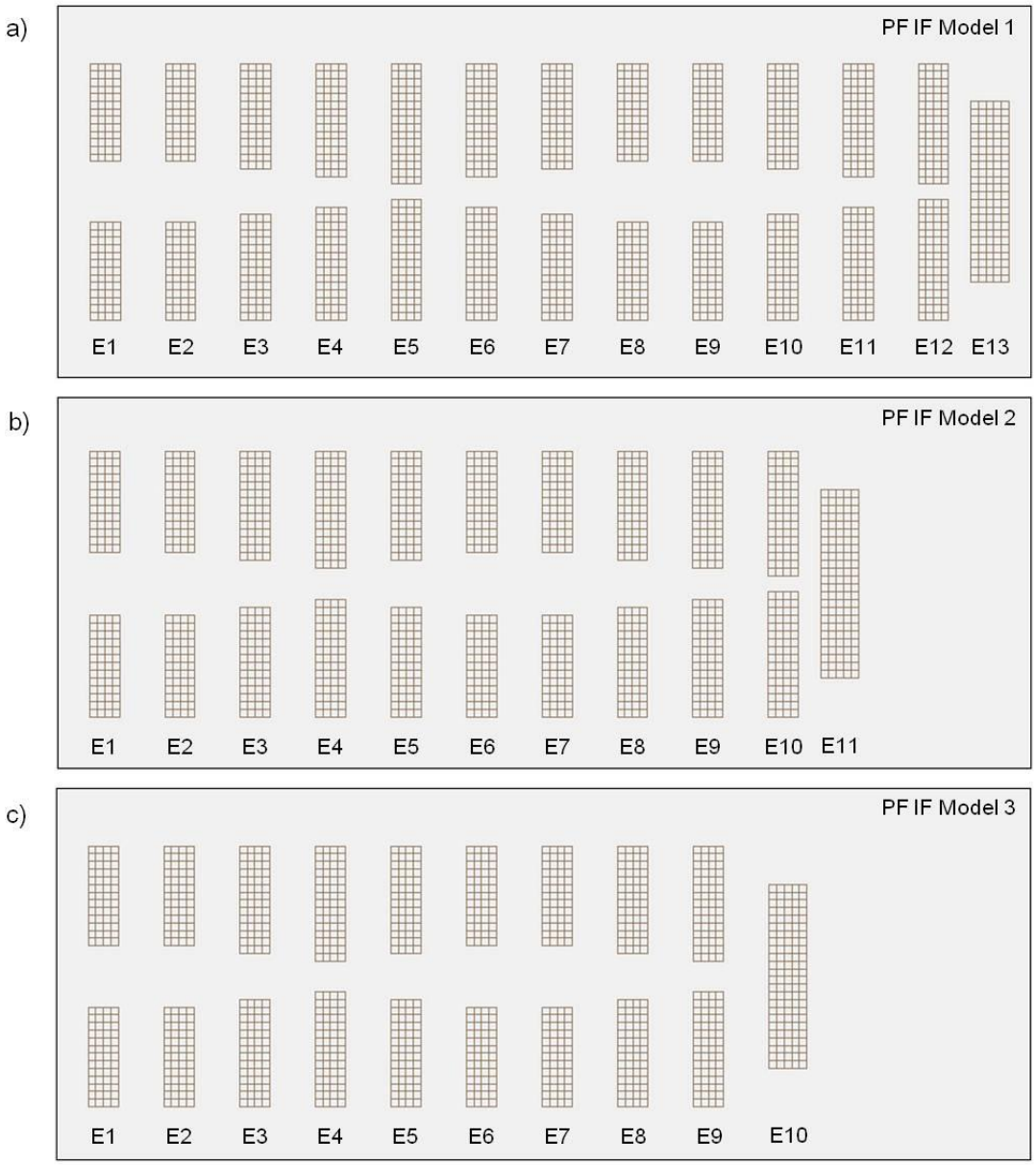

Figure 10: SIMION depictions of the various models of the PF IF combined with the PF IT.

	Electrode Inner Diameter, mm		
Electrode	Model 1	Model 2	Model 3
E1	8	8	8
E2	8	8	8
E3	6	6	6
E4	4	4	4
E5	2	6	6
E6	4	8	8
E7	6	8	8
E8	8	6	6
E9	8	4	4
E10	6	2	End Plate
E11	4	End Plate	—
E12	2	—	—
E13	End Plate	—	—

Table 3: Inner diameter of each electrode element for the PF IF-PF IT models is listed.

	Ion Transmission, %		
Charge State	Model 1	Model 2	Model 3
+1	59 ± 5	69 ± 6	93 ± 1
+2	86 ± 3	91 ± 3	97 ± 2
+3	88 ± 4	94 ± 1	99 ± 1
+4	89 ± 2	94 ± 2	99 ± 1
+5	91 ± 1	93 ± 2	98 ± 2
+6	93 ± 1	96 ± 2	99 ± 1
+7	94 ± 1	97 ± 2	99 ± 1
+8	93 ± 2	96 ± 1	99 ± 1
+9	95 ± 3	96 ± 2	100 ± 1
+10	93 ± 1	97 ± 1	100 ± 1

Table 4: Ion transmission of simulated $[C_{60}]^{\cdot+}$ ions is shown. Each charge state assumed a CCS value of 124 $Å^2$.

The ion transmission increases for all models as the charge state increases. This increase is most notable for model 1. As the charge increases, the kinetic energy the ions obtain while traversing the device also increases. Thus, the increased momentum is not quenched when the ion enters the 2mm inner diameter electrodes. It should be noted that this model assumes the CCS of all charge states of the modeled ions is the same and thus undergo similar numbers of collisions per unit distance. However, for biological systems, higher charge states are typically observed as the mass of the analyte increases and these higher charge states are often more elongated, i.e., a larger CCS.[65, 74, 113-114] An increase in CCS would subsequently increase the number of collisions per unit distance, i.e. increase axial momentum dampening, and decrease overall ion transmission. Nevertheless, the simulations of the PF IF-PF IT models show that an optimized geometry for the device is capable of transmitting >90% of ions that enter the device.

2.3.4 Designing the ESI source

Incorporating the PF IF-PF IT design into an ESI source presents several design challenges that must be addressed. The primary challenge is gas purity within the PF IF-PF IT electrodes. Because the radial focusing mechanism relies on the balance of momentum dampening and acceleration, the drift gas composition is critical to the performance of the device. Owing to increased mass and polarizibility, the momentum of the ion is quenched more readily with nitrogen than helium. Thus, as the partial pressure of nitrogen with the PF IF-PF IT region increases, ion transmission will decrease. Nitrogen is inherent with ESI sources as a continual stream of atmospheric gas

is directed into the instrument via the heated capillary or inlet. In order to maintain gas purity, the source was designed to contain two regions: the PF IF housing and the source housing (Figure 11). The PF IF electrodes are encased within a Delrin housing and sealed using O-rings; helium is supplied directly to this region. A counter flow of helium is established within the PF IF housing by pumping the second region of the source. The source housing is pumped using a 13 L min^{-1} rough pump.

ESI is facilitated through the use of a pulled silica tip emitter (not shown) and a heated capillary. The pulled silica emitter is positioned ~2-5 mm away from the capillary inlet, which is maintained at 343 K to facilitate desolvation of the ions upon ionization. The capillary is mounted on an adjustable bellows system to allow for the fine-tuning of capillary position to maximize ion transmission. The source housing is made of Delrin and sealed with O-rings. All parts for the source were designed using Solidworks software and machined in the Texas A&M University Chemistry Department machine shop. CAD drawings of all parts within the assembly are included in Appendix A.

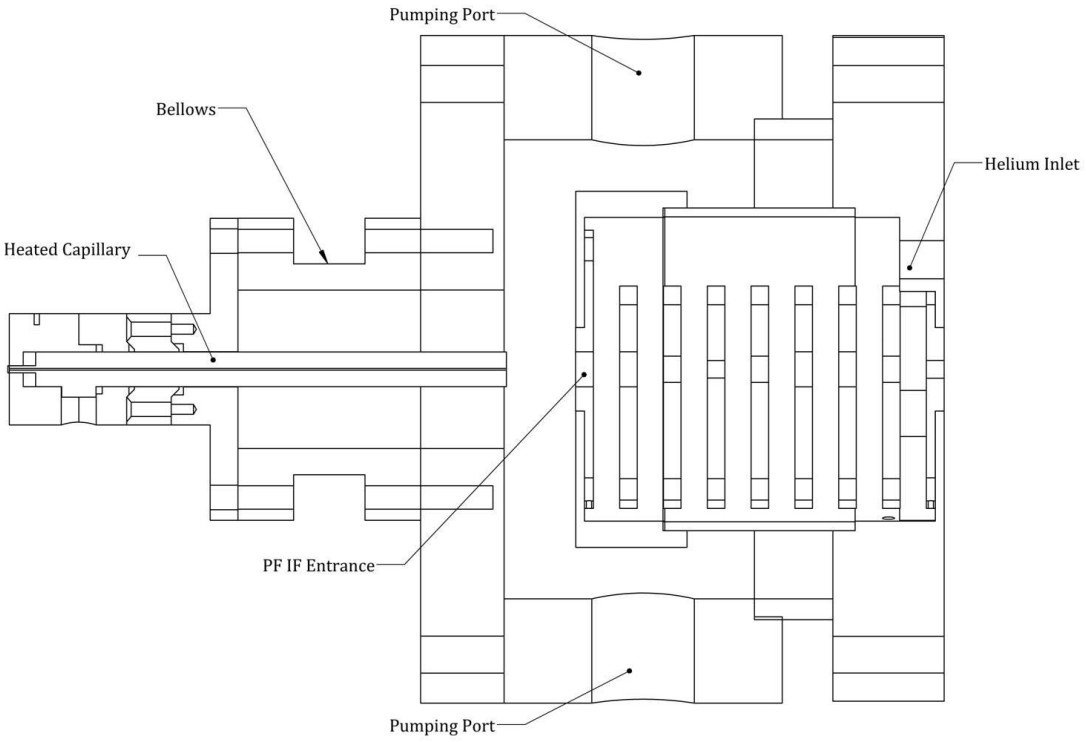

Figure 11: Cutaway schematic of the ESI source. The heated capillary, bellows, PF IF entrance, pumping ports, and helium inlets are marked. The PF IF is encapsulated in a Delrin housing and sealed using Buna O-rings. Helium is supplied directly to this region in order to establish a counter flow and prevent nitrogen contamination of the focusing electrodes.

Upon construction of the ESI source, the counter flow of helium was not adequate to prevent nitrogen from entering the PF IF housing. This is due to the pressure drop between atmosphere and the source housing, which is two orders of magnitude greater than the pressure drop between the PF IF housing and the source housing. Thus, the partial pressure of nitrogen within the PF IF region would decrease the overall ion transmission. To address this problem, the heated capillary can be positioned orthogonal to the PF IF entrance. The momentum of the atmospheric gas

would carry the majority of this gas past the PF IF housing and increase helium purity; however, with an orthogonal design, the ions must be extracted from the gas stream and turned toward the entrance of the funnel through the use of ion turning optics.

2.3.5 Development and simulation of orthogonal turning optics

Three different models of turning optics were characterized via ion trajectory simulation (Figure 12). The first model utilizes a quadrupole type design, which has 4 cylindrical rod electrodes that can be independently biased. Additionally, an added shielding electrode was added to the heated capillary to prevent penetrating fields from E1 from affecting the ion trajectory. The second and third turning optic models utilize a wedge and ring electrode. The potential on these elements can be independently varied. The wedge electrode dimensions are 12 mm length and width with a 45-degree angle with respect to the heated capillary. The ring electrode is 3 mm thick and has an inner diameter of 26mm, model 2, and 18 mm, model 3.

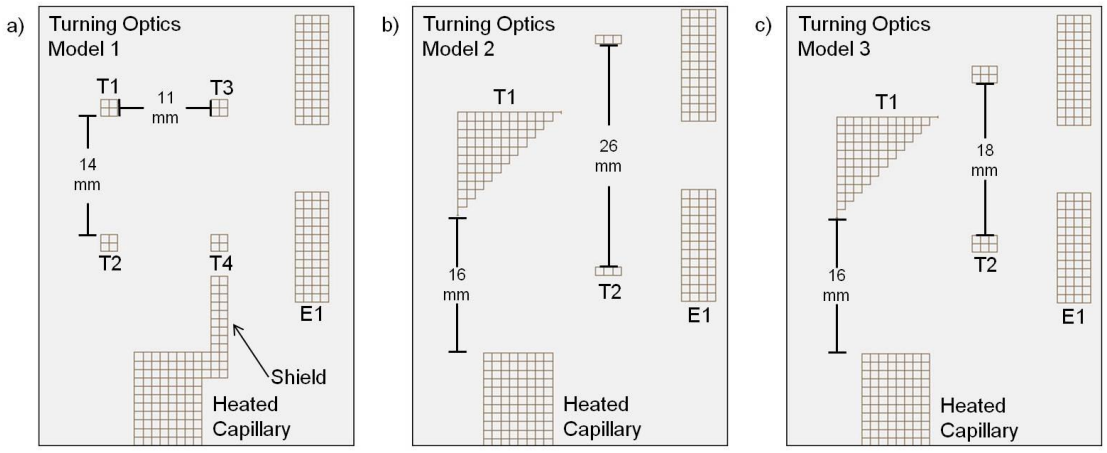

Figure 12: SIMION depictions of the three various turning optic models (a-c) that are examined to determine optimal ion extraction efficiency are shown. Model 1 consists of a quadrupole bender design, which consists of 4 rod electrodes (T1-T4). Model 2 and 3 consist of a wedge (T1) and ring (T2) electrode. The inner diameter of T2 is 26 mm for model 2 and 18 mm for model 3. The first electrode element (E1) of the PF IF-PF IT region is shown. Each depiction is truncated and the remainder of the PF IF-PF IT region is not shown.

Ion transmission as a function of pressure and charge state was determined for each turning optic model. C_{60} ions with a CCS of 124 $Å^2$ were used to simulate ion trajectories. Additionally, the charge state was varied from +1 to +11 to investigate the charge dependence of ion transmission for each model. Three different pressures, 0.75, 1.00, and 1.25 Torr, were simulated as they represent typical pressures achieved with the inline source design. Ions were considered transmitted upon entering the inner diameter of the PF IF-PF IT region and traversing the entire device. Ion transmission results are shown in Table 5.

Charge State	Turning Optics Model 1			Turning Optics Model 2			Turning Optics Model 3		
	0.75 Torr	1.00 Torr	1.25 Torr	0.75 Torr	1.00 Torr	1.25 Torr	0.75 Torr	1.00 Torr	1.25 Torr
+1	71 ± 3	72 ± 4	51 ± 4	75 ± 5	78 ± 3	54 ± 3	78 ± 7	80 ± 4	45 ± 7
+2	76 ± 1	77 ± 5	76 ± 5	79 ± 1	85 ± 2	85 ± 2	88 ± 2	95 ± 3	84 ± 3
+3	73 ± 6	80 ± 4	75 ± 5	84 ± 4	89 ± 3	88 ± 5	87 ± 4	96 ± 2	94 ± 3
+4	76 ± 4	79 ± 7	75 ± 4	83 ± 4	84 ± 4	89 ± 2	90 ± 3	95 ± 1	95 ± 2
+5	77 ± 4	77 ± 3	71 ± 4	83 ± 4	87 ± 4	88 ± 4	89 ± 2	98 ± 2	98 ± 2
+6	77 ± 4	78 ± 7	69 ± 4	84 ± 4	87 ± 3	90 ± 5	91 ± 3	98 ± 1	98 ± 2
+7	75 ± 4	82 ± 5	67 ± 5	87 ± 4	90 ± 5	86 ± 5	91 ± 5	96 ± 3	98 ± 1
+8	76 ± 4	79 ± 1	65 ± 4	87 ± 4	87 ± 2	87 ± 3	91 ± 1	98 ± 1	97 ± 1
+9	76 ± 6	78 ± 7	64 ± 6	85 ± 2	90 ± 2	87 ± 4	91 ± 2	99 ± 1	97 ± 2
+10	76 ± 6	78 ± 5	62 ± 3	89 ± 3	87 ± 3	87 ± 4	92 ± 3	96 ± 2	98 ± 1
+11	77 ± 5	75 ± 7	57 ± 4	83 ± 4	89 ± 2	84 ± 5	92 ± 3	98 ± 1	99 ± 2

Table 5: Average simulated ion transmission for turning optics model 1, 2, and 3 for various charge states of the C_{60} ion, assuming a constant CCS. The average value is reported with +/- one standard deviation. The initial placement of the ions was at the surface of the heated capillary and the initial kinetic energy was 3500 eV.

These ion simulation results demonstrate that model 3, the wedge and 18 mm inner diameter ring electrode, produces the highest ion transmission for all pressures investigated, with the exception of the singly and doubly charged ion at 1.25 Torr. Additionally, these data suggest that the optimal pressure needed is 1.00 Torr. At higher pressures, the ion transmission is reduced owing to diffusion and collisions with the ring electrode, which originates from a combination of effects. Because of the increased number density associated with higher pressure, the analyte ion will undergo increased number of collisions while traversing the device. Thus, these ions can be thermalized when present in the reduced axial field present in the electrodes. This is further demonstrated by the significant reduction in ion transmission for the $[M]^+$ versus the $[M]^{2+}$ species at all pressures. Owing increased kinetic energy imparted by having an additional charge, the $[M]^{2+}$ species is not thermalized and its ion transmission is ~25-50% greater than that of the $[M]^+$ species. Conservation of axial momentum can be

enhanced by increasing the axial electric field within the PF IF; however, this increase may not be advantageous as structural conversion and collision induced dissociation can occur at higher electric fields. Transmission is also reduced at higher pressure owing to the ions not focusing into center of the inner diameter of E1. Both effects are demonstrated by simulation of the $[BK + 2H]^{2+}$ ion at the three pressures (Figure 13). The initial kinetic energy of the ions is not completely dampened when the pressure is 0.75 and 1.00 Torr and thus the ion packet is directed into the inner diameter of E1; however, at 1.25 Torr, the initial kinetic energy is dampened and the ion optics direct the ions into E1. However, experimental tuning of the turning optics may increase the transmission efficiency in this region by varying the projection of the ion packet within the inner diameter of E1. Nevertheless, model 3 offers high ion transmission for multiple charges for pressures of 0.75-1 Torr and presents an option for incorporating an orthogonal source design in order to increase gas purity.

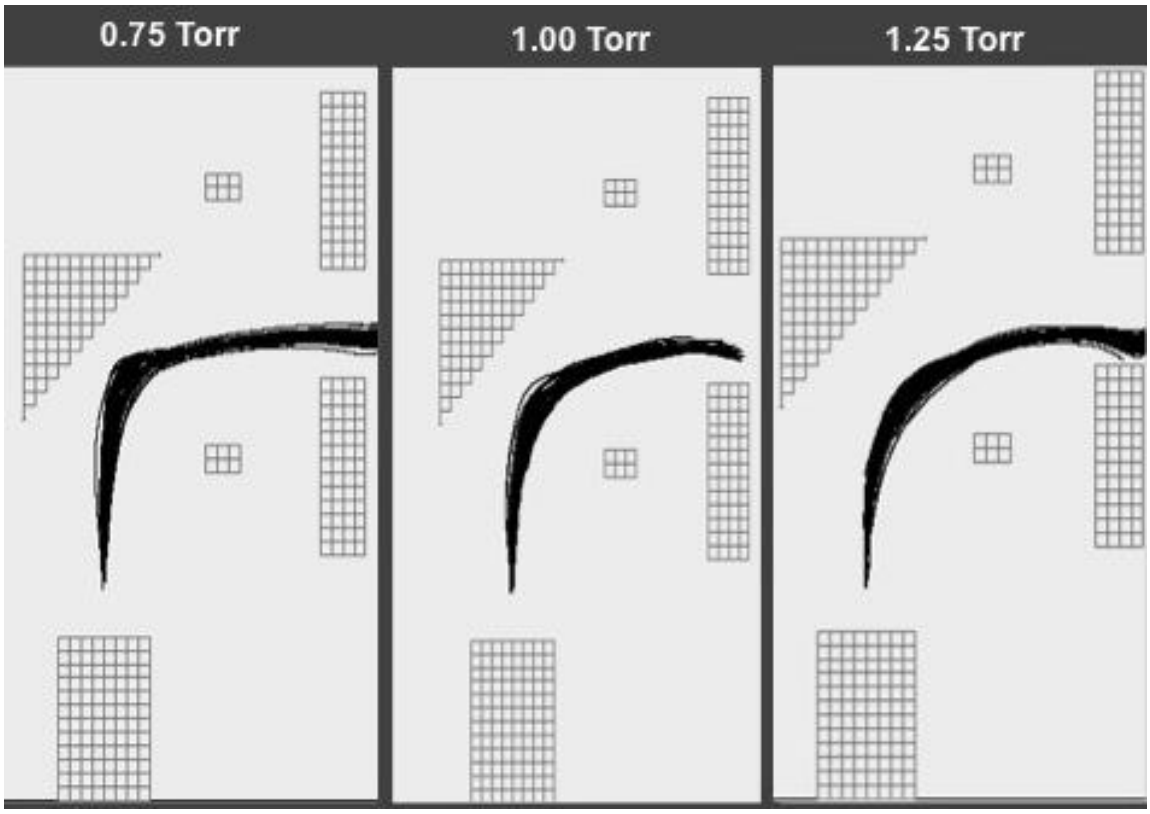

Figure 13: Ion trajectory simulations of the three turning optic models for $[BK + 2H]^{2+}$ ion for the three pressures measured: 0.75, 1.00, and 1.25 Torr.

2.3.6 Design of an orthogonal PF IF source

The orthogonal source design is depicted in Figure 14. The design in regards to the PF IF-PF IT region is very similar to the original source design as the electrodes are housed within a Delrin housing that is sealed with O-ring gaskets and the electrodes are assembled using ceramic ball spacers and compression. Helium is added directly to this region in order to maintain a high partial pressure of helium to minimize ion loss due to collisions with nitrogen. The front plate of the Delrin housing was redesigned in order to allow for mounting of the ring electrode at the correct spacing from the front face of

E1. The electrode is mounted to the front plate of the Delrin housing using four 4-40 thread screws (Figure 14). The wedge electrode is mounted using a nylon threaded rod, which connects to a base plate attached to the Delrin housing. It was vertically positioned to be centered with respect to the inner diameter of the ring electrode and rotated to have a 45 degree angle relative to the plane of the heated capillary. A nylon threaded rod, which is an electrical insulator, was used in order to avoid electrical breakdown to the source housing; however, it provide limited structural stability owing to the flexibility of the rod. In order to increase the stability, nylon nuts were added to the threaded rod. This provided rigidity to the mount and prevented the wedge electrode from moving during operation. Electrical connections were made using a 0-80 screw at top of both the wedge and ring electrode.

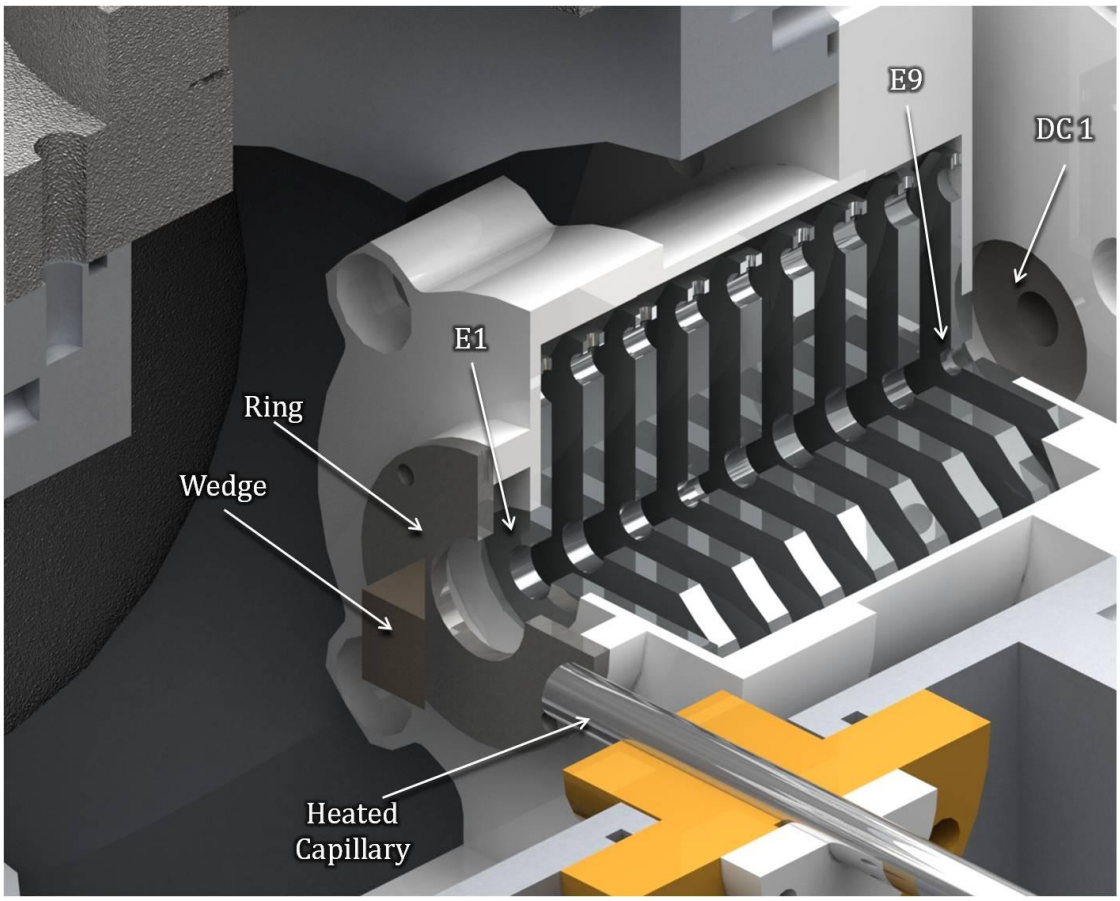

Figure 14: Solidworks rendering of the PF IF-PF IT orthogonal source design. The turning optics, which consist of a wedge and ring electrode, are labeled. Additionally, the first electrode of the PF IF (E1), the last electrode of the PF IT (E9), and the entrance to the mobility cell (DC1) are shown.

The ESI source housing was redesigned in order to accommodate an orthogonal geometry. While the first source consisted of a Delrin tube, the increased physical dimensions of the source prevent the use of this material. The orthogonal housing is a 6.5" aluminum cube design. Five sides of the housing include through holes consistent with a 6" Conflat (CF) flange system. Additionally, O-ring grooves were added for vacuum considerations. The sixth side was designed in order to position the heated

capillary inline with the wedge electrode. A PEEK flange was designed in order to electrically isolate the heated capillary from the source housing. The electrical connection to the heated capillary was made by applying a potential to the 1.33" CF flange used to seal the heated capillary. A 13 L s^{-1} rough pump was used to evacuate the pumping region and establish a helium counter flow out of the Delrin housing. After the ESI source, an 11 electrode PF IMS drift cell was added in order to facilitate IM measurements.

2.3.7 Experimental characterization of the orthogonal ESI source

By electrically isolating an electrode, the electrode can be used as a faraday detector[115], where ions impacting the electrode create a current that can be monitored by an electrometer. These measurements can be used to characterize the ion transmission efficiency of various regions of an instrument. Here we monitor ion current at 6 locations: the wedge electrode, the ring electrode, E1, DC1, the terminal electrode of the PF IMS drift cell (DC 12), and after the drift cell.

In order to determine the optimal potential difference between the heated capillary and the wedge electrode, ion current measurements were made on the ring electrode as a function of potential bias between the heated capillary. Figure 15 depicts the recorded ion current measurements. The maximum ion current measured was obtained at 48 V negative bias between the heated capillary and wedge electrode and produced an ion current of 19 nA. As the potential difference between the heated capillary and wedge electrode is increased, the ion current drops by up to 90%. This drop in current can arise from ions no longer being turned into the inner diameter of the

ring electrode or the ions are no longer colliding with the metallic surface of the electrode. Additionally, if the potential drop between the heated capillary and the wedge becomes too high, the ions may be accelerated into the surface of the wedge electrode.

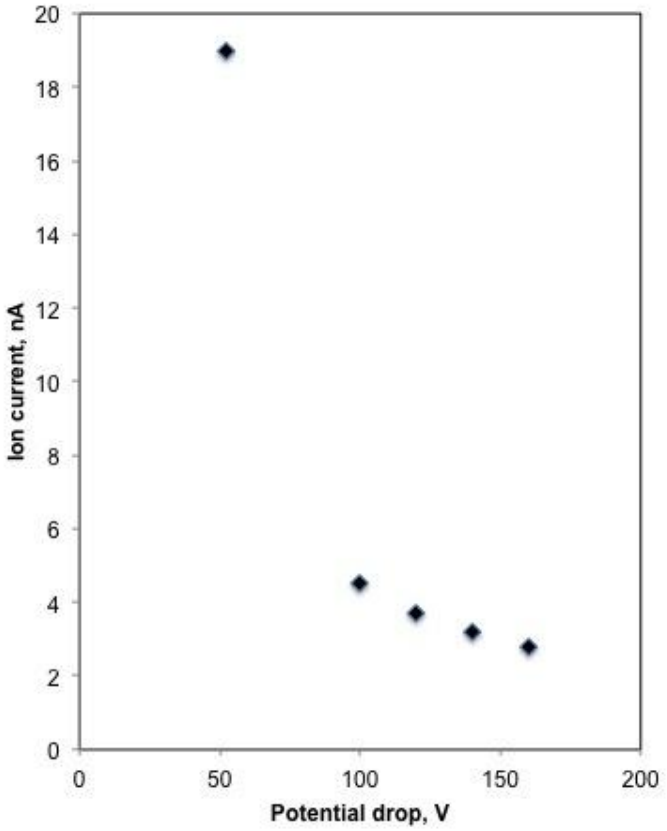

Figure 15: Ion current measured on the ring electrode as a function of potential drop between the heated capillary and the wedge electrode. The heated capillary potential was maintained at 400 V, while the potential of the wedge was varied. A 0.5 mg/mL solution of BK was infused into the heated capillary with a potential bias of 1.7 kV to facilitate ESI.

In order to optimize the voltage needed on the ring electrode to facilitate ion transmission to first electrode of the PF IF, ion current measurements were made on this electrode as a function of the potential difference between the ring and wedge electrode. The heated capillary and wedge electrode were maintained at 419 V and 371 V respectively, while the voltage on the ring electrode was varied from 0 to 400 V. As shown by Figure 16, no ion current is measured when the there in no potential drop between the two turning optic elements. The ion current increases to a maximum of ~150 nA; however, this amount of ion current is unreasonable to be attributed solely to ion impacts. Increases in ion current can arise from electrical discharges if the electric field exceeds the breakdown limit. Consistent with this, as the potential on the ring electrode exceeds the potential on the wedge, positive ions should be directed away from the PF IF and should lead to lower ion current measurements; however, at these potentials, the electric field between the two elements becomes higher and more likely to cause electric breakdown. As shown in Figure 16, the ion current is increased upon deflecting positive ions away from the PF IF entrance and is consistent with a pseudo ion current established by the high electric field. Further testing is needed to confirm the optimal turning optic bias; however, the response of ions to both the wedge and ring potentials suggests these elements are functioning and directing ions toward the PF IF. Regardless, the response of ion current as a function of potential difference between the heated capillary and wedge electrode, as well as, the potential drop between the ring and E1 demonstrates that the ions are being extracted from the gas stream and turned toward the entrance of the PF IF.

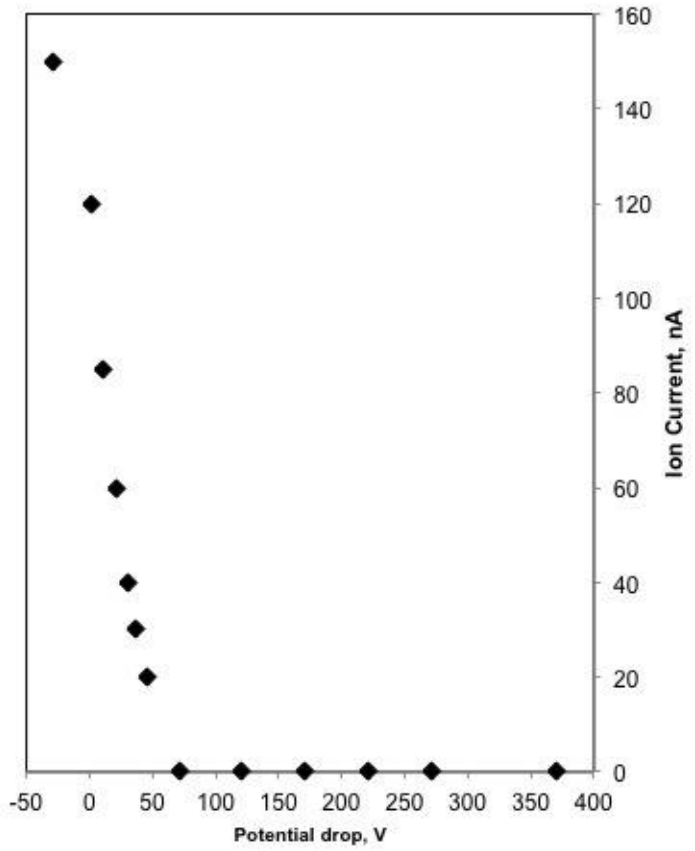

Figure 16: Ion current measured on E1 of the PF IF as a function of potential drop between the wedge and ring electrodes.

Owing to the influences of the electric field on ion current measurements when measuring on E1, further characterization of the turning optics was performed by measuring ion current on DC1. The voltage drop between E9 and DC1 is ~10 V, thus any electric field induced current should be minimized. Moreover, because this voltage is remaining constant, any minor current induced by this field will also remain constant. The PF IF was operated at an electric field of 32 V cm^{-1} $Torr^{-1}$. The pressure within the source was 0.75 Torr. The heated capillary was biased at 419 V and maintained at 343

K and the wedge and ring electrode potentials were varied. Ion current measurements are shown in Figure 17.

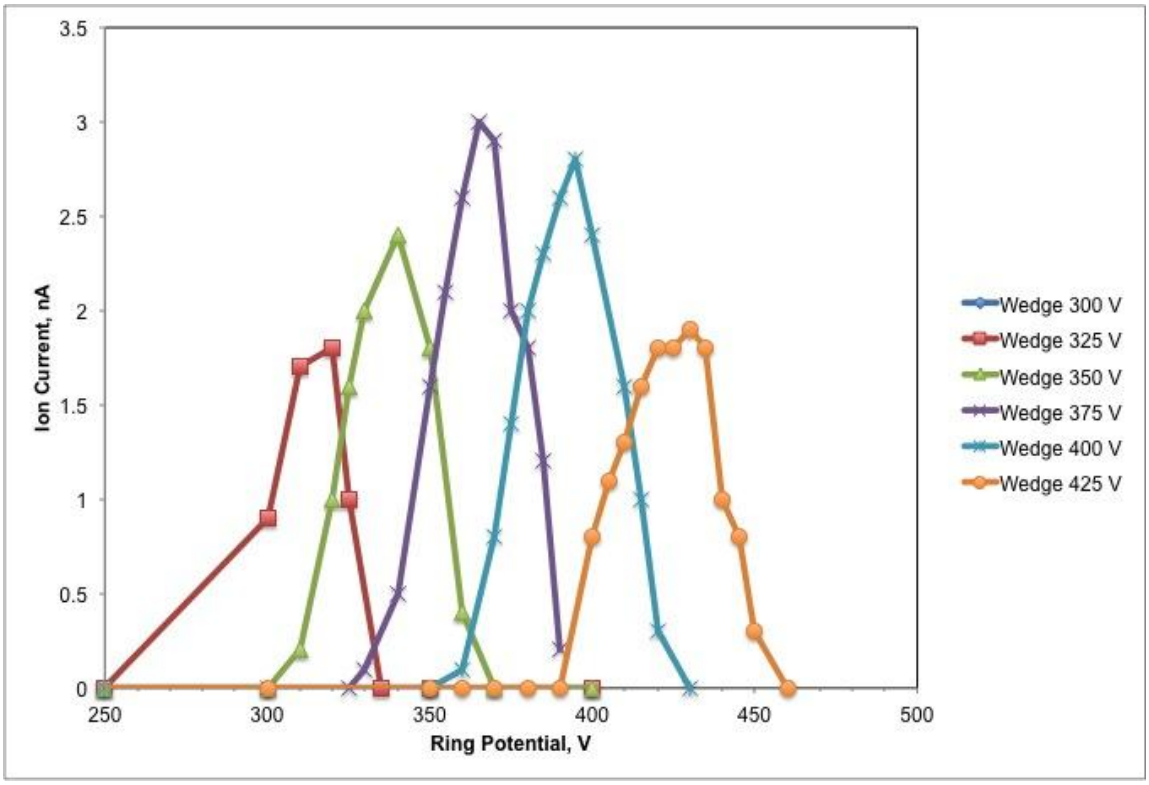

Figure 17: Ion current measurements on the first electrode of the drift cell as a function of wedge and ring electric potentials are shown.

The optimal ion current arises when the potential drop between the wedge electrode and the heated capillary, as well as, the wedge and ring electrode are 44 V and 10 V, respectively. Ion transmission is decreased when the potential drop between the wedge and ring is positive i.e., the ring is biased at a higher electric potential than the wedge electrode. This is expected owing to positive charge being repelled by this field

and suggests that the increase in ion current measure on E1 (Figure 16) at these values is indeed originating from electric field effects. Collectively, these data show that ions are being directed toward the entrance of the PF IF and that they are transmitted through this device.

As discussed previously, gas purity within the PF IF region is critical to transmission. In order to determine if the helium gas supplied to the Delrin housing maintains a high helium concentration within this region, ion current was measured on the front of the drift cell as a function of source pressure and gas composition. Helium and nitrogen were supplied directly to the PF IF housing. The heated capillary was maintained at 343 K. The electric potentials applied to the heated capillary, wedge, and ring electrodes were 420, 375, and 365 V, respectively. The axial electric field of the PF IF was 21.6 V cm^{-1} $Torr^{-1}$. The ion current is maximized when the bath gas is helium and minimized when nitrogen is used (Figure 18). The reduction in ion transmission arises from increased momentum loss when ions undergo collisions with nitrogen as compared to helium owing to the increased mass and polariziblity of the bath gas. When helium is used as a bath gas, the ion transmission decreases as the pressure within the source decreases, which is due to radial focusing properties of the PF IF, turning optic efficiency, and gas purity. Firstly, as the pressure or number density of the bath decreases, ions undergo fewer dampening collisions while traversing the device. As momentum dampening is critical to the observation of the radial ripple and central drift motion of the ion, if the ion's axial momentum is not sufficiently dampened the ion will not undergo radial focusing. This will lead to ion losses as the inner diameter is

decreased. Additionally, ion trajectory simulations have demonstrated that ion transmission decreases as the pressure of the source is decreased to 0.75 Torr. Thus the experimental decrease in transmission is consistent with simulated studies of turning optics. Finally, in order to decrease the pressure within the source, the amount of bath gas injected into the PF IF housing must be decreased. As this occurs, the counter flow of the bath gas out of the PF IF is decreased in magnitude, which can lead to an increase in atmospheric gas partial pressure within the PF IF housing. Consistent with this, the ion transmission for helium and nitrogen gases is similar when the source pressure is ~0.5, where the counter flow is the weakest.

While faraday detectors allow for continuous ion current measurements, in order to obtain arrival time distributions, ions must be gated into the drift cell. This gating causes the duty cycle of the instrument to be reduced to 1% and thus ion density will be ~1% of the continuous beam and may not induce an ion current that is detectable with the electrometer. The typical detector used in IM-MS instruments are microchannel plates (MCP) or electron multipliers; however, these devices require high vacuum (10^{-5} – 10^{-7} Torr) to operate. Thus, to include an electron multiplier into the instrument assembly, a vacuum region was added after the mobility drift cell. This region was pumped using a 550 L/s turbo molecular pump and during mobility operation, the pressure within this region was 10^{-5} Torr. The detector assembly consisted of a channeltron electron multiplier and five focusing electrodes (Figure 19).

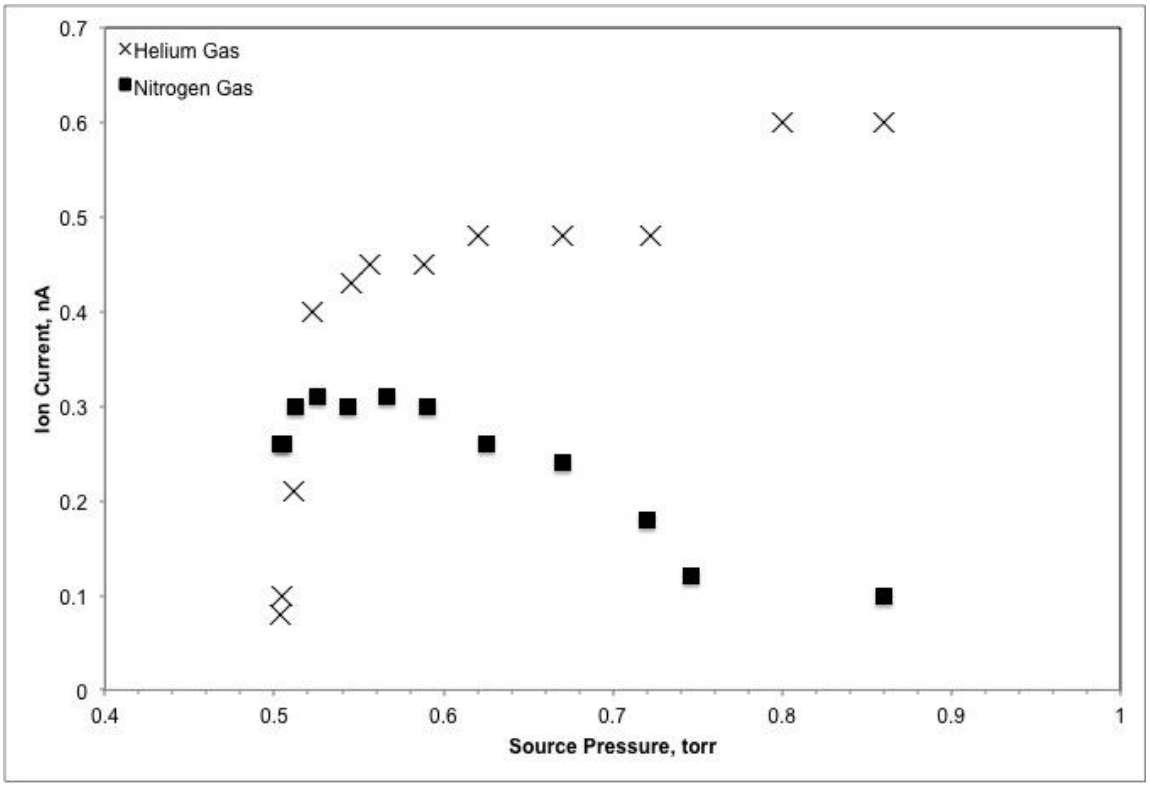

Figure 18: Ion current measured on the first electrode of the drift cell as a function of source pressure and gas composition.

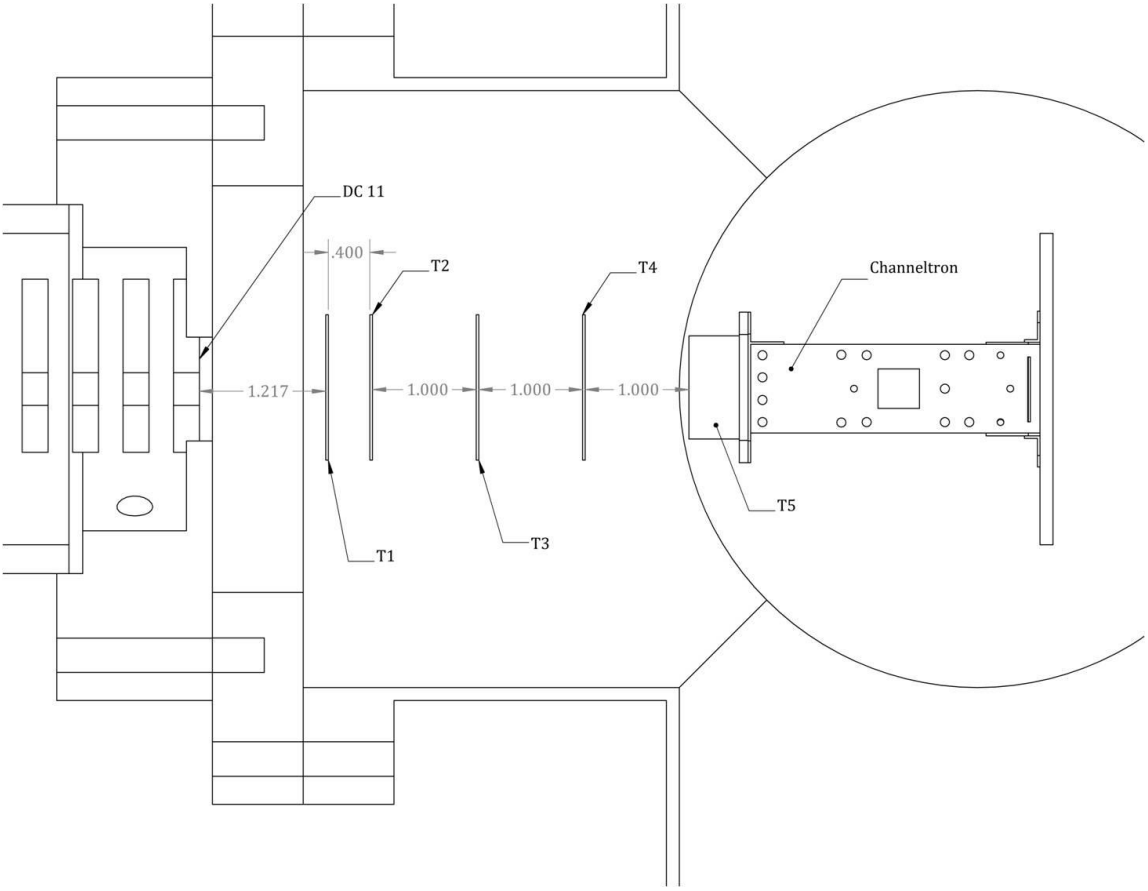

Figure 19: Solidworks depiction of the electron multiplier detector assembly. The transfer lens (T1-T5) and final electrode of the drift cell (DC 11) are labeled. The channeltron consists of a deflector electrode and the electron multiplier detector (not shown).

Optimal focusing voltages were determined by measuring the ion signal as a function of electric potential on T2. The source and drift cell pressures were 0.70 and 1.00 Torr, respectively. The heated capillary, wedge, and ring electrodes were biased at 620, 500, and 495 V, respectively. The electric field across the PF IF and drift cell was maintained at 20 V cm^{-1} $Torr^{-1}$. T1 and T3 were biased at -10 V. The front of the

electron multiplier and T4 were biased at -1.7 kV and 40 V, respectively. T2 was varied to optimize signal intensity.

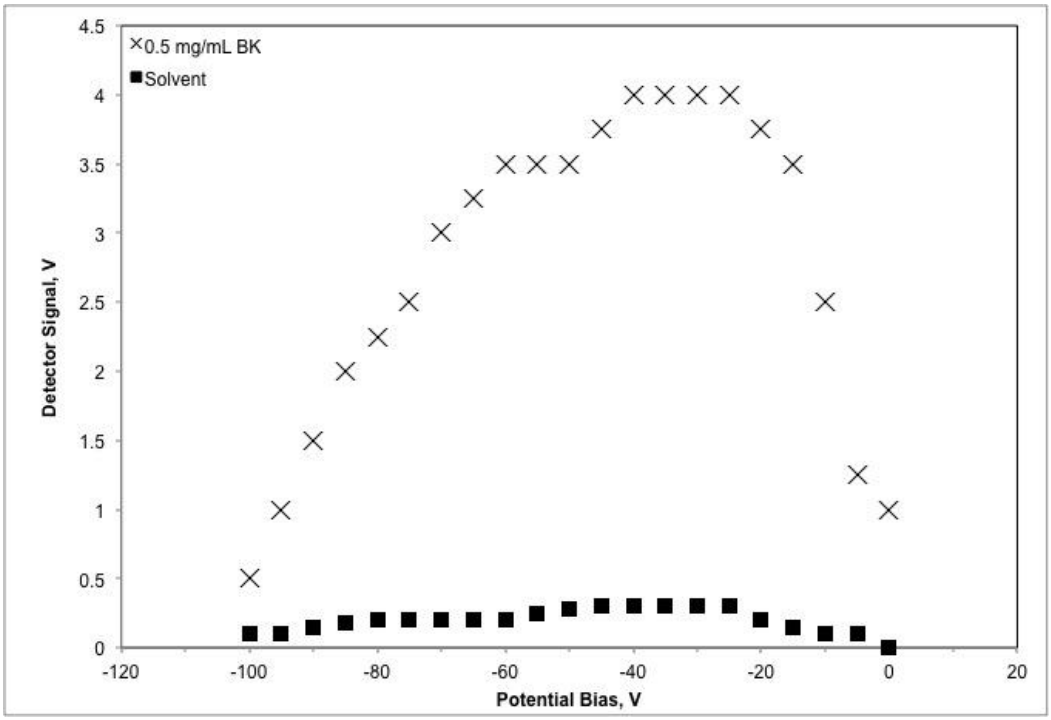

Figure 20: Detector signal as a function of electric potential of T2 for BK and a solvent blank.

The detector response as a function of the potential bias of T2 is shown in Figure 20. A solvent blank was analyzed to ensure that the signal being observed was produced via analyte ions. The detector signal is optimal when T2 is biased at -40 to -20 V. The maximum signal observed was ~4 V. The solvent blank produces ~0.3 V of detector signal when analyzed, indicating that peptide ions produces >90% of the detector signal under these conditions. Moreover, these data show that ions are turned into the PF IF,

can traverse this device and the drift cell, and are subsequently able to be detected. However, BK offers a narrow mass to charge range and as shown previously, transmission may vary as the *m/z* and the CCS of an analyte changes.

In order to investigate the transmission of larger mass analytes, cytochrome c, 12.3 kDa, was analyzed as a function of drift cell pressure and drift cell gas composition. The solution of cytochrome c was identical in solvent composition and solute concentration as the BK studies. The detector response for cytochrome c is ~3 times greater than the response recorded for BK (Figure 21). This can originate from two possibilities. The first possibility is that the transmission of cytochrome c is higher than that of BK. Owing to the size of cytochrome c, ESI produces higher charge states ions of this analyte as compared to BK. These charge states range from +19 to +7[74], while the charge states of BK range from 3+ to 1+.[52] Thus these higher charge states with larger CCS values may traverse the PF IF and drift cell region more efficiently. Secondly, these higher charge states may induce a larger detector response than the lower charge states of BK. Both BK and cytochrome c show no detector response when the drift gas is nitrogen owing to the increased thermalization.

The optimal transmission of BK is obtained when the source is maintained between 0.50 and 0.75 Torr; however, cytochrome c has optimal transmission at 0.54 Torr (Figure 21). The higher charge states of cytochrome c have been shown to adopt elongated conformations. The reduced pressure requirement of cytochrome c suggests that the extended conformations of the high charge states are transmitted most efficiently when the number density of the gas is reduced. At higher number densities or pressures,

these charge states may be thermalized and scattered owing to increased numbers of collisions. This is consistent with a sharp decrease in signal intensity at higher pressure for cytochrome C, where BK has a shallow decrease at higher pressures. The decrease of BK and cytochrome c at pressure below 0.50 Torr is consistent with the data presented in Figure 18, whereas the counter flow of helium is no longer sufficient to maintain gas purity within the PF IF housing. Nevertheless, these data show that the instrument is capable of transmitting both peptides and proteins when a helium bath gas is present.

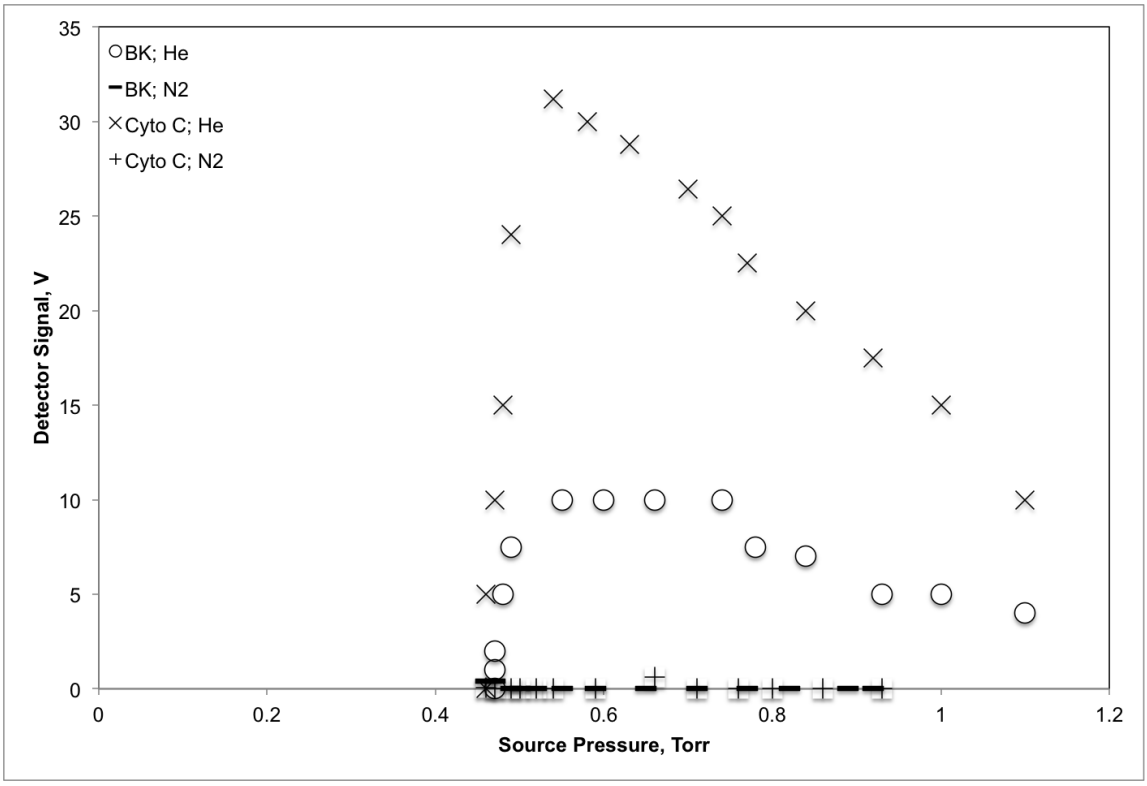

Figure 21: Detector signal as a function of source pressure, drift gas composition, and analyte. Cytochrome C produces the greatest signal owing to a higher charge state distribution as compared to bradykinin.

2.4 Conclusions

A novel DC only ion funnel and ion trap were designed and constructed. Ion trajectory simulations suggest that >90% of ions can be transmitted at optimal pressure conditions and electrode geometry. Simulations of the PF IT suggests that upon axial electric field reversal, ions oscillate and are trapped within this region with minimal ion losses (<10%). The frequency of the field reversal is dependent on the drift time through the device.

Of important consideration is the purity of the gas within the PF IF and PF IT. Helium purity is critical to the transmission properties of the PF IF and as such the PF IF is encased in a Delrin housing to establish a high partial pressure of helium; as well as, a counter flow to prevent atmospheric gas contamination. However, the counter flow does not adequately maintain gas purity during inline operation of the heated capillary. Thus, to address the problems associated with gas purity, an orthogonal ESI source was designed.

In order to extract ions toward the entrance of the PF IF, turning optics were developed. The optimal design consists of a wedge and ring electrode (18mm ID); however, efficient direction of ions to the PF IF is dependent on charge and pressure. Nevertheless, optimal transmission is obtained at 1.00 Torr and increases with charge state, which is advantageous as this pressure is typical for the constructed device and ESI produces multiply charge ion species.

Empirical characterization of the orthogonal ESI source shows that ion current is dependent on the potential drop between all turning optic elements, which is consistent

with extracting the ions from the gas stream of the heated capillary and directing them toward the PF IF. Studies show that the drift gas composition is indeed critical to ion transmission through the PF IF-PF IT and PF IMS drift cell. Furthermore, the partial pressure of helium within these regions is sufficiently high in order to facilitate transmission. However, the optimal potential drop between the ring electrode and E1 is ~60-70 V. This elevated field may induce structural conversion or even CID of liable molecules, thus in order to reduce the electric field requirements and subsequently limit the amount of collisional activation, further development of the PF IF is needed. Additionally, the practical application of the PF IT is limited owing to the high frequency at which the axial electric field must be alternated. Nevertheless, these data collectively demonstrate the orthogonal ESI source design, turning optics, and PF IF-PF IT are capable of transmitting ions throughout the device and short PF IMS drift cell.

3. IMPROVING THE UTILITY OF THE PERIODIC FOCUSING ION FUNNEL FOR STRUCTURAL STUDIES: THE 16-2 FUNNEL*

3.1 Introduction

The first generation PF IF demonstrated that a DC only IF, based on PF technology, was capable of transmitting ions through the device when coupled with an orthogonal ESI source design and turning optics. However, the first generation device required high electric field values between the ring electrode and E1, which may induce structural conversion via collisional activation and therefore limits the utility of the device when performing structural studies of biomolecule ions. Work herein describes the development of a second generation PF IF, which addresses the challenges inherent in the first generation design, specifically focused on an effort to decrease the electric field requirements for optimal ion transmission. Additionally, efforts are made to further characterize the ion motion and the radial confinement mechanism is described.

3.2 Experimental

The geometry of the PF IF was optimized by extensive simulation of ion trajectories using the *collision_hs1.lua* program provided by SIMION 81 (Scientific Instrument Services, Ringoes, NJ). The PF IF was simulated at electric fields between 6 and 43 V cm^{-1} at a static helium pressure of 0.75, 1.00, and 1.25 Torr using the $[BK + 2H]^{2+}$ ion (*m/z*: 530, CCS: 242$Å^2$). A uniform inner diameter device was also modeled

* Part of this chapter is reprinted with permission from: Fort, K. L.; Silveira, J. A.; Russell, D. H. *Anal. Chem.* **2013**, *85*, 9543-9548. Copyright 2013 American Chemical Society.

for comparison. The initial starting conditions for the simulated ion population are denoted below. Axial, radial, and axial ion velocity was determined at 0.1 mm radial and axial increments across the device. Simulations of transfer optics also utilized the $[BK + 2H]^{2+}$ ion.

Solutions of bradykinin were prepared to a concentration of 0.5 mg mL^{-1} in 50:49:1% methanol:water:acetic acid, v:v. These solutions was infused into a pulled silica ESI emitter at 500 nL min^{-1}, where the emitter was biased at +1.7-2.0 kV with respect to the heated capillary. Ion current measurements were performed on various electrodes in the source and drift cell assembly in order to determine optimal transmission tuning voltages, ion gate width, and pressure. The drift cell and funnel use ultrapure helium (99.999%).

3.3 Results and Discussion

The requirement of a high electric field between the ring electrode and E1 in the first generation PF IF design suggests that ions need to be accelerated upon entering this region in order to facilitate transmission through the device. One possible hypothesis to explain this requirement is that the difference between the inner diameter of the ring electrode (18 mm) and E1 (8 mm) necessitates the ion packet to be tightly focused through use of high electric fields. Thus, by more closely matching the inner diameter of the ring electrode with the PF IF entrance electrode, the electric field required to facilitate transmission may be reduced.

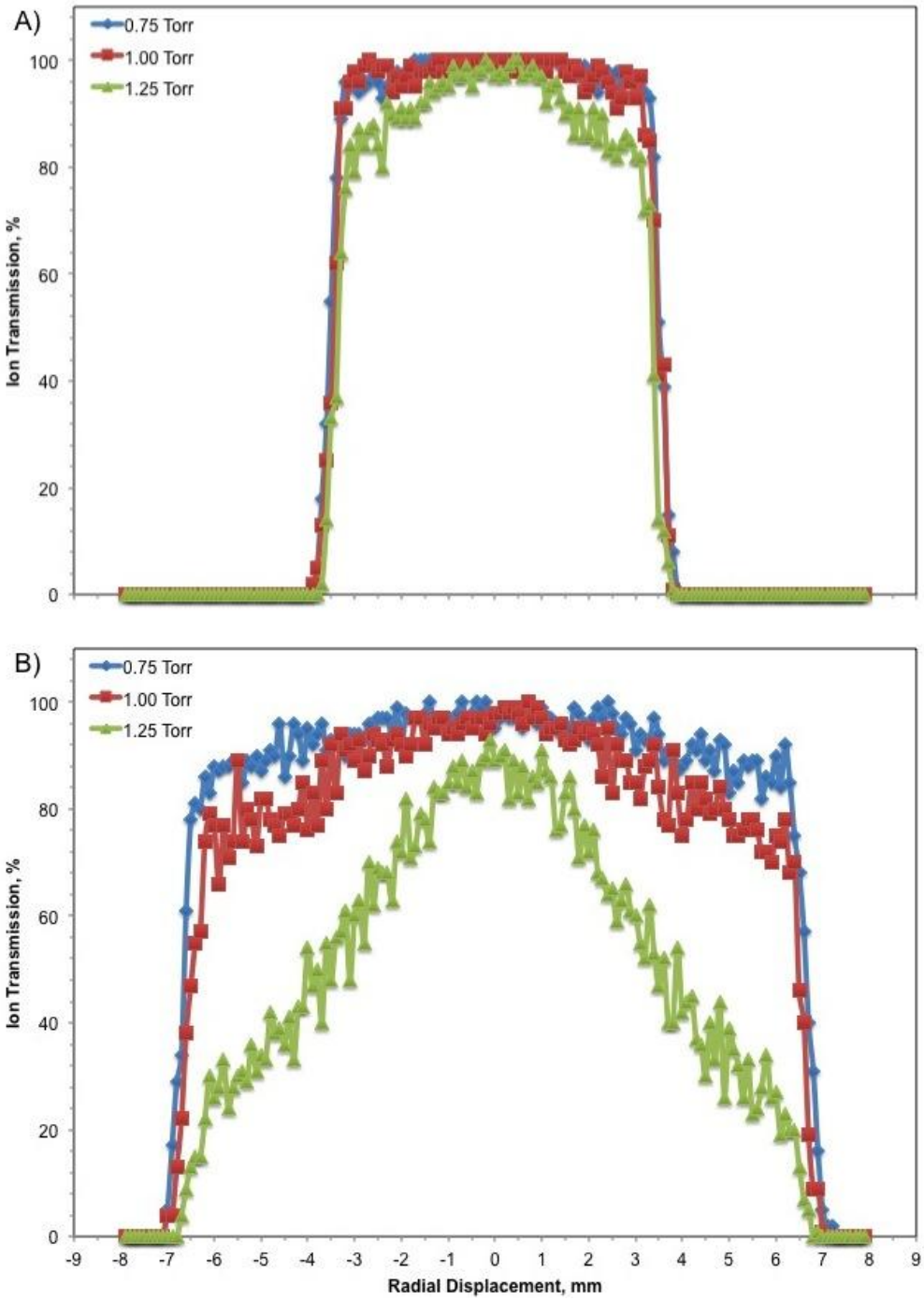

Figure 22: The simulated ion transmission of $[BK + 2H]^{2+}$ as a function of radial displacement in the PF $IF_{8\text{-}4}$ (a) and the PF $IF_{16\text{-}2}$ (b). The initial ion kinetic energy was 10 eV.

3.3.1 Comparison of the 8-4 and 16-2 PF IFs

The second generation PF IF, termed the PF $IF_{16\text{-}2}$, utilizes the same width (4 mm) and spacing (6 mm) of the original design; however, the inner diameter of the first electrode (E1) is 16 mm. The inner diameter of the subsequent electrodes is reduced by 2 mm until a final value of 2 mm for E9. SIMION simulations were preformed to compare the ion transmission of the PF $IF_{16\text{-}2}$ with the original design. The ion transmission was studied as a function of radial displacement (r) from the central drift axis.

The first generation PF IF, the PF $IF_{8\text{-}4}$, demonstrated a simulated ion transmission of 87.8, 86.5, and 78.6% for 0.75, 1.00, and 1.25 Torr, respectively. The larger inner diameter PF $IF_{16\text{-}2}$ showed lower transmission with 78.1, 71.3, and 45.7% for 0.75, 1.00, and 1.25 Torr, respectively. However, when comparing the ion transmission between r = 0 and 4 mm, the radial region where the PF $IF_{8\text{-}4}$ design is capable of ion transmission, the ion transmission for each design is comparable (Figure 22). Moreover, owing to the increase inner diameter of the electrodes, the PF $IF_{16\text{-}2}$ design is capable of more efficiently transmitting a radially diffuse (r > 4mm) ion cloud when the pressure less than or equal to 1.00 Torr, as shown by ion transmission remaining >75% for r = 4 to 6 mm. While transmission remains >75% at $r < 6mm$ at pressures of 0.75 and 1.00 Torr, when the pressure is 1.25 Torr, ion transmission decreases as r increases. This data suggests that momentum dampening, originating from increased gas number density, more greatly impacts the transmission of the PF $IF_{16\text{-}2}$ design as compared to the PF $IF_{8\text{-}4}$ design. Additionally, ions that are started near the

central drift axis (r = 0) may be allowed to radially diffuse before the radial focusing mechanism is apparent. The calculated ion transmission for each radial displacement is reflective of the initial radial displacement of the ion, as such; any displacement to larger *r*-values is unaccounted for and may reduce the calculated ion transmission. Nevertheless, the PF $IF_{16\text{-}2}$ design is capable of ion transmission similar to that of the first generation design between $r = 0$ to 4 mm, while providing increased ion transmission at larger *r*-values. This increased transmission may decrease the magnitude of the electric field between the ring electrode and E1 that is required to transmit ions and thereby reduce the amount of collisional activation the analyte ions undergo within this region.

3.3.2 Characterizing ion motion in the PF IF

In order to fully understand the ion motion within the PF $IF_{16\text{-}2}$, extensive simulations were performed in order to characterize the electric fields within the device, as well as, the potential impact these fields have on transmission and collisional activation of the analyte.

Figure 23 contains equipotential lines (a) and ion trajectories (b) in the PF $IF_{16\text{-}2}$. The trajectories clearly show that ions both on- and off-axis are efficiently transmitted through the exit aperture by the central drift motion that is enhanced by the conical shape of the device. To gain insight into this outcome, the axial ($E_z(z)$, Figure 24a) and radial ($E_r(z)$, Figure 24b) electric fields were extracted from SIMION. Similar to the PF IMS drift tube, the $E_z(z)$ and $E_r(z)$ oscillations are 90° out-of-phase from one another while the amplitude of these oscillations increases at larger $\vec{r}$-values. However, the amplitudes

of the axial ($E_{0,z}$) and radial ($E_{0,r}$) waveforms in the PF IF also display a z-dependence that is not present in PF IMS. That is, $E_{0,z}$ and $E_{0,r}$ increase not only as ions drift near the electrode surface, but also as ions traverse the device. Oscillations in the both the axial and radial electric field lead to interesting variations in the ion velocity, *viz.* the axial ion velocity profile contains local minima at the tailing edge of each electrode—an effect that is enhanced toward the back of the device where $E_z(z)$ oscillations are largest (Figure 25a). Moreover, owing to the reduced axial velocity of the ions on the tailing edge, the ions are present within this region for a greater amount of time as compared to the leading edge of the electrode. The increased time the ion spends at the tailing edge is critical to the radial confinement mechanism as ions obtain higher radial velocity at the tailing edge as compared to the leading edge of the electrode (Figure 25b). Over multiple electrode cycles, this effect gives rise to the overall radial correction, *i.e*. central drift, which occurs as ions traverse the device. Collectively, these oscillations, both in the axial and radial electric field, lead to the overall radial confinement mechanism.

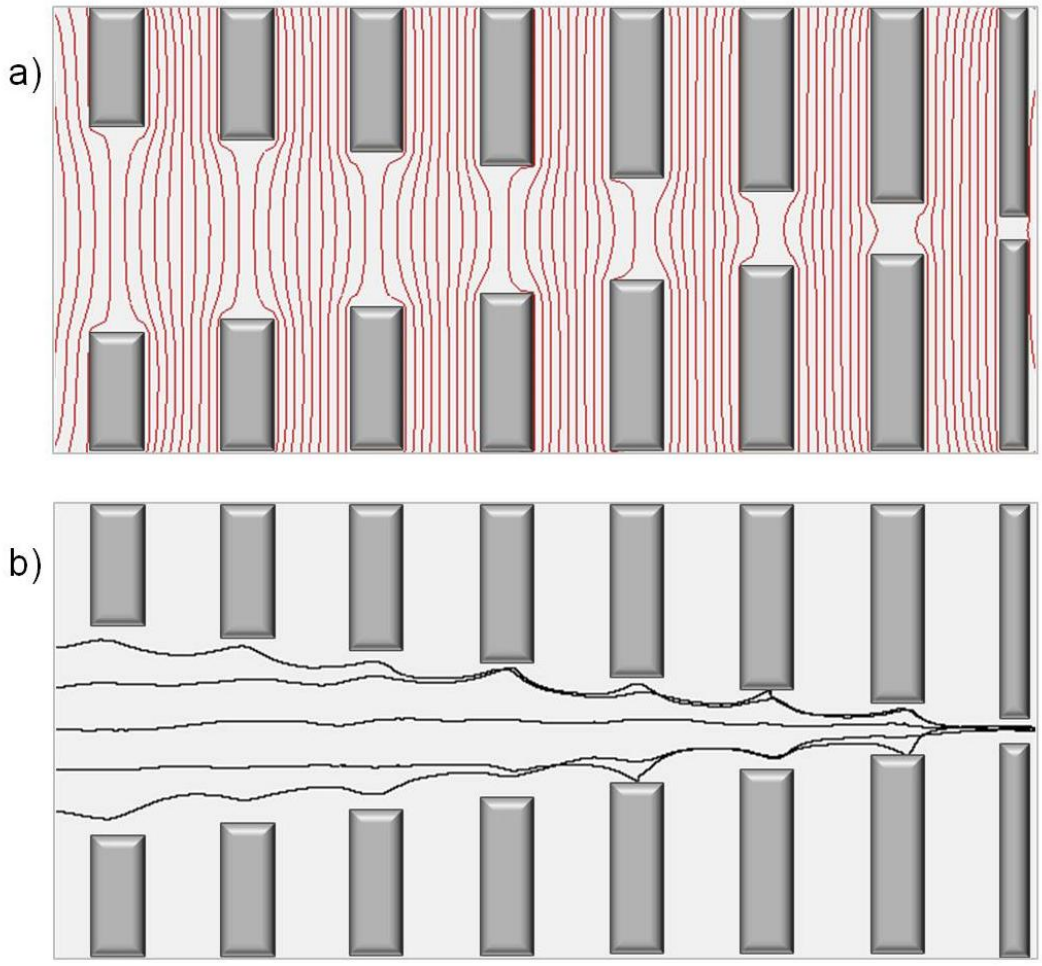

Figure 23: SIMION models of the PF $IF_{16\text{-}2}$. The equipotential lines (a) bend within the inner diameter of the electrode elements. Simulated ion trajectories (b) show that the ions will follow the contours of the equipotential lines.

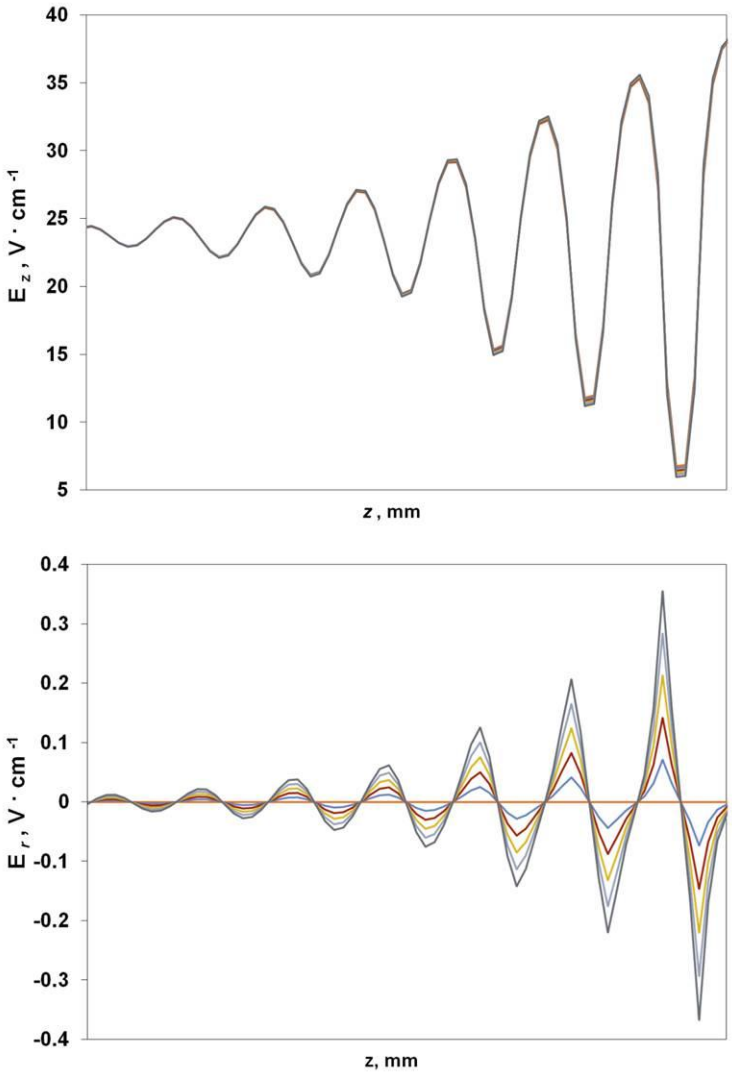

Figure 24: Axial (a) and radial (b) electric fields in the PF IF as a function of *z*-position and several *r*-positions (r = 0.0 mm to r = 0.5 mm with 0.1 mm increments) as indicated by the legend.

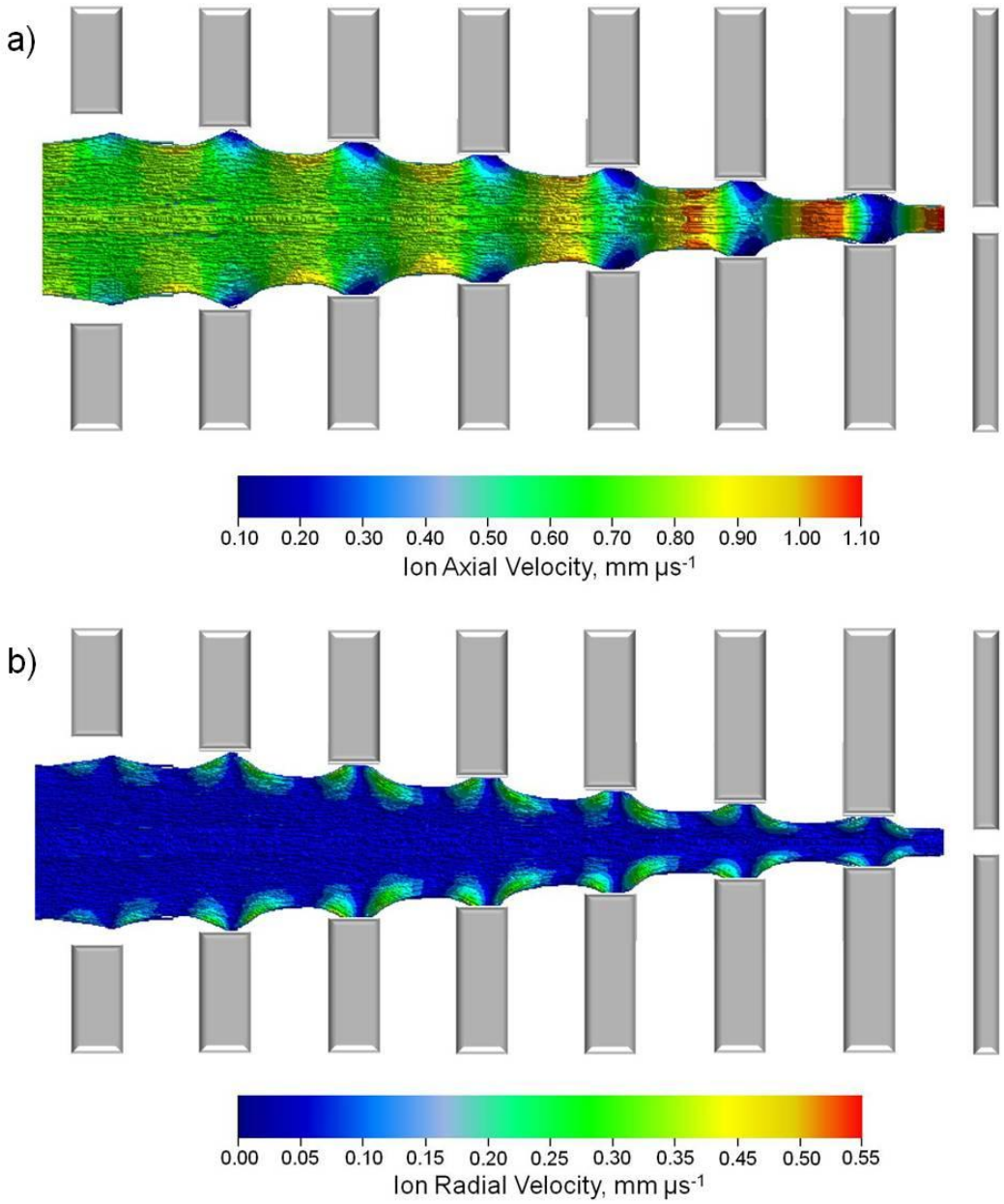

Figure 25: The axial (a) and radial (b) ion velocity of $[BK + 2H]^{2+}$ as determined by SIMION ion trajectory simulations. The axial velocity shows local minimums are present in the inner diameter of the electrodes owing to the oscillations in the axial electric field. The radial ion velocity shows local maxima at the front and tail edge of electrode. However, the radial velocity is conserved for longer at the tailing edge of the electrode, which is consistent with the central drift transport mode.

The theoretical basis for the central drift motion in periodic focusing devices has been attributed to collisionally dampened effective potentials produced by the ~kHz effective RF experienced by ions traversing the device.[95-96] The effective potential (V^*) is given by,

$$\boldsymbol{V^* = \frac{q^2 E_r(\vec{r})^2}{4m\Omega_{eff}{}^2}} \tag{14}$$

where q is the charge state of the ion, m is the mass of the ion, and Ω_{eff} is the effective RF frequency given by,

$$\boldsymbol{\Omega_{eff} = \frac{2\pi v_z}{\lambda}} \tag{15}$$

where v_z is the axial velocity of the ion and λ is the wavelength (the sum of the electrode width and spacing). Combining eqs. (14) and (15), the effective potentials produced for $[BK + 2H]^{2+}$ were determined according to the principles described by Silveira *et al*. However, in the present work, V^* shown in Figure 26 also considers the radial variations in v_z since this term is not negligible in the case of the PF IF (see Figure 25). Generally, the magnitude of V^* is low near the central drift axis and relatively high near the electrode edges. In the PF IF, the effective potentials follow the conical shape of the device such that ions are more tightly confined as they approach the exit aperture thereby enhancing the central drift motion. Similar to the RF IF, shallow effective potential wells are present within the PF IF.[101] These potential wells produce axial barriers, which can result in stagnation and reduced ion transmission if axial momentum

is collisionally quenched, leading to reduced ion transmission. Hence, the electric field must be sufficiently high to partially conserve the momentum of the ion.

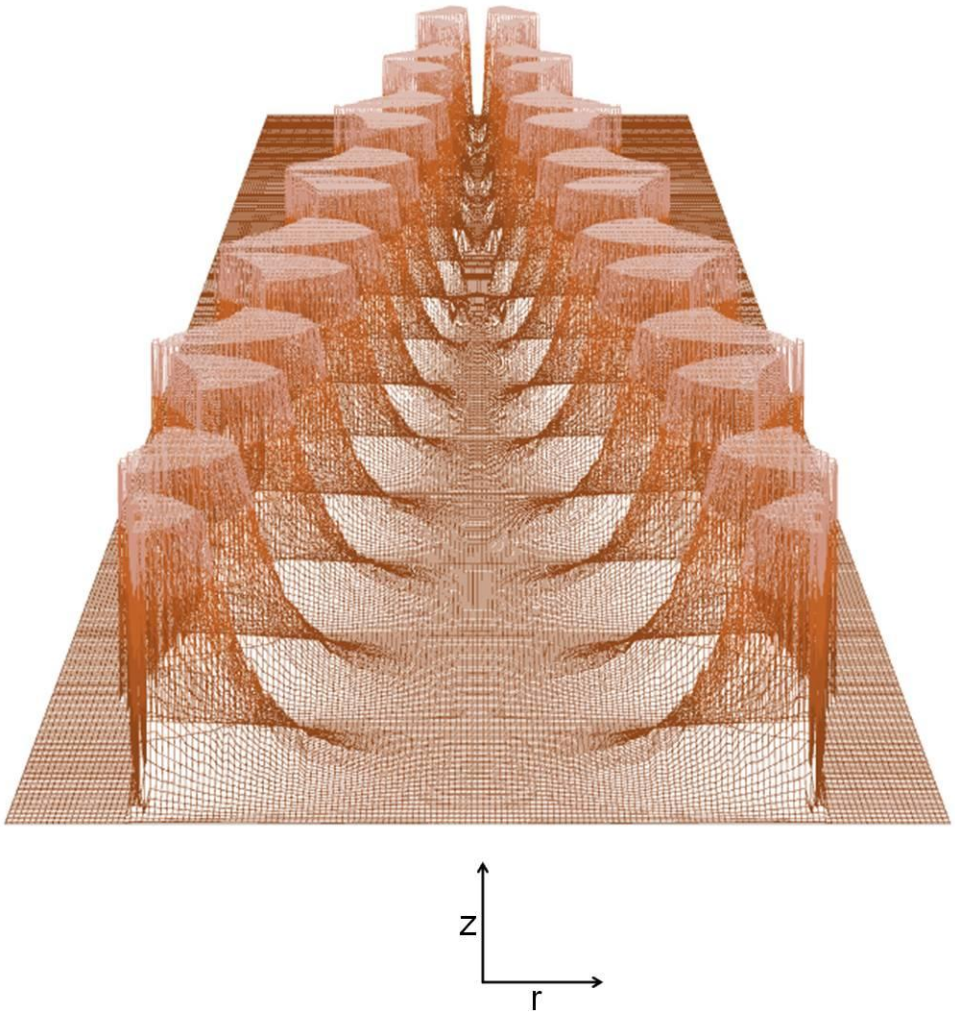

Figure 26: The calculated effective potentials in the PF IF (E2-E8) projected from cylindrical coordinates into three dimensions.

In order to demonstrate the importance of electrode geometry to the transmission properties of the PF IF, the ion transmission as a function of axial electric field was determined for two geometries, the first geometry being the PF IF and the second being a uniform geometry (Figure 27).

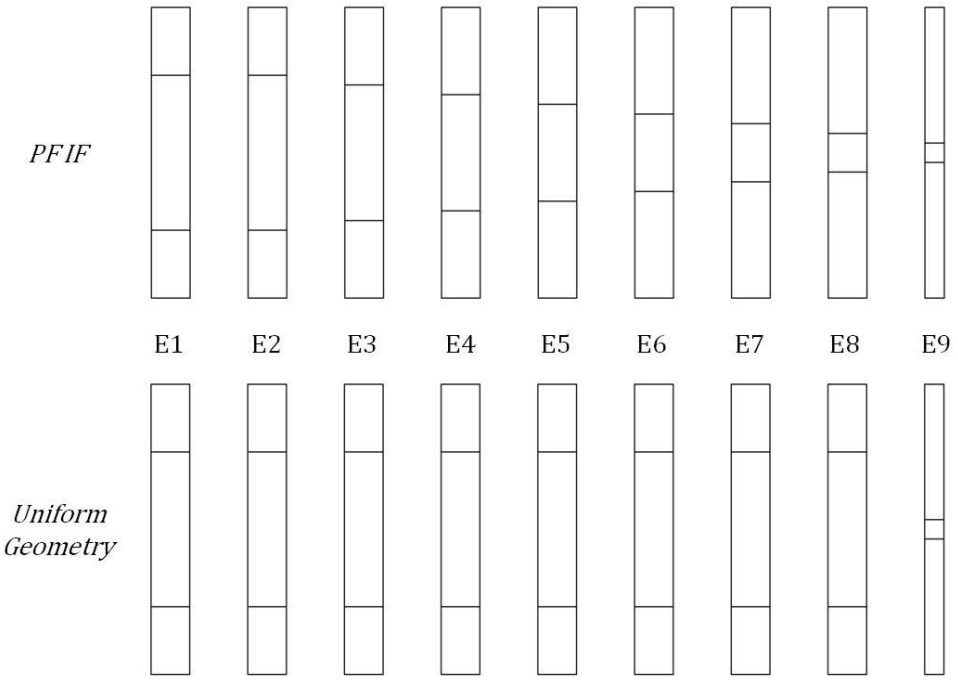

Figure 27: A schematic of the PF $IF_{16\text{-}2}$ and the uniform geometry device. Ion transmission was calculated for both devices to determine the importance of the conical nature of the PF $IF_{16\text{-}2}$.

Figure 28 shows the simulated ion transmission for $[BK + 2H]^{2+}$ as a function of the applied electric field for the PF $IF_{16\text{-}2}$ and uniform geometry, which was included for comparison. In the case of the uniform geometry, the inner diameter of the electrodes is

large such that only the E_z component acts upon the ion swarm and field oscillations are negligible. In this case, ion transmission remains fairly constant (~5%) irrespective of the applied electric field owing to the absence of a radial ion confinement mechanism. Conversely, the plot for the PF $IF_{16\text{-}2}$ shows a characteristic sigmoidal relationship between ion transmission and the applied field. At lower electric fields, ions do not possess sufficient axial velocity and are mostly thermalized inside of electrodes where *V** creates shallow axial potential wells. The region of the curve surrounding the inflection point (~15 V cm^{-1} $Torr^{-1}$) is indicative of the onset of momentum conservation such that ion velocities are sufficient to overcome the axial *V** barriers. As the electric field is further increased, ion transmission maximizes at >90%. These data suggest that the PF $IF_{16\text{-}2}$, herein referred to as PF IF, design is capable of increased ion transmission owing to the proposed radial confinement mechanism.

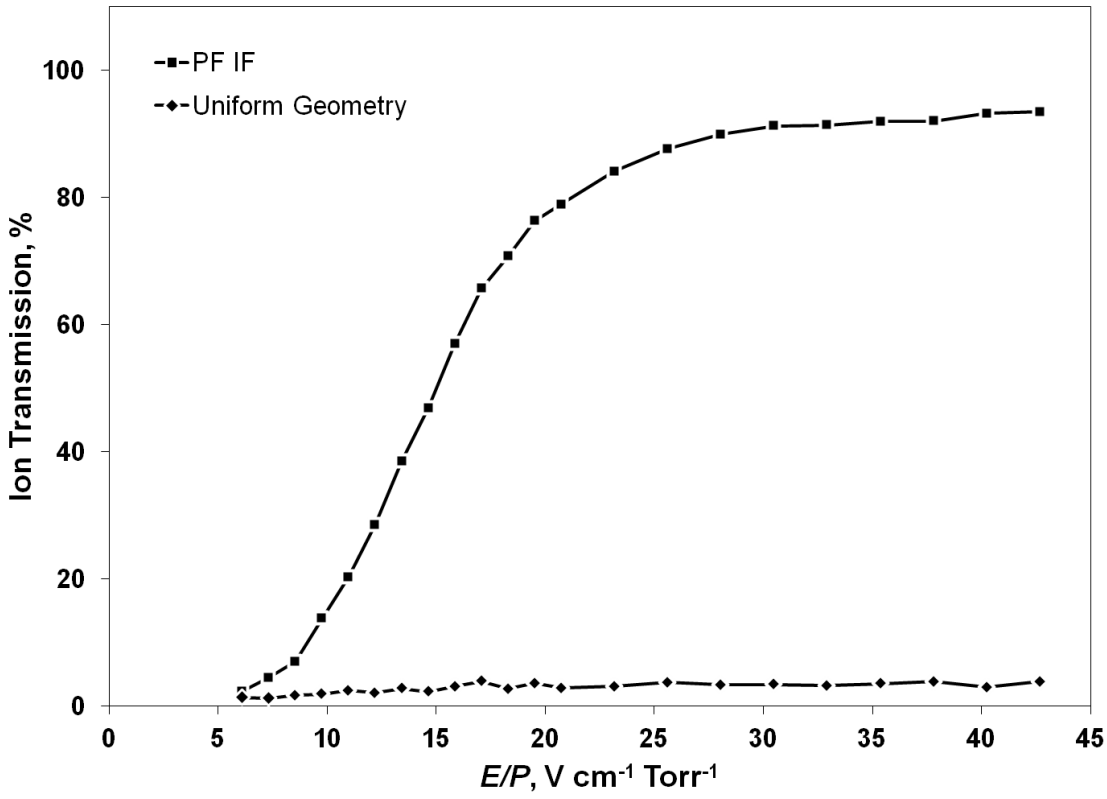

Figure 28: The simulated ion transmission of $[BK + 2H]^{2+}$ in the PF IF versus the uniform geometry model.

3.3.3 Optimizing the turning optics for the PF IF

Owing to the same number of electrode elements, as well as identical width and spacing, the PF IF is a direct replacement for the smaller diameter funnel (Figure 29). In order to test the hypothesis that the large inner diameter would decrease magnitude of the voltage drop between the ring electrode and E1, ion current measurements were made as a function of turning optic potential (Figure 30).

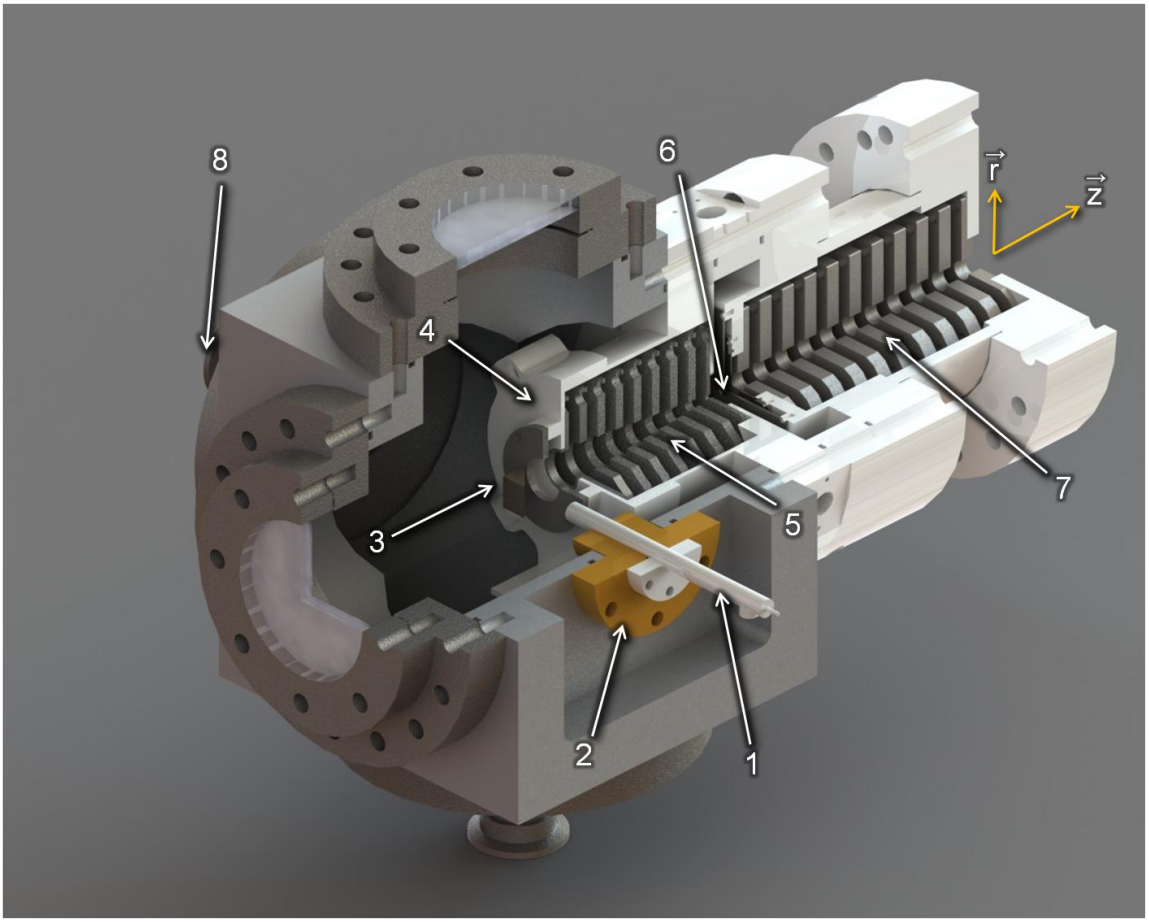

Figure 29: Cutaway diagram of the PF IF source region. Parts are labeled as follows: (1) heated capillary ion inlet, (2) PEEK electrical/thermal isolation flange, (3) turning optics, (4) PF IF housing, (5) PF IF electrodes, (6) DC 1, (7) PF IMS drift cell, and (8) pumping port. The coordinate system referred to herein is also provided.

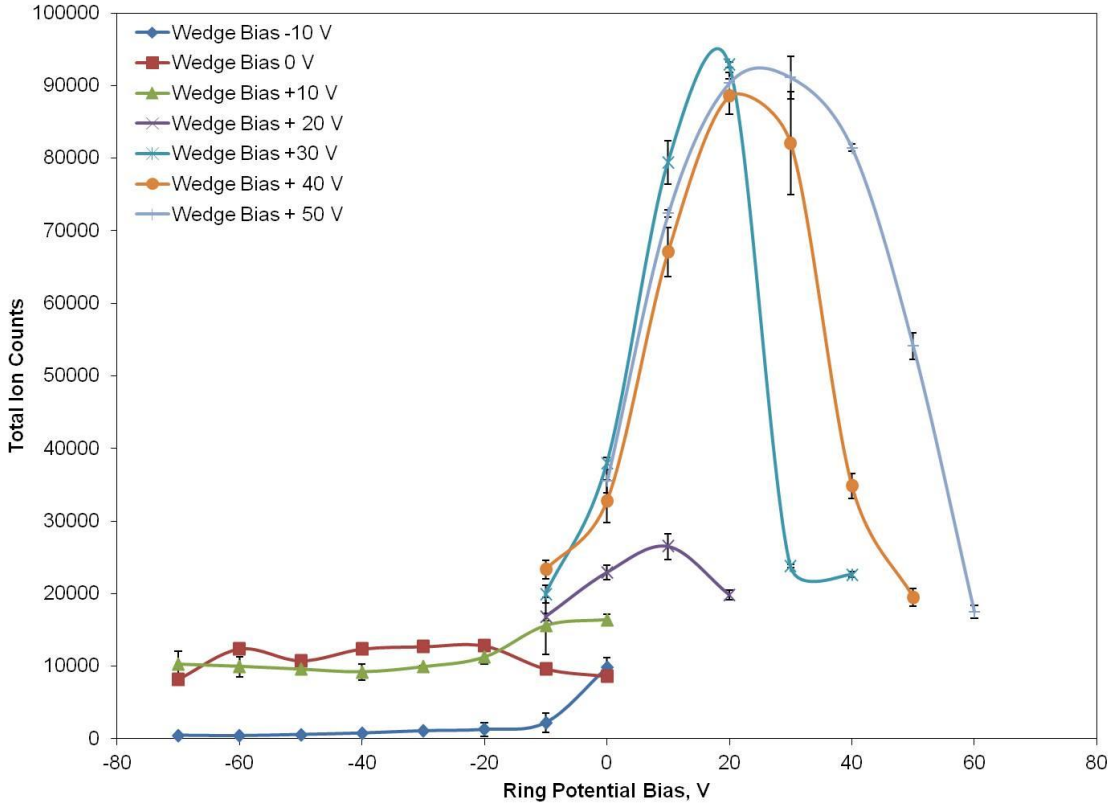

Figure 30: Total ion counts as a function of wedge and ring potential bias with respect to E1. The drift cell was maintained at an electric field of 16.6 V cm^{-1} $Torr^{-1}$. The heated capillary was maintained at +150 V with respect to the wedge and 348 K.

As previously discussed, the optimal ion transmission for PF IF_{8-4} occurred when the potential drop between the ring and E1 was ~60-70 V. With the new design of the PF IF, the optimal ion current occurs when the wedge and ring electrode are biased at +30V and + 20V with respect to E1. This significantly reduces the electric field that is established between the ring and E1, which would in turn reduce the amount of collisional activation that the analyte ions undergo within this region. Moreover, these

data confirms our hypothesis that the by increasing the inner diameter of the PF IF, the field requirement to optimize ion transmission through the instrument will be reduced.

3.3.4 Incorporation of an ion gate in order to perform mobility analysis

Owing to the continuous ion production inherent with ESI and dispersive nature of PF IMS, the ion beam must be attenuated into discrete packets and injected into the mobility drift. Beam modulation is typically performed by using a "gate" electrode, which is maintained at an electric field that blocks or deflects ions from entering the drift cell and then is pulsed to a electric potential that allows ions to enter the drift cell. The initial opening of the ion mobility gate establishes the start of the mobility experiment and allows for the measurement of drift time through the drift cell. Moreover, the precision at which the ion gate is able to be pulsed from a deflection mode to a transmission mode can greatly impact the signal to noise of the measurement as well as the separation between distinct mobility profiles. If the ion gate does not efficiently deflect ions from entering the drift cell, ions may traverse the drift cell without any temporal correlation (i.e. chemical noise). Additionally, mobility resolution is dependent on the initial ion packet width. As the temporal width of the transmission mode increases, mobility resolving power decreases.[70] One of the most common types of ion gate is a Bradbury-Nielsen gate.[116] This gate design consists of a parallel set of wires that are orthogonal to the ion beam and are electrically isolated. One wire, the common wire, is maintained at the transmission potential while the other, the deflection wire, is maintained at a potential which causes the ions to be deflected up or down, which in turn prevents ions from entering the drift cell. In order to transmit ions, the

deflection wire is pulsed to the match the transmission potential applied to the other wire. This causes the ions to traverse the gate unperturbed and enter the drift cell. In order to incorporate an ion gate into the PF IF instrument, a Bradbury-Nielson gate was designed and incorporated into the ESI source (Figure 31). Ion gate placement is critical to the mobility separation; the further the ion gate is from the entrance to the drift cell, the more spatial broadening the ion packet can undergo due to diffusion and coulombic repulsion. Thus, the gate was designed to modulate the ion beam after the PF IF. This serves two purposes; the first purpose is by having the ion gate post-PF IF, the transmission properties of the funnel should not be altered, and secondly, this position is the closest to the entrance of the mobility cell and minimizes any potential spatial broadening.

In order to test the effectiveness of the ion gate, a 0.5 mg mL^{-1} solution of BK was infused. The electrical potential on E9 and DC1 were measured directly and G2 was biased to a median value between these two elements. In typical operation, G1 was biased 35V higher than G2 during a blocking mode of operation. This potential was then pulsed down to match that of G2 and allows for transmission of ions.

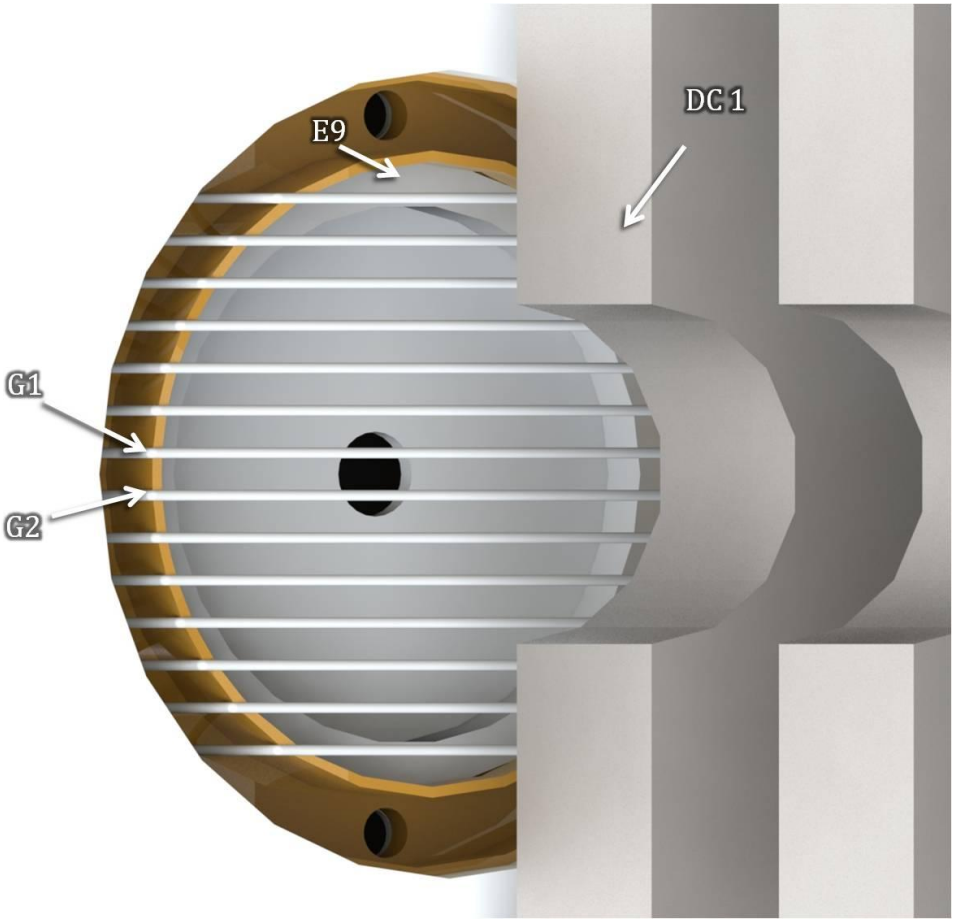

Figure 31: Solidworks representation of the ion gate used to create ion packets for mobility analysis. The common wire, G2, and the deflection wire, G1, are isolated using a PEEK electrode design. E9 is a metallic insert that was designed to match the inner diameter and width of the non-gated electrode. The ion gate is placed directly in front of the entrance to the drift cell, DC1.

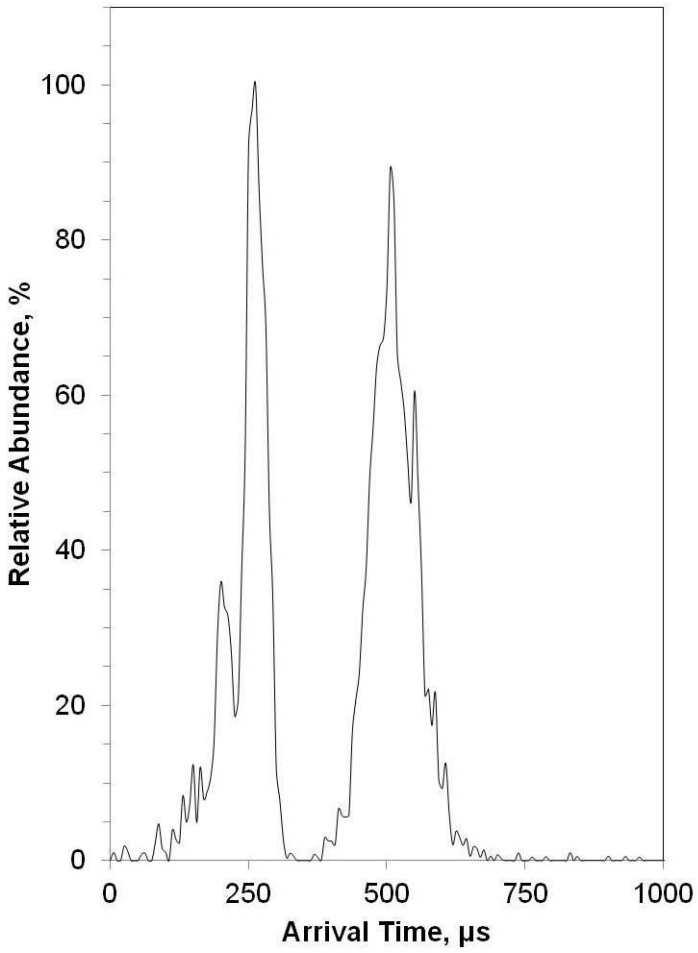

Figure 32: The first mobility arrival time distribution (ATD) collected on the PF IF-PF IMS instrument.

Upon modulation of the ion beam, the collected spectra consisted on two main populations (Figure 32). The first is in 100% relative abundance and is centered on 250 µs. This population also has a partially resolved fronting shoulder. The second population is approximately 90% relative abundance and is centered on ~500 µs. Additionally, the peak width of the second population is significantly broader than the

first population. This can arise from increased diffusion, unresolved conformations, or overlapping compounds. Interestingly, BK has been shown to produce multiple charge states, namely the $[M + H]^+$, $[M+2H]^{2+}$, and $[M+3H]^{3+}$ species by ESI.[20, 59, 66] As the mobility of analytes will increase with charge, assuming no significant change is gross conformation, higher charged species will migrate faster than lower charge species. The three charge states could potentially correspond to the three partially resolved populations, with the $[M+3H]^{3+}$ species corresponding to the partially resolved shoulder, the $[M+2H]^{2+}$ species corresponding to the main distribution centered on 250 μs, and finally the $[M+H]^+$ species corresponding to the distribution centered on 500 μs. However, owing to the one-dimensional nature of the current instrument, further identification of these species is limited. Incorporation of a mass analyzer will aid in de-convoluting the mobility ATD. Nevertheless, these populations indicate that the ion gate is modulating the ion beam in such a way that mobility analysis is possible. In order to further investigate the ion gate design, ion counts were monitored as a function of gate width, which was varied from 5 to 20 μs in 5 μs intervals. If the ion gate is functioning correctly, the ion counts should increase with an increased gate width or transmission time.

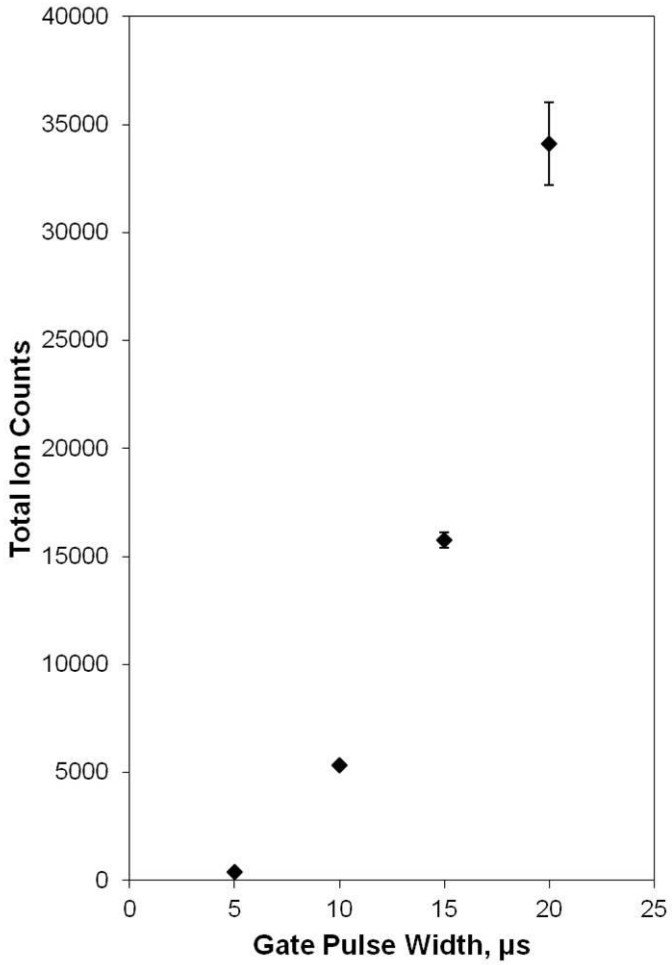

Figure 33: Total ion counts as a function of gate pulse width. Each data point was average over three 60 second acquisitions. Error bars represent on standard deviation.

The maximum ion counts occurred when the gate width was maximized at 20 µs and dropped off as the gate width was decrease, as expected (Figure 33). Moreover, the collected ATD for the 5µs gate width did not include any correlated peaks, while the ATDs collected for 10-20 µs did. This indicates that the ion density in a 5 µs ion packet is not sufficient to transmit a detectable signal. While this requires the use of higher gate

widths, the nominal ion counts collected at 5μs suggests that the designed ion gate is effectively deflection ions from entering the drift cell.

Now that an ion gate has be incorporated into the instrument design and mobility analysis is possible, it is of interest to examine the effects of the turning optic potentials on the ATD. In order to do so, the gate width was maintained at 20 μs and the voltage drop between the wedge and E1 was maintained at 30 V. The ring voltage was varied from +30V to 0V with respect to E1. The spectra were allowed to acquire for 60 seconds (Figure 34).

When the potential drop between the wedge and ring electrode is 0V, the ions should not be directed toward the entrance of the PF IF. Consistent with this, the ATD shows no discernible signal for these turning optic settings (Figure 34a). When there is a potential drop between the wedge and ring electrode, the two main populations are observed again (Figure34 b-g) owing to the ions being directed to the PF IF by the turning optics. When the potential drop between the ring and E1 is 0V, there is an interesting shift in the ATD. The population centered on 500 μs becomes the dominant ion signal. Assuming that these populations correspond to the various charge states of BK, this shows that the $[M+H]^+$ species is most efficiently focused into the PF IF. As the potential drop between the wedge and ring is -30V, the higher charged ions may be over steered by the turning optics and collide with the ring electrode or spatial focused at radial extremes, i.e. r > 6mm, of the PF IF, where transmission is reduced. These results show that by tuning the turning optics, the ion swarm can be focused into an area of the PF IF where transmission is increased. Moreover, this is the first empirical

evidence that ions are able to be transmitted at a lower potential drop than was required for the previous PF $IF_{8\text{-}4}$ model.

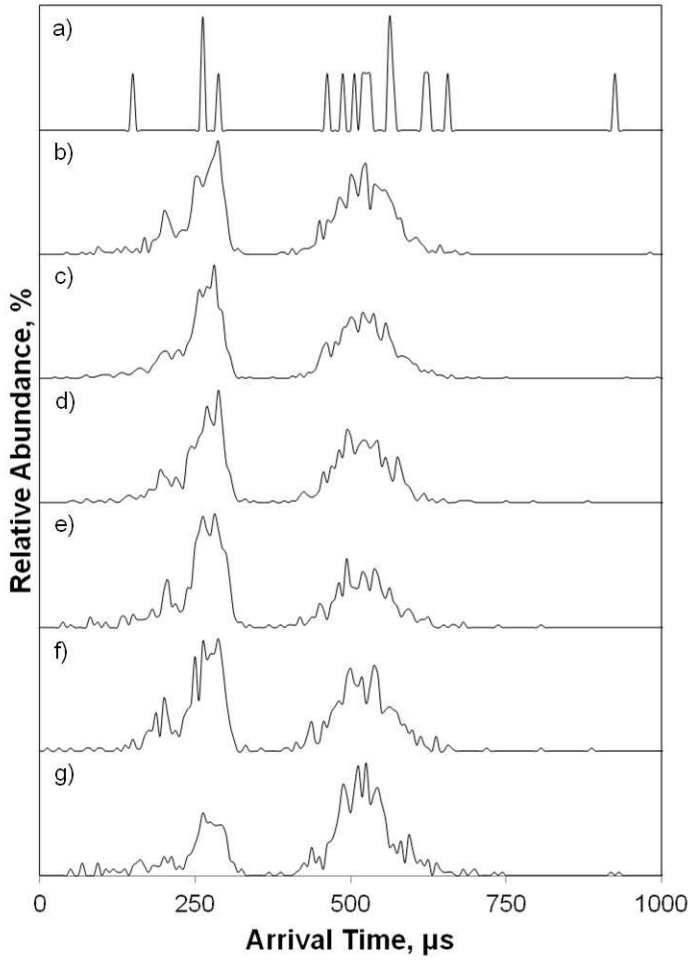

Figure 34: The ATD of BK collected at variable turning voltages. The ring electrode bias was varied so the potential drop between the wedge and ring electrodes and the ring electrode and E1 were: (a) 0V and +30V, (b) -5V and +25V, (c) -10V and +20V, (d) -15V and +15V, (e) -20 V and +10V, (f) -25V and +5V, and (g) -30V and 0V, respectively.

3.4 Conclusions

Previous work with the PF IF has shown that the electric field needed to optimally focus ions into the device was higher than desired. The proposed origin of the high field requirement was the discrepancy between the inner diameter of the ring electrode and E1. Work presented here tests this hypothesis by redesigning the PF IF to increase the inner diameter of E1 and subsequent electrodes. Through ion trajectory modeling, the ion transmission properties of the larger inner diameter funnel were compared to the first generation, PF $IF_{8\text{-}4}$, funnel. Within the same radial region, $r = 0$ to 4 mm, the two devices had comparable transmission. However, the new design offered increased ion transmission at greater r values.

Further modeling of the PF IF shows that the oscillations in the axial and radial electric field, typical of PF IMS drift cells, were in fact enhanced by the conical nature of the design. This gave rises to increased radial confinement of the ions as they traversed the device owing to the progressively smaller inner diameters. Velocity mapping of the ions both in the axial and radial direction showed that ions respond to these oscillations and they are critical to the radial confinement mechanism. Moreover, the radial velocity mapping demonstrated the most definitive evidence for the central drift to date. Upon combining the axial and radial electric fields with the axial velocity, the effective potential of the PF IF was calculated. Similar to the effective potentials established in the RF IF, the PF IF shows barriers that provide focusing of the ion swarm. Additionally, this effective potential also creates axial potential wells that the

ions much overcome to traverse the device. The impact of these axial barriers is demonstrated by the calculated ion transmission as a function of field strength.

A comparative study was preformed to relate the impact of the conical nature of the PF IF to a uniform geometry device, which should not posses any radial confinement mechanism. At the lowest electric field studied, the ion transmission values for both devices were comparable, <10%. The low transmission for the PF IF arises from ion not possessing sufficient axial momentum to overcome the axial barriers produced by the effective potential. As the electric field is increased, the transmission for the PF IF also increases in a sigmoidal fashion. The inflection point, present at 15 V cm^{-1} $Torr^{-1}$, is indicative of the onset of momentum conservation within the device. Simulated ion transmission in the PF IF approaches values of >90% at the highest fields investigated. Conversely, the transmission for the uniform geometry device shows no dependence on the electric field applied and calculated values remain <10%.

The larger inner diameter funnel was then incorporated into the orthogonal ESI source and empirical characterization of the device was performed. Ion current measurements were performed at a variety of turning optic potentials and optimal transmission occurred at 10V bias between the ring electrode and E1, confirming the proposed hypothesis. Moreover, a Bradbury-Nielson type ion gate was implemented post PF IF. This addition allowed for the modulation of the continuous ion beam to allow for mobility analysis. The ATD of BK showed two main distributions and a partially resolved shoulder, which may correspond to the various charge states of BK. Finally, ATDs of BK were collected as a function of turning potential. When there is no

potential drop between the wedge and ring electrode, no ion populations were detected by mobility analysis, while correlated ion signal returned upon adding a potential bias between these two elements. In order to correctly identify the ions that comprise these mobility population incorporation of a mass analyzer is needed. Additionally, in order to obtain higher mobility resolution, the orthogonal ESI-PF IF source must be incorporated with a PF IMS drift cell capable of high mobility resolution, >60. These data are the first empirical evidence that the ion current being transmitted through the instrument corresponds to analyte ions and the transmission of these ions may be tuned by the turning optics and gated into the drift cell.

4. INCORPORATION OF A HIGH RESOLUTION MOBILITY DRIFT CELL AND A MASS ANALYZER TO THE PF IF*

4.1 Introduction

Increasing the resolution of the mobility analysis allows for the separation of increasingly complex mixtures and conformational heterogeneous populations. The diffusion limited resolution of ion mobility spectrometry can be increased by changes of various parameters including: increasing the charge of the ion, the electric field, and the length of the drift cell, as well as, decreasing the temperature of the spectrometer.[71] Altering each variable to increase resolution presents a unique set of instrumentation challenges. Using ESI as the ionization method increases the average charge state of the ions produced; however, there is a concomitant gas load increase, which requires increased vacuum requirements. By increasing the electric fields, ions may undergo collisional activation that leads to structural rearrangements, whereas, decreasing the temperature results in engineering challenges such as thermal expansion and contraction, cryogenic sealing, and dewar assemblies.

Increasing the length of the drift cell provides the fewest instrumentation challenges and thus is the most common approach. However, the ion transmission through the drift cell decreases with an increase in the mobility length owing to radial diffusion.[15] Typically long drift cells utilize RF ion funnels to increase ion transmission

* Part of this chapter is reprinted with permission from: Fort, K. L.; Silveira, J. A.; Russell, D. H. *Anal. Chem.* **2013**, *85*, 9543-9548. Copyright 2013 American Chemical Society.

through these devices.[14] However, PF IMS has been shown to provide increased ion transmission through the use of DC electric fields.[15, 72] It has previously been shown that a mobility resolution (FWHM) of ~82 is achievable through the use of a 125 cm PF IMS drift cell coupled to a MALDI ionization source.[72] Work herein describes the incorporation of a high resolution 125 cm PF IMS drift cell and linear time-of-flight (TOF) mass analyzer to the orthogonal ESI-PF IF source.

4.2 Experimental

Simulations to optimize detector and time-of-flight mass analyzer designs were performed using the *collision_hs1.lua* program provided by SIMION 81 (Scientific Instrument Services, Ringoes, NJ). The simulated ion was [BK + 2H]2+ and assumed no background gas pressure. All instrumentation components were designed using Solidworks (Waltham, WA) and fabricated by the Texas A&M, Department of Chemistry Machine Shop.

Solutions of bradykinin were prepared to a concentration of 0.5 mg mL^{-1} in 50:49:1% methanol:water:acetic acid, v:v. These solutions was infused into a pulled silica ESI emitter at 500 nL min^{-1}, where the emitter was biased at +1.7-2.0 kV with respect to the heated capillary. Arrival time distributions and mass spectra were collected using Ionwerks acquisition software.

4.3 Results and Discussion

4.3.1 Construction of the high resolution PF IMS drift cell

The construction of the high resolution PF IMS drift cell was carried out very similar to that of the PF IF. However, the electrodes have a width, spacing, and inner

diameter of 6, 6, and 8 mm, respectively (Figure 35). The electrodes are spaced using nonporous ceramic ball spaces and are compressed using custom designed Delrin end-caps. The electrodes are housed inside of a ceramic tube and sealed using o-ring gaskets at both end-caps. The end-caps were designed to allow for direct assembly of the ESI-PF IF source to the drift cell. A complete schematic of the PF IMS drift cell is shown in Figure 35.

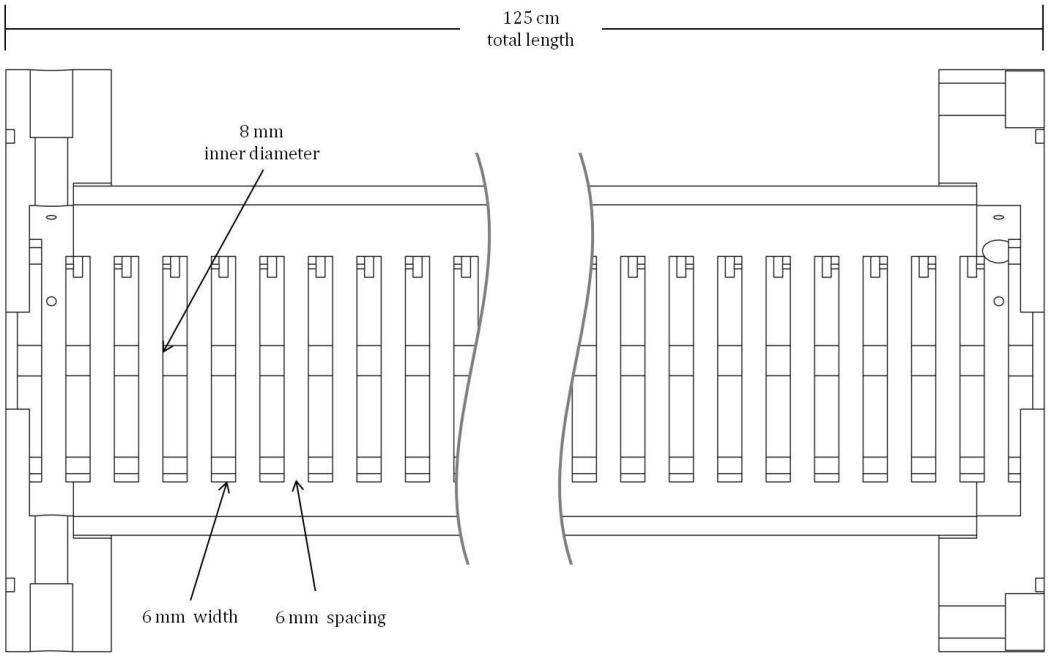

Figure 35: Solidworks broken view schematic of the PF IMS drift cell is shown. The total length of the device is 125 cm. The width, spacing, and inner diameter of the electrodes is denoted.

Owing to the radial confinement mechanism, PF IMS drift cell are typically operated using electric fields of 10 to 20 V cm^{-1} $Torr^{-1}$.[97] For a drift cell with a length of 125 cm and a maximum operating pressure of 1.4 Torr, the voltage needed to establish as 20 V cm^{-1} $Torr^{-1}$ electric field is 3.5 kV. In order to establish this voltage across the drift cell, the source will either be required to be biased at ~ +4kV and the terminal electrode of the drift cell maintained at ground or the source maintained at ground and the terminal electrode at ~ -4kV. The advantage of maintaining the source at + 4kV is that it decreases the voltage at which the mass analyzer and detector must be biased, however, the increased pressures of the source increase the risk of electrical discharge at these elevated voltages. The advantage of maintaining the source at ground is that the risk of electrical discharge is decreased, however, the mass analyzer and detector must now be biased to ~ -6kV, which complicates the circuitry of the detector and increases the power supply requirements. Additionally, by biasing the terminal electrode of the drift cell at ~ -4kV, the channeltron detector assembly utilized in the early characterization of the ESI-PF IF source is no longer able to be used owing to it requiring a ground potential. After several attempts to bias the source region at a high potential, electric breakdown prevented this configuration and thus a new detector assembly, one that is amenable to being biased at high negative potentials, is needed. Previously, a post acceleration detector (PAD) has been used in similar applications.[117] Thus, incorporation of a PAD would allow for the incorporation and characterization of the high resolution drift cell.

4.3.2 Incorporation of the post acceleration detector

In order to characterize the PAD detector design, SIMION ion trajectory modeling was performed. The initial SIMION model (Figure 36) incorporates transfer optics similar to those described previously.[72] Briefly, they consist of 4 PF IMS drift cell geometry (T1-T4) electrodes followed by 3 cylindrical electrodes to establish an einzel lens (T5-T7). The first two lenses of the einzel lens assembly are 1.000" in length and have an inner diameter of 0.625". The third lens is 0.750" in length and has an inner diameter of 0.875". These lenses are spaced 0.100" using precision ceramic spacers. The PAD electrode (T8) and detector (T9) were placed orthogonal to the central axis of the simulation (r = 0). Additionally, the terminal electrode of the drift cell (T0) was simulated to mimic the field used to extract the ions toward the PAD.

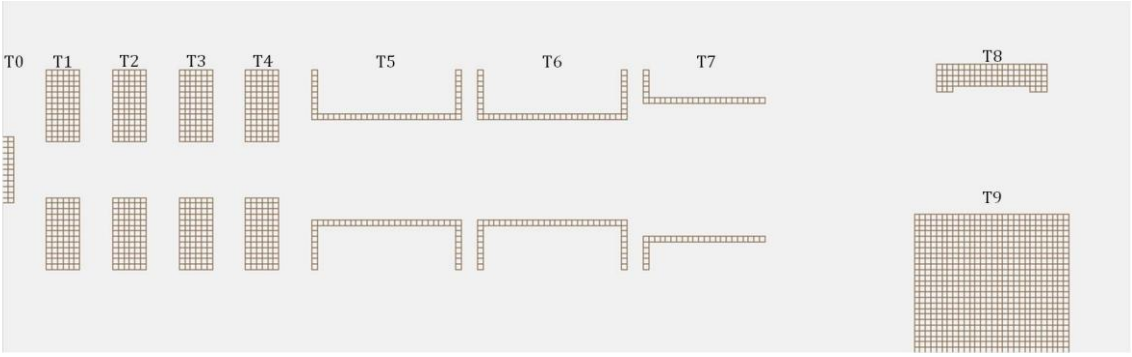

.

Figure 36: SIMION depiction of the transfer optics (T1-T7), the PAD (T8), and channeltron (T9) electrodes used to simulate ion transmission post PF IMS drift cell (T0).

The initial simulations that were performed biased T9 at -1800V, which is representative of a typical gain for a channeltron multiplier; however, when the $[BK + 2H]^{2+}$ ion was simulated, the ion packet did not collide with the PAD detector owing to the repulsive field established between T7 and T9. This is shown by the ion packet being directed toward the PAD upon traversing T7, but not colliding with the surface of T8 (Figure 37a). In order to prevent this repulsive field, the electrical potential of T9 needed to be maintained at the same potential as T7. When this is done, the ions collide with the surface and a secondary emission of electrons is shown (Figure 37b). One challenge with this modified operational design is the bias needed to facilitate transmission, which will cause electrical discharge across the detector. Thus, a shield electrode (T10) was designed to shield the bias of T9 from the ion packet, while maintaining the functionality of the detector. Additionally T7 was lengthened to further shield the ions. When T10 is biased at the same potential as T8, the ion packet strikes the surface of T8 while maintaining a bias of -1800 on T9 (Figure 37c).

Once a working SIMION model of the PAD detector was established, the device was constructed and implemented on the ESI-PF IF source and 125 cm PF IMS drift cell. Initially, ion transmission throughout the instrument was tested without mobility gating. Data acquisitions were performed with and without the ESI spray potential. When the spray potential was applied, there are ~3300 ion counts in all arrival time bins (Figure 38). For comparison, when no spray potential is applied and the ESI process is not occurring, the ion counts are below 200 (Figure 38). This data indicates that ions are being produced by the ESI emitter and being transferred to the PAD detector.

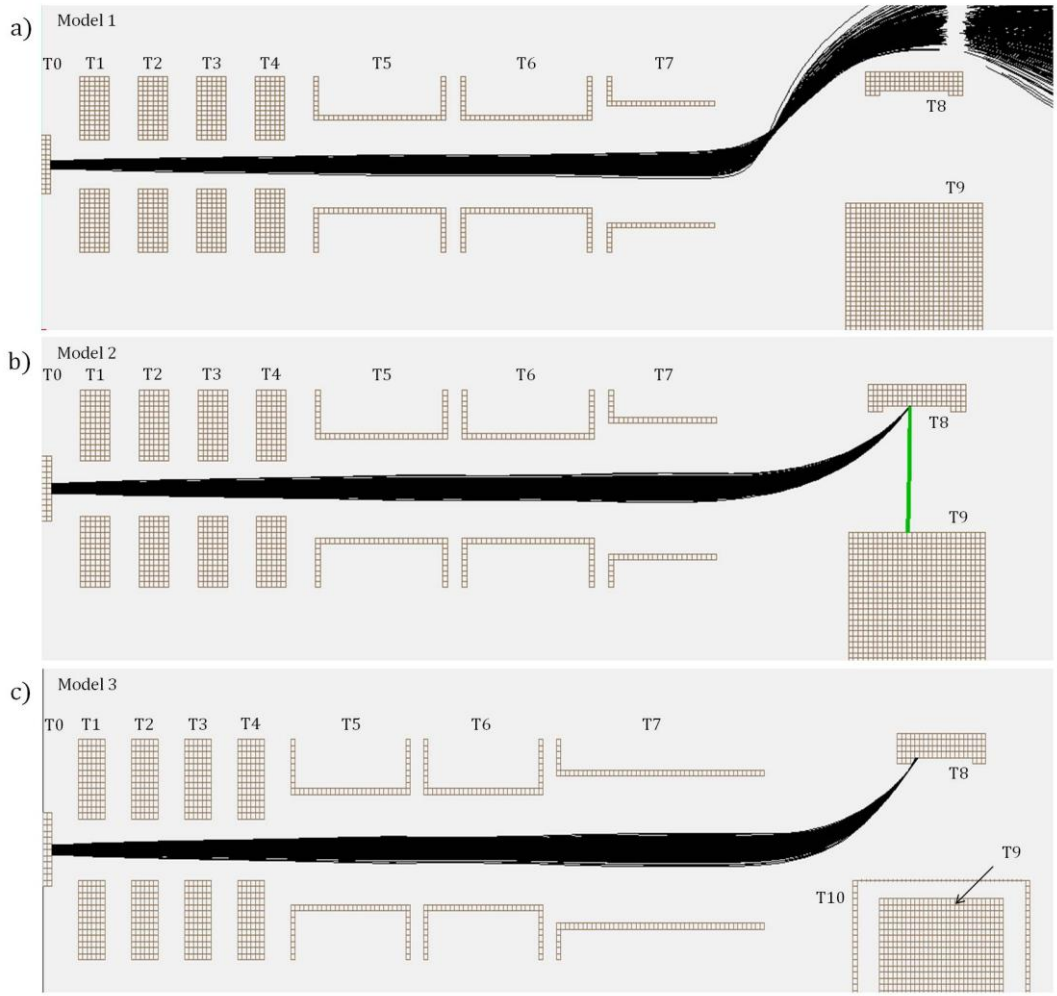

Figure 37: SIMION ion trajectory simulations of the $[BK + 2H]^{2+}$ ion for multiple transfer designs. Model 1 (a) shows that the bias on T9 deflects the ions and prevents them from colliding with the surface of the PAD (T8). When the bias of T9 is matched to that of T7, model 2 (b), ions impact the PAD and cause an emission of secondary electrons (green), which subsequently are directed to the detector (T9). While this facilitates ion transmission to the PAD, the bias of T9 is prohibitively high. Model 3 incorporates a shielding electrode (T10) that can be biased at the same potential of T7 and allows for the detector be biased at -1800 V. Ions were initially started at the center of T0 with 0.1 eV of kinetic energy.

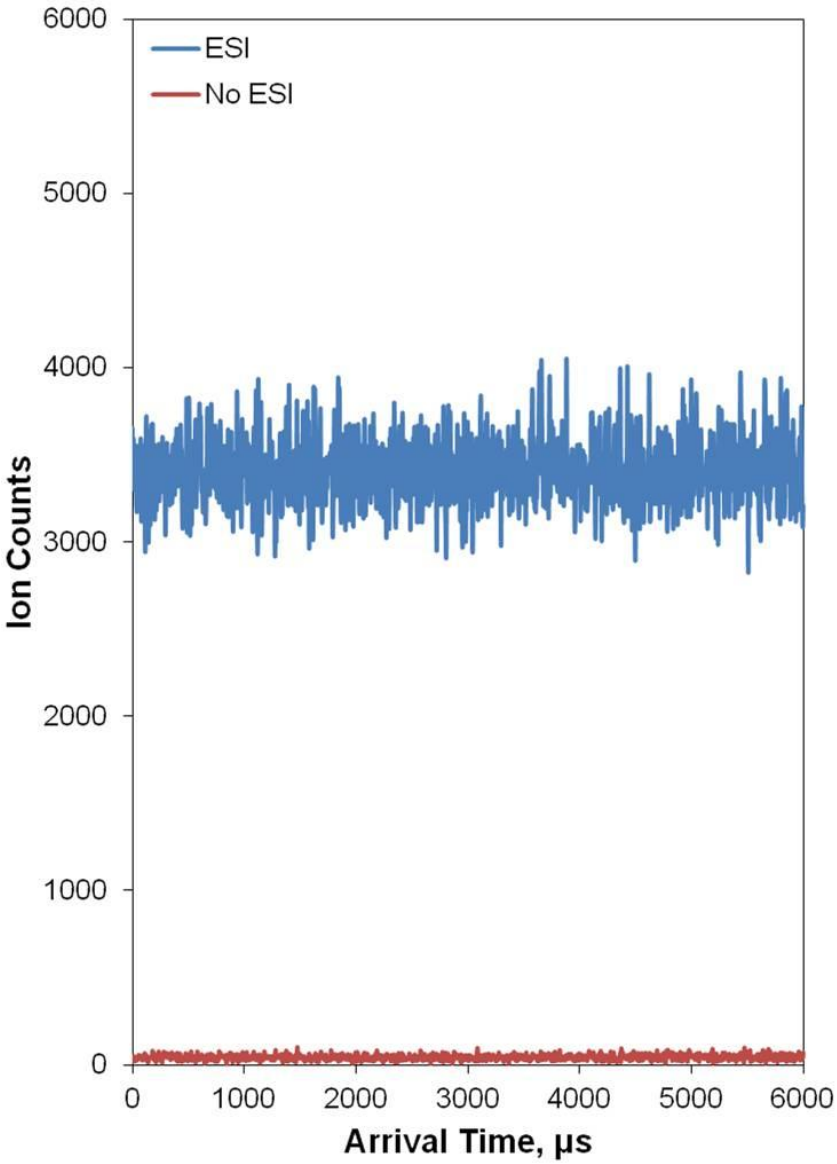

Figure 38: A graph comparing the detector response to BK as a function of application of electrical potential to the ESI emitter. When the potential is applied (ESI, blue), ESI is facilitated and ions are produced. When the potential is not applied (No ESI, red), ions are not produced. The increase in ion counts for "ESI" compared to those of "No ESI" show that ions are traversing the entirety of the instrument and being recorded with the PAD detector.

Upon measuring transmitted ions and confirming the PAD detector assembly was operational, the ATD of BK was collected as a function of gate width. The gate width was varied from 25 μs to 100 μs in 25 μs steps (Figure 39). At 100 μs, the ATD shows three distributions similar to that observed with the low resolution drift cell, however, now the higher mobility distribution, is completely resolved and centered around ~1350 μs. Additionally, there is a second distribution that is centered on ~1600 μs, and finally a third distribution centered on ~2700 μs. The lower mobility distribution is the dominate peak as it is 100% relative abundance as compared to the two other peaks (Figure 39). However, as the gate width is decreased, the relative abundance of lowest mobility population is decreased. This indicates that there is a mobility discrimination with the gating (i.e., as the gate width becomes shorter, lower mobility ions are preferentially deflected). Nevertheless, these data suggest indicate that the high resolution PF IMS drift cell is capable of transmitting ions and that the mobility resolution is increased with the increased drift cell length.

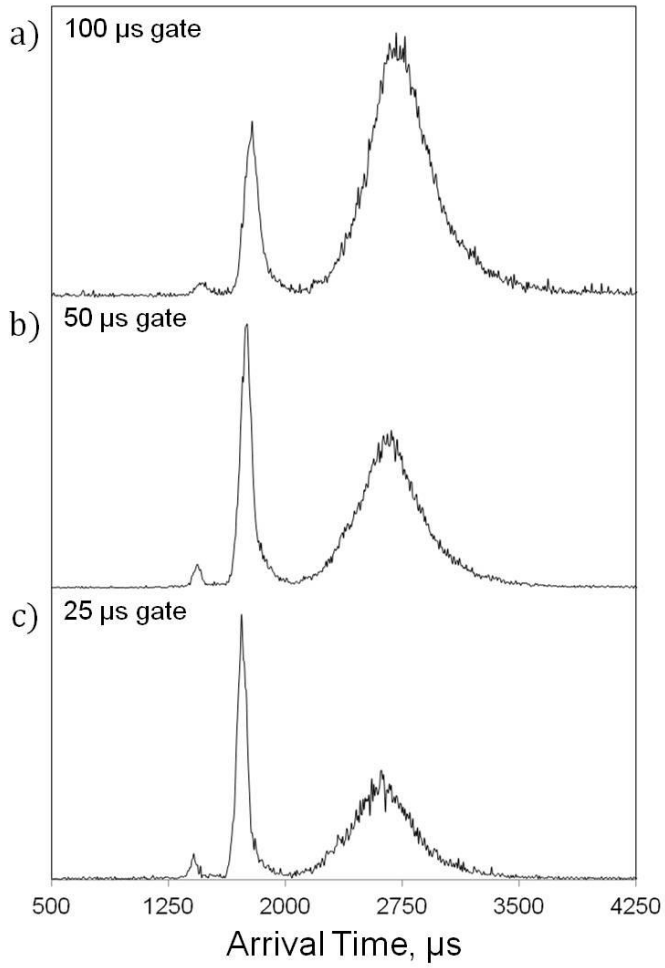

Figure 39: The ATD of BK is shown as a function of gate width. At a gate width of 100 µs (a), the lowest mobility distribution is at 100% relative abundance; however, as this gate width is lowered, 50 µs (b) and 25 µs (c), this distribution is reduced in relative abundance. These data indicate a low mobility discrimination of the ion gate.

4.3.3 Incorporation of a time-of-flight mass analyzer

Currently the instrument is able to transmit ions through the 125 cm drift cell, however, the identity of each mobility distribution is still unclear owing to a lack of mass information. Thus the incorporation of a mass analyzer is needed. Herein the design and implementation of a linear TOF mass analyzer is described.

Traditionally, a TOF mass analyzer can be incorporated orthogonally to the mobility axis.[14, 17] Ions enter an extraction region and an electrical pulse causes them to enter the field free region of the mass analyzer. By knowing the potential of the pulse used to extract the ions, as well as, the total distance of the mass analyzer, the mass to charge of the ions can be obtained.[102] SIMION ion trajectory simulations were performed in order to design a TOF mass analyzer that would be compatible with the high resolution PF IMS drift cell (Figure 40). The design utilizes the transfer optics for the PAD detector; however, a differential pumping area was designed to facilitate the use of a MCP detector. Currently, the pressure in the PAD chamber is ~$5x10^{-5}$ Torr. A MCP detector will be used and these require pressures of ~10^{-6} Torr to prevent electrical breakdown. In order to achieve these pressures, the TOF region must be isolated and differentially pumped from the transfer region. Thus, the TOF field free region will be encapsulated in a metal flange and ions will be extracted into this region. The TOF design was then simulated using the $[BK + H]^+$ ion. The push and pull electrodes were pulsed +650 and -650 V, respectively. The timing of the pulse was synchronized with the ions entering the extraction region of the simulation. Owing to the extraction voltages, the ions are deflected toward the detector and would register as an ion count (Figure 41). The SIMION model of the TOF mass analyzer was designed in Solidworks and machined.

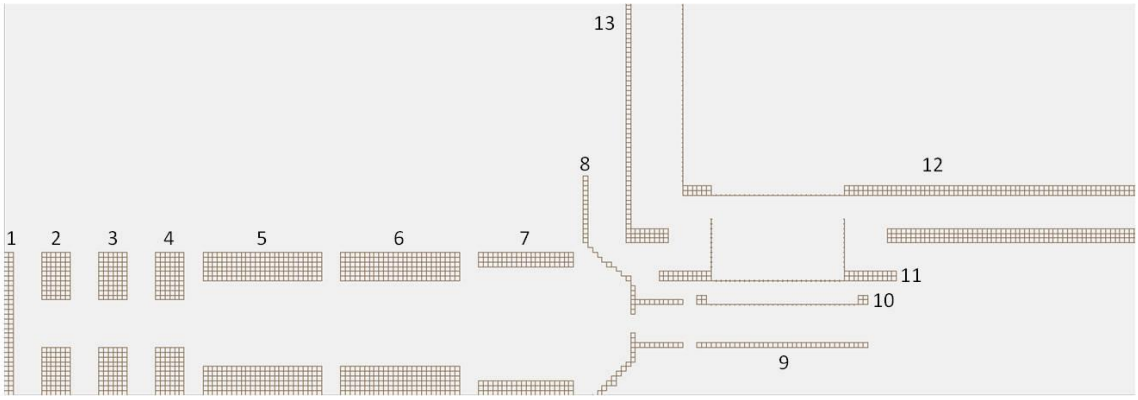

Figure 40: The SIMION model of the TOF extraction region. The transfer optics (1-7) are the same as those used with the design of the PAD detector. The TOF field free region (12) is housed in a grounded vacuum barrier (13) for differential pumping. A shielding electrode (8) prevents the ions from being deflected by this ground potential. The push (9), pull (10), and common (11) electrode are all represented.

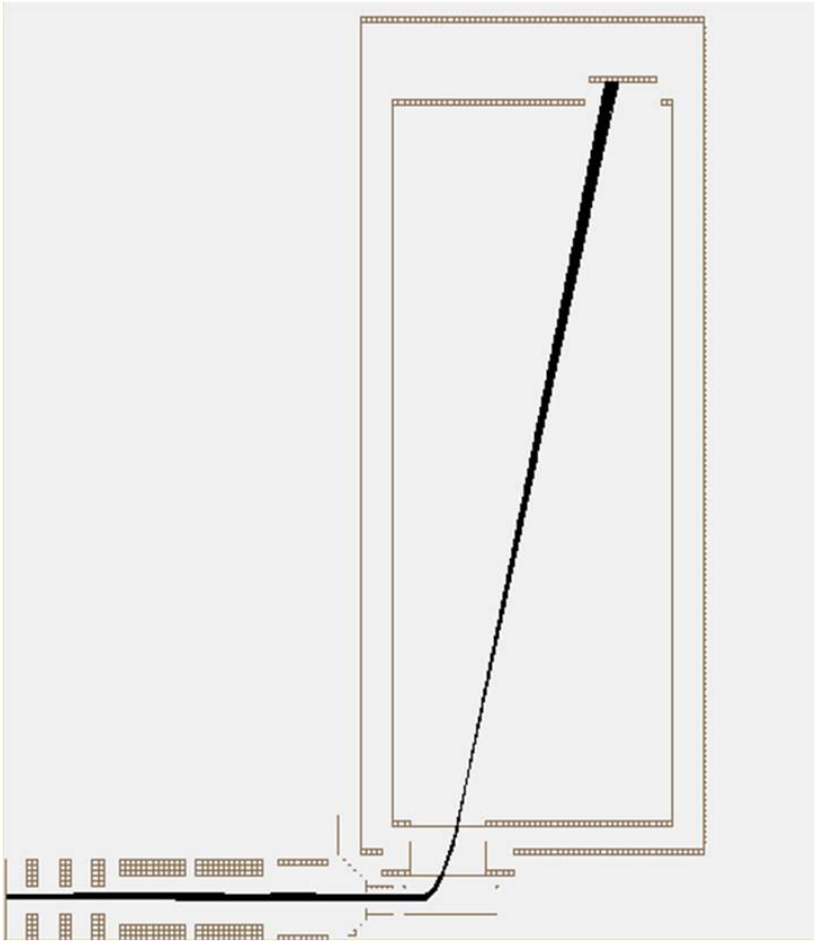

Figure 41: The SIMION model using [BK + H]+ ions and a simulated extraction pulse of +650 V (push) and -650 V (pull). The ions are projected onto the detector and would register as an ion strike.

The TOF mass analyzer was constructed to mimic the SIMION model (Figure 42). The transfer lenses were incorporated from the PAD detector and the extraction lens are housed in PEEK. The base of the TOF housing flange was modified to PEEK to prevent electrical breakdown between the TOF field free region and this flange. The TOF field free region is constructed with a stainless steel cylinder that is 26.5 cm in length. During typical operation, this is maintained at -6kV.

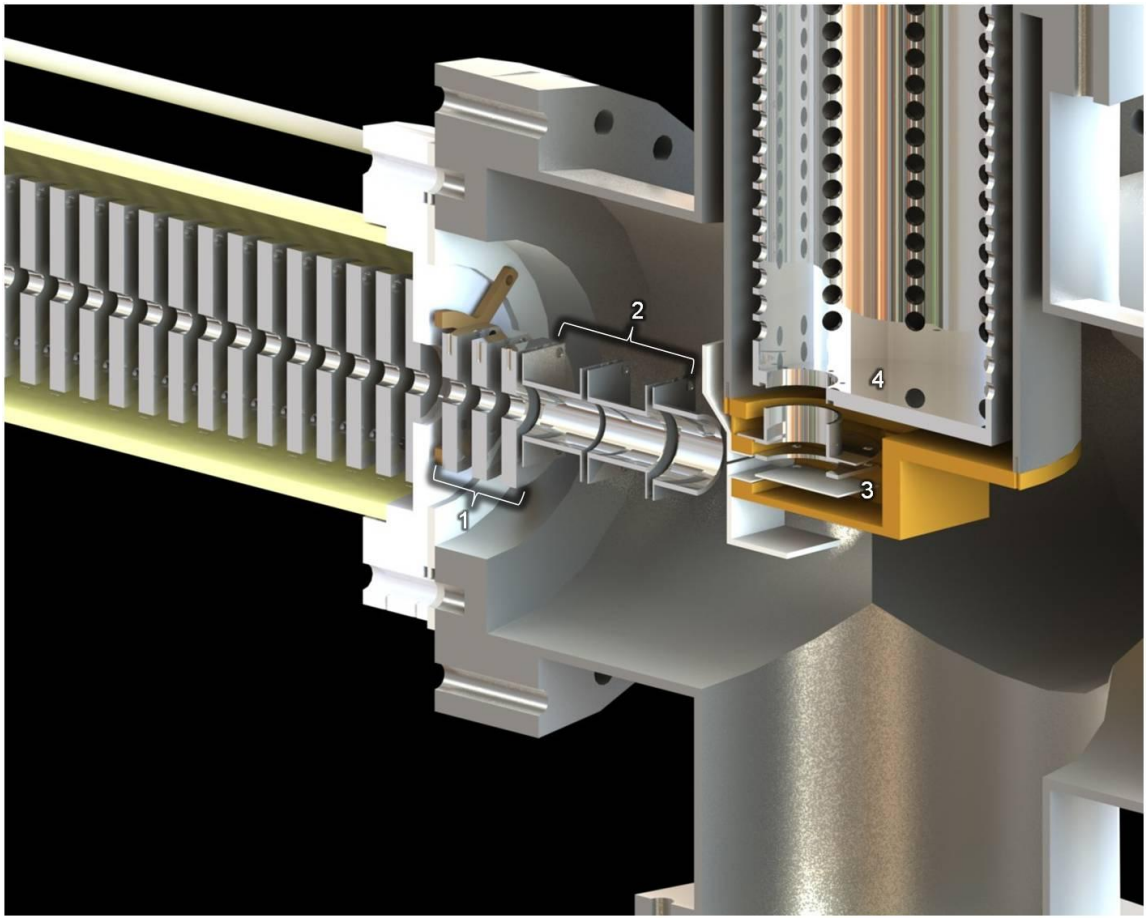

Figure 42: The Solidworks design of the TOF mass analyzer. The PF IMS extraction lens (1) and einzel lenses (2) are incorporated from the PAD detector. Ions enter the extraction region (3) and are pulsed into the TOF field free region (4). This region is housed in a stainless steel flange to allow for differential pumping.

Prior to operation of the TOF, the pressure in various regions of the instrument was monitored as a function of gas load in the source and drift cell. The TOF region is pumped using 200 L s^{-1} and a 70 L s^{-1} turbomolecular pumps. The transfer region is pumped using a 550 L s^{-1} turbomolecular pump. When the heated capillary is closed and no helium is added to the drift cell, the pressure within the mass analyzer is 4.5×10^{-7} Torr. When the heated capillary is open and the drift cell pressure is increased to 1.7

Torr, the pressure in the mass analyzer is increased to $1.4x10^{-6}$ Torr. This is within the range acceptable for use of a MCP detector and thus the TOF can be utilized. Further pressures in the various regions (Figure 43) of the instrument as a function drift cell pressure are listed in Table 6.

An additional modification of the drift cell was performed to stabilize the pressure within this region. Owing to the large (8mm) inner diameter of DC1 electrode, the pressure in the drift cell fluctuates. In order to stabilize this, a front 1 mm aperture was added to the drift cell. This addition brought the length of the drift cell to 138 cm and added a ring electrode between the PF IF and the entrance aperture of the drift cell. Owing to the added distance between the gate and DC1 with this addition, the aperture is now used to modulate the ions into the drift cell.

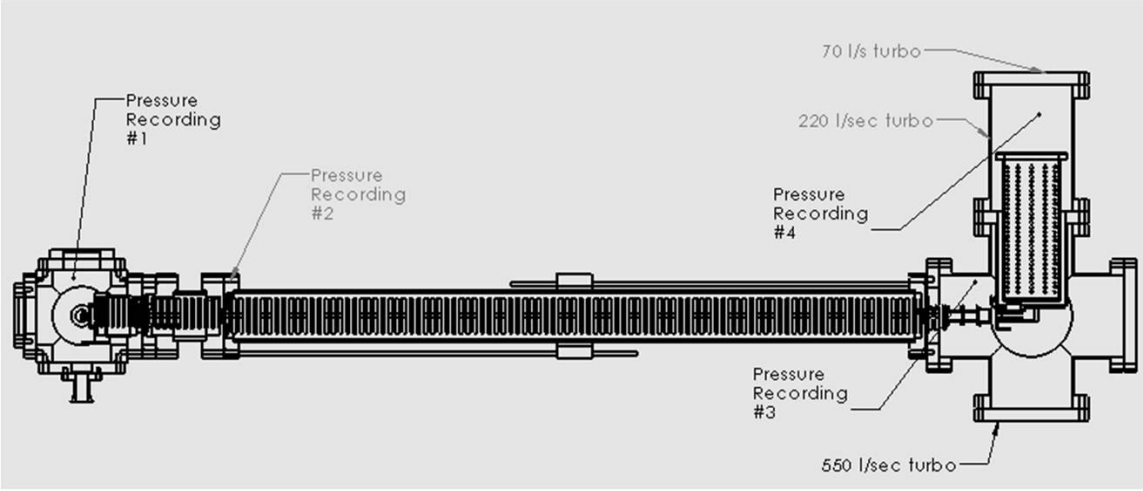

Figure 43: Location of the pressure readings in the source (pressure 1), drift cell (pressure 2), transfer region (pressure 3), and TOF region (pressure 4). The speed of the turbomolecular pumps that are used in the transfer and TOF region are noted.

Pressure 1	Pressure 2	Pressure 3	Pressure 4
N/A	1.4E-01	3.2E-06	4.5E-07
5.0E-01	6.6E-01	2.8E-05	6.5E-07
5.1E-01	9.8E-01	3.0E-05	9.2E-07
5.1E-01	1.1E+00	2.9E-05	1.0E-06
5.2E-01	1.4E+00	3.0E-05	1.3E-06
5.4E-01	1.8E+00	3.4E-05	1.7E-06

Table 6: The pressure (Torr) of the four various locations in the instrument. At the highest pressure in the drift cell (pressure 2), the pressure in the TOF region (pressure 4) remains within the working limits of the MCP detector.

4.3.4 Characterization of the PF IF with high resolution ion mobility-mass spectrometry

The simulated ion transmission of $[BK + 2H]^{2+}$ ions in the PF IF was previously shown to have a sigmoidal shape owing to the onset of momentum conservation. With the incorporation of the mass analyzer, the mass spectra of BK can be collected and allows for experimental characterization of the ion transmission of the $[BK + 2H]^{2+}$ ion. The experimental and simulated ion transmissions plots are quite similar, both in terms of transmission efficiency and general shape (Figure 44). Although the exact experimental inflection point is difficult to discern, the data clearly show a significant increase in ion counts upon increasing the electric field from 6 to 38 V cm $^{-1}$ Torr $^{-1}$. This increase corresponds to a ~40-fold gain in the amount of ions transmitted during a fixed period of time. Note that below 6 V cm $^{-1}$ Torr $^{-1}$ no ion counts were detected. While the simulated data suggest that ion transmission reaches a maximum at ~25-30 V cm^{-1} Torr^{-1}, the experimental ion transmission does not plateau until slightly higher electric fields (~35-40 V cm^{-1} Torr^{-1}). The small difference between the theoretical and experimental

data is likely due to: (1) the presence of the helium counter flow in the instrument and (2) the potential presence of neutral contaminants (air and solvent) inside the PF IF housing. Neither effect is accounted for in the SIMION model and both effects lead to an additional dampening of the ions' axial velocity such that additional force is required for momentum conservation. Finally, it should be noted that while the PF IF shows an increase in ion counts similar to the simulated transmission efficiency, the number of ions emitted from the heated capillary that are transmitted to the detector may be less than the simulated model due to expansion of the ions exiting the heated capillary. Nevertheless, simulated results suggest that the PF IF is capable of transmitting >90% of ions that enter the device ($\vec{r} \leq 6$ mm from the central drift axis).

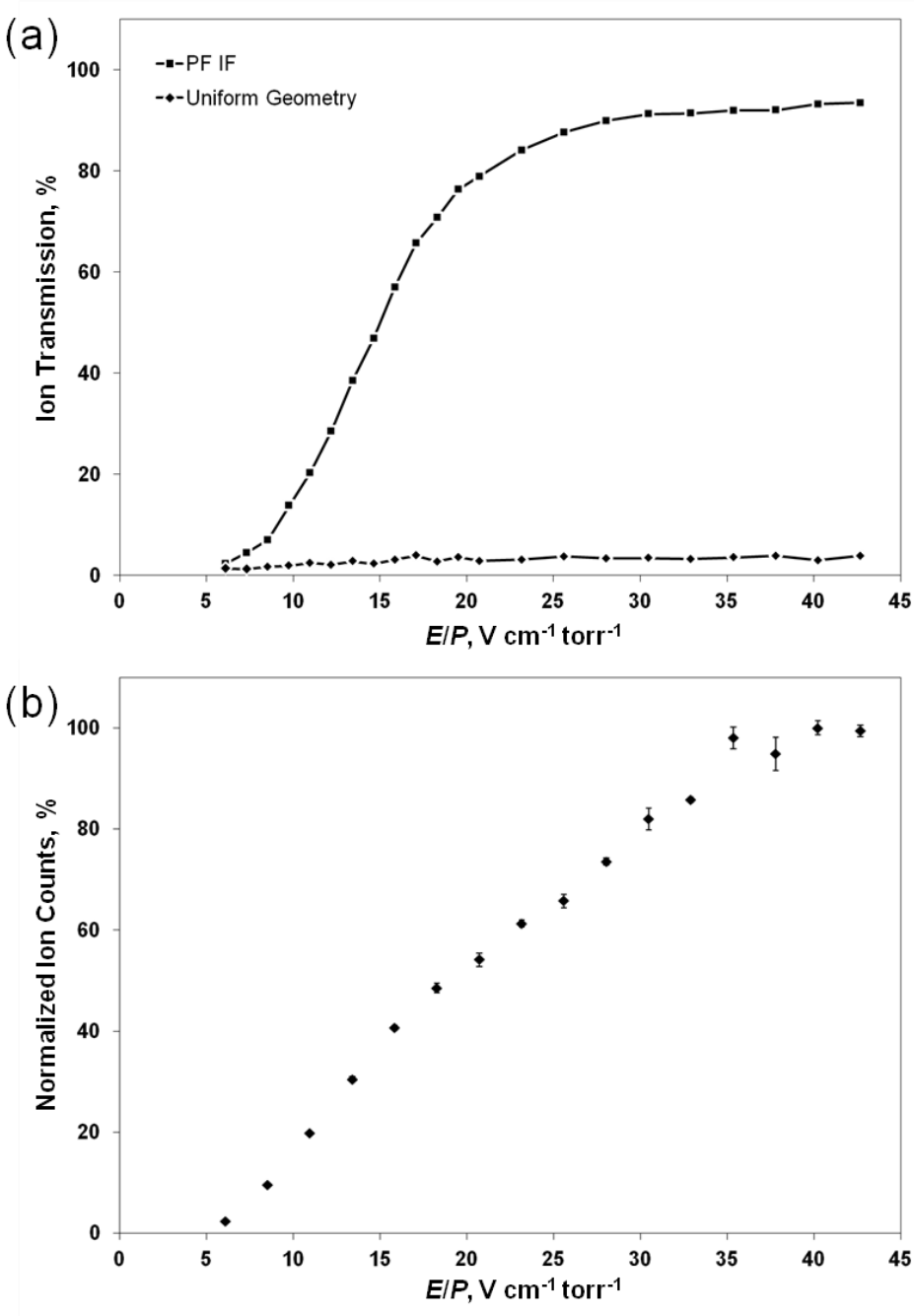

Figure 44: Theoretical (a) and experimental (b) ion transmission across the PF IF as a function of electric field strength. Panel a contains the results from SIMION modeling for $[BK + 2H]^{2+}$. Panel b contains the experimental results obtained for the doubly charged bradykinin ion.

While the oscillatory axial and radial electric fields facilitate ion focusing, Figure 24 clearly shows that the local E_z maxima exceeds the applied field between adjacent electrodes. This effect is further illustrated in Figure 25 as maximum ion velocity is observed between adjacent electrodes near the back of the device. The increase in ion velocity between adjacent electrodes may increase the local effective ion temperature (T_{eff}) when ions traverse these regions, and under extreme conditions may lead to collision-induced dissociation (CID).[88, 100-101, 118] To investigate the effects of ion heating on the IM and MS data, three model peptides BK, gramicidin s (GS), and trpzip1 (TZ), were selected for experimental studies. The mass spectra for each of the three analytes (Figure 45a-c) show that multiply charged peptide ions produced by ESI are efficiently transmitted through the PF IF. No fragment ions were observed, indicating that T_{eff} is below the threshold of dissociation.

However, the absence of fragment ions in the mass spectra does not necessarily demonstrate that ion heating is not present. The potential energy surface for thermally labile biomolecules, such as peptides, proteins, and their complexes, contain multiple local minima that may be accessed via mild collisional activation in the gas phase.[52, 57, 59] These structural changes are hidden in the mass spectra but revealed by structurally sensitive techniques such as IM. Here, high resolution IM is employed to investigate the impact of ion heating on the conformer distributions. Figure 45d-f contains plots of ion ATDs for $[GS + 2H]^{2+}$, $[BK + 2H]^{2+}$, and $[TZ + 3H]^{3+}$ at several PF IF electric field strengths. In each case, the IM profiles for each ion remain unchanged by the presence/absence of additional translational energy, suggesting that the nascent

conformer distribution produced upon ESI remains unperturbed by the heating/cooling cycles experienced inside the PF IF. This outcome is especially interesting in the case of $[BK + 2H]^{2+}$ where a quasi-equilibrium distribution of conformer states that readily interconvert has been reported by Papadopoulos *et al*.[66, 119]

Pierson et *al.* demonstrated that like $[BK +2H]^{2+}$, the $[BK + 3H]^{3+}$ ion also adopts multiple conformational states in the gas phase.[52, 59] Tandem IM analysis (used to select and activate each conformation in the nascent distribution) revealed that a distribution of $[BK + 3H]^{3+}$ states is established prior to dissociation. In order to further assess the effect of field-induced heating in the PF IF, the ATDs of $[BK + 3H]^{3+}$ were collected at varied E_z values. Though the resolution of the PF IMS drift tube is unable to resolve all conformers, Figure 46a clearly shows that at low field strength, the ATD is indeed similar to the nascent distribution observed by Pierson *et al*. prior to activation. However, when the field strength is increased (Figure 46c), the quasi-equilibrium distribution is observed. Based upon the relative abundance of each species, the more abundant conformer observed at 3000 μs is consistent with the conformer previously termed C, whereas the more compact conformers A and B (~2750 μs) are unresolved. These data indicate that the PF IF can preserve kinetically-trapped species or induce gas-phase rearrangement prior to IM-MS analysis.

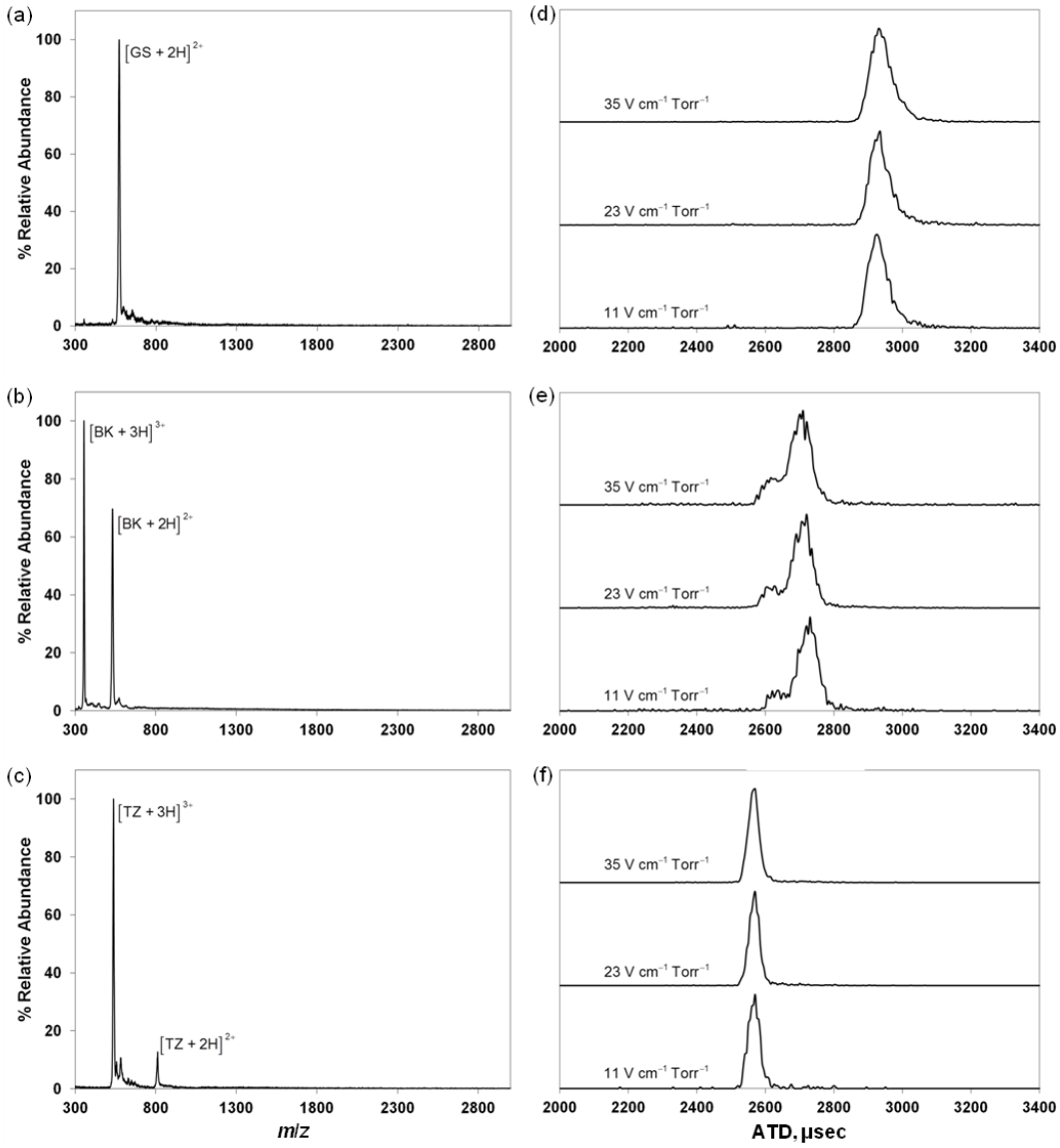

Figure 45: Representative mass spectra of gramicidin S (a), bradykinin (b), and tripzip 1 (c) collected at a field strength of 23 V cm^{-1} Torr $^{-1}$ in the PF IF and arrival time distributions of $[GS + 2H]^{2+}$ (d), $[BK + 2H]^{2+}$ (e), and $[TZ + 3H]^{3+}$ (f) as a function of field strength across the PF IF.

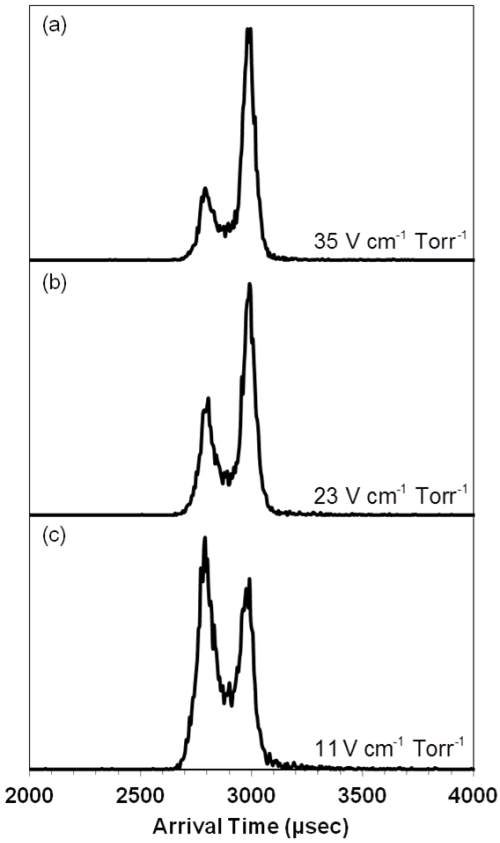

Figure 46. The arrival time distribution of $[BK + 3H]^{3+}$ as a function of PF IF field strength. The PF IMS electric field was maintained at 14.8 V cm^{-1} $Torr^{-1}$ and the heated capillary was biased +70 V relative to the wedge electrode.

4.4 Conclusions

A 138 cm PF IMS drift cell was incorporated with the ESI-PF IF source. Owing to the voltage requirements, which are inherent with the increased length the of drift cell, a PAD detector was added to the instrument. SIMION characterization allowed for design of the detector assembly. The ATD of BK was collected and showed three distributions. This is consistent with the ATDs collected on the low resolution drift cell, which showed two main distributions and a third partially resolved distribution. Upon

obtaining ion transmission through the drift cell, incorporation of a mass analyzer was required. A SIMION simulation of the mass analyzer was designed and a pulse scheme was incorporated into the program to mimic the push/pull pulses required to extract ions. Once the simulated ions were projected on to the detector via the SIMION model, the mass analyzer was designed and implemented onto the ESI-PF IF-PF IMS instrument. With this incorporation, the empirical ion transmission of $[BK + 2H]^{2+}$ ions, as a function of PF IF axial electric field, was determined and compared to the previously simulated results. The two transmission curves, simulated and empirical, were both similar in shape owing to the onset of conservation of axial momentum. However, the empirical transmission plot was shifted to higher electric field values, which may originate owing to the counter flow of helium, which was not accounted for in the simulation, within the PF IF. However, the maximum signal plateaus similarly to the simulated transmission curve, indicating that the PF IF is performing comparably to the simulated model.

Further characterization was performed by analyzing the mass spectrum and ATD of three peptides: GS, BK, and TZ. The mass spectra of these three analytes showed that signals that corresponded to multiply charged intact ions of the individual peptide, i.e. no fragment ions. This indicates that the PF IF is not heating the ions to the point that dissociation of covalent bonds is occurring. Ion heating was further explored by analysis the ATD of $[GS + 2H]^{2+}$, $[BK + 2H]^{2+}$, and $[TZ + 3H]^{3+}$ at a range of PF IF axial electric fields. All the ATDs remained constant in both peak centroid and shape indicating that there was no conformational rearrangement that occurring owing to

heating that was resolvable at the current mobility resolution. Finally, the analysis of $[BK + 3H]^{3+}$ ions, which have been shown to undergo conformation conversion, suggested that the PF IF is capable of preserving "kinetically trapped" conformations and, at increased axial field strengths, anneal these species to study conversion of these conformations to the energetically preferred conformation. Collectively, these data suggest that the PF IF not only is capable of increasing ion transmission, but also provides an analytical tool for the study of "native" and/or "kinetically trapped" conformations, an attribute that is critical to the use of IM-MS to structural biology.

5. SUMMARY: "FROM SOLUTION TO THE GAS PHASE: STEPWISE DEHYDRATION AND KINETIC TRAPPING OF SUBSTANCE P REVEALS THE ORIGIN OF PEPTIDE CONFORMATIONS"*

5.1 Introduction

IM-MS studies allow for the determination of CCS of dehydrated biomolecular ions; however, of ongoing debate is the correlation between the conformations measured in the gas phase and those present in solution. It has been previously shown that peptides and proteins can retain conformations that are specific to their solutions, which suggest that there is some solution memory effect; which indicates that evaporative cooling allows for the kinetic trapping of non-energetically preferred conformations during mobility analysis.[52, 59]

ESI begins with the production of large, macro charged solvent droplets and ultimately produces multiply charged desolvated ions.[43] However, the exact mechanism for the formation of these desolvated ions is still under debate. One potential mechanism, the charge residue model (CRM), proposes that fission events produce a charge droplet, which contains an analyte, that undergoes stepwise dehydration until a dehydrated, multiply charged ion is produced.[120-121] Additionally, it has been proposed that ions can produced by an ion evaporation model (IEM), whereas ions will migrate to the surface of a charge solvent droplet and upon the droplet becoming sufficiently small,

* This chapter is adapted with permission from: Silveira, J. A.; Fort, K. L.; Kim, D.; Servage, K. A.; Pierson, N. A.; Clemmer, D. E.; Russell, D. H. *J. Am. Chem. Soc.* **2013**, *135*, 19147-19153. Copyright 2013 American Chemical Society.

the charge allows for the analyte ion to be ejected from the surface.[109] Recently, an additional mechanism, named the chain ejection mechanism, has been proposed for extended biomolecular ions.[122-124] However, owing to a lack of experimental techniques to can provide insight into these mechanisms via study of partially solvated ions, there is a dearth of information pertaining to the question posed by McLafferty and Breuker; "for how long, under what conditions, and to what extent, can solution structure be retained without solvent?"[125] Work presented herein utilizes cryogenic IM-MS analysis of substance P (SP, RPKPQQFFGLM-NH_2) to empirically determine the ESI mechanism for these ions. The data suggests that SP ions are formed exclusively by the CRM ESI mechanism. Moreover, amino acid mutations and collisional activation studies, utilizing the PF IF, show that the origin and stability of "kinetically trapped" conformations can be discerned.

5.2 Experimental

5.2.1 Sample preparation

SP was purchased from Sigma Aldrich and had a purity of 95%. Mutant SP (RPKPAAFFGLM-NH_2) was purchased from MoCell Biotech Co. Both peptides were used without further purification. Solutions of the peptides were prepared in 18 MΩ water and methanol. The final concentration and solvent composition were 10-50 μM and 90/10 water/methanol (vol:vol) with 1% acetic acid. Cryogenic hydration studies were performed using peptide solutions with a solvent composition of pure water and 0.1% formic acid.

5.2.2 IM-MS measurements

Experimental details and description of the cryogenic IM-MS instrument have been previously described.[78, 89] Briefly, peptide solutions are directly infused into a ESI emitter that is biased 1.8-2.2 kV with respect to the heated capillary inlet. The extent of hydrated clusters observed is controlled by varying the temperature of the heated capillary inlet from 353 to 380 K. Upon elution from the heated capillary, hydrated clusters and dehydrated ions are transported to the cryogenically cooled IM drift cell, which is 30.2 cm in length and filled with ~1.6 Torr of helium. The temperature of the helium and drift cell electrodes is 80 ± 2 K. The drift cell electric field is maintained at 9.1 $V \cdot cm^{-1}$. Upon eluting the drift cell, ions are transported to an orthogonal time-of-flight mass spectrometer for mass analysis.

Ambient collisional activation studies were performed on a 1.38 m long PF IMS drift cell that has been previously described.[79] Ion activation was performed in the PF IF region of the instrument by varying the applied axial electric field between 11 and 43 V cm^{-1} $Torr^{-1}$. The ion swarm was then injected into the drift cell to facilitate mobility analysis. Determination of CCS values were performed as previously described.[49, 97]

5.2.3 Molecular dynamic simulations

Molecular dynamics (MD) and quantum mechanics simulations were performed using AMBER 11 and GAUSSIAN 03. GAUSSIAN 03 (HF/6-31+) was utilized in order to optimize the structure of custom amino acid residues, while charge fitting was performed using the R.E.D III program.[126] Common residues utilized the AMBER FF99SB force field. The charge locations were the N-terminus, the guanidine group of

arginine, and the ε-amino group of lysine. MD simulations were performed at 300 and 550 K. Simulated annealing was performed by heating the simulation to 1000K and ramping the temperature to 300 K over 5 ns. Analysis of candidate structures was performed as previously described.[51] MOBCAL was utilized to calculate CCS of simulated structures.[127]

5.3 Results and Discussion

The mass spectra of SP collected with a heated capillary maintained at 353, 360, and 380 K is shown in Figure 47. At the lowest heated capillary temperature, there are two peaks that originate from dehydrated ions of SP, namely, the $[SP + 3H]^{3+}$ and $[SP + 2H]^{2+}$ ions. The $[SP + 2H]^{2+}$ distribution has shows extensive hydrations as hydrated clusters range from $0 < n \leq 60$ water molecules. While not extensively populated, $0 < n \leq 30$, the $[SP + 3H]^{3+}$ ion also shows hydration. As the heated capillary temperature is increased, the rate of dehydration is also increased and, subsequently, the mean cluster size is reduced. At a heated capillary temperature of 380 K, the hydrated clusters for both ion populations have been eliminated. These data indicate that by controlling the heated capillary temperature, the extent of desolvation can be controlled and that these cluster are representative of the final stages of desolvation.

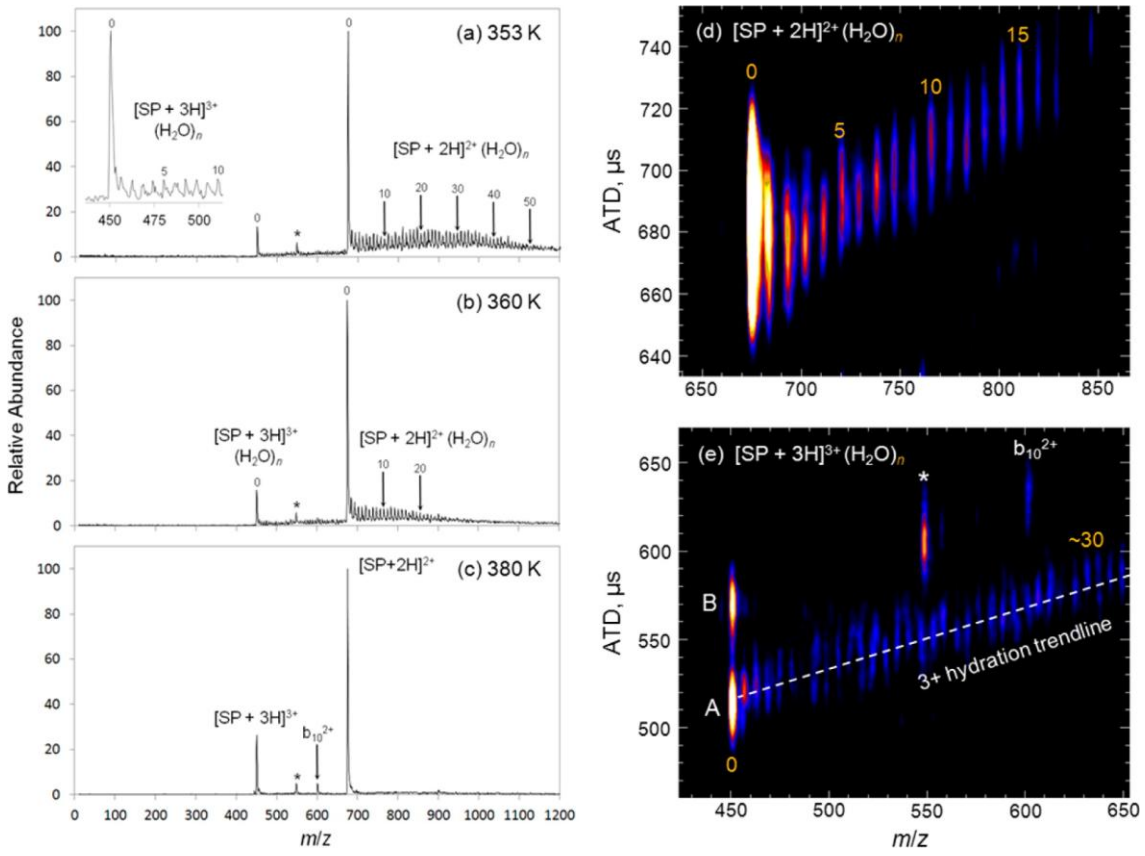

Figure 47: The mass spectra of SP collected at a heated capillary temperature of (a) 353, (b) 360, and (c) 380 K. The two dimensional ATD versus mass to charge plot for the (d) $[SP + 2H]^{2+}$ and (e) $[SP + 3H]^{3+}$ ions show that the dehydrated ions are formed from a charge residue model of ionization. Figure is adapted from reference 77.

In order to determine the conformational changes that occur as solvent becomes limited, ion mobility measurements were employed in combination with a heated capillary temperature that produces extensive hydration clusters. This will provide empirical evidence that addresses the question posed by McLafferty and Bruker that asked "for how long, under what conditions, and to what extent, can solution structure be retained without solvent?"[125] The ATDs of $[SP + 2H]^{2+}$ and $[SP + 3H]^{3+}$ show a linear decrease in arrival time of progressively desolvated cluster ions (Figure 47). These data

indicated that no gross structural change, which can be resolved with the current resolution of the drift cell, occurs as water molecules are removed. For $[SP + 2H]^{2+}$, the dehydrated ion shows a single broad distribution and the hydrated trendline extends to this ion. This indicates that this dehydrated conformer arises directly from the desolvation process, i.e., the charge residue model (CRM). The ATD for $[SP + 3H]^{3+}$ the ATD shows two, resolved populations; the first, higher mobility peak is denoted as $\mathbf{A}_{SP,}$ 315 $Å^2$, and the second, lower mobility peak is denoted as $\mathbf{B}_{SP,}$ 363 $Å^2$. Interestingly, when following the hydration trendline for the $[SP + 3H]^{3+}$ ion, the hydrated clusters extends solely to the $\mathbf{A}_{SP}$ conformation. As with the $[SP + 2H]^{2+}$ hydration trendline, these data indicate that $\mathbf{A}_{SP}$ originates from a CRM ionization mechanism. However, the absence of a hydration trendline for $\mathbf{B}_{SP}$ presents two possibilities for the origin of this conformation (Figure 48a): (1) $\mathbf{B}_{SP}$ is formed by an alternate ionization mechanism or (2) $\mathbf{B}_{SP}$ is formed via conformational rearrangement of $\mathbf{A}_{SP}$ upon complete desolvation. In addition to CRM, possible ESI mechanisms include the ion evaporation model (IEM) and the chain ejection model (CEM). Both the CEM and IEM would produce a conformer absent of a hydration trendline; however, empirical examination of this hypothesis is difficult.

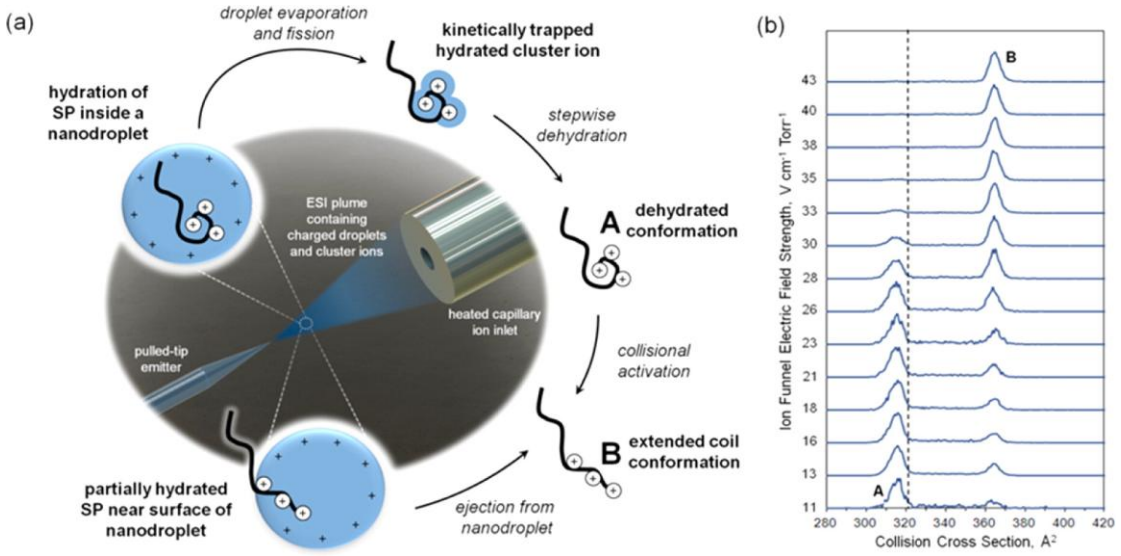

Figure 48: A schematic of the two potential mechanisms for the formation of $\mathbf{B}_{SP}$ (a). A CRM mechanism (top) shows that $\mathbf{A}_{SP}$ is formed and then is followed by collisional activation to form $\mathbf{B}_{SP}$. Alternatively, $\mathbf{B}_{SP}$ can be formed in the droplet and under ejection via the IEM mechanism (bottom). The mass selected ATD of [SP + 3H]3+ ions as a function of PF IF electric field strength (b) show that at the lowest fields $\mathbf{A}_{SP}$ is the most abundant conformation. However, as the field strength is increased, $\mathbf{A}_{SP}$ is quantitatively converted to $\mathbf{B}_{SP}$, supporting the CRM mechanism. Figure is adapted from reference 77.

In order to test the latter hypothesis, collisional activation prior to ambient ion mobility was performed using the PF IF. The data from the collisional activation study (Figure 48b) show that at reduced electric fields $\mathbf{A}_{SP}$ is the predominant conformation. As the electric field is increased, $\mathbf{A}_{SP}$ converts to $\mathbf{B}_{SP}$, which is consistent with the proposed hypothesis that $\mathbf{B}_{SP}$ originates from conformational rearrangement of $\mathbf{A}_{SP}$. Taken together, these data demonstrate that $[SP + 3H]^{3+}$ ions are formed is the CRM and the conformational evolution of these ions is as follows (Figure 49):

$$[\mathrm{SP}+3\mathrm{H}]^{3+}(aq.) \xrightarrow{droplet\ evaporation\ and\ fission} [\mathrm{SP}+3\mathrm{H}]_A^{3+}\,(\mathrm{H_2O})_{n\lesssim 30}$$

$$\xrightarrow{stepwise\ dehydration} [\mathrm{SP}+3\mathrm{H}]_A^{3+} \xrightarrow{activation} [\mathrm{SP}+3\mathrm{H}]_B^{3+} \xrightarrow{activation} fragments$$

Figure 49: The conversion of $[SP + 3H]^{3+}$ (*aq.*) to fragment ions in the gas phase. Figure is adapted from reference 77.

Previous NMR results have suggested that SP exists as multiple conformations in the aqueous phase; additionally, SP has been shown to adopt a helical conformation when inserted into the lipid membrane.[128-129] These data are consistent with the observed $\mathbf{A}_{SP}$ and $\mathbf{B}_{SP}$ conformations, whereas, $\mathbf{A}_{SP}$ is a compact conformation and $\mathbf{A}_{SP}$ is an extend or helical conformation. One hypothesis that explains the compaction of $\mathbf{A}_{SP}$ is that intramolecular interactions involving the charge sites and polar and/or aromatic residues, namely Q^5/Q^6 and F^7/F^8. In order to test this hypothesis, mutant SP (M, RPKPAAFFGLM-NH_2) was analyzed, where by replacing Q5/Q6 with alanine (A), interactions that are dependent on these amino acids will be eliminated.

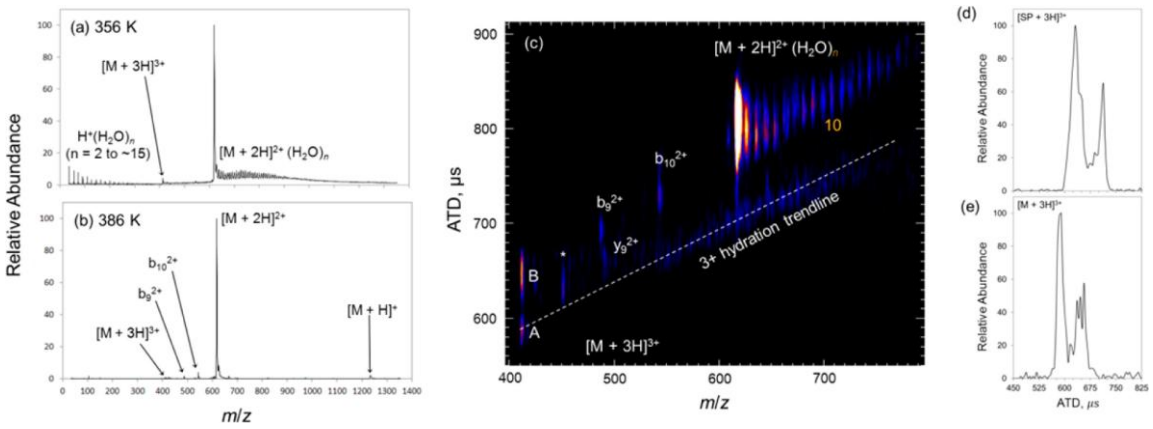

Figure 50: The mass spectrum of mutant SP collected at (a) 356 and (b) 386 K. The two-dimensional plot of mutant SP. The $[M + 3H]^{3+}$ ion shows two distinct conformations that are consistent with $\mathbf{A}_{SP}$ and $\mathbf{B}_{SP}$. When comparing the $[SP + 3H]^{3+}$ and $[M + 3H]^{3+}$ ATDs (d), the peak width of the compact conformation for the mutant is reduced compared to native SP owing to a reduction in conformational heterogeneity. Figure is adapted from reference 77.

The mass spectra of mutant SP is shown in Figure 50a-b. The spectra are very similar to SP in regard to hydration, i.e., hydrated clusters are observed for the $[M + 2H]^{2+}$ ion. However, the relative abundance of the $[M + 3H]^{3+}$ ion is significantly reduced. IM-MS studies of mutant SP show that even while the ion abundance is reduced, the $[M + 3H]^{3+}$ ion exhibits two distribution, $\mathbf{A}_M$ and $\mathbf{B}_M$, which are consistent with the conformations observed for $[SP + 3H]^{3+}$ (Figure 50c). Interestingly, the peak width of $\mathbf{A}_M$ is reduced when compared to $\mathbf{A}_{SP}$ (Figure 50d), suggesting that upon elimination of Q5/Q6 as possible interactions sites the conformational heterogeneity of the compact conformation is reduced. Collectively, these data support the hypothesis that the compact conformation is partially stabilized by interactions involving Q5/Q6.

While the presence of Q^5/Q^6 appears to be important to the stability of $\mathbf{A}_{SP}$, the reduction in the production of the triply charged ion indicates that these residues also

play a role in the production of this charge state. The number of basic residues in a peptide or protein influence the observed charge state distribution upon ESI.[130] However, it has been shown that if charge sites are localized, Coulombic repulsion leads to a reduction in the apparent gas-phase basicity of the residues and thus will lead to a reduction in average charge state.[131] Recently, it has been shown that the average charge state of SP can be increased from 2.4 to 2.8 with the addition of 1% sulfolane, a known supercharging reagent.[80] One possible hypothesis for this average charge state increase is that sulfolane interacts with the charge sites and shields these charges, which minimizes the effects of Coulombic repulsion. Adducts of SP and sulfolane were previously observed and capable of being dissociated upon mild collisional activation.[80] This is analogous to the compaction of $\mathbf{A}_{SP}$, whereas, interactions with Q5/Q6 shield the charge sites, minimize Coulombic repulsion, and thus increase the average charge state. As the ions undergo collisional activation in the PF IF, these interactions are disrupted and elongation to form $\mathbf{B}_{SP}$ occurs. Upon elimination of these residues, these shielding interactions are no longer present which leads to an increase in Coulombic repulsion and, subsequently, a reduction in gas-phase basicity and average charge state distribution.

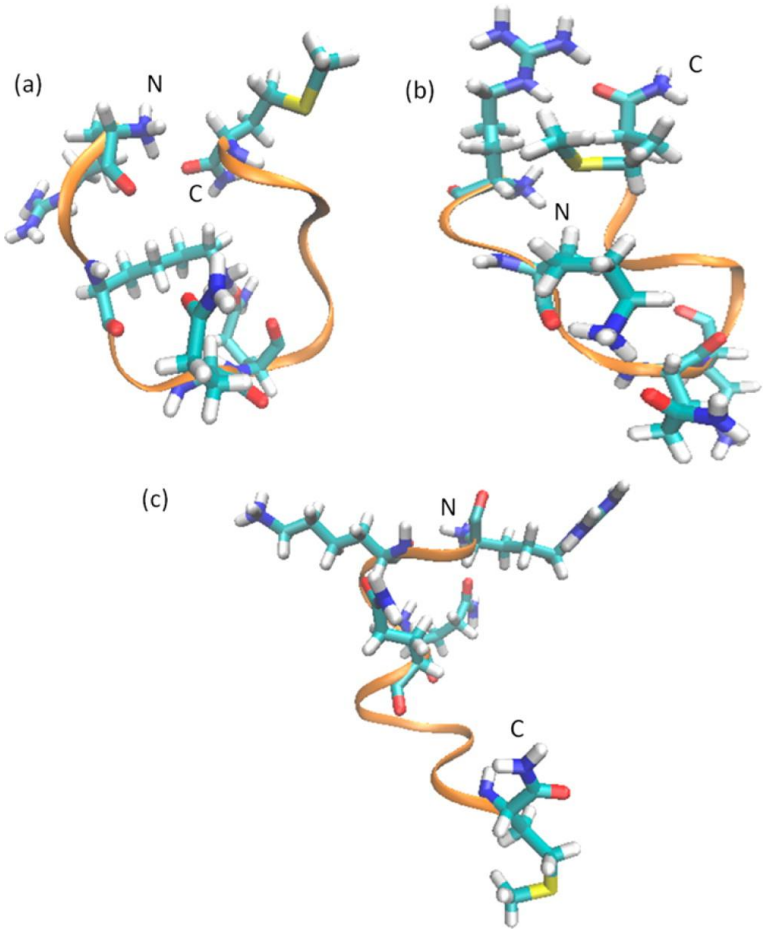

Figure 51: Representative conformations as obtained from molecular dynamic simulations performed at (a) 300 K and (b) 550 K. Simulated annealing (c) shows that upon increased temperature, the $[SP + 3H]^{3+}$ ion undergoes elongation. Figure is adapted from reference 77.

Molecular dynamic (MD) simulations are consistent with this proposed hypothesis. Conformations that were obtained at 300 K and 550 K show that Q^5 and Q^6 solvate the charge site on K^3 (Figure 51a-b). Further interactions are suggested by these data, namely the interaction of the charge N-terminus and the amide C-terminus and interactions between R^1 and the amide C-terminus. The conformations that exhibit these interactions are consistent with $\mathbf{A}_{SP}$ as they are compact and have an average CCS of

~330 $Å^2$. Additionally, upon simulated annealing (Figure 51c), the interactions are eliminated and the ion is consistent with an extended coil structure and has a CCS of 370 $Å^2$. These data, in conjunction with the mutant SP data, support the hypothesis that the compaction of $\mathbf{A}_{SP}$ is facilitated via intramolecular interactions.

5.4 Conclusions

Cryogenic IM-MS allows for the preservation of hydrated clusters of biomolecular ions and subsequently allows for the empirical determination of structural changes that occur during the final stages of desolvation. Moreover, by analyzing the ATD of progressively desolvated ions, the origin of the dehydrated conformations can be elucidated. For SP, there appears to be no significant conformational change that occurs during the final stages of desolvation for either $[SP + 2H]^{2+}$ or $[SP + 3H]^{3+}$ ions. For $[SP + 2H]^{2+}$ dehydrated ions, the ATD is comprised of a single board peak and the hydration trendline extends directly to this conformation. These data suggests this conformation arises directly from desolvation, i.e., the CRM mechanism of ionization. $[SP + 3H]^{3+}$ dehydrated ions adopt two distinct conformations: $\mathbf{A}_{SP}$ and $\mathbf{B}_{SP}$. Interestingly, the hydration trendline extends exclusively to the $\mathbf{A}_{SP}$ conformation, which is consistent with a CRM mechanism. However, the origin of $\mathbf{B}_{SP}$ is initially ambiguous owing to a lack of a hydration trendline. Collisionally activation studies performed in the PF IF suggest that $\mathbf{A}_{SP}$, after complete dehydration, can undergo structural rearrangement for form $\mathbf{B}_{SP}$. These data show the analytical utility of cryogenic IM-MS and the PF IF in terms of determining the origin of conformations observed by IM-MS studies. Moreover, the data clearly shows that SP ions are formed via the CRM mechanism.

Owing to $\mathbf{A}_{SP}$ converting to $\mathbf{B}_{SP}$ upon collisional activation, it appears that evaporative cooling kinetically traps this conformation in the gas phase. One possible hypothesis for the kinetic trapping of this conformation is that intramolecular interactions between the charge sites and aromatic/polar residues are formed upon desolvation and provide stability to $\mathbf{A}_{SP}$. In order to test this hypothesis, mutant SP, where Q^5/Q^6 were replaced with A, was analyzed by cryogenic IM-MS. The ATD of $[M + 3H]^{3+}$ ions show two distinct conformations, $\mathbf{A}_M$ and $\mathbf{B}_M$, that are consistent with $\mathbf{A}_{SP}$ and $\mathbf{B}_{SP.}$ However, the compact $\mathbf{A}_M$ conformation is narrower as compared to $\mathbf{A}_{SP}$, indicating that the structural heterogeneity of this conformation has been reduced upon elimination of Q^5/Q^6 and additional stabilizing interactions are present. MD simulations data further supports the kinetic trapping hypothesis as the compact conformation shows interactions between the charge sites and polar/aromatic residues. Furthermore, upon simulated annealing, the CCS of $[SP + 3H]^{3+}$ increases owing to a disruption of these stabilizing interactions. In order to further characterize the stabilizing interactions responsible for kinetic trapping, further amino acid mutations should be employed. Nevertheless, these data show that by eliminating polar amino acid residues that the stability of $\mathbf{A}_{SP}$ can be affected. Moreover, the conversion of origin of multiple conformations observed in IM-MS can be understood.

6. SUBSTANCE P FROM SOLUTION TO THE GAS PHASE PART II: FACTORS THAT INFLUENCE KINETIC TRAPPING OF SUBSTANCE P IN THE GAS PHASE

6.1 Introduction

Peptide and protein structures are dictated by intrinsic intramolecular interactions involving hydrophobic and hydrophilic regions in their molecules, interactions with other species in the solution (cations, anions, detergents, and other solubilizing agents), and interactions with the solvent. Unraveling the contributions of each of the individual interactions and how their collective effects alter conformational preferences are major challenges to understanding peptide/protein structure/function relationships. Studies of gas-phase/solvent-free biomolecule ions provide a means to investigate conformational preferences because intra- and intermolecular interactions are effectively decoupled under these conditions.[132-135] Ion mobility-mass spectrometry (IM-MS) is increasingly used for studies of gas-phase peptide/protein ion conformations, and provides unparalleled capabilities for deconvoluting conformational heterogeneity of peptide/protein systems. A potential concern with this approach is that during the transition from solution to the gas phase during electrospray ionization (ESI), biomolecules must undergo dehydration reactions that may affect conformer preferences and potentially alter the population distribution of conformers.[77, 89, 136] For example, as solvent is removed, stabilization afforded by water is diminished and intramolecular electrostatic interactions (e.g. salt bridges and/or hydrogen bonds) become increasingly more important.[64, 125] On the other hand, there is a growing body of evidence that

suggests "native-like" states of gaseous ions are kinetically trapped in local minima along their potential energy surface owing to evaporative cooling and reduced rates of inter-conversion among energetically accessible states.[48, 52, 54, 59, 61-67, 119, 125, 137-138] Of critical importance to the study of conformational preferences of biomolecules by IM-MS is the preservation of these "native-like" or kinetically trapped conformations. Skinner *et al.*[139] and Breuker[64] presented data obtained from electron capture dissociation (ECD) that further supports the idea that intramolecular interactions between charge sites and polarizable amino acid side chains are formed upon complete desolvation, and such interactions afford stability to kinetically trapped conformations. Breuker recently reported ECD data for horse and tuna cytochrome c that show differences in fragmentation can be rationalized on the basis of electrostatic interactions.[140] This interpretation of the ECD data is also consistent with studies of the cytochrome c ion complexed with crown ethers,[141] where it was shown that coordination of the lysine ammonium ion by 18-crown-6 inhibits formation of intramolecular hydrogen bonding in cytochrome c ions thereby shifting their conformer preferences.

While there is very little empirical data on the processes associated with the structural transitions that occur during the final stages of dehydration of the electrosprayed solvent droplets, a number of studies have demonstrated that under mild ESI conditions, biomolecule ions can retain memory of their solution structures.[55, 93, 142-143] Cryogenic IM-MS provided the first experimental data on the conformational changes that occur during the final stages of the dehydration process.[77-78, 89] The data clearly showed that $[M + 3H]^{3+}$ ions of substance P (SP) (an undecapeptide:

RPKPQQFFGLM-NH_2) do not undergo significant conformational changes during the final steps (loss of the last ~100 water molecules) of the dehydration process. Furthermore, the dominant conformer formed by dehydration, under cold conditions, was a "kinetically trapped" state, which upon collisional heating rearranged to adopt the thermodynamically more stable gas-phase ion conformation. Molecular dynamics (MD) simulations illustrated that the kinetically trapped conformation is stabilized through interactions between the charge sites (the N-terminus, the arginine (R) side chain guanidinium ion, and the ε-ammonium of the lysine (K) side chain) and polar residues, specifically glutamines (Q) at positions 5 and 6 and possibly phenylalanines (F) at positions 7 and 8. Moreover, simulated annealing studies showed that at increased temperatures, these interactions are disrupted and structural rearrangement of the collapsed coil to an extended coil conformation occurs. Here, we explore the effects of specific intramolecular interactions on conformer preferences and the stability of the kinetically trapped conformer of substance P $[M + 3H]^{3+}$ ions by using specific amino acid mutations that eliminate salt bridge formation, specifically, substitution of alanine for Q at positions 5 and 6 and for F at positions 7 and 8, and by altering the backbone orientation of the charge carrying sites through proline (P) substitutions at positions 2, 4, and 9.

6.2 Experimental

6.2.1 Peptides and ionization

The nomenclature, sequence, CCS, and purity of each peptide analyzed are listed in Table 7. SP and its reverse sequence (RS) were purchased from American Peptide (Sunnyvale, CA). Mutant peptides Q5A, Q6A, P2A, P4A, P2,4A, and G9P were purchased from Mocell (Shanghai, China); P2,4A G9P, Q5,6A F7,8A, Q5,6A, and F7,8A peptides were purchased from Gen Script (Piscataway, NJ). Each lyophilized peptide was dissolved in 1 mL of water and stored at -20 C No further purification steps were performed. Aliquots of each stock solution were diluted with 50:49:1 methanol:water:acetic acid to create ~10 μM solutions. Samples were directly infused into the instrument through a pulled-tip fused silica emitter at 500 nL min^{-1}. The emitter was biased 1.8 – 2.0 kV relative to the heated capillary inlet to facilitate ESI.

Peptide	Sequence	% Purity	Collision Cross Section, Å²			
			A		B	
SP	RPKPQQFFGLM-NH_2	>95	315 ± 3.6		363 ± 3.1	
P4A	RPKAQQFFGLM-NH_2	85	298 ± 1.3		345 ± 1.3	
P2,4A	RAKAQQFFGLM-NH_2	82	288 ± 2.8		338 ± 2.7	
Q6A	RPKPQAFFGLM-NH_2	84	298 ± 1.9		362 ± 1.7	
F7,8A	RPKPQQAAGLM-NH_2	84	280 ± 6.6		323 ± 6.5	
			A_1	A_2	B	
P2A	RAKPQQFFGLM-NH_2	73	301 ± 0.7	312 ± 2.4	350 ± 1.8	
Q5A	RPKPAQFFGLM-NH_2	80	287 ± 4.0	293 ± 4.1	343 ± 4.9	
			A		B_1	B_2
G9P	RPKPQQFFPLM-NH_2	75	301 ± 2.4		358 ± 3.1	366 ± 2.0
P2,4A G9P	RAKAQQFFPLM-NH_2	90	299 ± 1.4		349 ± 1.3	363 ± 1.2
					B	
Q5,6A	RPKPAAFFGLM-NH_2	83	—[a]		344 ± 0.5	
Q5,6A F7,8A	RPKPAAAAGLM-NH_2	>95	—[b]		293 ± 1.6	
RS	MLGFFQQPKPR-NH2	>95	—[b]		343 ± 1.2	

Table 7: The abbreviation, sequence, purity, and CCS values for all peptides analyzed. [a] observation of $\mathbf{A}_{Q5,6A}$ was achieved at reduced PF IF and PF IMS drift cell electric fields. [b] Q5,6A F7,8A and RS show only one peak in their ATD; these peaks were assigned to **B** owing to collisional activation studies and CCS correction.

6.2.2 Instrumentation and data acquisition

ATDs and mass spectra were collected on a home-built ion mobility-mass spectrometer that has been described previously.[79] Briefly, the instrument consists of a PF IF, a 138 cm-long PF IMS drift tube, and an orthogonal acceleration time-of-flight mass analyzer. Ions are introduced into the instrument through a heated capillary inlet that is maintained at 70 C to facilitate desolvation. The heated capillary is positioned orthogonal to the entrance of the PF IF to inhibit unwanted neutral contaminants from entering the mobility analyzer. Turning optics are used to direct ions from the flow of gas into the PF IF where ions are radially focused. A discrete packet of ions is pulsed into the drift tube by modulation of the potential on a ring electrode positioned at the back of the PF IF. Helium gas (99.999% purity) is added to the PF IF and PF IMS drift

cell yielding pressures of ~1.0 and 1.28 Torr, respectively. Collisional activation studies can be performed prior to IMS analysis by increasing the electric field in the PF IF from 23 to 38 V cm^{-1} $Torr^{-1}$. CCS values were obtained as described previously[97] using drift fields ranging from 19.2 to 14.7 V cm^{-1} $Torr^{-1}$.

6.3 Results and Discussion

6.3.1 Identifying intramolecular interactions

Previous cryogenic mobility results have demonstrated that $[SP + 3H]^{3+}$ (Figure 47e) adopts a compact conformation, denoted $\mathbf{A}_{SP}$, that is not representative of the preferred gas-phase structure, $\mathbf{B}_{SP}$. Moreover, MD simulations have shown that candidate structures representative of the compact conformation are primarily stabilized by interactions between charge sites, i.e. N-terminus, R^1, and K^3, and $Q^{5/6}$. Of interest here is the identification of specific interaction sites and the importance of each site to the collective stabilization of the compact conformer. In order to identify residues critical to this stabilization, amino acid mutations are employed to eliminate possible interaction sites. Site-specific mutations of amino acids to alanine are commonly utilized in molecular biology and biochemistry to evaluate the importance of specific amino acids on protein structure and function.[144-149] Thus, mutations of possible stabilizing residues to alanine were preformed.

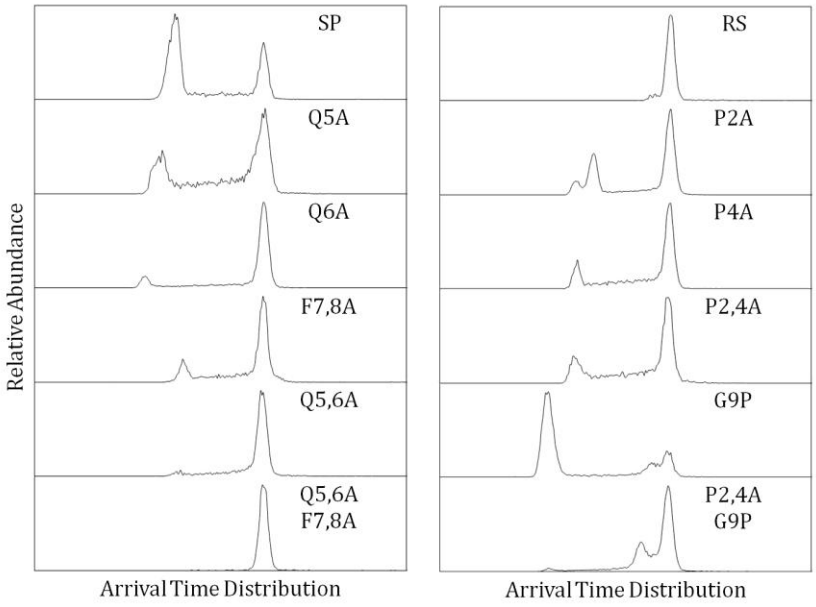

Figure 52: The ATDs of SP and SP mutant $[M + 3H]^{3+}$ ions.

The ATDs of single Q to A mutants, Q5A and Q6A, show two distinct peaks consistent with a compact (**A**) and elongated (**B**) conformation (Figure 52). The relative abundances, with respect to the elongated conformer, of $\mathbf{A}_{Q5A}$ and $\mathbf{A}_{Q6A}$ are ~20% and ~10%, respectively. The peak width for $\mathbf{A}_{Q6A}$ is reduced as compared to $\mathbf{A}_{SP}$. Additionally, comparing the ATD of $[Q6A + 3H]^{3+}$ to $[SP + 3H]^{3+}$ shows that the relative abundance of the compact conformer is reduced. Consistent with these observations is a decrease in unresolved conformer heterogeneity; i.e. by removing Q^6, conformations stabilized through interactions with this residue have been eliminated. Interestingly, the ATD of $[Q5A + 3H]^{3+}$ shows a decrease in the relative abundance of the compact conformer; however, the peak width remains comparable to that of $\mathbf{A}_{SP}$. Upon further investigation, two compact conformations ($\mathbf{A}_{1,Q5A}$ and $\mathbf{A}_{2,Q5A}$) are partially resolved at

reduced drift fields, while $\mathbf{A}_{SP}$ remains an unresolved distribution of conformers (Figure 53). At higher drift fields, both $\mathbf{A}_{1,Q5A}$ and $\mathbf{A}_{2,Q5A}$ undergo structural conversion during mobility analysis to adopt the elongated conformation, which leads to the comparable peak width between $\mathbf{A}_{SP}$ and $\mathbf{A}_{Q5A}$. Nevertheless, these data show that through the elimination of a single possible interaction site, certain compact conformations are destabilized, which leads to a reduction in the structural heterogeneity of the distribution. Furthermore, as shown by comparable peak widths, the elongated conformation remains largely unaltered by the mutations. The conversion of compact to elongated conformers is also maintained with the elimination of single intramolecular interaction sites (Figure 54), suggesting that the adoption of the elongated conformation is independent of these interactions.

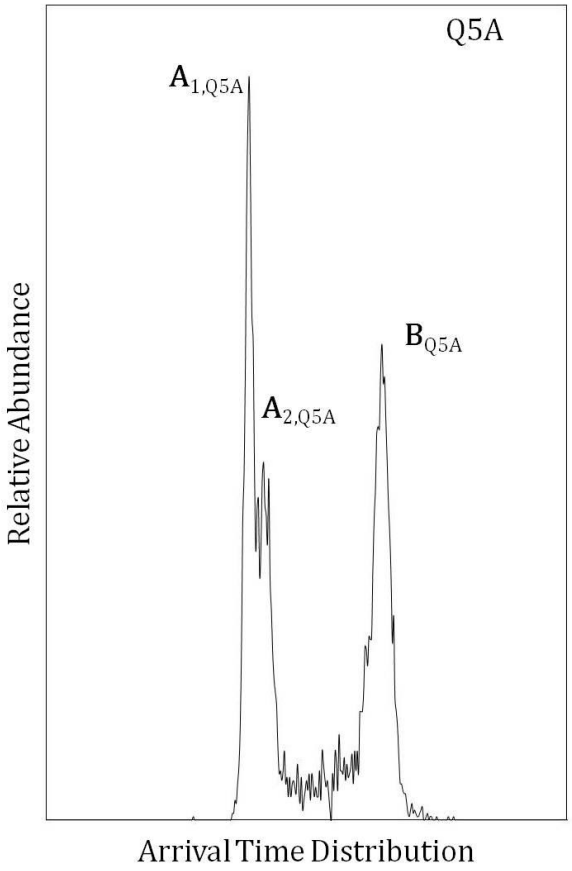

Figure 53: The ATD of $[Q5A + 3H]^{3+}$ collected at a 15.5 V cm^{-1} $Torr^{-1}$ drift field. The compact distribution consists of two partially resolved populations.

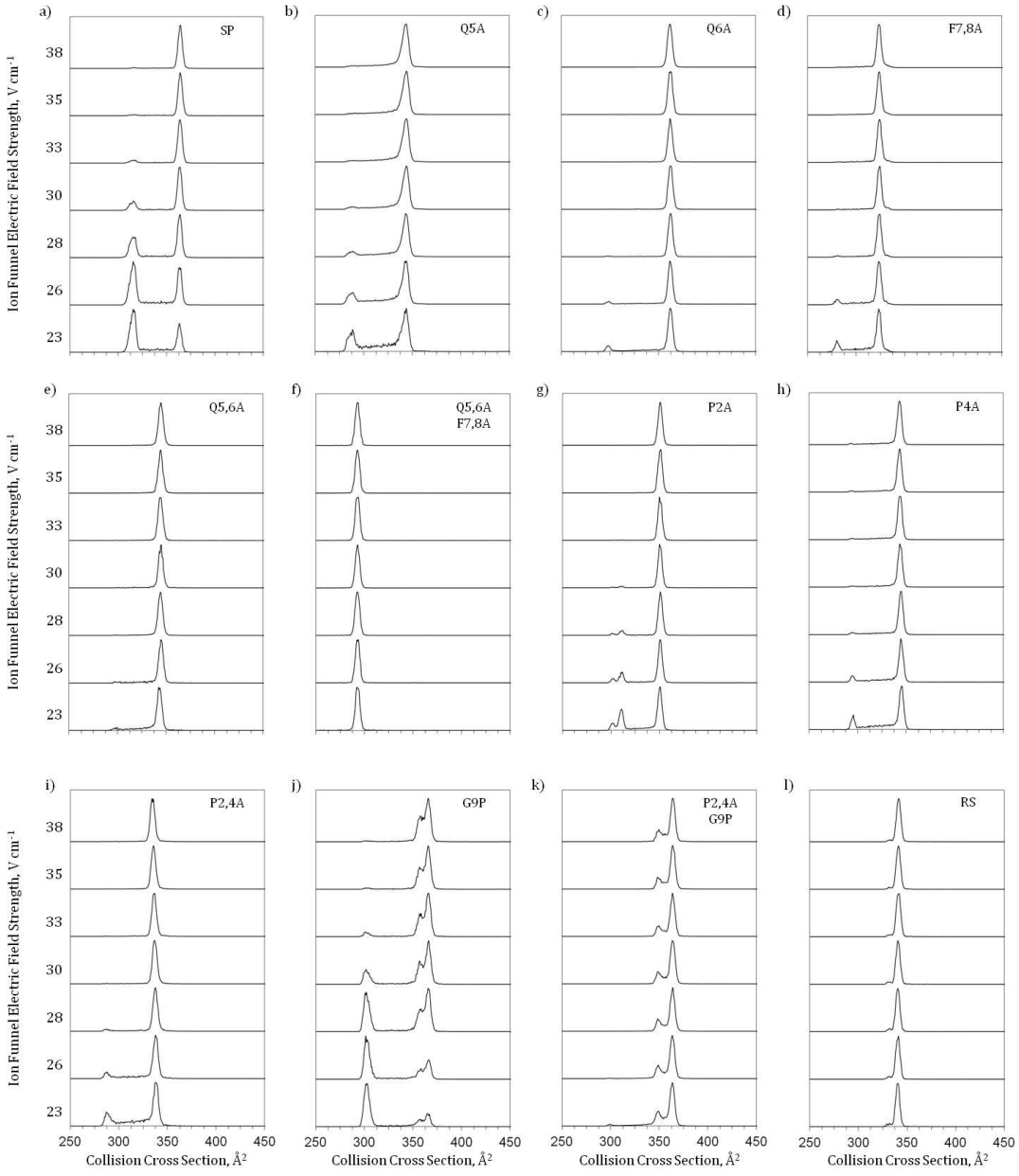

Figure 54: The collisional activation of all SP and SP mutant $[M + 3H]^{3+}$ ions. Collisional activation was performed by varying axial electric field in the PF IF from 23 to 38 V cm^{-1}.

The stabilizing contributions established through pi-cation interactions with F^7 and F^8 are examined with the F7,8A mutant. The ATD of F7,8A exhibits the

characteristic compact and elongated conformers (Figure 51). The peak width of $\mathbf{A}_{F7,8A}$ is reduced relative to $\mathbf{A}_{SP}$ and the relative abundance, with respect to the $\mathbf{B}_{F7,8A}$, is ~15%. Similar to the single-point mutations, the decrease in peak width for the compact distribution is indicative of an elimination of conformers that are stabilized by pi-cation interactions with F^7 and F^8. The reduction in relative abundance of the compact conformer observed for the double mutation of $F^{7/8}$ to A is comparable to the reduction observed for single Q mutations, suggesting that interactions between the charge sites and F^7/F^8 provide less stability than those established with Q^5/Q^6. This is exhibited further by the mutant Q5,6A, in which $\mathbf{A}_{Q5,6A}$ has a relative abundance of <5%. When compared to F7,8A, the further reduction of the compact conformer abundance indicates that interactions between the charge sites and Q^5/Q^6 afford the greatest stabilization to this distribution.

In order to examine if any remaining interaction sites are present, the mutant Q5,6A F7,8A, which eliminates all interactions with Q or F residues, was analyzed. Interestingly, the ATD shows a single conformer distribution (Figure 51). Owing to the absence of a second conformer distribution, the assignment of the single distribution to the compact or elongated form is initially ambiguous. To aid in the assignment, collisional activation prior to mobility analysis was performed. As previously shown, upon activation, the compact conformation of $[SP + 3H]^{3+}$, adopts the elongated conformation (Figure 54a). However, the collisional activation of Q5,6A F7,8A (Figure 54f) shows no change in the ATD, suggesting that the distribution corresponds to the elongated conformation. Additionally, CCS correction based on individual mutations

shows that the CCS for this mutant is consistent with the value expected for the elongated conformation.[150] Finally, when instrumentation parameters are tuned to minimize the effects of collisional activation, a distribution of <20% relative abundance is observed at smaller CCS values in addition to the elongated conformation observed at 293 $Å^2$ (Figure 55). These data suggest that the single distribution observed is representative of the elongated conformation and that the elimination of Q^5/Q^6 and F^7/F^8 decreases the stability of the compact conformation to a point that it is not observed under these experimental conditions. The appearance of a small distribution when the effective temperature is minimized suggests that while intramolecular interactions between the charge sites and Q/F residues are the main stabilizing factors, there are minor interactions that aid in the stabilization of the compact conformer. This is consistent with previous MD studies where stabilizing interactions between the charge sites and the C-terminus were shown.[77] Nevertheless, these data demonstrate the intramolecular interactions formed between the charge sites and that the Q/F residues are critical to the stabilization of the compact conformation.

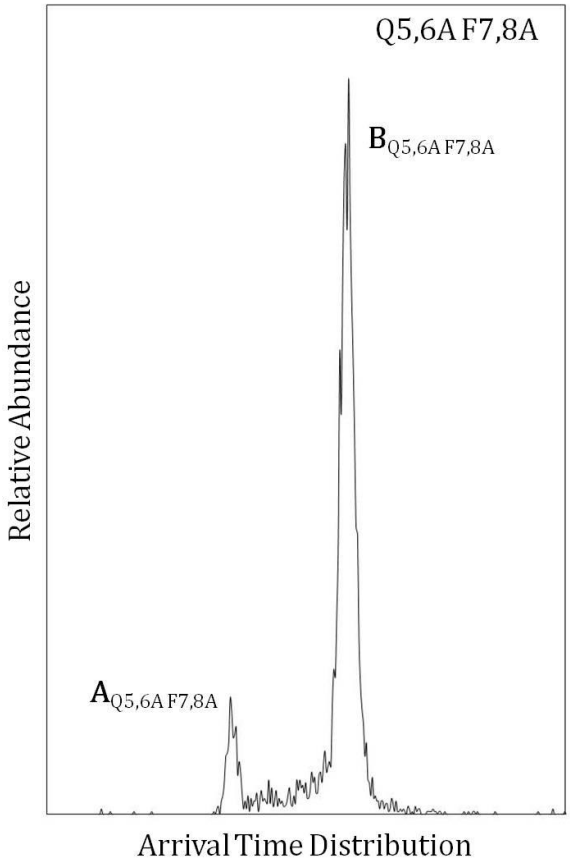

Figure 55: The ATD of [Q5,6A F7,8A + 3H]$^{3+}$ collected with 90 V in the PF IF and a drift field of 15.5 V cm^{-1} Torr^{-1}. By minimizing the electric fields, the compact distribution ($\mathbf{A}_{Q5,6A\ F7,8A}$) is observed in small abundance.

6.3.2 Implications of intramolecular interactions in the formation of conformer $\boldsymbol{B}_{SP}$

We have shown that the interactions between the charge sites and Q^5/Q^6 and F^7/F^8 are critical to the conservation of the compact conformation; however, it is interesting to consider the implications of these interactions with respect to the formation of the elongated conformation, $\mathbf{B}_{SP}$. Upon collisional activation, the compact conformation converts to an elongated conformation for SP and all Q/F to A mutants (Figure 54) through the disruption of the aforementioned interactions. One hypothesis

that explains the elongation of the $[M + 3H]^{3+}$ species is that upon elimination of these interactions, Coulombic repulsion of the localized charges, in combination with the energy deposited via collisional activation, leads to the transfer of a proton from the N-terminal region of the peptide to the C-terminus, i.e. a mobile proton model. Consistent with this hypothesis, it has been shown that as the proximity of the charge sites is increased, the apparent gas-phase basicity of the charge sites and, subsequently, the energy required to deprotonate these sites decreases.[151] Moreover, Wysocki and coworkers have shown that doubly protonated peptides, where the charge sites are localized on the N-terminus, require less energy to mobilize a proton and undergo charge-directed fragmentation than peptides where the charge sites are separated on the N- and C-terminal regions of the peptide.[152]

This transfer and charge separation can lead to the formation of the elongated conformation. IM-MS studies have shown that Coulombic repulsion from charge sites can impact the structural preferences of analytes in the gas phase.[57-58, 153] Additionally, Williams and coworkers have shown that when charge sites are on opposing ends of an aliphatic chain, Coulombic repulsion drives elongation of the ion.[154] In order to test the hypothesis that Coulombic repulsion, through charge separation, can induce structural elongation, analysis of the reverse sequence of SP (RS) was performed. The RS peptide mimics the final charge distribution that would be observed after collisional activation and a mobile proton transfer as the charge sites are now located on the N-terminus and C-terminus residues K^9 and R^{11}.

The ATD of $[RS + 3H]^{3+}$ shows a single conformer distribution and a partially resolved leading shoulder (Figure 51). The peak width of the distribution is consistent with that observed for $\mathbf{B}_{SP}$. Interestingly, upon collisional activation (Figure 54l) the ATD does not undergo any change in centroid, peak shape, or peak width, thus indicating that the conformation distribution does not undergo a structural rearrangement that is resolvable with the current experimental conditions. This is in good agreement with the proposed hypothesis that by separating the charge sites on opposite ends of the peptide, the repulsion between charges now drives elongation of the peptide backbone. The absence of the compact conformation may indicate that the stability of the intramolecular interactions involving Q and F residues has decreased due to competition between the charge sites for solvating interactions or that initial repulsion, owing to the charge separation, prevents these interactions from being formed. Nevertheless, the RS mutant adopts a narrow distribution of elongated conformers in the gas phase, similar to $\mathbf{B}_{SP}$ and is consistent with the hypothesis that conformer $\mathbf{B}_{SP}$ arises from a charge repulsion, elongation mechanism.

6.3.3 The proline effect

Within the realm of structural biology, some uncertainty as to the importance of *cis-/trans-* isomer preferences of proline with respect to the conformer preferences, both in solution and in the gas phase, exists. While the majority of naturally occurring amino acids adopt a *trans-* configuration, as it is favored by ~3.5 kJ mol^{-1}, proline is able to adopt either isomer when present in an amino acid sequence.[155] This arises from the *cis-/trans-* isomers of proline being approximately isoenergetic; the *trans-* isomer is

energetically favored by ~0.5 kJ mol^{-1}.[156] Thus, the *cis-/trans-* isomer heterogeneity of proline may impact the conformational preferences of the analyte ion. The most relevant study regarding this issue was previously reported by Pierson *et al.*, where mutations eliminating the *cis-* isomer depopulated select conformations of the $[M + 3H]^{3+}$ ion of bradykinin.[150] Owing to the proximity of the P^2 and P^4 residues to the charge sites for substance P, it is interesting to consider the implications of the *cis-*/*trans-* isomers with regard to the formation of the stabilizing intramolecular interactions. Mutation of P to A causes the amino acid residue to adopt a *trans-* only orientation. This mutation has been used extensively to study the conformational effects of *cis-* proline both in the solution and gas phases.[150, 157-158] Mutations of P^2 and P^4 were preformed to investigate the effect of the *cis-* isomer on the stabilization of the compact conformer.

The ATD of P2A shows three conformer distributions (Figure 51). The first two peaks, $\mathbf{A}_{1,P2A}$ and $\mathbf{A}_{2,P2A}$, have reduced relative abundances when compared to $\mathbf{A}_{SP}$, indicating that the *cis-* isomer of proline facilitates formation of specific intramolecular interactions which are depopulated when this isomer is eliminated. Additionally, the peak widths of both $\mathbf{A}_{1,P2A}$ and $\mathbf{A}_{2,P2A}$ are also decreased with respect to SP, which is a board distribution. Consistent with the observations from previous mutations, this suggests that by eliminating the *cis-* isomer at the 2nd residue position, the conformer heterogeneity of the kinetically trapped distribution is reduced. Upon collisional activation, the ratio of $\mathbf{A}_{1,P2A}$ to $\mathbf{A}_{2,P2A}$ remains constant (Figure 54i), indicating that each distribution is stabilized by independent combinations of intramolecular interactions. The two partially resolved **A** peaks in the ATD of P2A could be due to the presence of

both *cis*- and *trans*- P^4, resulting in alternate orientations of intramolecular interactions dictated by the charge sites. This hypothesis is tested below with additional SP mutant peptides, for which predicted residue-specific isomer distributions and possible *cis-/trans*- isomers are listed in Table 8.

Peptide Name	Isomer Distribution			Conformer Distribution			
	2nd Residue	4th Residue	9th Residue	**A** Peaks		**B** Peaks	
				Expected	Observed	Expected	Observed
P2A	*trans*-	*cis-/trans*-	*trans*-	2	2	1	1
P4A	*cis-/trans*-	*trans*-	*trans*-	2	2*	1	1
P2,4A	*trans*-	*trans*-	*trans*-	1	1	1	1
G9P	*cis-/trans*-	*cis-/trans*-	*cis-/trans*-	1**	1	2	2
P2,4A G9P	*trans*-	*trans*-	*cis-/trans*-	1	1	2	2

Table 8: The possible *cis-/trans*- isomer distributions for the 2nd, 4th, and 9th residue positions. For ions with a *cis-/trans*- isomer distribution in the 2nd and 4th residues, the expected number of **A** peaks is two. When the *cis-/trans*- isomer distribution is located in the 9th residue position, **B** is split into two peaks. * The two peaks for **A** were observed at reduced PF IMS drift cell fields. ** The expected number of **A** peaks is one owing to the native sequence of amino acids 1-8.

Upon mutation of P^4, the 4th residue position is now in a *trans*- configuration, while the 2nd residue should be able to adopt a *cis*- or *trans*- isomer. Based on the P2A data, the predicted ATD for P4A should consist of two distributions for the compact conformation and one distribution for the elongated conformation. However, this does not hold true for this mutation as the ATD exhibits only a single distribution for the compact conformer (Figure 51). This deviation from the predicted distribution may originate from the location of the *cis-/trans*- isomer heterogeneity. While the isomer preference of P^4 can influence the location of three amino acid residues, including each

charge site, the isomer preference of P^2 affects only the orientation of the arginine side chain. Thus, the difference in CCS caused by different orientations of the arginine side chain, originating from the *cis*- and *trans*- isomers of P^2, may not be resolvable under current experimental conditions. The ATD for P4A collected at higher mobility resolutions where two distributions are partially resolved are consistent with this assignment (Figure 56). Interestingly, the ratio of $\mathbf{A}_{1,P4A}$ to $\mathbf{A}_{2,P4A}$ is unique, compared to that observed for P2A. The variation in this ratio may be due to electrostatic interactions between the guanidinium ion of arginine and P^2. Interactions between proline and the guanidinium ion have been previously shown to influence the activity of enzymes, suggesting that the presence of arginine can play an important role in determining the *cis-/trans*- isomer distribution of the neighboring proline residue.[159] Nevertheless, the reduction of the relative abundance of the compact conformation and the decrease in peak width observed for $\mathbf{A}_{P4A}$ is consistent with the elimination of stabilizing interactions facilitated by the *cis*- isomer of P^4.

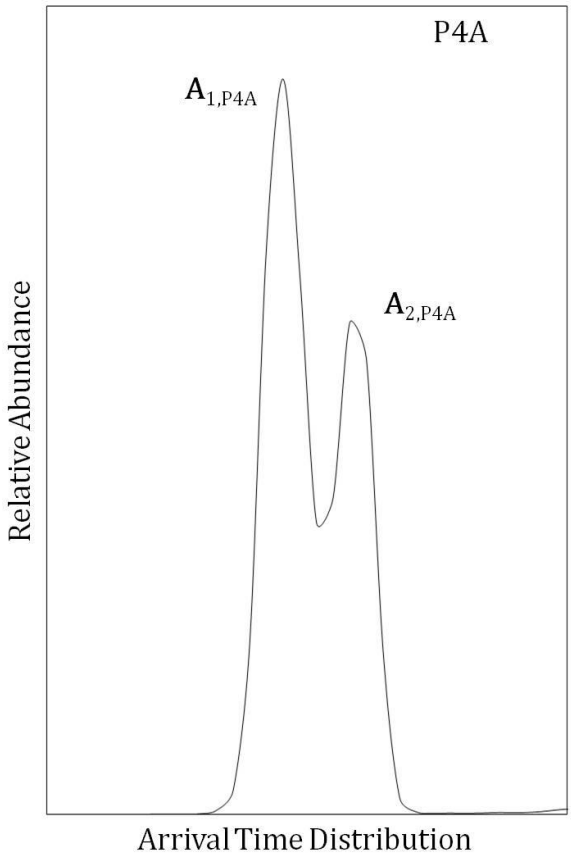

Figure 56: The ATD of the compact conformation of P4A collected with high resolution IM, which allows for the resolution of the *cis-/trans-* distributions of $\mathbf{A}_{P4A}$.

Mutation of both P^2 and P^4, P2,4A, eliminates all *cis-* isomers and thus eliminates any *cis-/trans-* effect. The elimination of this effect should produce a single distribution for the compact conformer (Table 8). In agreement with the predicted distribution, the ATD shows the presence of only one compact conformer population. Additionally, there is a reduction in the relative abundance of $\mathbf{A}_{P2,4A}$ and a decrease in the peak width (Figure 51) owing to the elimination of *cis-* dependent interactions. Collectively, these data indicate that upon adoption of a solely *trans-* isomer orientation in the 2^{nd} and/or 4^{th}

residue positions, the conformer preferences of the compact distribution $\mathbf{A}_{SP}$ are altered. This is further supported by the decrease in the peak width observed for the compact distributions of P2A, P4A, and P2,4A. This suggests that upon eliminating the *cis*-isomer, the structural heterogeneity of A is reduced through elimination of conformations dependent on this isomer. Additionally, the observance of two distinct compact conformer populations for P2A and P4A, suggests that a *cis-/trans*- isomer heterogeneity may induce splitting of the conformer population. It is of interest to investigate the ability to induce this conformer heterogeneity into other regions of the peptide via incorporation of additional proline mutations within the primary structure of SP.

6.3. 4 Inducing the cis-/trans- isomer effect within conformer $\boldsymbol{B}_{SP}$

The ATDs of all the mutant peptides analyzed thus far have shown little influence on the conformer heterogeneity of the elongated conformation. The absence of any variation of this conformation originates from the mutations being isolated to residues which establish the intramolecular interactions that stabilize the compact conformer i.e. R^1 through F^8. Thus, mutations performed in the C-terminal region (G^9 through M^{11}) may influence the conformational preferences of the elongated species, i.e., inclusion of P within these residues may induce a conformer splitting similar to that observed for P2A.

By introducing proline into the C-terminal region of the molecule, the elongated conformation should exhibit two conformer distributions; one arises from the *cis*-isomer, while the other from the *trans*- isomer (Table 8). The ATD of G9P shows three

conformer distributions; however, unlike previous mutants, the extended conformation has now been altered (Figure 51). The extended conformation exhibits two partially resolved peak distributions, $\mathbf{B}_{1,G9P}$ and $\mathbf{B}_{2,G9P}$. The splitting of B upon this mutation indicates that by inducing *cis-/trans-* isomer heterogeneity at the 9^{th} residue, a new, non-native conformer population has been introduced, consistent with the predicted distribution. The relative abundance of these distributions is <20%. The relative abundance of compact conformations $\mathbf{A}_{G9P}$ and $\mathbf{A}_{SP}$ is 1:1, and the two peaks have comparable widths. These observations indicate that by mutating P for G^9, the intramolecular interactions which stabilize $\mathbf{A}_{SP}$ are not altered. The reduction in the relative abundance of $\mathbf{B}_{G9P}$, as compared to $\mathbf{B}_{SP}$, arises from the mutation partitioning the extended conformation into two conformer populations. These data are consistent with both of the aforementioned hypotheses, i.e., the compact conformation is determined by intramolecular interactions established between the charge sites located toward the N-terminus and the Q^5/Q^6 and F^7/F^8 residues, the conformational preferences of the elongated species can be altered by mutations localized to the C-terminal residues, and the *cis-/trans-* isomer effect can induce two distinct conformer populations. Collisional activation data (Figure 54j) demonstrate that one extended population is not preferentially populated upon disruption of stabilizing interactions. Additionally, the ratio of $\mathbf{B}_{1,G9P}$ to $\mathbf{B}_{2,G9P}$ remains constant when $\mathbf{A}_{SP}$ is completely depopulated, suggesting that both conformations are representative of a gas-phase quasiequilibrium distribution.

To explore the possibility of combining the effects of the destabilization of $\mathbf{A}_{SP}$ and the induction of *cis-/trans-* isomer heterogeneity in conformer $\mathbf{B}_{SP}$, mutant P2,4A G9P was analyzed. If our previous hypotheses are correct, this mutant should exhibit a reduction of the compact conformation through elimination of *cis-* dependent interactions, as well as, show two distributions for the elongated conformation through induction of a *cis-/trans-* heterogentity. The ATD of P2,4A G9P shows a compact conformer $\mathbf{A}_{P2,4A\ G9P}$ that is <10% relative Å abundance and an extended conformation comprised of two partially resolved distributions; $\mathbf{B}_{1,P2,4A\ G9P}$ and $\mathbf{B}_{2,P2,4A\ G9P}$ (Figure 51). Collisional activation shows that both elongated conformations are stable in the gas phase. These data are consistent with a combination of the effects observed for the individual mutants P2,4A and G9P (Table 8). The relative abundance of $\mathbf{A}_{P2,4A\ G9P}$ is reduced, owing to the destabilization of the intramolecular interactions dependent on the *cis-* isomers of P^2 and/or P^4, while conformation **B** has been split through the introduction of a *cis-*/*trans-* isomer heterogeneity. Further reduction of $\mathbf{A}_{P2,4A\ G9P}$ as compared to that of $\mathbf{A}_{P2,4A}$ may suggest that the *cis-* isomer in the ninth residue position destabilizes the minor interactions not associated with Q or F residues. Nevertheless, these data confirm our aforementioned hypotheses by demonstrating that the combination of destabilization and inclusion of isomer heterogeneity can be achieved through select mutations.

6.4 Conclusions

Specific amino acid mutations of SP were utilized to examine the conformational effects of eliminating possible intramolecular interaction sites. Upon elimination of

single Q residues, the relative abundance of the kinetically trapped, compact conformer population was reduced to ~20%, while the peak width was decreased owing to a reduction in structural heterogeneity. Double residue mutations of Q^5/Q^6 and F^7/F^8 show that that Q^5/Q^6 are critical to the formation of the kinetically trapped, compact conformer population, while interactions with F^7/F^8 provide stability to a lesser extent. Upon elimination of all Q/F residues, the compact conformer is completely destabilized and the preferred gas-phase structure is observed. Once these interactions are disrupted, Coulombic repulsion and reduced gas-phase basicity may induce a proton migration to the C-terminal region as part of the elongation mechanism. Consistent with this, the RS mutant, which has charge sites on the N- and C-termini, adopts the elongated conformation. Therefore, these stabilizing interactions are critical to the preservation of the kinetically trapped species in the gas phase.

The impact of *cis-/trans-* isomers of proline is an ongoing issue of research within the realm of structural biology. Two proline residues occur in the N-terminal region of SP and are in close proximity to the charge sites. The effect of these isomers on the formation of stabilizing interactions between the charge sites and Q/F residues was investigated through the use of proline to alanine mutations, which eliminate the *cis-* isomer. Upon elimination of this isomer, the conformational heterogeneity of the compact conformer was reduced, suggesting that the *cis-* isomer does facilitate the formation of certain interactions. Additionally, upon elimination of the *cis-* isomer at P^2 or P^4, the compact population was resolved into two distinct distributions, which could originate from the *cis-* and *trans-* isomers of the remaining P residue. In order to

investigate the ability to induce conformational splitting from *cis-/trans-* isomers, proline was mutated into the C-terminal region of SP. This mutation showed no impact on the compact conformation, but introduced an additional population for the preferred gas-phase distribution, which is consistent with a *cis-*/*trans-* population. The combined effects of destabilization and induction of *cis-/trans-* heterogeneity were explored with the mutation P2,4A G9P. IM-MS analysis of this mutant confirmed that the effects could be combined, i.e., the compact conformation was nearly eliminated, while the preferred gas-phase distribution split into two peaks, indicative of the presence of *cis-* and *trans-* populations. Collectively, these results show that the isomeric preferences of proline can directly impact the conformation adopted from the dehydration process as well as influence the preferred gas-phase conformation.

7. CONCLUSIONS

7.1 Conclusions

Initial modeling of the PF IF_{8-4} shows that the optimal electrode geometry is a 4 mm wide electrode that has a spacing of 6 mm. Simulations of this model suggest that >90% of C_{60} ions are transmitted. Owing to the reduced duty cycle associated with dispersive IMS techniques, the PF IT was developed to allow for ion trapping during the IMS analysis. Simulations show that ions can be trapped within the device with ~5-10% ion loss per cycle. Moreover, when the PF IF and the PF IT are incorporated, the optimized PF IF-PF IT model shows that the ion transmission is comparable to the PF IF. The initial source design utilized an inline heated capillary-PF IF design; however, the gas purity within the ion funnel was compromised. Thus, an orthogonal source design was established, which included turning optics to extract ions toward the PF IF. Ion current measurements show that the turning optics are directing ions toward the device and that these ions are subsequently being transported through the PF IF-PF IT. Bath gas composition studies show that the partial pressure of helium within the PF IF region is being maintained via the combination of the counterflow and the orthogonal design. However, optimal ion transmission is obtained when the field between the ring electrode and E1 is high. This high electric field can cause structural rearrangement and, possibly, covalent bond dissociation. In order to address this high field requirement, a second generation PF IF was developed.

The second generation PF IF utilizes a larger inner diameter design, which more closely matches the inner diameter of the E1 and the ring electrode. This allows for

reduced electric field requirements between these two elements. Moreover, the increase in the inner diameter allows for increased transmission of a more radial diffuse ion packet as compared to the PF $IF_{8\text{-}4}$. Extensive simulations were performed to characterize the ion motion within the PF IF. Determination of the axial and radial electric fields show that these values oscillate similarly to the fields present in the PF IMS drift cells; however, owing to the conical nature of the device, these field oscillations also have an axial component associated with them, i.e., as the inner diameter gets smaller, the oscillations become larger. These data demonstrate that radial confinement is enhanced for the PF IF as compared to the PF IMS drift cell. Axial and radial velocity mapping shows that effect of field oscillations within the device and provide the best evidence for the central drift motion to date. Moreover, the calculated V* potentials show that the device is analogous to the RF IF. Inclusion of an ion gate allows for the modulation of the ion beam into a PF IMS drift and collection of ATDs. These data show that the PF IF and source design are capable of transmitting ions and producing ATDs.

Upon completion of the ESI-PF IF source, incorporation of a high-resolution PF IMS drift cell was performed. In order to obtain the correct electric field across the drift cell, the terminal electrode was biased at ~-4kV. This high negative electrical bias made the channeltron detector obsolete and required the development of new transfer optics to a PAD detector. SIMION modeling was used to optimize these elements. Upon incorporation of the high-resolution drift cell and PAD detector, the ATD of BK was compared to that obtained on the previous, 11 electrode, low-resolution drift cell.

Owing to increased mobility resolution, the three main distributions are now completely resolved; however, the actual identity of each distribution is still unknown due to the one-dimensional nature of IMS. Thus, development of a TOF mass analyzer was performed. With the incorporation of the mass analyzer, the simulated ion transmission versus empirical transmission of the PF IF for $[BK + 2H]^{2+}$ ions was able to be investigated. Generally, the empirical transmission curved followed the same sigmoidal shape as the simulated transmission curve. Ion signal showed a 40-fold gain as the electric field in the PF IF was increased. Moreover, the mass spectra showed a dearth of fragment ions suggesting that the PF IF was not collisional activating ions to the point of covalent bond dissociation. ATD analysis of BK, GS, and TZ showed that the PF IF did not alter the conformer population of these analyte ions at a range of axial electric fields. Finally, analysis of $[BK + 3H]^{3+}$ showed that the PF IF is capable of maintaining kinetically trapped conformations and, at increased electric fields, annealing these conformations to study the conversion of these conformations to the more energetically preferred conformations.

The utility of the PF IF was demonstrated by the study of $[SP + 3H]^{3+}$. $[SP + 3H]^{3+}$ shows two conformations, $\mathbf{A_{SP}}$ and $\mathbf{B}_{SP}$. Cyro-IM MS shows that $\mathbf{A}_{SP}$ comes directly from the desolvation process, while $\mathbf{B}_{SP}$ has an alternate origin. Collision activation studies performed on the PF IF show that $\mathbf{A}_{SP}$ is converted to $\mathbf{B}_{SP}$ at increased electric field values. These data suggest that $\mathbf{A}_{SP}$ is a kinetically trapped conformer population, while $\mathbf{B}_{SP}$ is representative of the energetically preferred conformer population. It was hypothesized that $\mathbf{A}_{SP}$ was kinetically trapped owing to stabilizing

intramolecular interactions that were formed upon complete desolvation. In order to test this hypothesis, amino acid mutations that eliminate possible interaction sites were performed. Mutations of specific amino acid residues of SP show that Q^5/Q^6 provide the greatest stability to the kinetically trapped conformer populations, while interactions between F^7/F^8 play a more minor role. Upon elimination of both the Q and F residues, the stability of $\mathbf{A}_{SP}$ was reduced to a point where it was no longer observed at the current instrument parameters. Additionally, the *cis-/trans-* isomers of P^2 and P^4 where shown to impact the formation of these interactions. These results demonstrate the importance of intramolecular interactions to the stability of kinetically trapped conformations during IM-MS analysis. Collectively, these data show the strength of the PF IF for analysis of multiple conformations of biomolecular ions as the device is capable of preserving kinetically trapped conformations and inducing conformational conversion.

The work presented herein provides the foundation for a multitude of future studies, both in terms of instrumentation development and fundamental applications. The effective temperature of the PF IF can be qualitatively determined through the use of "thermometer" ions such as benzyl salts and leucine enkephalin. This characterization would allow for the estimation of an ion's effective temperature as they traverse the PF IF. In order to modify the effective temperature the ions achieve while traversing the PF IF, there are potentially two avenues of research: physical design and gas temperature. The electrode geometry of the PF IF has been optimized for transmission, not for optimal ion effective temperature. A systematic study of ion effective temperature versus ion transmission for a range of electrode geometries may reveal an electrode

design that is capable of providing an increase in ion transmission while reducing the collisional activation. The activation the ions experience within the PF IF can be further modified with variation of the funnel gas temperature, i.e., by heating or cooling the funnel gas, the collisional activation an ion undergoes can be enhanced or diminished, respectively. Upon further characterization of the ion's effective temperature within the PF IF, studies focused on the stability afford by additional electrostatic interaction, such as salt bridges between a positive charge site and a phosphate group, are of potential interest.

The results and conclusions demonstrated with the investigation of SP and SP mutant ions provides the basis for further studies regarding the fundamentals of the ESI process. While the work presented herein focuses on the stabilizing interactions formed upon desolvation and how these interactions affect the stability of kinetically-trapped conformations, there are multiple affects afforded by the destabilization of the interactions; namely the charge state distribution and the hydration of the mutant ions. The presence of the intramolecular interactions delocalize the charge sites and help reduce the coulombic repulsion within the $[M + 3H]^{3+}$ ion. Upon disruption, this delocalization of the charge is reduced while coulombic repulsion is increased; this potentially can lead to the destabilization and reduced formation of the $[M + 3H]^{3+}$ ion. Thus, the formation and stability of the $[M + 3H]^{3+}$ ion can be studied as a function of intramolecular interactions with the SP and SP mutant system. Finally, the study of how the elimination of intramolecular interactions affects the solvation of both conformer **A**

and conformer **B** can potentially lend insight to the implication of analyte ion' structure on the local solvent environment.

REFERENCES:

1. Mason, E. A.; McDaniel, E. W., *Transport Properties of Ions In Gases*. WILEY-VCH Verlag GmbH & Co. : 1988.

2. McLean, J. A.; Ruotolo, B. T.; Gillig, K. J.; Russell, D. H. *Int. J. Mass Spectrom.* **2005**, *240*, 301-315, DOI: 10.1016/j.ijms.2004.10.003.

3. Borsdorf, H.; Eiceman, G. A. *Appl Spectrosc Rev* **2006**, *41*, 323-375, DOI: Doi 10.1080/05704920600663469.

4. Dwivedi, P.; Wu, C.; Matz, L. M.; Clowers, B. H.; Siems, W. F.; Hill, H. H. *Anal. Chem.* **2006**, *78*, 8200-8206, DOI: 10.1021/ac0608772.

5. Bohrer, B. C.; Mererbloom, S. I.; Koeniger, S. L.; Hilderbrand, A. E.; Clemmer, D. E. *Annu Rev Anal Chem* **2008**, *1*, 293-327, DOI: DOI 10.1146/annurev.anchem.1.031207.113001.

6. Guharay, S. K.; Dwivedi, P.; Hill, H. H. *Ieee T Plasma Sci* **2008**, *36*, 1458-1470, DOI: Doi 10.1109/Tps.2008.927290.

7. Hill, H. H.; Kanu, A. B.; Dwivedi, P.; Tam, M.; Matz, L. *J Mass Spectrom* **2008**, *43*, 1-22, DOI: Doi 10.1002/Jms.1383.

8. Revercomb, H. E.; Mason, E. A. *Anal. Chem.* **1975**, *47*, 970-983.

9. Shvartsburg, A.; Ibrahim, Y.; Smith, R. *J. Am. Soc. Mass Spectrom.* **2014**, *25*, 480-489, DOI: 10.1007/s13361-013-0797-4.

10. Shvartsburg, A.; Tang, K.; Smith, R. *J. Am. Soc. Mass Spectrom.* **2005**, *16*, 2-12, DOI: 10.1016/j.jasms.2004.09.009.

11. Shvartsburg, A.; Seim, T.; Danielson, W.; Norheim, R.; Moore, R.; Anderson, G.; Smith, R. *J. Am. Soc. Mass Spectrom.* **2013**, *24*, 109-114, DOI: 10.1007/s13361-012-0517-5.

12. Belov, M. E.; Ibrahim, Y. M.; Shvartsburg, A. A.; Smith, R. D. *Anal. Chem.* **2011**, *83*, 5617-5623, DOI: 10.1021/ac200719n.

13. Guevremont, R. *J Chromatogr A* **2004**, *1058*, 3-19, DOI: 10.1016/j.chroma.2004.08.119.

14. Wyttenbach, T.; Kemper, P. R.; Bowers, M. T. *Int. J. Mass Spectrom.* **2001**, *212*, 13-23, DOI: 10.1016/s1387-3806(01)00517-6.

15. Gillig, K. J.; Ruotolo, B. T.; Stone, E. G.; Russell, D. H. *Int. J. Mass Spectrom.* **2004**, *239*, 43-49, DOI: 10.1016/j.ijms.2004.09.005.

16. Smith, R. D.; Shvartsburg, A. A. *Anal. Chem.* **2008**, *80*, 9689-9699, DOI: 10.1021/ac8016295.

17. Bowers, M. T.; Kemper, P. R.; Dupuis, N. F. *Int. J. Mass Spectrom.* **2009**, *287*, 46-57, DOI: 10.1016/j.ijms.2009.01.012.

18. Cohen, M. J.; Karasek, F. W. *Journal of Chromatographic Science* **1970**, *8*, 330-337.

19. Pringle, S. D.; Giles, K.; Wildgoose, J. L.; Williams, J. P.; Slade, S. E.; Thalassinos, K.; Bateman, R. H.; Bowers, M. T.; Scrivens, J. H. *Int. J. Mass Spectrom.* **2007**, *261*, 1-12, DOI: 10.1016/j.ijms.2006.07.021.

20. Wyttenbach, T.; von Helden, G.; Bowers, M. T. *J. Am. Chem. Soc.* **1996**, *118*, 8355-8364, DOI: 10.1021/ja9535928.

21. Asbury, G. R. K., J; Hill, H. H. *Talanta* **1999**, *50*, 1291-1298.

22. McDaniel, E. W.; Martin, D. W.; Barnes, W. S. *Rev Sci Instrum* **1962**, *33*, 2-7, DOI: 10.1063/1.1717656.

23. Albritto.Dl; Miller, T. M.; Martin, D. W.; McDaniel, E. W. *Physical Review* **1968**, *171*, 94-&, DOI: 10.1103/PhysRev.171.94.

24. McDaniel, E. *J. Chem. Phys.* **1970**, *52*, 3931-&, DOI: 10.1063/1.1673592.

25. Clowers, B. H.; Hill, H. H. *Anal. Chem.* **2005**, *77*, 5877-5885, DOI: 10.1021/ac050700s.

26. Clowers, B. H.; Hill, H. H. *J Mass Spectrom* **2006**, *41*, 339-351, DOI: 10.1002/jms.994.

27. McAfee, K. B.; Edelson, D. *Proceedings of the Physical Society of London* **1963**, *81*, 382-&, DOI: 10.1088/0370-1328/81/2/125.

28. McAfee, K. B.; Sipler, D.; Edelson, D. *Physical Review* **1967**, *160*, 130-&, DOI: 10.1103/PhysRev.160.130.

29. McKnight, L. G.; McAfee, K. B.; Sipler, D. P. *Physical Review* **1967**, *164*, 62-&, DOI: 10.1103/PhysRev.164.62.

30. Bluhm, B. K.; Gillig, K. J.; Russell, D. H. *Rev Sci Instrum* **2000**, *71*, 4078-4086, DOI: 10.1063/1.1288235.

31. Woods, A. S.; Ugarov, M.; Egan, T.; Koomen, J.; Gillig, K. J.; Fuhrer, K.; Gonin, M.; Schultz, J. A. *Anal. Chem.* **2004**, *76*, 2187-2195, DOI: 10.1021/ac035376k.

32. Russell, D. H.; Becker, C.; Qian, K. N. *Anal. Chem.* **2008**, *80*, 8592-8597, DOI: 10.1021/ac801473f.

33. Pai, P. J.; Cologna, S. M.; Russell, W. K.; Vigh, G.; Russell, D. H. *Anal. Chem.* **2011**, *83*, 2814-2818, DOI: 10.1021/ac1029743.

34. Shrestha, B.; Vertes, A. *Anal. Chem.* **2014**, *86*, 4308-4315, DOI: 10.1021/ac500007t.

35. Kurulugama, R. T.; Nachtigall, F. M.; Valentine, S. J.; Clemmer, D. E. *J. Am. Soc. Mass Spectrom.* **2011**, *22*, 2049-2060, DOI: 10.1007/s13361-011-0217-6.

36. Fenn, L. S.; Kliman, M.; Mahsut, A.; Zhao, S. R.; McLean, J. A. *Anal Bioanal Chem* **2009**, *394*, 235-244, DOI: 10.1007/s00216-009-2666-3.

37. Yol, A. M.; Wesdemiotis, C. *React. Funct. Polym.* **2014**, *80*, 95-108, DOI: 10.1016/j.reactfunctpolym.2014.03.010.

38. Bowers, M. T.; Wyttenbach, T.; Batka, J. J.; Weis, P.; Gidden, J. *Abstr Pap Am Chem S* **1997**, *213*, 29-Poly.

39. Becker, C.; Fernandez-Lima, F. A.; Russell, D. H. *Spectroscopy* **2009**, *24*, 38-42.

40. Russell, D. H.; Fernandez-Lima, F. A.; Becker, C.; McKenna, A. M.; Rodgers, R. P.; Marshall, A. G. *Anal. Chem.* **2009**, *81*, 9941-9947, DOI: 10.1021/ac901594f.

41. Robertson, A. D.; Murphy, K. P. *Chem Rev* **1997**, *97*, 1251-1268, DOI: 10.1021/cr960383c.

42. Gardner, K. H.; Kay, L. E. *Annual Review of Biophysics & Biomolecular Structure* **1998**, *27*, 357.

43. Fenn, J. B.; Mann, M.; Meng, C. K.; Wong, S. F.; Whitehouse, C. M. *Science* **1989**, *246*, 64-71, DOI: 10.1126/science.2675315.

44. Wyttenbach, T.; Baker, E. S.; Bernstein, S. L.; Ferzoco, A.; Gidden, J.; Liu, D. F.; Bowers, M. T. *Adv Mass Spectrom* **2004**, *16*, 189-200.

45. Thalassinos, K.; Slade, S. E.; Jennings, K. R.; Scrivens, J. H.; Giles, K.; Wildgoose, J.; Hoyes, J.; Bateman, R. H.; Bowers, M. T. *Int. J. Mass Spectrom.* **2004**, *236*, 55-63, DOI: 10.1016/j.ijms.2004.05.008.

46. Bleiholder, C.; Dupuis, N. F.; Wyttenbach, T.; Bowers, M. T. *Nat Chem* **2011**, *3*, 172-177, DOI: 10.1038/Nchem.945.

47. Scrivens, J. H.; Hilton, G. R.; Thalassinos, K.; Grabenauer, M.; Sanghera, N.; Slade, S. E.; Wyttenbach, T.; Robinson, P. J.; Pinheiro, T. J. T.; Bowers, M. T. *J. Am. Soc. Mass Spectrom.* **2010**, *21*, 845-854, DOI: 10.1016/j.jasms.2010.01.017.

48. Wyttenbach, T.; Bowers, M. T. *J. Phys. Chem. B* **2011**, *115*, 12266-12275, DOI: 10.1021/jp206867a.

49. Tao, L.; McLean, J. R.; McLean, J. A.; Russell, D. H. *J. Am. Soc. Mass Spectrom.* **2007**, *18*, 1232-1238, DOI: 10.1016/j.jasms.2007.04.003.

50. McLean, J. R.; McLean, J. A.; Wu, Z. X.; Becker, C.; Perez, L. M.; Pace, C. N.; Scholtz, J. M.; Russell, D. H. *J. Phys. Chem. B* **2010**, *114*, 809-816, DOI: 10.1021/jp9105103.

51. Chen, L. X.; Shao, Q.; Gao, Y. Q.; Russell, D. H. *J. Phys. Chem. A* **2011**, *115*, 4427-4435, DOI: 10.1021/jp110014j.

52. Pierson, N. A.; Chen, L.; Valentine, S. J.; Russell, D. H.; Clemmer, D. E. *J. Am. Chem. Soc.* **2011**, *133*, 13810-13813, DOI: 10.1021/ja203895j.

53. Chen, L. X.; Gao, Y. Q.; Russell, D. H. *J. Phys. Chem. A* **2012**, *116*, 689-696, DOI: 10.1021/jp209430q.

54. Barrera, N. P.; Di Bartolo, N.; Booth, P. J.; Robinson, C. V. *Science (Washington, DC, U. S.)* **2008**, *321*, 243-246, DOI: 10.1126/science.1159292.

55. Ruotolo, B. T.; Benesch, J. L. P.; Sandercock, A. M.; Hyung, S.-J.; Robinson, C. V. *Nat. Protocols* **2008**, *3*, 1139-1152.

56. Bush, M. F.; Hall, Z.; Giles, K.; Hoyes, J.; Robinson, C. V.; Ruotolo, B. T. *Anal. Chem.* **2010**, *82*, 9557-9565, DOI: 10.1021/ac1022953.

57. Hall, Z.; Politis, A.; Bush, M. F.; Smith, L. J.; Robinson, C. V. *J. Am. Chem. Soc.* **2012**, *134*, 3429-3438, DOI: 10.1021/ja2096859.

58. Hall, Z.; Robinson, C. *J. Am. Soc. Mass Spectrom.* **2012**, *23*, 1161-1168, DOI: 10.1007/s13361-012-0393-z.

59. Pierson, N. A.; Valentine, S. J.; Clemmer, D. E. *J. Phys. Chem. B* **2010**, *114*, 7777-7783, DOI: 10.1021/jp102478k.

60. Shi, H.; Pierson, N. A.; Valentine, S. J.; Clemmer, D. E. *J. Phys. Chem. B* **2012**, *116*, 3344-3352, DOI: 10.1021/jp210797x.

61. van den Heuvel, R. H. H.; Heck, A. J. R. *Curr. Opin. Chem. Biol.* **2004**, *8*, 519-526, DOI: 10.1016/j.cbpa.2004.08.006.

62. Ruotolo, B. T.; Giles, K.; Campuzano, I.; Sandercock, A. M.; Bateman, R. H.; Robinson, C. V. *Science (Washington, DC, U. S.)* **2005**, *310*, 1658-1661, DOI: 10.1126/science.1120177.

63. van der Spoel, D.; Marklund, E. G.; Larsson, D. S. D.; Caleman, C. *Macromol. Biosci.* **2011**, *11*, 50-59, DOI: 10.1002/mabi.201000291.

64. Breuker, K.; Brueschweiler, S.; Tollinger, M. *Angew. Chem., Int. Ed.* **2011**, *50*, 873-877, S873/1-S873/3, DOI: 10.1002/anie.201005112.

65. Skinner, O. S.; McLafferty, F. W.; Breuker, K. *J. Am. Soc. Mass Spectrom.* **2012**, *23*, 1011-1014, DOI: 10.1007/s13361-012-0370-6.

66. Papadopoulos, G.; Svendsen, A.; Boyarkin, O. V.; Rizzo, T. R. *J. Am. Soc. Mass Spectrom.* **2012**, *23*, 1173-1181, DOI: 10.1007/s13361-012-0384-0.

67. Deng, Z.; Thontasen, N.; Malinowski, N.; Rinke, G.; Harnau, L.; Rauschenbach, S.; Kern, K. *Nano Lett.* **2012**, *12*, 2452-2458, DOI: 10.1021/nl3005385.

68. Laganowsky, A.; Reading, E.; Allison, T. M.; Ulmschneider, M. B.; Degiacomi, M. T.; Baldwin, A. J.; Robinson, C. V. *Nature* **2014**, *510*, 172-175

69. Freeke, J.; Bush, M. F.; Robinson, C. V.; Ruotolo, B. T. *Chem. Phys. Lett.* **2012**, *524*, 1-9, DOI: 10.1016/j.cplett.2011.11.014.

70. Kanu, A. B.; Gribb, M. M.; Hill, H. H. *Anal. Chem.* **2008**, *80*, 6610-6619, DOI: 10.1021/ac8008143.

71. Rokushika, S.; Hatano, H.; Baim, M. A.; Hill, H. H. *Anal. Chem.* **1985**, *57*, 1902-1907, DOI: 10.1021/ac00286a023.

72. Blase, R. C.; Silveira, J. A.; Gillig, K. J.; Gamage, C. M.; Russell, D. H. *Int. J. Mass Spectrom.* **2011**, *301*, 166-173, DOI: DOI 10.1016/j.ijms.2010.08.016.

73. Verbeck, G. F.; Gillig, K. J.; Russell, D. H. *Eur J Mass Spectrom* **2003**, *9*, 579-587, DOI: 10.1255/ejms.591.

74. Sundarapandian, S.; May, J. C.; McLean, J. A. *Anal. Chem.* **2010**, *82*, 3247-3254, DOI: 10.1021/ac902980r.

75. Wyttenbach, T.; Bowers, M. T. *Chemical Physics Letters* **2009**, *480*, 1-16, DOI: 10.1016/j.cplett.2009.08.042.

76. May, J. C.; Russell, D. H. *J. Am. Soc. Mass Spectrom.* **2011**, *22*, 1134-1145, DOI: 10.1007/s13361-011-0148-2.

77. Silveira, J. A.; Fort, K. L.; Kim, D.; Servage, K. A.; Pierson, N. A.; Clemmer, D. E.; Russell, D. H. *J. Am. Chem. Soc.* **2013**, *135*, 19147-19153, DOI: 10.1021/ja4114193.

78. Servage, K. A.; Silveira, J. A.; Fort, K. L.; Russell, D. H. *J. Phys. Chem. Lett.* **2014**, *5*, 1825-1830, DOI: 10.1021/jz500693k.

79. Fort, K. L.; Silveira, J. A.; Russell, D. H. *Anal. Chem.* **2013**, *85*, 9543-9548, DOI: 10.1021/ac401629b.

80. Miladinović, S. M.; Fornelli, L.; Lu, Y.; Piech, K. M.; Girault, H. H.; Tsybin, Y. O. *Anal. Chem.* **2012**, *84*, 4647-4651, DOI: 10.1021/ac300845n.

81. Sterling, H. J.; Kintzer, A. F.; Feld, G. K.; Cassou, C. A.; Krantz, B. A.; Williams, E. R. *J. Am. Soc. Mass Spectrom.* **2012**, *23*, 191-200, DOI: 10.1007/s13361-011-0301-y.

82. Iavarone, A. T.; Williams, E. R. *Int. J. Mass Spectrom.* **2002**, *219*, 63-72, DOI: 10.1016/s1387-3806(02)00587-0.

83. Lomeli, S. H.; Peng, I. X.; Yin, S.; Loo, R. R. O.; Loo, J. A. *J. Am. Soc. Mass Spectrom.* **2010**, *21*, 127-131, DOI: 10.1016/j.jasms.2009.09.014.

84. Sterling, H. J.; Williams, E. R. *J. Am. Soc. Mass Spectrom.* **2009**, *20*, 1933-1943, DOI: 10.1016/j.jasms.2009.06.012.

85. Lisovskiy, V. A.; Koval, V. A.; Yegorenkov, V. D. *Phys. Lett. A* **2011**, *375*, 1986-1989, DOI: 10.1016/j.physleta.2011.03.035.

86. Yamada, T.; Ishida, T.; Hayakawa, N.; Okubo, H. *Dielectrics and Electrical Insulation, IEEE Transactions on* **2001**, *8*, 137-142, DOI: 10.1109/94.910436.

87. Zhou, M.; Huang, C.; Wysocki, V. H. *Anal. Chem. (Washington, DC, U. S.)* **2012**, *84*, 6016-6023, DOI: 10.1021/ac300810u.

88. Fernandez-Lima, F. A.; Becker, C.; Gillig, K. J.; Russell, W. K.; Tichy, S. E.; Russell, D. H. *Anal. Chem.* **2009**, *81*, 618-624, DOI: Doi 10.1021/Ac801919n.

89. Silveira, J. A.; Servage, K. A.; Gamage, C. M.; Russell, D. H. *J. Phys. Chem. A* **2013**, *117*, 953-961, DOI: 10.1021/jp311278a.

90. Wyttenbach, T.; vonHelden, G.; Batka, J. J.; Carlat, D.; Bowers, M. T. *J. Am. Soc. Mass Spectrom.* **1997**, *8*, 275-282.

91. Clemmer, D. E.; Koeniger, S. L.; Merenbloom, S. I.; Valentine, S. J.; Jarrold, M. F.; Udseth, H. R.; Smith, R. D. *Anal. Chem.* **2006**, *78*, 4161-4174, DOI: 10.1021/ac051060w.

92. Tang, K.; Shvartsburg, A. A.; Lee, H.-N.; Prior, D. C.; Buschbach, M. A.; Li, F.; Tolmachev, A. V.; Anderson, G. A.; Smith, R. D. *Anal. Chem.* **2005**, *77*, 3330-3339, DOI: 10.1021/ac048315a.

93. Morsa, D.; Gabelica, V.; De Pauw, E. *Anal. Chem.* **2011**, *83*, 5775-5782, DOI: 10.1021/ac201509p.

94. Merenbloom, S.; Flick, T.; Williams, E. *J. Am. Soc. Mass Spectrom.* **2012**, *23*, 553-562, DOI: 10.1007/s13361-011-0313-7.

95. Silveira, J. A.; Gamage, C. M.; Blase, R. C.; Russell, D. H. *Int. J. Mass Spectrom.* **2010**, *296*, 36-42, DOI: 10.1016/j.ijms.2010.07.019.

96. Gamage, C. M.; Silveira, J. A.; Blase, R. C.; Russell, D. H. *Int. J. Mass Spectrom.* **2011**, *303*, 154-163, DOI: DOI 10.1016/j.ijms.2011.01.025.

97. Silveira, J. A.; Jeon, J.; Gamage, C. M.; Pai, P. J.; Fort, K. L.; Russell, D. H. *Anal. Chem.* **2012**, *84*, 2818-2824, DOI: 10.1021/ac203294q.

98. Guan, S. H.; Marshall, A. G. *J. Am. Soc. Mass Spectrom.* **1996**, *7*, 101-106, DOI: 10.1016/1044-0305(95)00605-2.

99. Shaffer, S. A.; Tang, K. Q.; Anderson, G. A.; Prior, D. C.; Udseth, H. R.; Smith, R. D. *Rapid Commun. Mass Spectrom.* **1997**, *11*, 1813-1817.

100. Smith, R. D.; Shaffer, S. A.; Prior, D. C.; Anderson, G. A.; Udseth, H. R. *Anal. Chem.* **1998**, *70*, 4111-4119.

101. Kim, T.; Tolmachev, A. V.; Harkewicz, R.; Prior, D. C.; Anderson, G.; Udseth, H. R.; Smith, R. D.; Bailey, T. H.; Rakov, S.; Futrell, J. H. *Anal. Chem.* **2000**, *72*, 2247-2255, DOI: 10.1021/ac991412x.

102. Weickhardt, C.; Moritz, F.; Grotemeyer, J. *Mass Spectrom Rev* **1996**, *15*, 139-162.

103. Zubarev, R. A.; Makarov, A. *Anal. Chem. (Washington, DC, U. S.)* **2013**, *85*, 5288-5296, DOI: 10.1021/ac4001223.

104. Dawson, P. H. *Mass Spectrom Rev* **1986**, *5*, 1-37.

105. Eberlin, M. N.; Corilo, Y. E.; Vaz, B. G.; Simas, R. C.; Nascimento, H. D. L.; Klitzke, C. F.; Pereira, R. C. L.; Bastos, W. L.; Neto, E. V. S.; Rodgers, R. P. *Anal. Chem.* **2010**, *82*, 3990-3996, DOI: 10.1021/ac100673v.

106. Karas, M.; Bachmann, D.; Hillenkamp, F. *Anal. Chem.* **1985**, *57*, 2935-2939, DOI: 10.1021/ac00291a042.

107. Karas, M.; Hillenkamp, F. *Anal. Chem.* **1988**, *60*, 2299-2301, DOI: 10.1021/ac00171a028.

108. Karas, M.; Bachmann, D.; Bahr, U.; Hillenkamp, F. *Int. J. Mass Spectrom. Ion Process.* **1987**, *78*, 53-68, DOI: http://dx.doi.org/10.1016/0168-1176(87)87041-6.

109. Nguyen, S.; Fenn, J. B. *Proc. Natl. Acad. Sci. U.S.A.* **2007**, *104*, 1111-1117, DOI: 10.1073/pnas.0609969104.

110. Smith, R. D.; Kelly, R. T.; Tolmachev, A. V.; Page, J. S.; Tang, K. Q. *Mass Spectrom Rev* **2010**, *29*, 294-312, DOI: 10.1002/mas.20232.

111. Smith, R. D.; Tolmachev, A. V.; Kim, T.; Udseth, H. R.; Bailey, T. H.; Futrell, J. H. *Int. J. Mass Spectrom.* **2000**, *203*, 31-47.

112. Smith, R. D.; Page, J. S.; Tolmachev, A. V.; Tang, K. Q. *J. Am. Soc. Mass Spectrom.* **2006**, *17*, 586-592, DOI: 10.1016/j.jasms.2005.12.013.

113. Zhou, M.; Dagan, S.; Wysocki, V. H. *Analyst (Cambridge, U. K.)* **2013**, *138*, 1353-1362, DOI: 10.1039/c2an36525a.

114. Bohrer, B. C.; Atlasevich, N.; Clemmer, D. E. *J. Phys. Chem. B* **2011**, *115*, 4509-4515, DOI: 10.1021/jp2008495.

115. Brown, K. L.; Tautfest, G. W. *Rev Sci Instrum* **1956**, *27*, 696-702, DOI: doi:http://dx.doi.org/10.1063/1.1715674.

116. Bradbury, N. E.; Nielsen, R. A. *Physical Review* **1936**, *49*, 388-393.

117. Wang, G. H.; Aberth, W.; Falick, A. M. *Int. J. Mass Spectrom. Ion Process.* **1986**, *69*, 233-237, DOI: http://dx.doi.org/10.1016/0168-1176(86)87037-9.

118. Smith, R. D.; Tolmachev, A. V.; Vilkov, A. N.; Bogdanov, B.; Pasa-Tolic, L.; Masselon, C. D. *J. Am. Soc. Mass Spectrom.* **2004**, *15*, 1616-1628, DOI: 10.1016/j.jasms.2004.07.014.

119. Papadopoulos, G.; Svendsen, A.; Boyarkin, O. V.; Rizzo, T. R. *Faraday Discuss.* **2011**, *150*, 243-255, DOI: 10.1039/c0fd00004c.

120. Dole, M.; Mack, L. L.; Hines, R. L.; Mobley, R. C.; Ferguson, L. D.; Alice, M. B. *The Journal of Chemical Physics* **1968**, *49*, 2240-2249, DOI: doi:http://dx.doi.org/10.1063/1.1670391.

121. Mack, L.; Mack *The Journal of Chemical Physics* **1970**, *52*, 4977.

122. Consta, S.; Consta, A.; Malevanets *Physical Review Letters* **2012**, *109*.

123. Konermann, L.; Rodriguez, A. D.; Liu, J. *Anal. Chem.* **2012**, *84*, 6798-6804, DOI: 10.1021/ac301298g.

124. Ahadi, E.; Konermann, L. *J. Am. Chem. Soc.* **2011**, *133*, 9354-9363, DOI: 10.1021/ja111492s.

125. Breuker, K.; McLafferty, F. W. *P Natl Acad Sci USA* **2008**, *105*, 18145-18152, DOI: 10.1073/pnas.0807005105.

126. Dupradeau, F.-Y.; Pigache, A.; Zaffran, T.; Savineau, C.; Lelong, R.; Grivel, N.; Lelong, D.; Rosanski, W.; Cieplak, P. *Phys Chem Chem Phys* **2010**, *12*, 7821-7839, DOI: 10.1039/c0cp00111b.

127. Jarrold, M. F. www.indiana.edu/~nano/software.html

128. Auge, S.; Bersch, B.; Tropis, M.; Milon, A. *Biopolymers* **2000**, *54*, 297-306, DOI: 10.1002/1097-0282(20001015)54:5<297::aid-bip10>3.0.co;2-9.

129. Gayen, A.; Goswami, S. K.; Mukhopadhyay, C. *Biochim. Biophys. Acta, Biomembr.* **2011**, *1808*, 127-139, DOI: 10.1016/j.bbamem.2010.09.023.

130. Covey, T.; Covey, R.; Bonner, B.; Shushan, J.; Henion, R. K.; Boyd *Rapid Commun. Mass Spectrom.* **1988**, *2*, 249-256.

131. Schnier, P.; Schnier, D.; Gross, E.; Williams *J. Am. Soc. Mass Spectrom.* **1995**, *6*, 1086-1097.

132. Nagornova, N. S.; Rizzo, T. R.; Boyarkin, O. V. *Science (Washington, DC, U. S.)* **2012**, *336*, 320-323, DOI: 10.1126/science.1218709.

133. Garand, E.; Kamrath, M. Z.; Jordan, P. A.; Wolk, A. B.; Leavitt, C. M.; McCoy, A. B.; Miller, S. J.; Johnson, M. A. *Science (Washington, DC, U. S.)* **2012**, *335*, 694-698, DOI: 10.1126/science.1214948.

134. Prell, J. S.; Correra, T. C.; Chang, T. M.; Biles, J. A.; Williams, E. R. *J. Am. Chem. Soc.* **2010**, *132*, 14733-14735, DOI: 10.1021/ja106167d.

135. Prell, J. S.; Chang, T. M.; O'Brien, J. T.; Williams, E. R. *J. Am. Chem. Soc.* **2010**, *132*, 7811-7819, DOI: 10.1021/ja102765w.

136. Nagornova, N. S.; Rizzo, T. R.; Boyarkin, O. V. *Science (Washington, DC, U. S.)* **2012**, *336*, 320-323, DOI: 10.1126/science.1218709.

137. Shi, H. L.; Pierson, N. A.; Valentine, S. J.; Clemmer, D. E. *J. Phys. Chem. B* **2012**, *116*, 3344-3352, DOI: 10.1021/jp210797x.

138. Myung, S.; Badman, E. R.; Lee, Y. J.; Clemmer, D. E. *J. Phys. Chem. A* **2002**, *106*, 9976-9982, DOI: 10.1021/jp0206368.

139. Skinner, O. S.; Breuker, K.; McLafferty, F. W. *J. Am. Soc. Mass Spectrom.* **2013**, *24*, 807-810, DOI: 10.1007/s13361-013-0603-3.

140. Schennach, M.; Breuker, K. *Angew. Chem., Int. Ed.* **2014**, *53*, 164-168, DOI: 10.1002/anie.201306838.

141. Warnke, S.; von Helden, G.; Pagel, K. *J. Am. Chem. Soc.* **2013**, *135*, 1177-1180, DOI: 10.1021/ja308528d.

142. Merenbloom, S. I.; Flick, T. G.; Williams, E. R. *J. Am. Soc. Mass Spectrom.* **2012**, *23*, 553-562, DOI: 10.1007/s13361-011-0313-7.

143. Zhou, M.; Dagan, S.; Wysocki, V. H. *Angew. Chem., Int. Ed.* **2012**, *51*, 4336-4339, DOI: 10.1002/anie.201108700.

144. Hacke, M.; Gruber, T.; Schulenburg, C.; Balbach, J.; Arnold, U. *FEBS Journal* **2013**, *280*, 4454-4462, DOI: 10.1111/febs.12406.

145. Kotarba, A. E.; Aucoin, D.; Hoos, M. D.; Smith, S. O.; Van Nostrand, W. E. *Biochemistry* **2013**, *52*, 2565-2573, DOI: 10.1021/bi4001936.

146. Coffa, S.; Breitman, M.; Spiller, B. W.; Gurevich, V. V. *Biochemistry* **2011**, *50*, 6951-6958, DOI: 10.1021/bi200745k.

147. Lowman, H. B.; Bass, S. H.; Simpson, N.; Wells, J. A. *Biochemistry* **1991**, *30*, 10832-8, DOI: 10.1021/bi00109a004.

148. Cunningham, B. C.; Henner, D. J.; Wells, J. A. *Science (Washington, D. C., 1883-)* **1990**, *247*, 1461-5, DOI: 10.1126/science.2321008.

149. Cunningham, B. C.; Wells, J. A. *Science (Washington, D. C., 1883-)* **1989**, *244*, 1081-5, DOI: 10.1126/science.2471267.

150. Pierson, N. A.; Chen, L.; Russell, D. H.; Clemmer, D. E. *J. Am. Chem. Soc.* **2013**, DOI: 10.1021/ja3114505.

151. Sterner, J. L.; Johnston, M. V.; Nicol, G. R.; Ridge, D. P. *J. Am. Soc. Mass Spectrom.* **1999**, *10*, 483-491, DOI: 10.1016/s1044-0305(99)00020-3.

152. Dongré, A. R.; Jones, J. L.; Somogyi, Á.; Wysocki, V. H. *J. Am. Chem. Soc.* **1996**, *118*, 8365-8374, DOI: 10.1021/ja9542193.

153. Clemmer, D. E.; Jarrold, M. F. *J. Mass Spectrom.* **1997**, *32*, 577-592, DOI: 10.1002/(sici)1096-9888(199706)32:6<577::aid-jms530>3.0.co;2-4.

154. Demireva, M.; O'Brien, J. T.; Williams, E. R. *J. Am. Chem. Soc.* **2012**, *134*, 11216-11224, DOI: 10.1021/ja303313p.

155. Ramachandran, G. N.; Sasisekharan, V. *Advan. Protein Chem.* **1968**, *23*, 283-438.

156. Stewart, D. E.; Sarkar, A.; Wampler, J. E. *Journal of Molecular Biology* **1990**, *214*, 253-260, DOI: http://dx.doi.org/10.1016/0022-2836(90)90159-J.

157. Dodge, R. W.; Scheraga, H. A. *Biochemistry* **1996**, *35*, 1548-59.

158. Zscherp, C.; Aygün, H.; Engels, J. W.; Mäntele, W. *Biochimica et Biophysica Acta (BBA) - Proteins and Proteomics* **2003**, *1651*, 139-145, DOI: http://dx.doi.org/10.1016/S1570-9639(03)00263-2.

159. Reimer, U.; Mokdad, N. E.; Schutkowski, M.; Fischer, G. *Biochemistry* **1997**, *36*, 13802-13808, DOI: 10.1021/bi9713916.

APPENDIX A:

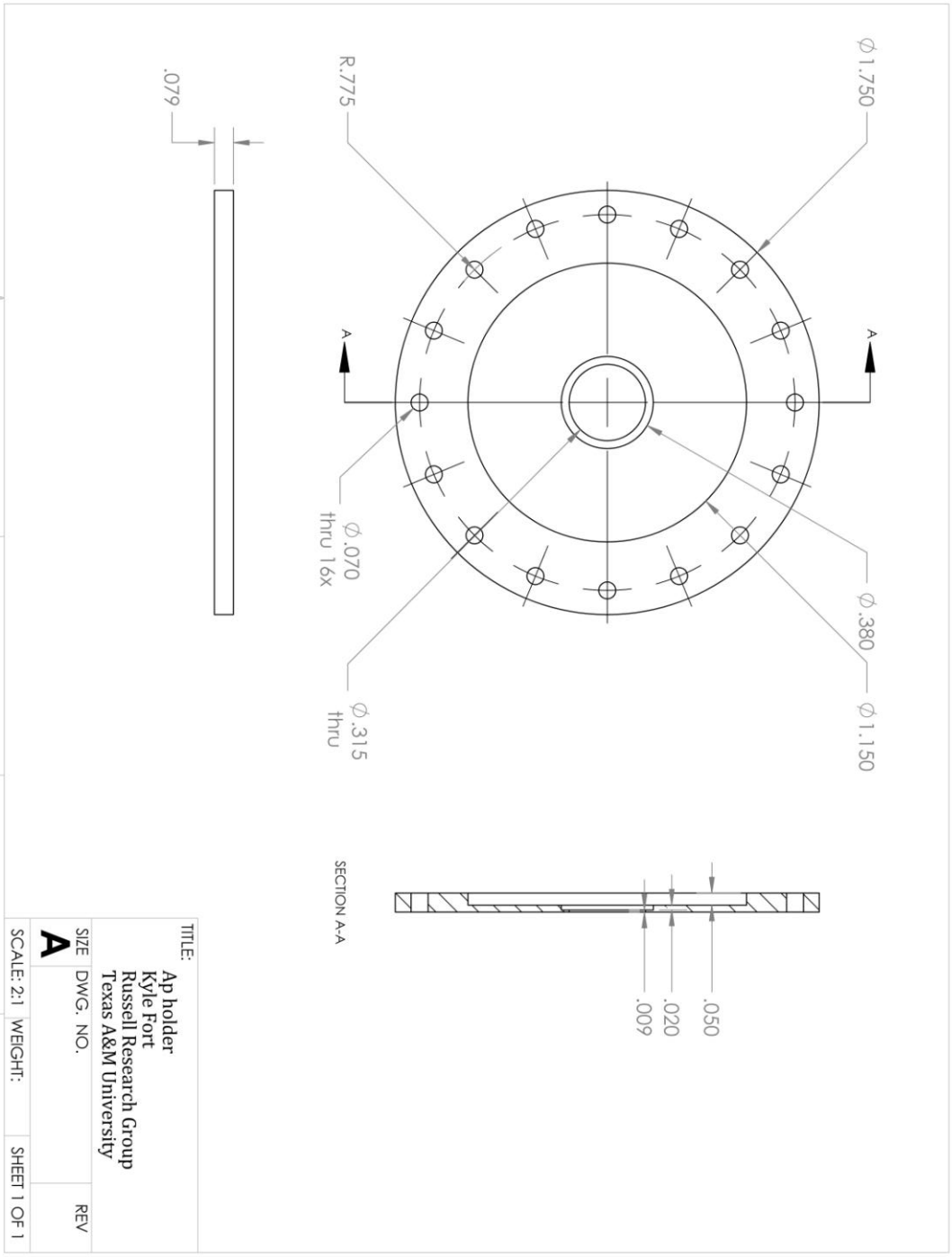
Ø1.750
R.775
.079
A
A
Ø.070
thru 16x
Ø.315
thru
Ø.380
Ø1.150
SECTION A-A
.050
.020
.009
TITLE:
Ap holder
Kyle Fort
Russell Research Group
Texas A&M University
SIZE
A
DWG. NO.
REV
SCALE: 2:1
WEIGHT:
SHEET 1 OF 1
5
4
3
2
1

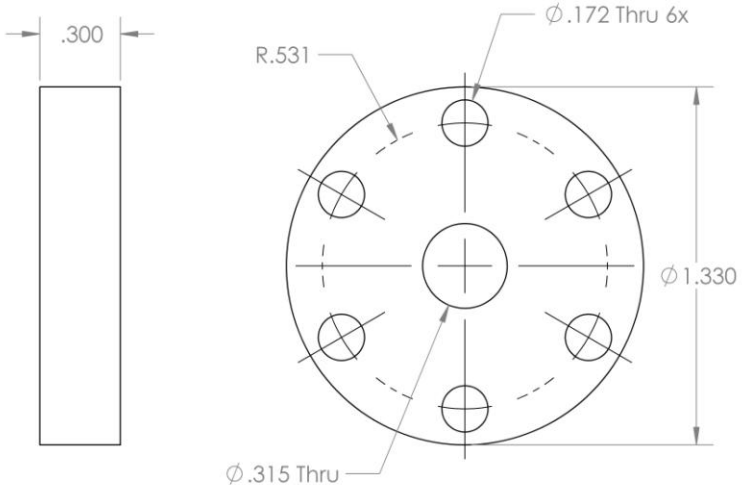

TITLE: Capillary flange Kyle Fort Russell Research Group Texas A&M University		
SIZE A	DWG. NO.	REV
SCALE: 2:1	WEIGHT:	SHEET 1 OF 1

5 4 3 2 1

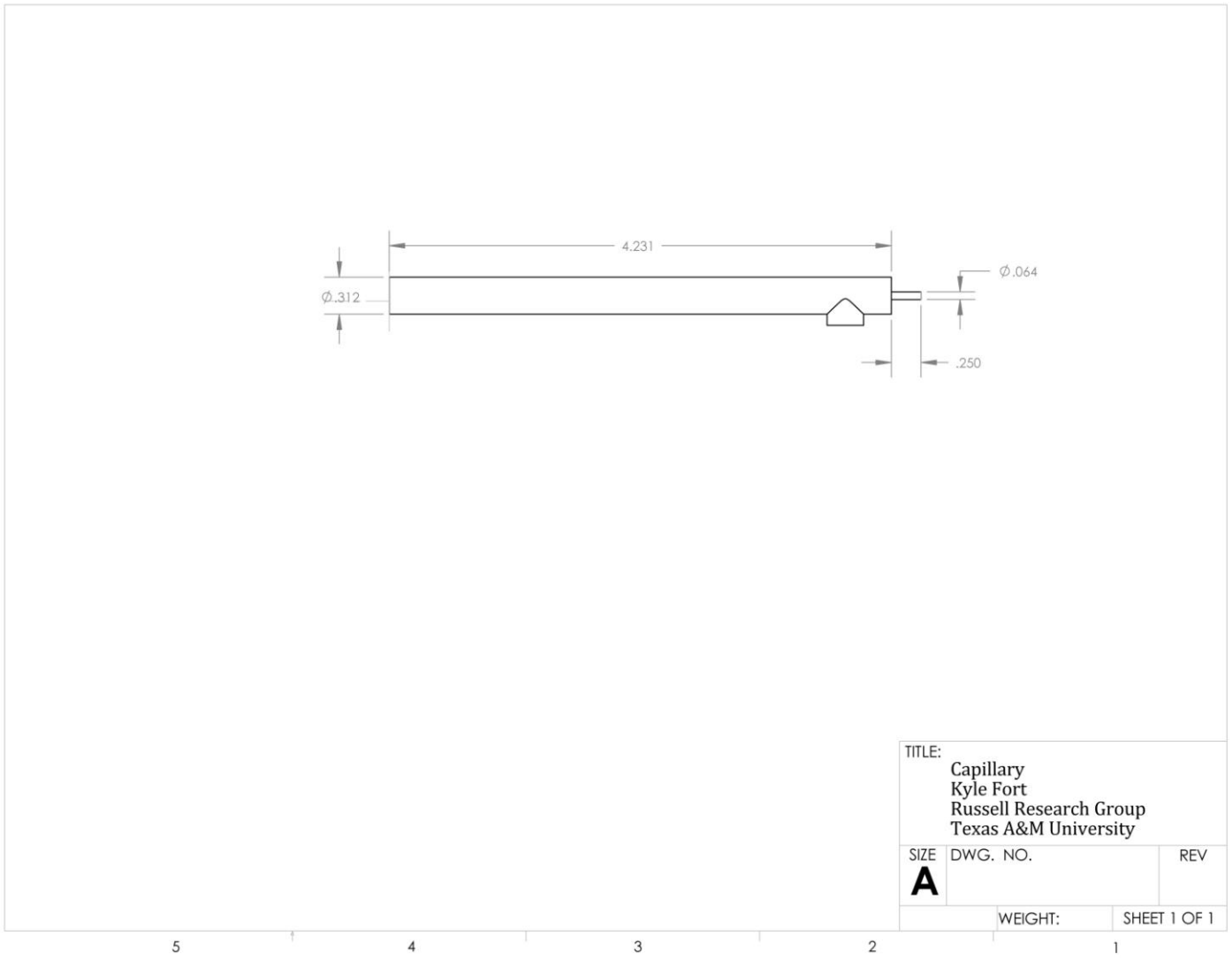
4.231
Ø.064
Ø.312
.250
TITLE:
Capillary
Kyle Fort
Russell Research Group
Texas A&M University
SIZE
A
DWG. NO.
REV
WEIGHT:
SHEET 1 OF 1
5
4
3
2
1

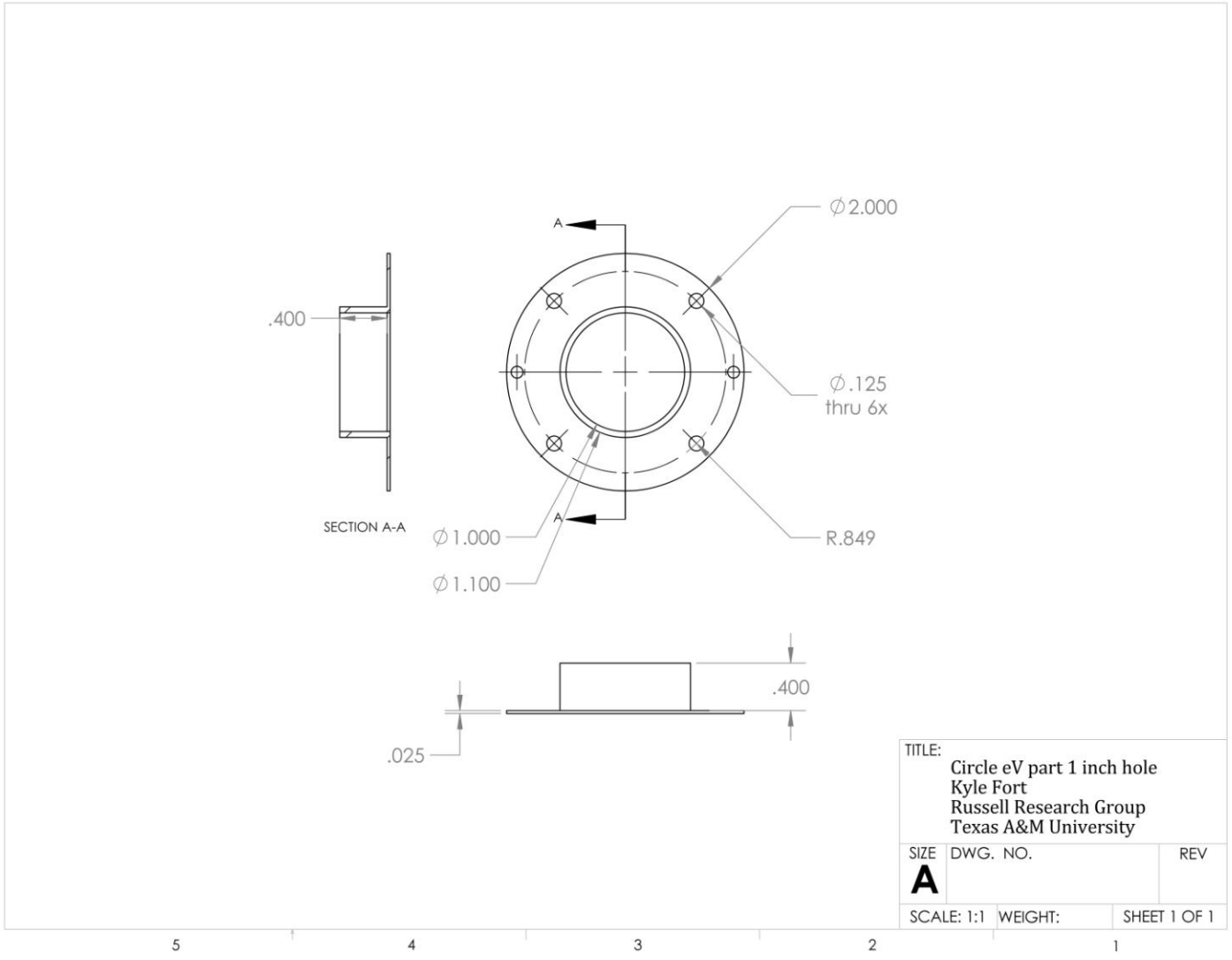
∅2.000
A
.400
∅.125
thru 6x
SECTION A-A
A
∅1.000
R.849
∅1.100
.400
.025
TITLE:
Circle eV part 1 inch hole
Kyle Fort
Russell Research Group
Texas A&M University
SIZE
A
DWG. NO.
REV
SCALE: 1:1
WEIGHT:
SHEET 1 OF 1
5
4
3
2
1

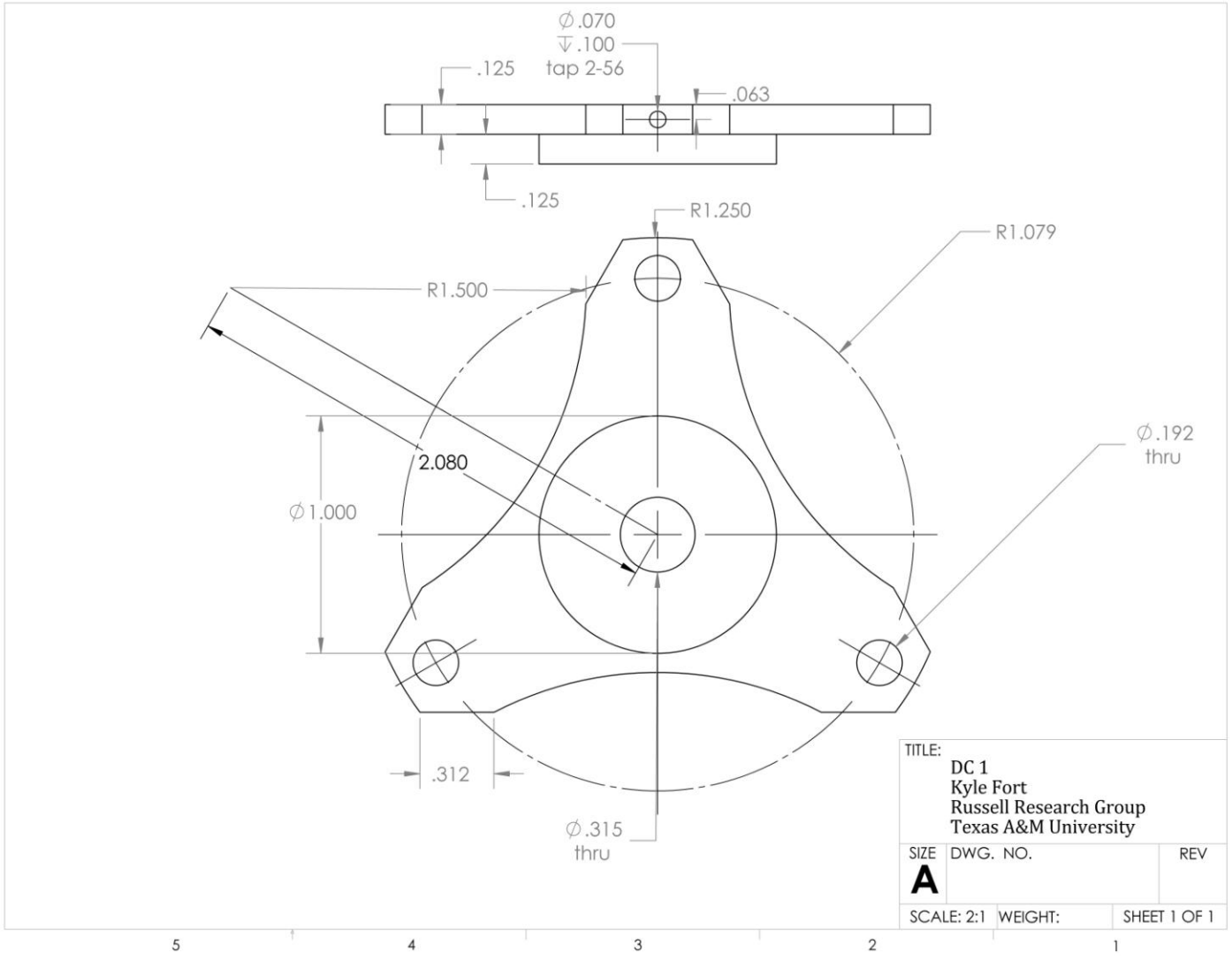
∅.070
↧.100
tap 2-56
.125
.063
.125
R1.250
R1.079
R1.500
2.080
∅1.000
∅.192
thru
.312
∅.315
thru
TITLE:
DC 1
Kyle Fort
Russell Research Group
Texas A&M University
SIZE
A
DWG. NO.
REV
SCALE: 2:1
WEIGHT:
SHEET 1 OF 1
5
4
3
2
1

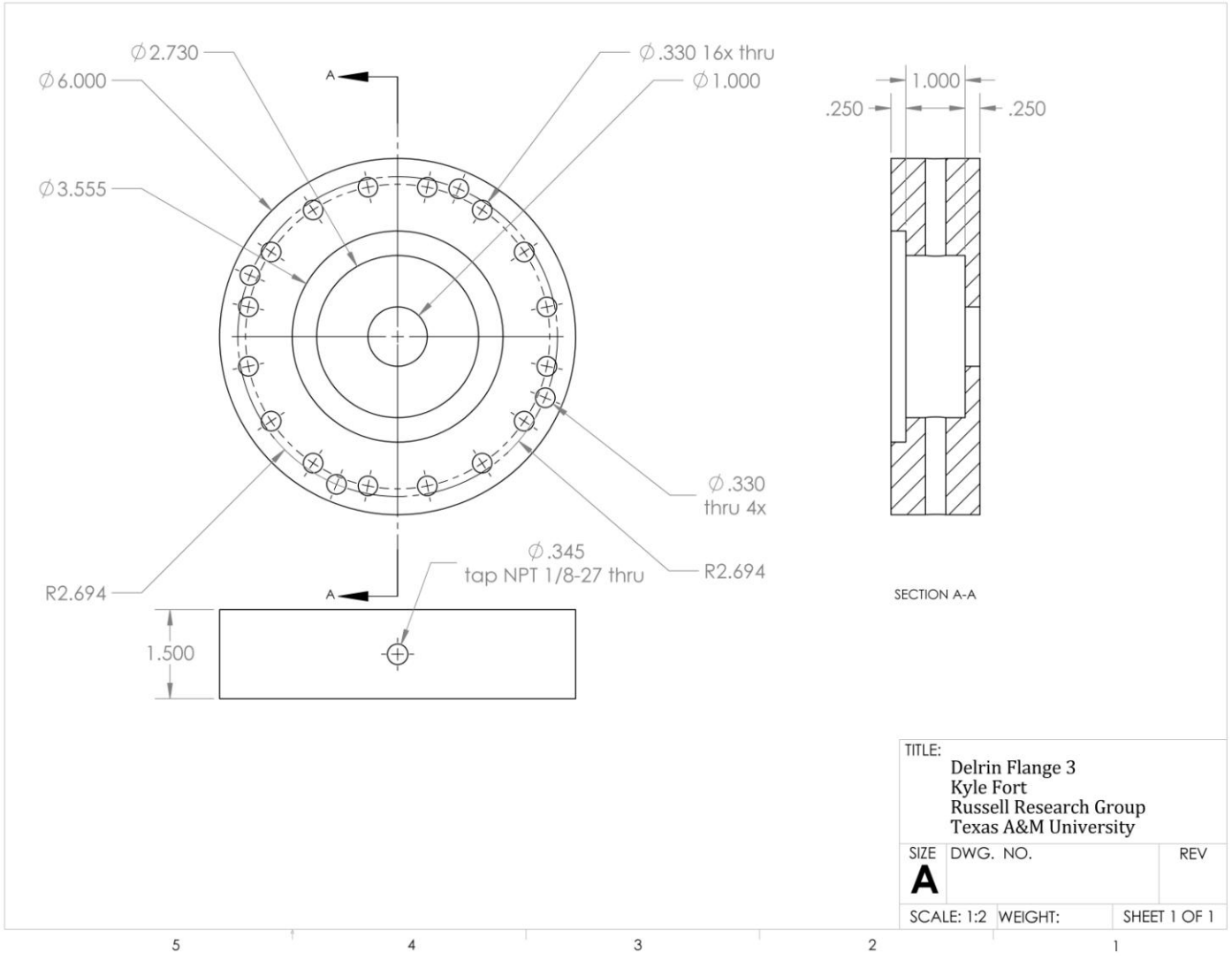
∅2.730
∅6.000
∅3.555
∅.330 16x thru
∅1.000
∅.330
thru 4x
∅.345
tap NPT 1/8-27 thru
R2.694
R2.694
1.500
A
A
1.000
.250
.250
SECTION A-A
TITLE:
Delrin Flange 3
Kyle Fort
Russell Research Group
Texas A&M University
SIZE
A
DWG. NO.
REV
SCALE: 1:2
WEIGHT:
SHEET 1 OF 1
5
4
3
2
1

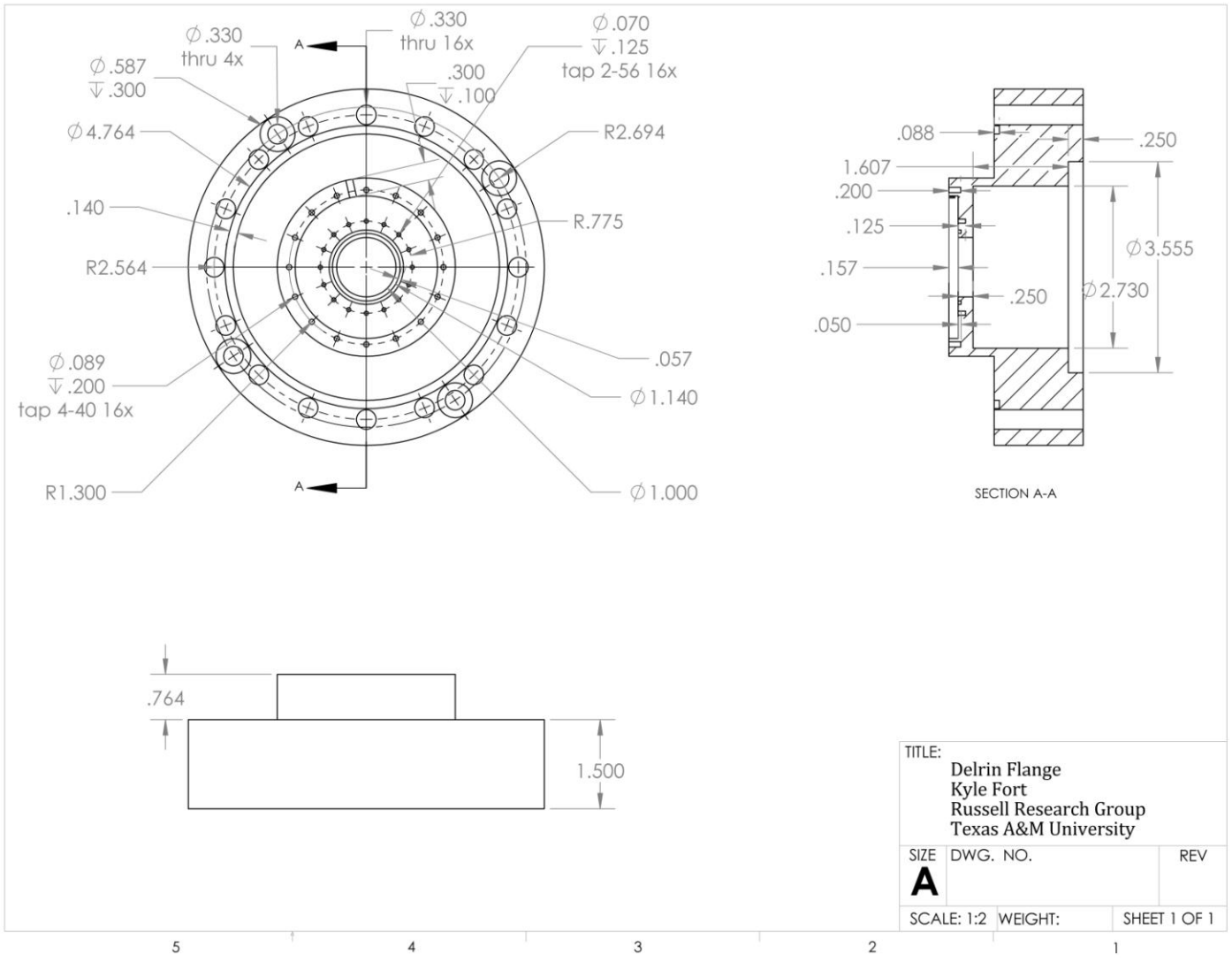
∅.330
thru 4x
∅.330
thru 16x
∅.070
↧.125
tap 2-56 16x
∅.587
↧.300
.300
↧.100
∅4.764
R2.694
.140
R.775
R2.564
.057
∅.089
↧.200
tap 4-40 16x
∅1.140
R1.300
∅1.000
A
A
.088
.250
1.607
.200
.125
∅3.555
.157
∅2.730
.250
.050
SECTION A-A
.764
1.500
TITLE:
Delrin Flange
Kyle Fort
Russell Research Group
Texas A&M University
SIZE
A
DWG. NO.
REV
SCALE: 1:2
WEIGHT:
SHEET 1 OF 1
5
4
3
2
1

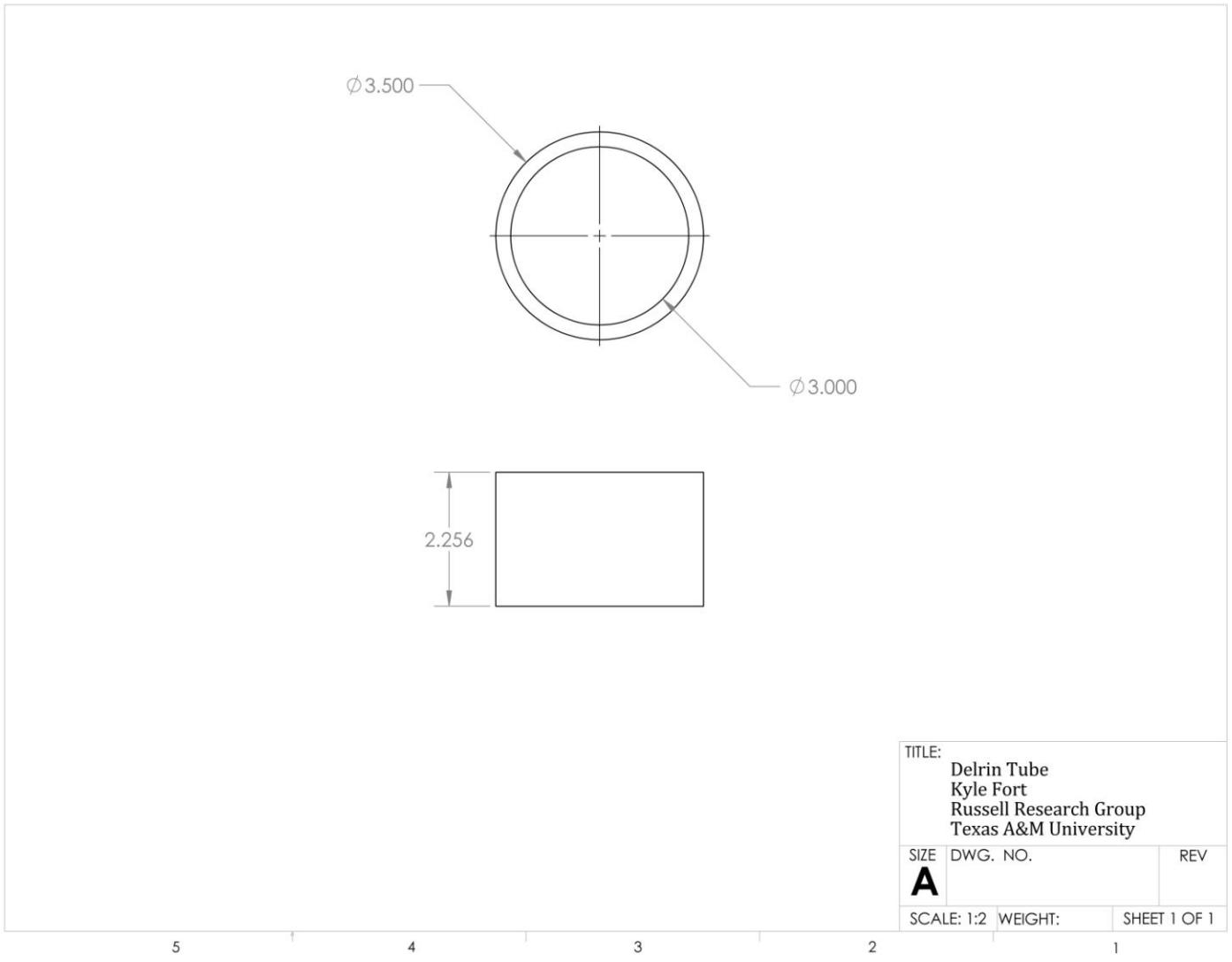
∅3.500
∅3.000
2.256
TITLE:
Delrin Tube
Kyle Fort
Russell Research Group
Texas A&M University
SIZE
A
DWG. NO.
REV
SCALE: 1:2
WEIGHT:
SHEET 1 OF 1
5
4
3
2
1

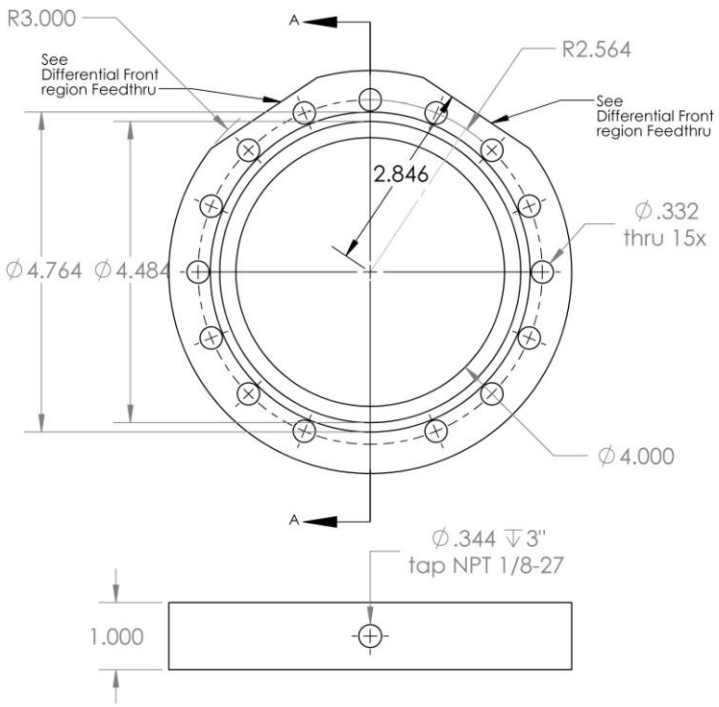

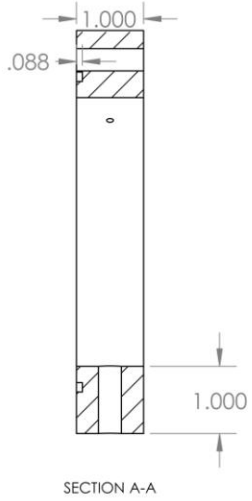

TITLE: Differential Front region Front Kyle Fort Russell Research Group Texas A&M University		
SIZE A	DWG. NO.	REV
SCALE: 1:2	WEIGHT:	SHEET 1 OF 1

5 4 3 2 1

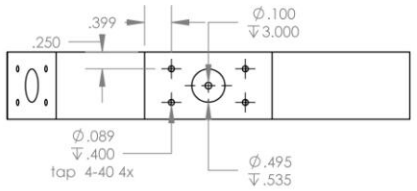

TITLE: Differential Front region Feedthru Kyle Fort Russell Research Group Texas A&M University		
SIZE A	DWG. NO.	REV
SCALE: 1:2	WEIGHT:	SHEET 1 OF 1

5 4 3 2 1

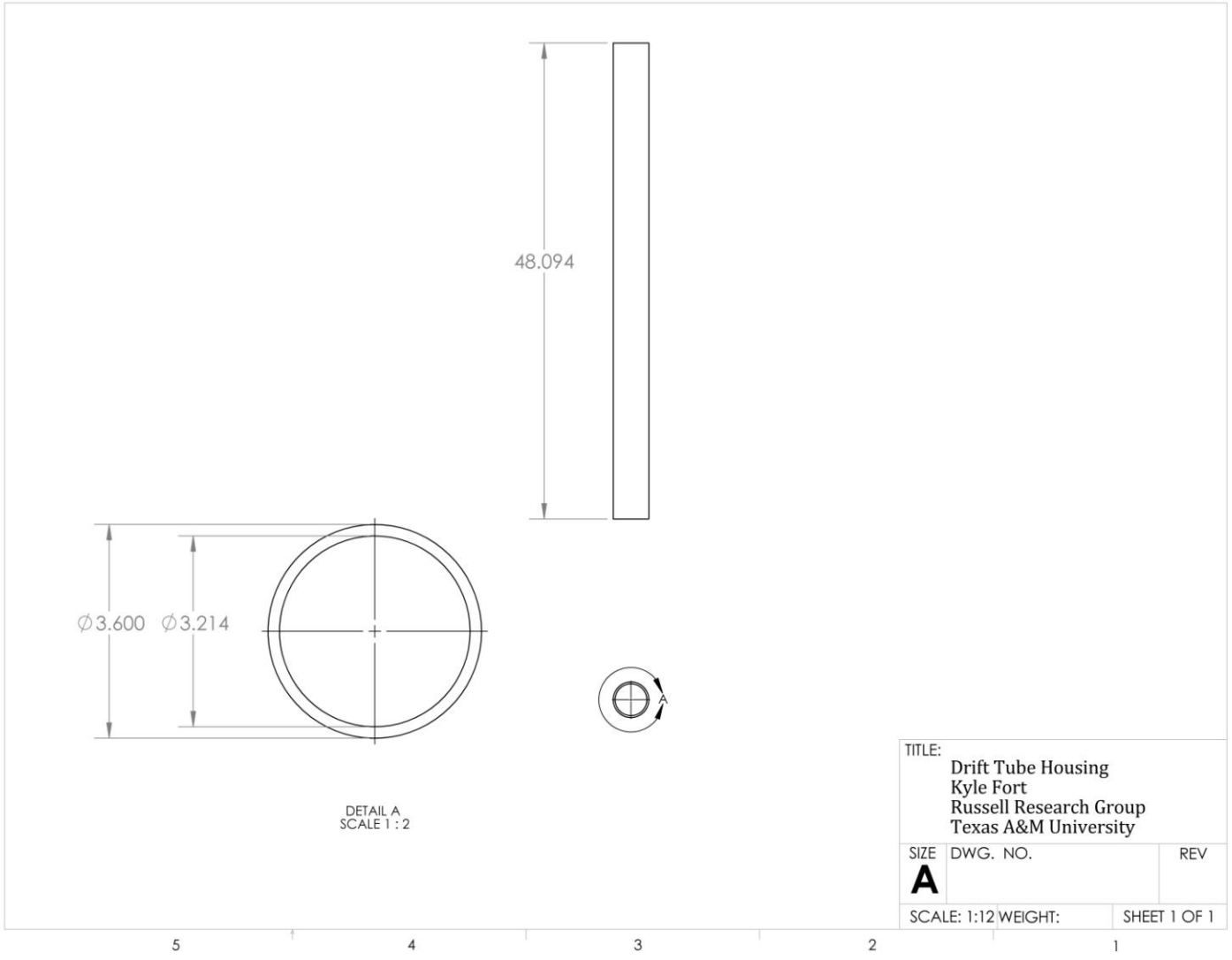
48.094
∅3.600
∅3.214
A
DETAIL A
SCALE 1 : 2
TITLE:
Drift Tube Housing
Kyle Fort
Russell Research Group
Texas A&M University
SIZE
A
DWG. NO.
REV
SCALE: 1:12
WEIGHT:
SHEET 1 OF 1
5
4
3
2
1

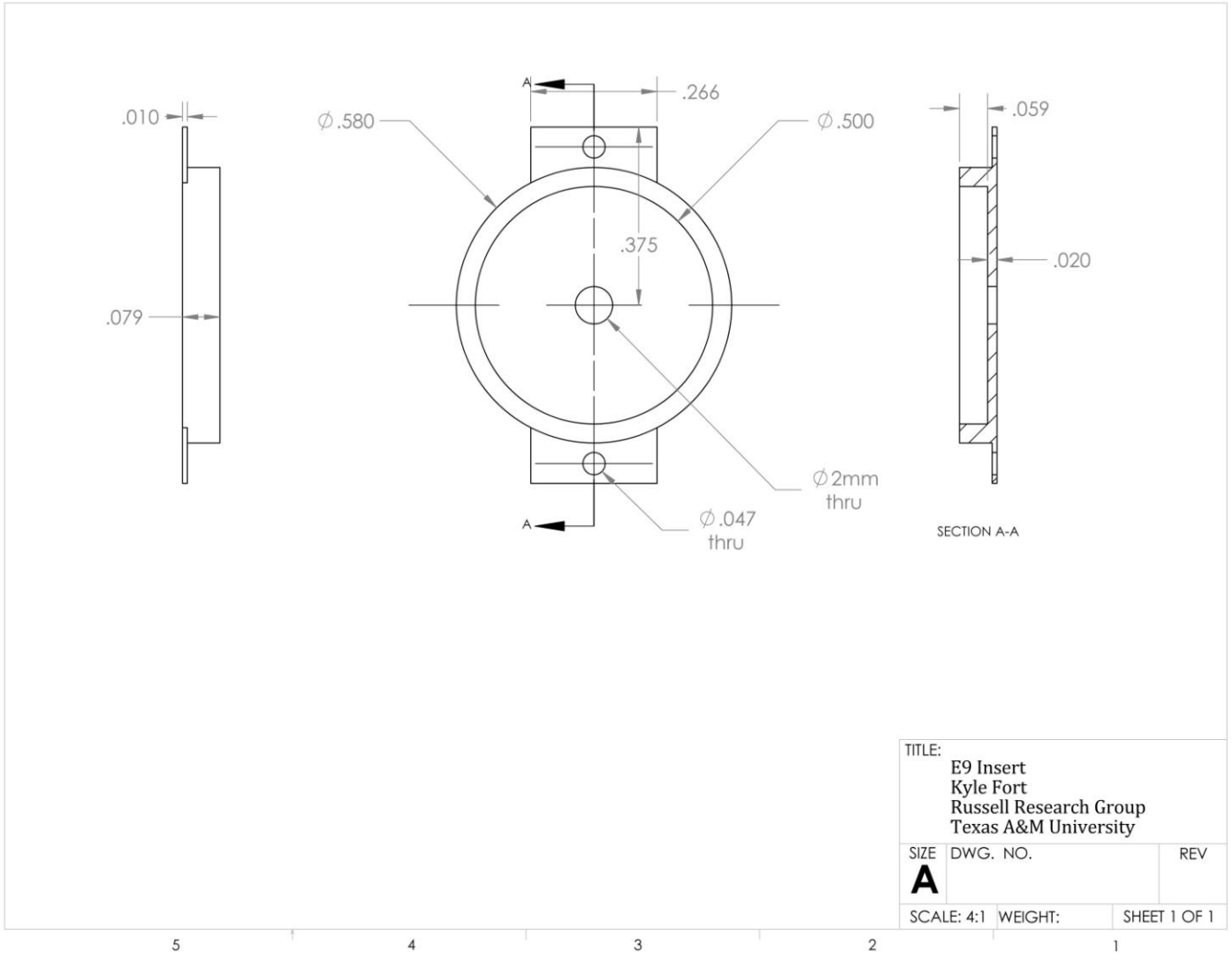
.010
.079
A
.266
∅.580
∅.500
.375
∅2mm
thru
∅.047
thru
A
.059
.020
SECTION A-A
TITLE:
E9 Insert
Kyle Fort
Russell Research Group
Texas A&M University
SIZE
A
DWG. NO.
REV
SCALE: 4:1
WEIGHT:
SHEET 1 OF 1
5
4
3
2
1

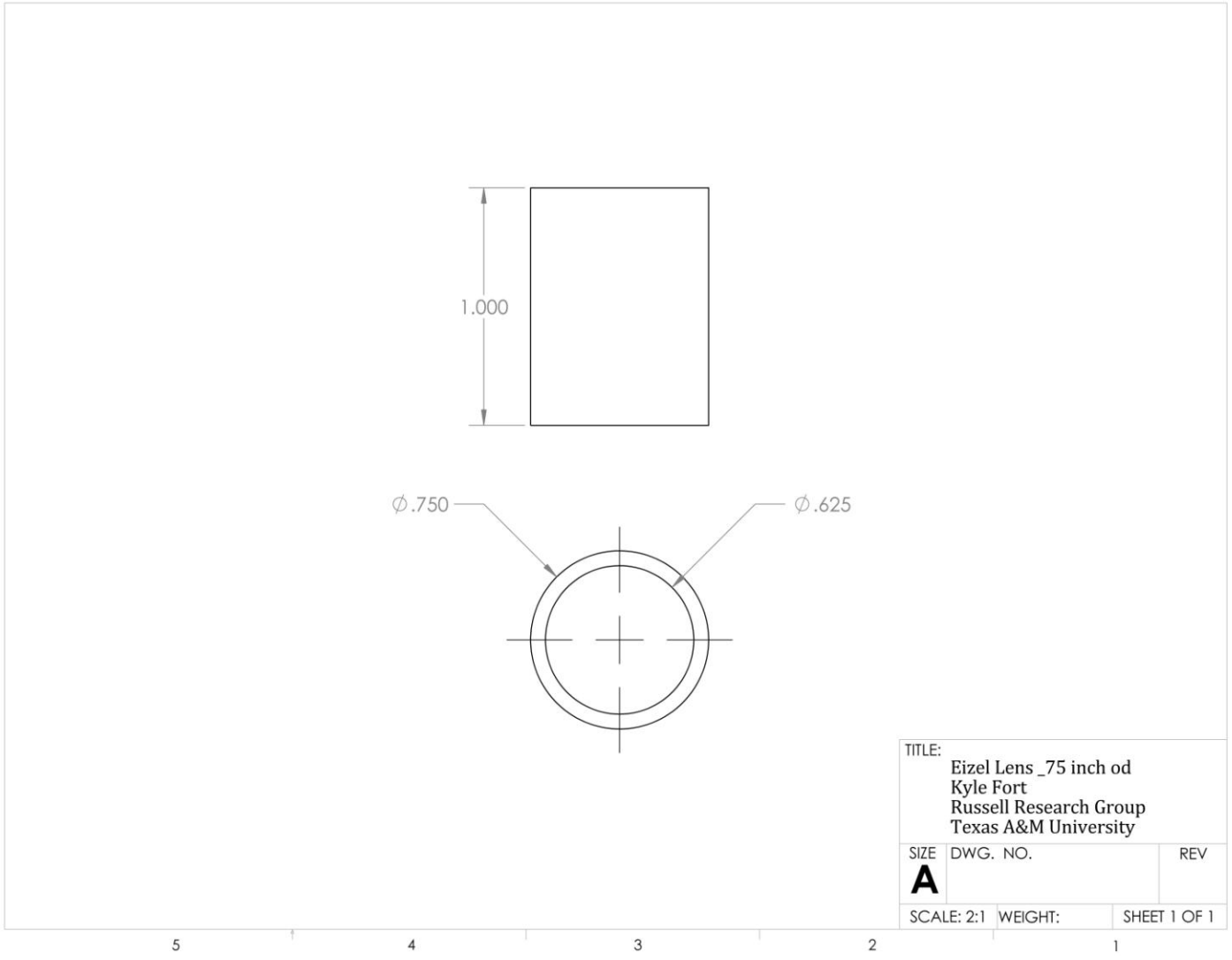
1.000
∅.750
∅.625
TITLE:
Eizel Lens _75 inch od
Kyle Fort
Russell Research Group
Texas A&M University
SIZE
A
DWG. NO.
REV
SCALE: 2:1
WEIGHT:
SHEET 1 OF 1
5
4
3
2
1

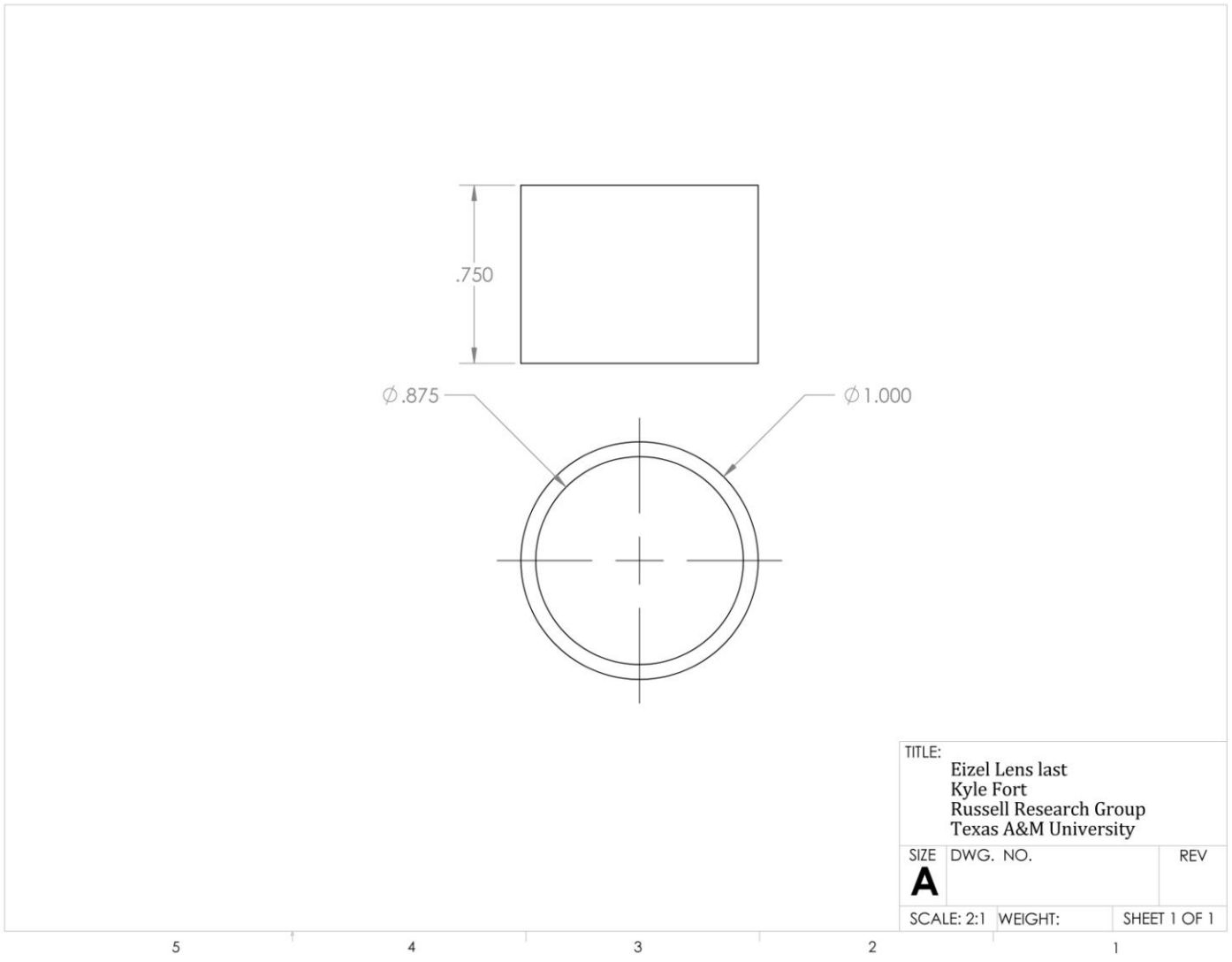
.750
Ø.875
Ø1.000
TITLE:
Eizel Lens last
Kyle Fort
Russell Research Group
Texas A&M University
SIZE
A
DWG. NO.
REV
SCALE: 2:1
WEIGHT:
SHEET 1 OF 1
5
4
3
2
1

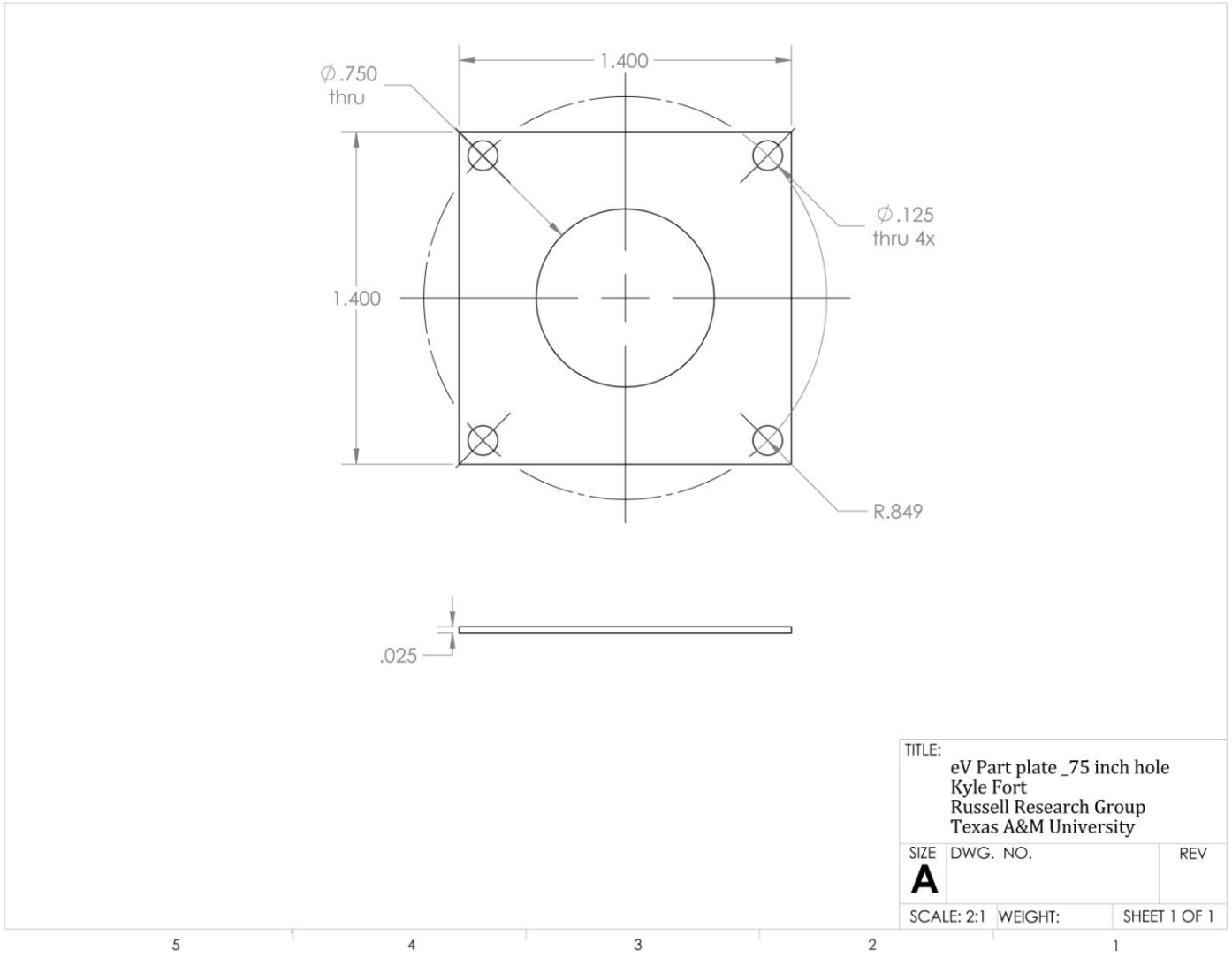
1.400
Ø.750
thru
Ø.125
thru 4x
1.400
R.849
.025
TITLE:
eV Part plate _75 inch hole
Kyle Fort
Russell Research Group
Texas A&M University
SIZE
A
DWG. NO.
REV
SCALE: 2:1
WEIGHT:
SHEET 1 OF 1
5
4
3
2
1

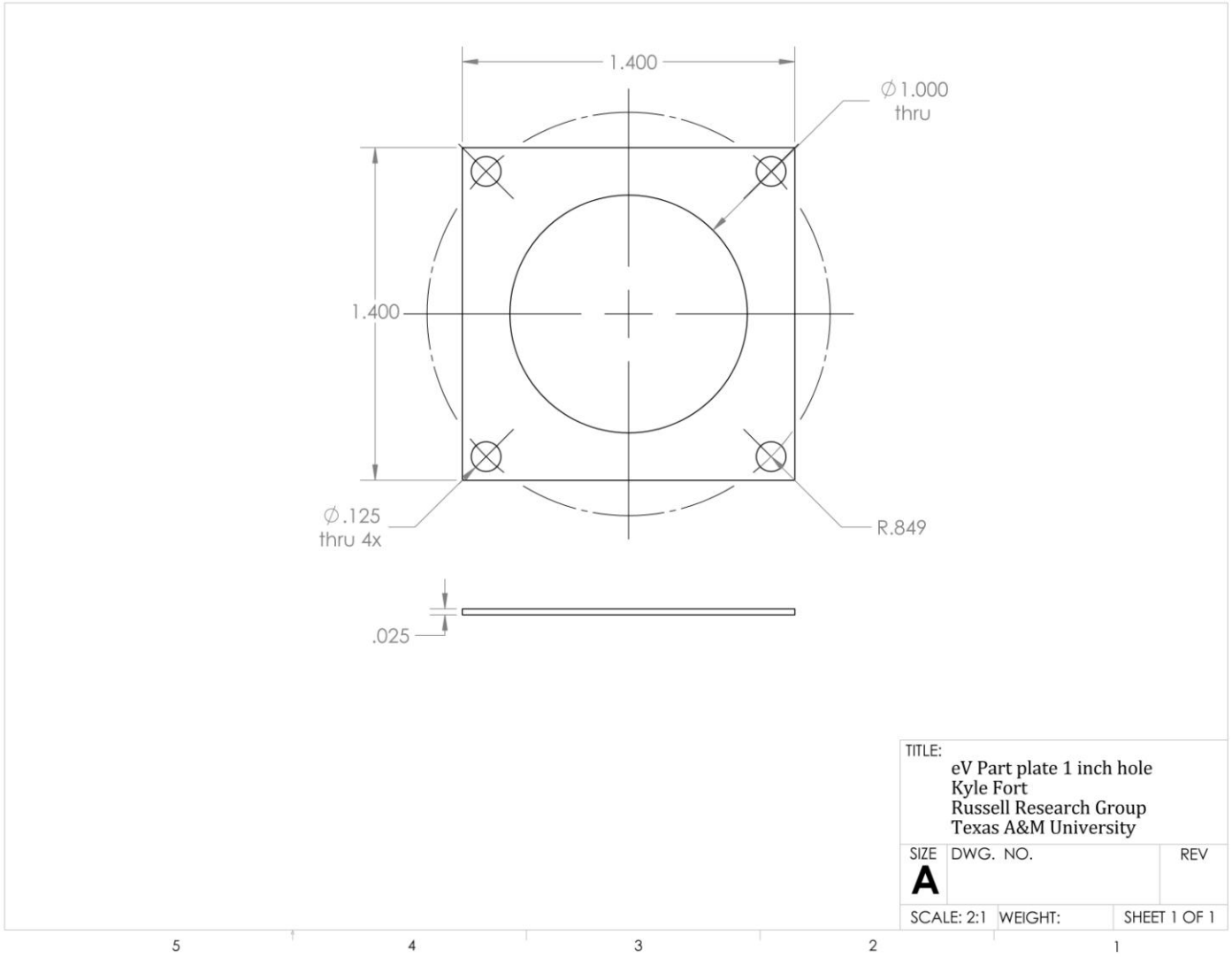
1.400
∅1.000
thru
1.400
∅.125
thru 4x
R.849
.025
TITLE:
eV Part plate 1 inch hole
Kyle Fort
Russell Research Group
Texas A&M University
SIZE
A
DWG. NO.
REV
SCALE: 2:1
WEIGHT:
SHEET 1 OF 1
5
4
3
2
1

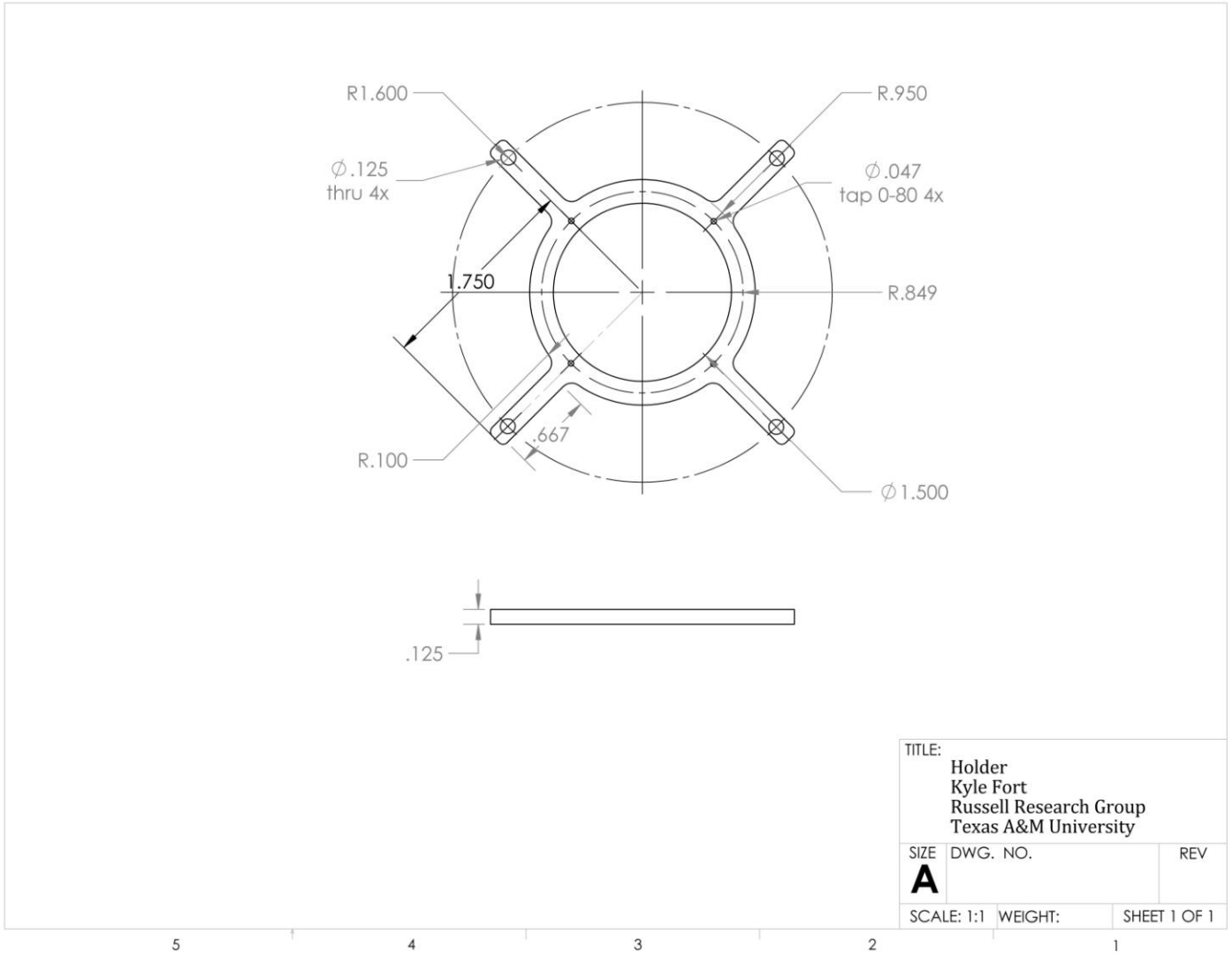
R1.600
R.950
∅.125
thru 4x
∅.047
tap 0-80 4x
1.750
R.849
.667
R.100
∅1.500
.125
TITLE:
Holder
Kyle Fort
Russell Research Group
Texas A&M University
SIZE
A
DWG. NO.
REV
SCALE: 1:1
WEIGHT:
SHEET 1 OF 1
5
4
3
2
1

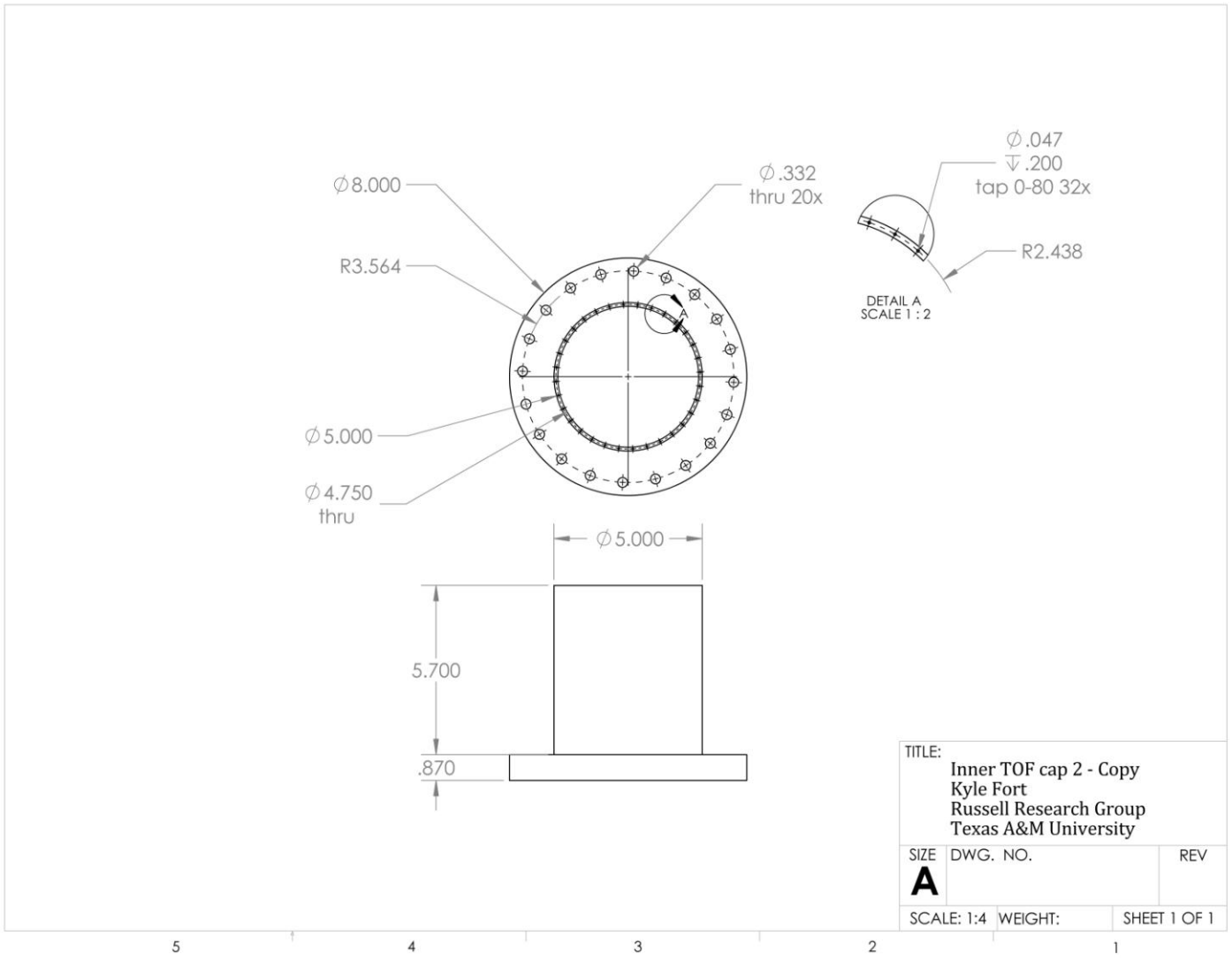
∅8.000
∅.332
thru 20x
R3.564
∅5.000
∅4.750
thru
∅.047
↧.200
tap 0-80 32x
R2.438
DETAIL A
SCALE 1 : 2
∅5.000
5.700
.870
TITLE:
Inner TOF cap 2 - Copy
Kyle Fort
Russell Research Group
Texas A&M University
SIZE
A
DWG. NO.
REV
SCALE: 1:4
WEIGHT:
SHEET 1 OF 1
5
4
3
2
1

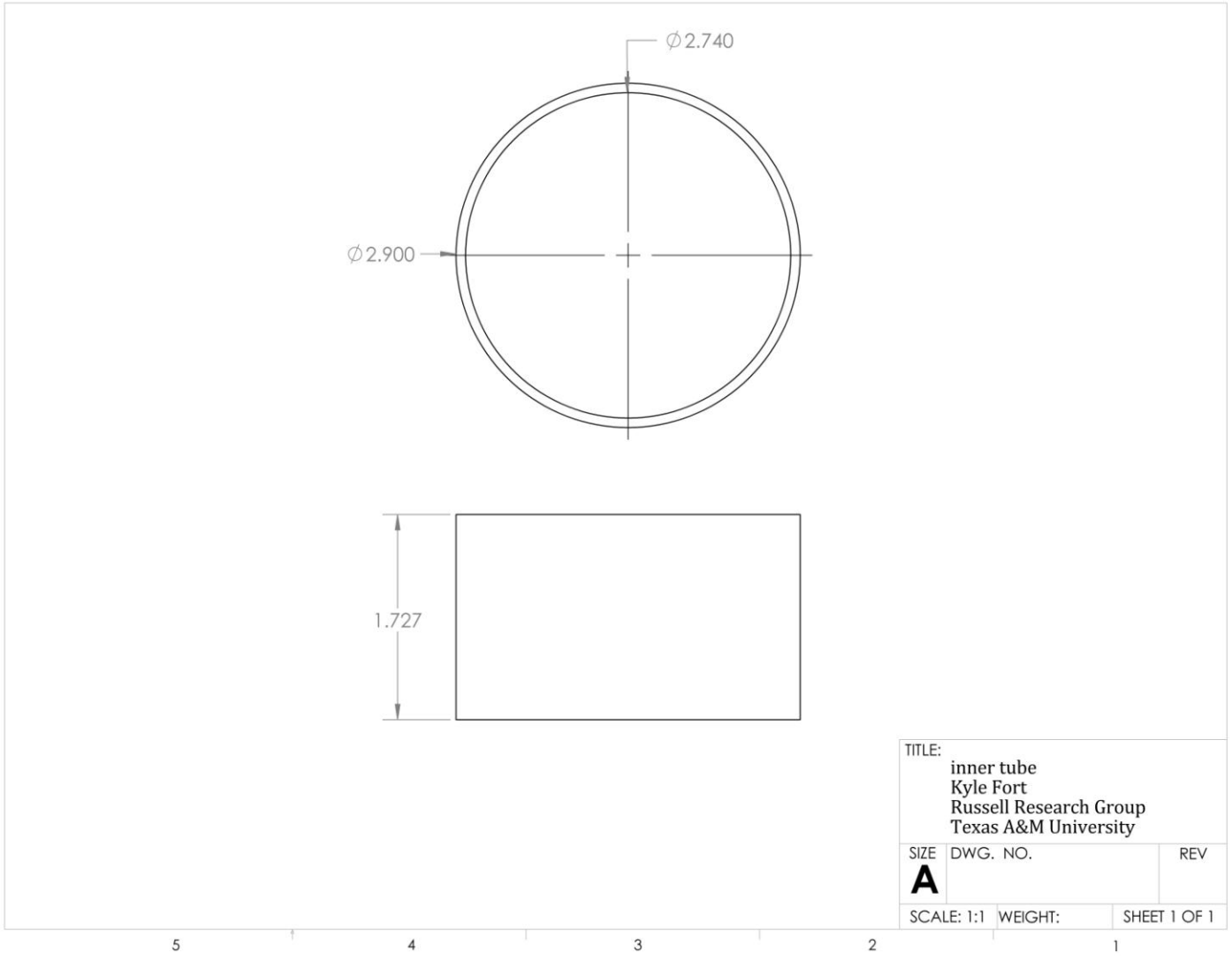
∅2.740
∅2.900
1.727
TITLE:
inner tube
Kyle Fort
Russell Research Group
Texas A&M University
SIZE
A
DWG. NO.
REV
SCALE: 1:1
WEIGHT:
SHEET 1 OF 1
5
4
3
2
1

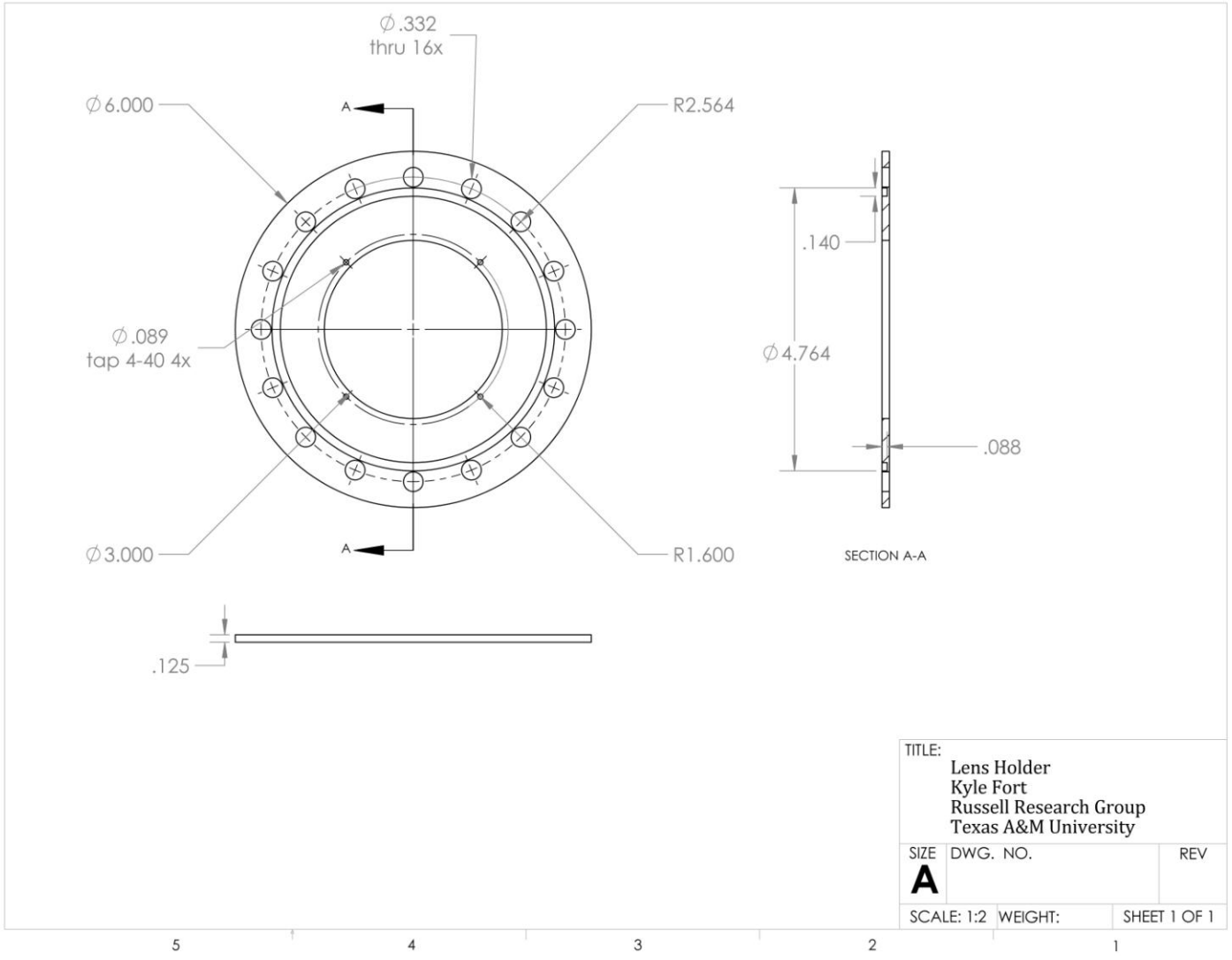
∅.332
thru 16x
∅6.000
R2.564
A
A
∅.089
tap 4-40 4x
∅3.000
R1.600
.125
.140
∅4.764
.088
SECTION A-A
TITLE:
Lens Holder
Kyle Fort
Russell Research Group
Texas A&M University
SIZE
A
DWG. NO.
REV
SCALE: 1:2
WEIGHT:
SHEET 1 OF 1
5
4
3
2
1

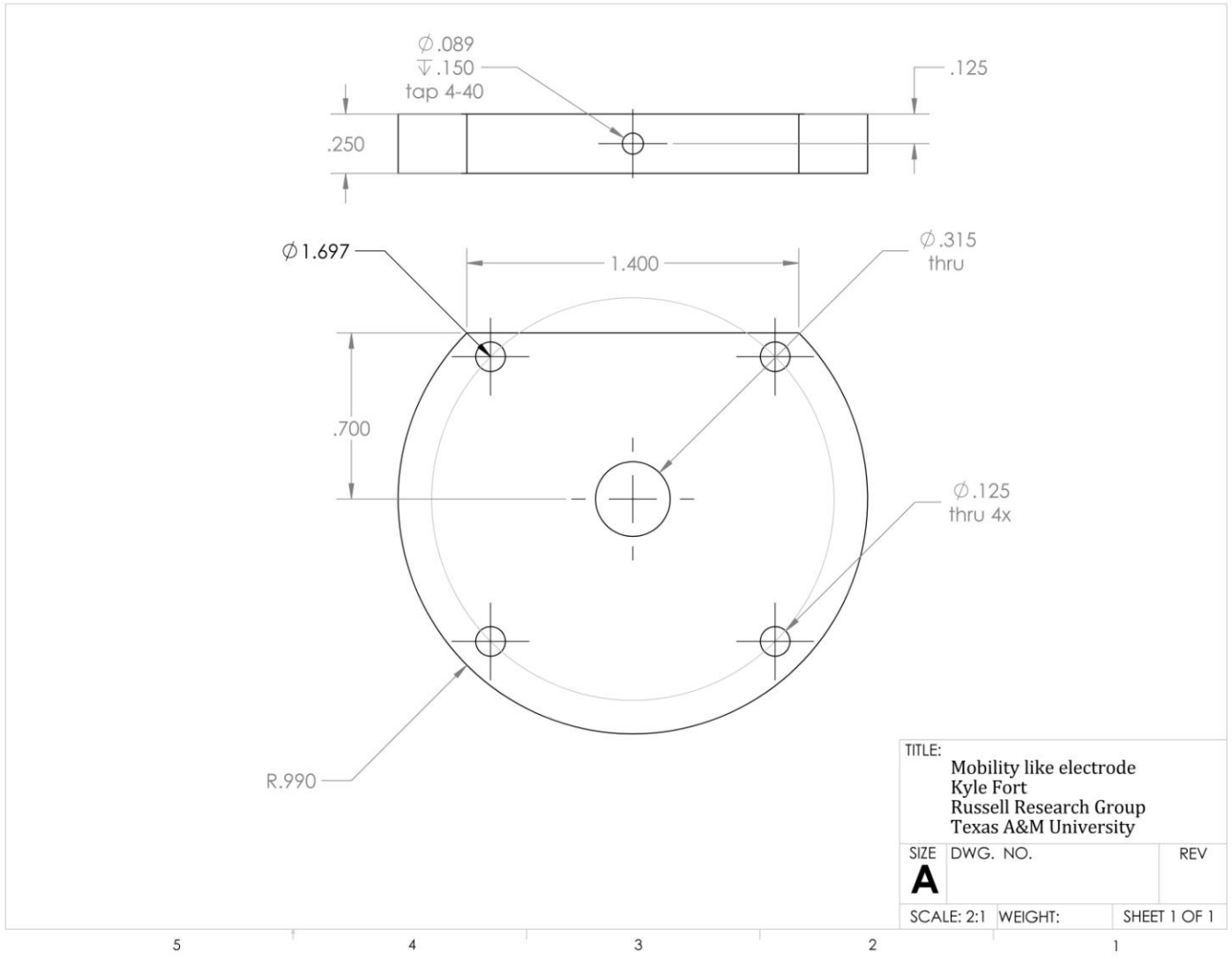
∅.089
↧.150
tap 4-40
.125
.250
∅1.697
1.400
∅.315
thru
.700
∅.125
thru 4x
R.990
TITLE:
Mobility like electrode
Kyle Fort
Russell Research Group
Texas A&M University
SIZE
A
DWG. NO.
REV
SCALE: 2:1
WEIGHT:
SHEET 1 OF 1
5
4
3
2
1

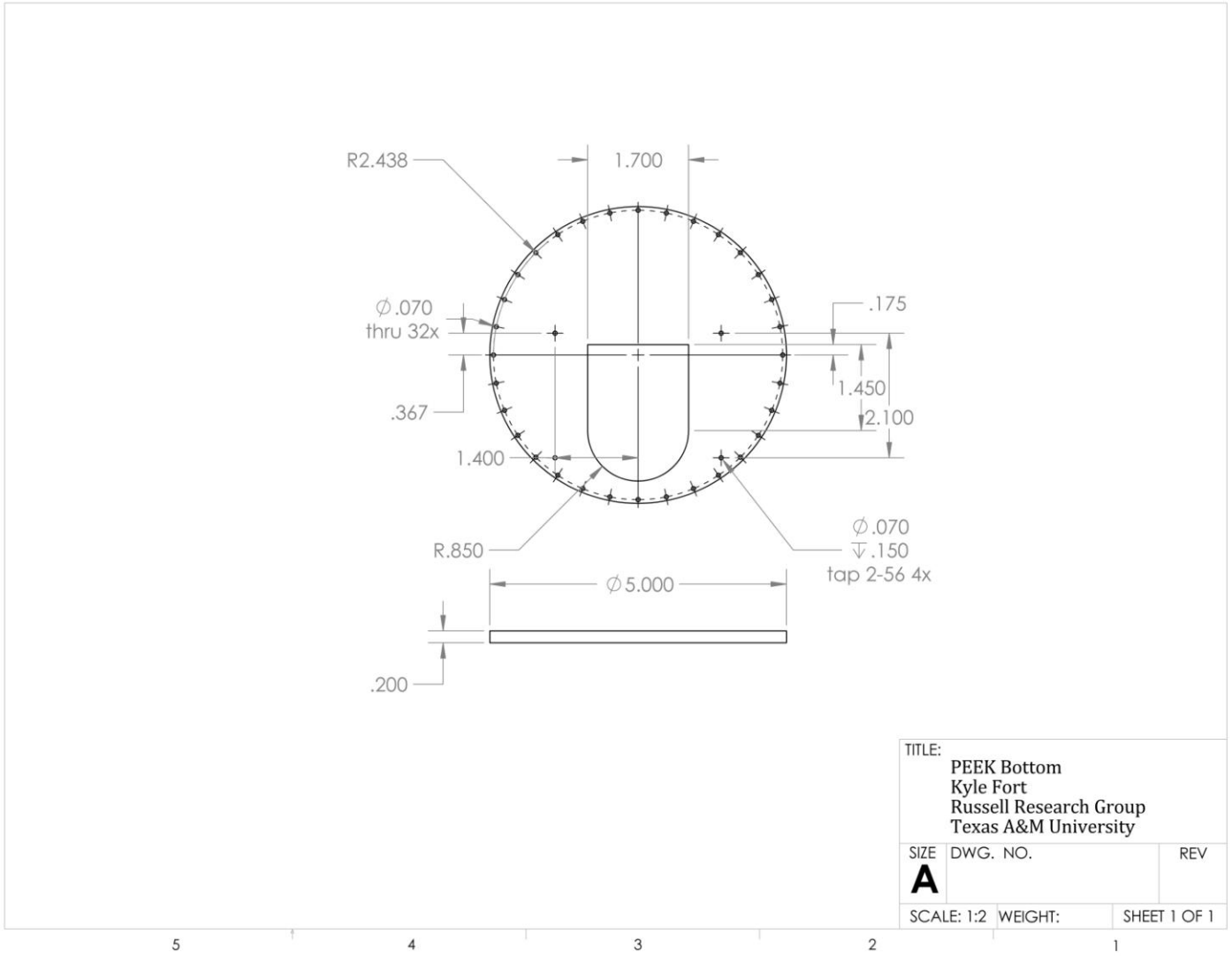
R2.438
1.700
∅.070
thru 32x
.175
1.450
2.100
.367
1.400
R.850
∅.070
↧.150
tap 2-56 4x
∅5.000
.200
TITLE:
PEEK Bottom
Kyle Fort
Russell Research Group
Texas A&M University
SIZE
A
DWG. NO.
REV
SCALE: 1:2
WEIGHT:
SHEET 1 OF 1
5
4
3
2
1

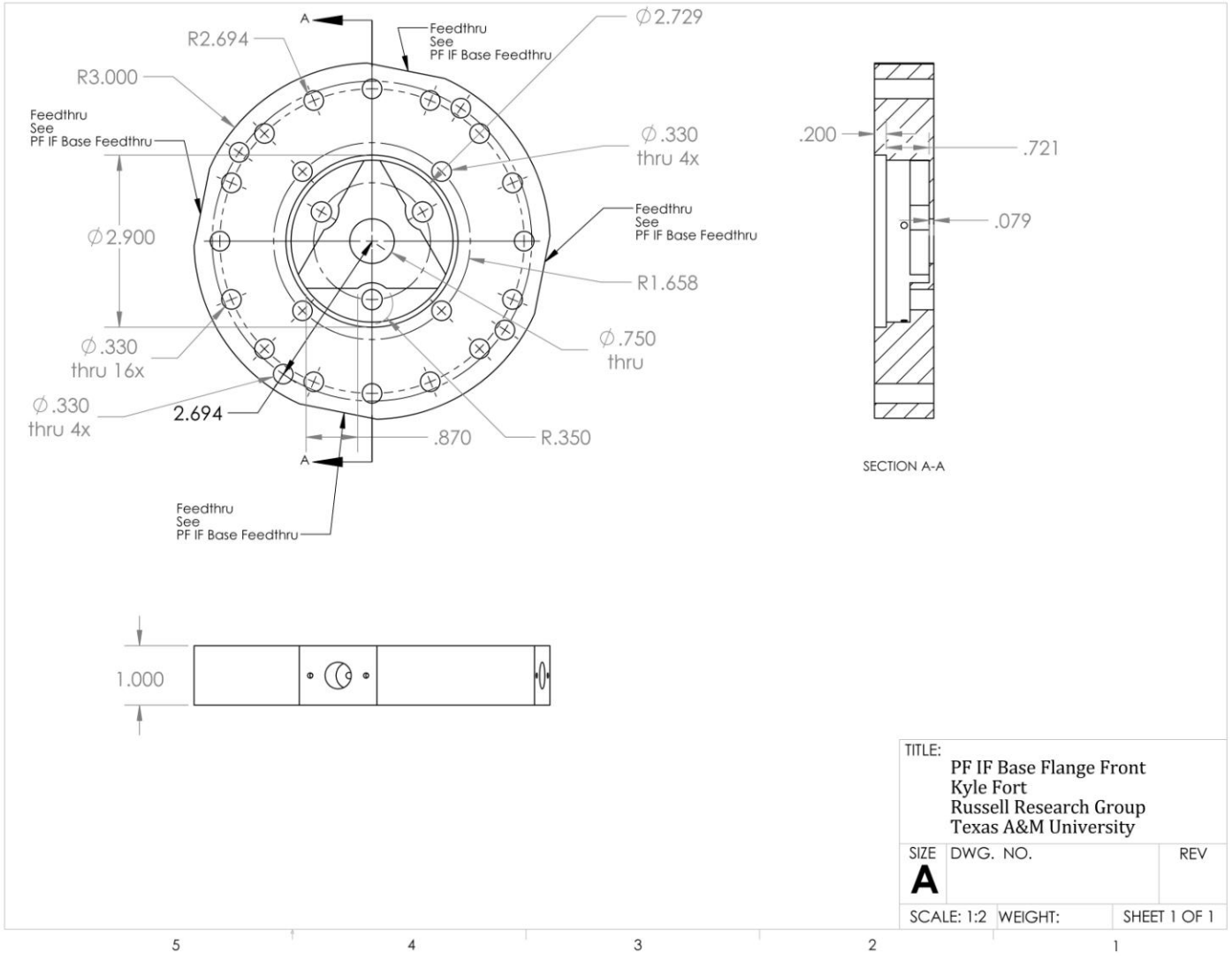
A
R2.694
R3.000
Feedthru
See
PF IF Base Feedthru
Ø2.729
Ø.330
thru 4x
Feedthru
See
PF IF Base Feedthru
Ø2.900
R1.658
Ø.750
thru
Ø.330
thru 16x
Ø.330
thru 4x
2.694
.870
R.350
A
Feedthru
See
PF IF Base Feedthru
.200
.721
.079
SECTION A-A
1.000
TITLE:
PF IF Base Flange Front
Kyle Fort
Russell Research Group
Texas A&M University
SIZE
A
DWG. NO.
REV
SCALE: 1:2
WEIGHT:
SHEET 1 OF 1
5
4
3
2
1

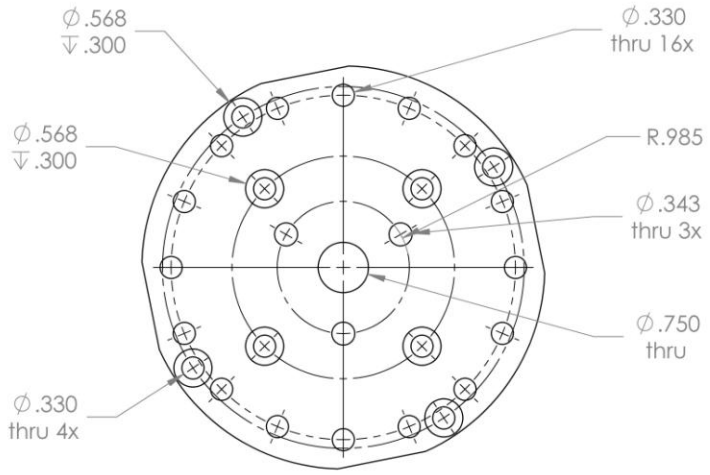

TITLE: PF IF Base Flange Back Kyle Fort Russell Research Group Texas A&M University		
SIZE A	DWG. NO.	REV
SCALE: 1:2	WEIGHT:	SHEET 1 OF 1

5 4 3 2 1

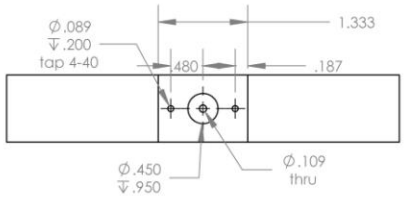

TITLE: PF IF Base Flange Feedthru Kyle Fort Russell Research Group Texas A&M University		
SIZE A	DWG. NO.	REV
SCALE: 1:2	WEIGHT:	SHEET 1 OF 1

5 4 3 2 1

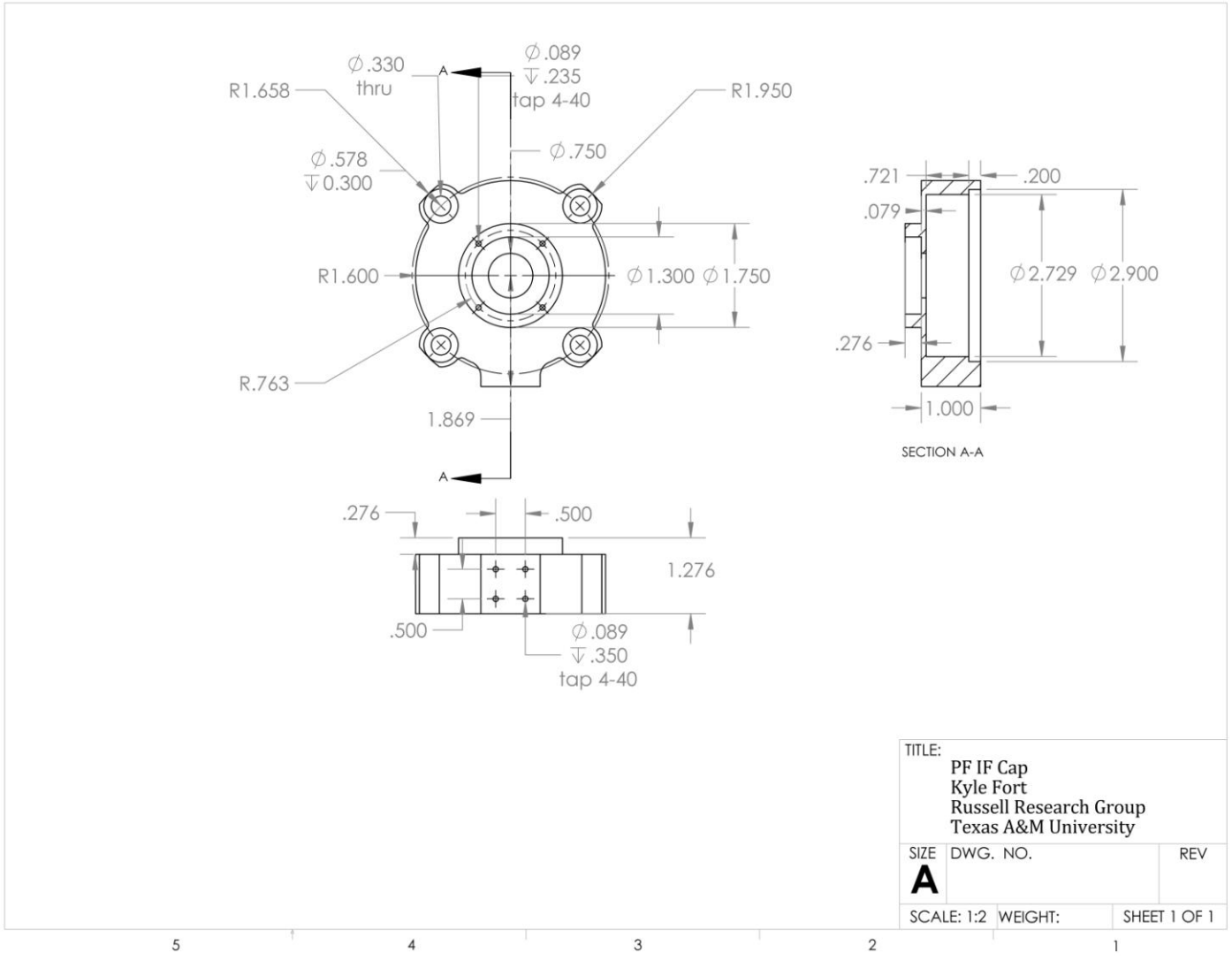
∅.330
thru
∅.089
↧.235
tap 4-40
R1.658
R1.950
∅.750
∅.578
↧0.300
R1.600
∅1.300
∅1.750
R.763
1.869
A
A
.276
.500
1.276
.500
∅.089
↧.350
tap 4-40
.721
.200
.079
∅2.729
∅2.900
.276
1.000
SECTION A-A
TITLE:
PF IF Cap
Kyle Fort
Russell Research Group
Texas A&M University
SIZE
A
DWG. NO.
REV
SCALE: 1:2
WEIGHT:
SHEET 1 OF 1
5
4
3
2
1

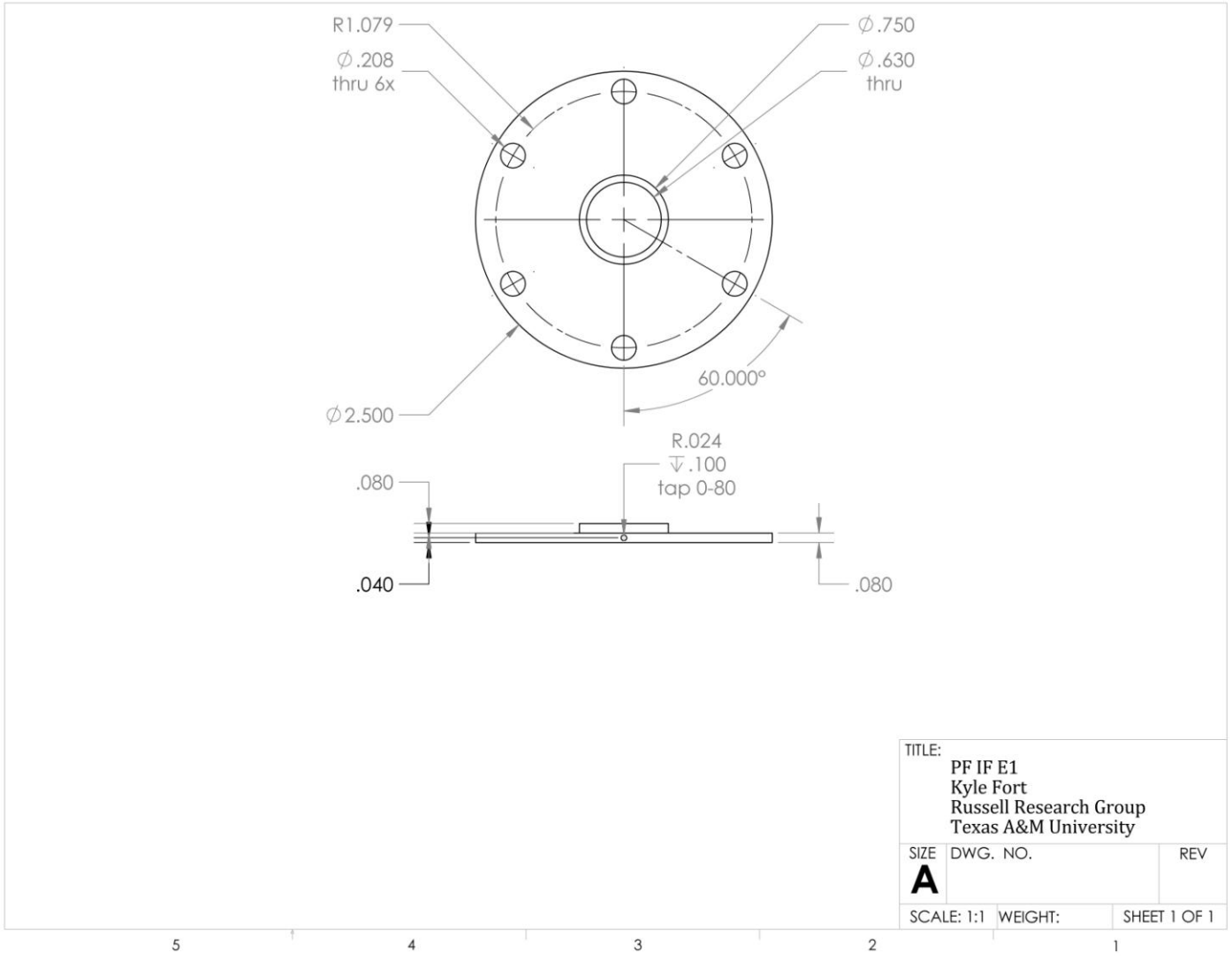
R1.079
∅.208
thru 6x
∅.750
∅.630
thru
60.000°
∅2.500
R.024
↧.100
tap 0-80
.080
.040
.080
TITLE:
PF IF E1
Kyle Fort
Russell Research Group
Texas A&M University
SIZE
A
DWG. NO.
REV
SCALE: 1:1
WEIGHT:
SHEET 1 OF 1
5
4
3
2
1

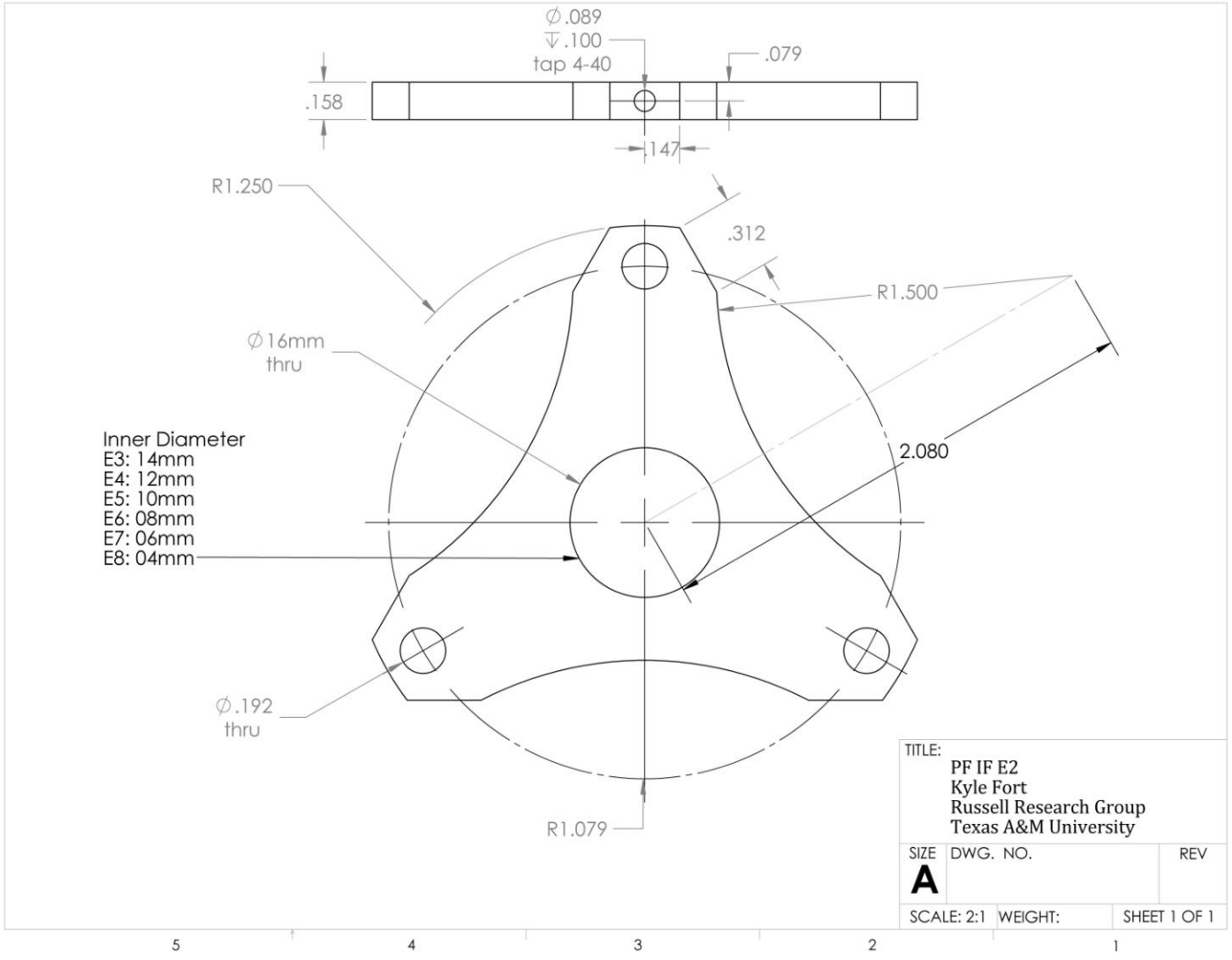
∅.089
↧.100
tap 4-40
.079
.158
.147
R1.250
.312
R1.500
∅16mm
thru
Inner Diameter
E3: 14mm
E4: 12mm
E5: 10mm
E6: 08mm
E7: 06mm
E8: 04mm
2.080
∅.192
thru
R1.079
TITLE:
PF IF E2
Kyle Fort
Russell Research Group
Texas A&M University
SIZE
A
DWG. NO.
REV
SCALE: 2:1
WEIGHT:
SHEET 1 OF 1
5
4
3
2
1

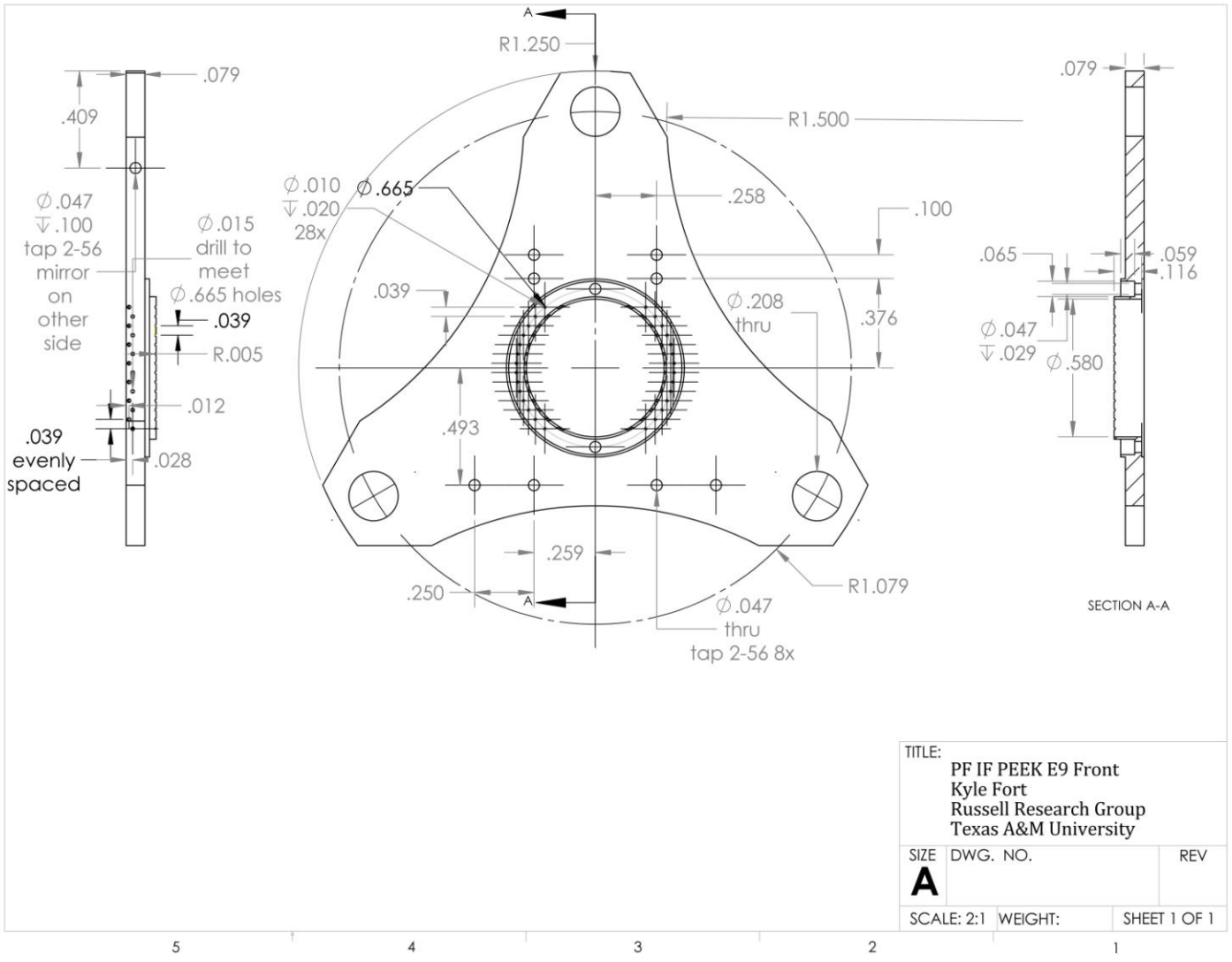
A
R1.250
.079
.409
∅.047
↧.100
tap 2-56
mirror
on
other
side
∅.015
drill to
meet
∅.665 holes
.039
R.005
.012
.039
evenly
spaced
.028
∅.010
↧.020
28x
∅.665
R1.500
.258
.100
.039
∅.208
thru
.376
.493
.259
.250
A
R1.079
∅.047
thru
tap 2-56 8x
.079
.065
.059
.116
∅.047
↧.029
∅.580
SECTION A-A
TITLE:
PF IF PEEK E9 Front
Kyle Fort
Russell Research Group
Texas A&M University
SIZE
A
DWG. NO.
REV
SCALE: 2:1
WEIGHT:
SHEET 1 OF 1
5
4
3
2
1

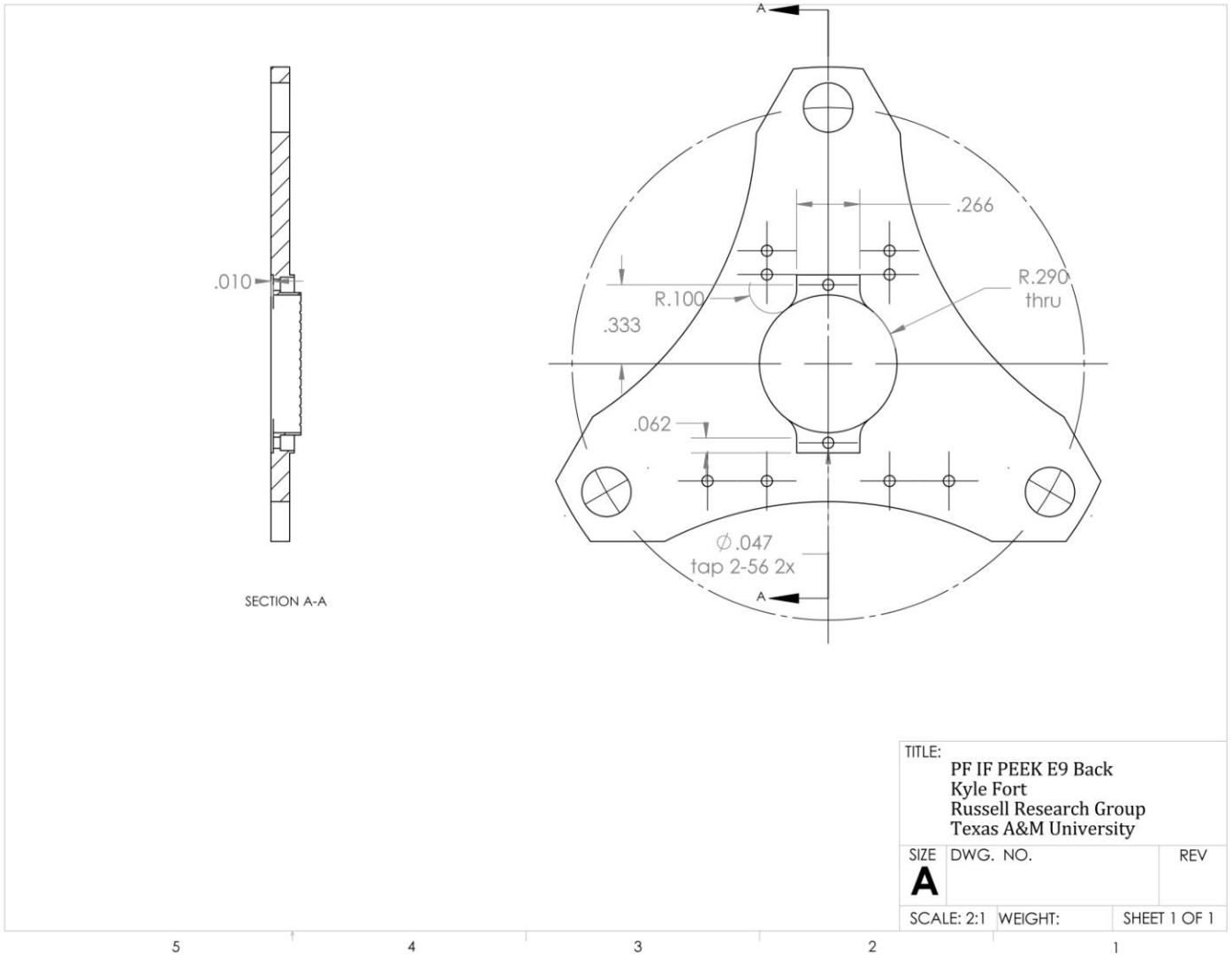
A
.010
SECTION A-A
.266
R.290
thru
R.100
.333
.062
∅.047
tap 2-56 2x
A
TITLE:
PF IF PEEK E9 Back
Kyle Fort
Russell Research Group
Texas A&M University
SIZE
A
DWG. NO.
REV
SCALE: 2:1
WEIGHT:
SHEET 1 OF 1
5
4
3
2
1

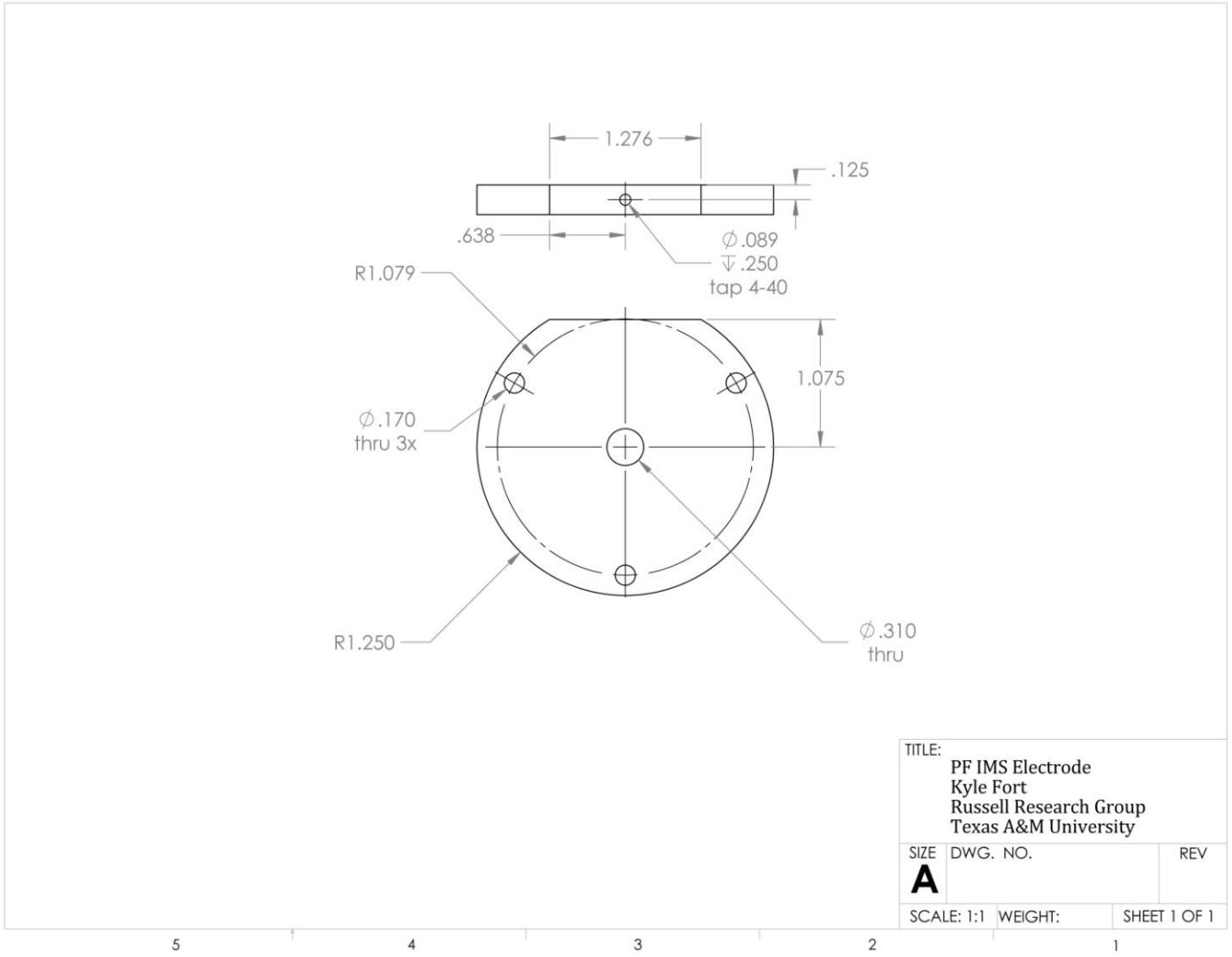
1.276
.125
.638
∅.089
↧.250
tap 4-40
R1.079
1.075
∅.170
thru 3x
R1.250
∅.310
thru
TITLE:
PF IMS Electrode
Kyle Fort
Russell Research Group
Texas A&M University
SIZE
A
DWG. NO.
REV
SCALE: 1:1
WEIGHT:
SHEET 1 OF 1
5
4
3
2
1

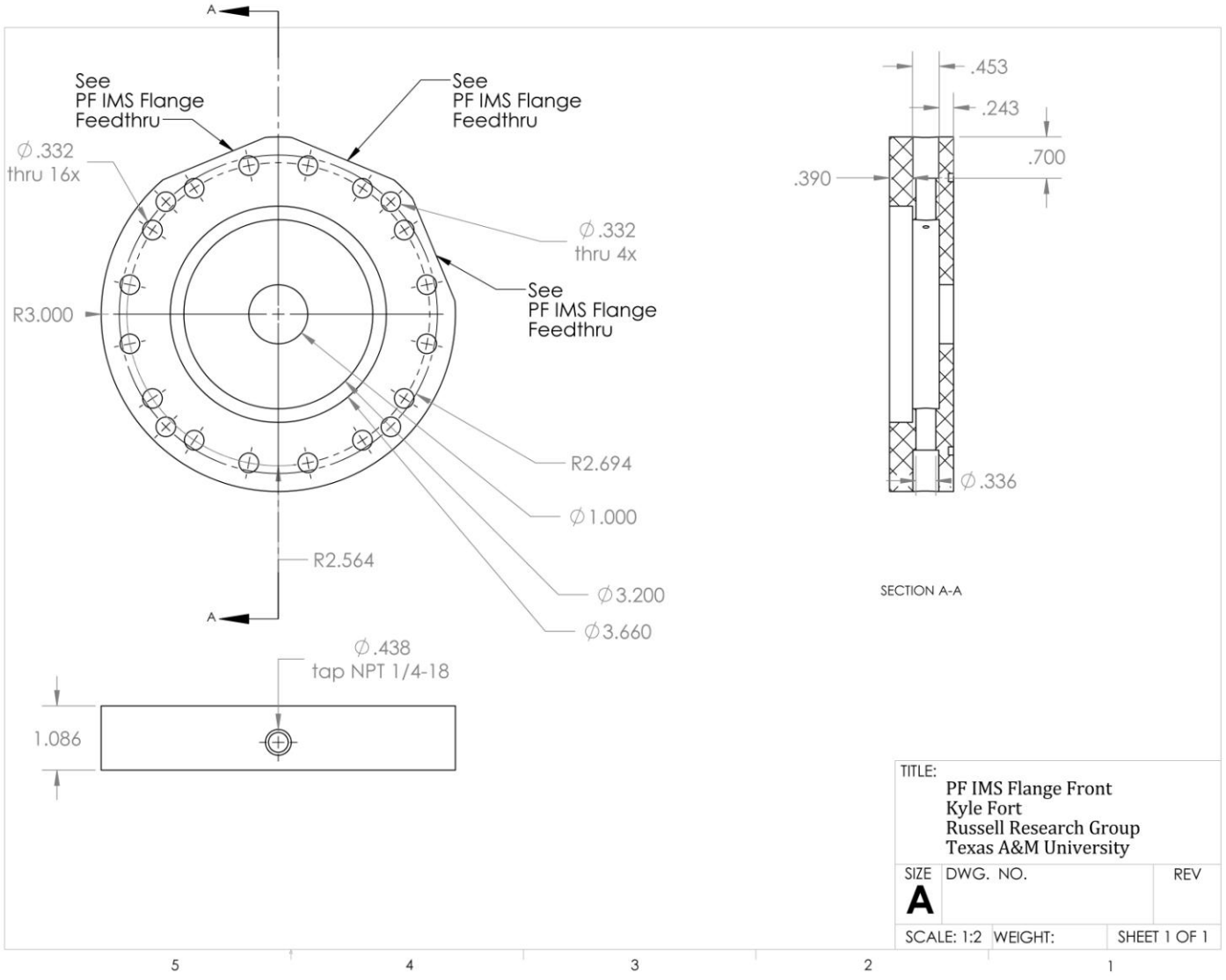
A
See
PF IMS Flange
Feedthru
See
PF IMS Flange
Feedthru
∅.332
thru 16x
∅.332
thru 4x
See
PF IMS Flange
Feedthru
R3.000
R2.694
∅1.000
R2.564
∅3.200
∅3.660
A
∅.438
tap NPT 1/4-18
1.086
.453
.243
.700
.390
∅.336
SECTION A-A
TITLE:
PF IMS Flange Front
Kyle Fort
Russell Research Group
Texas A&M University
SIZE
A
DWG. NO.
REV
SCALE: 1:2
WEIGHT:
SHEET 1 OF 1
5
4
3
2
1

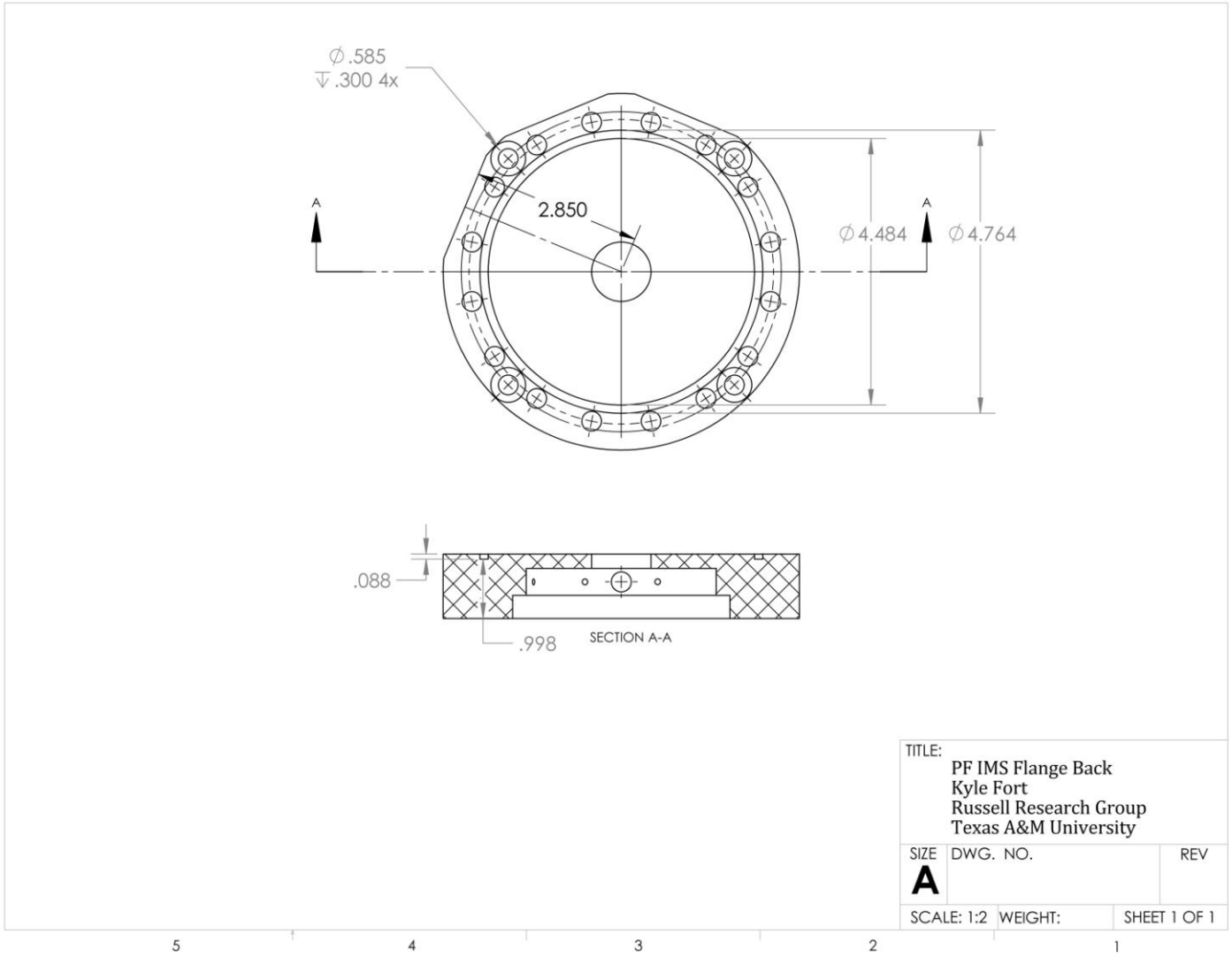
∅.585
⌵.300 4x
2.850
A
A
∅4.484
∅4.764
.088
.998
SECTION A-A
TITLE:
PF IMS Flange Back
Kyle Fort
Russell Research Group
Texas A&M University
SIZE
A
DWG. NO.
REV
SCALE: 1:2
WEIGHT:
SHEET 1 OF 1
5
4
3
2
1

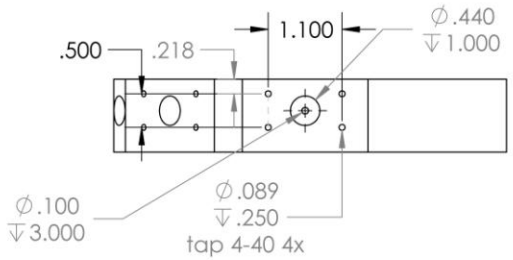

TITLE: PF IMS Flange Feedthru Kyle Fort Russell Research Group Texas A&M University		
SIZE A	DWG. NO.	REV
SCALE: 1:2	WEIGHT:	SHEET 1 OF 1

5 4 3 2 1

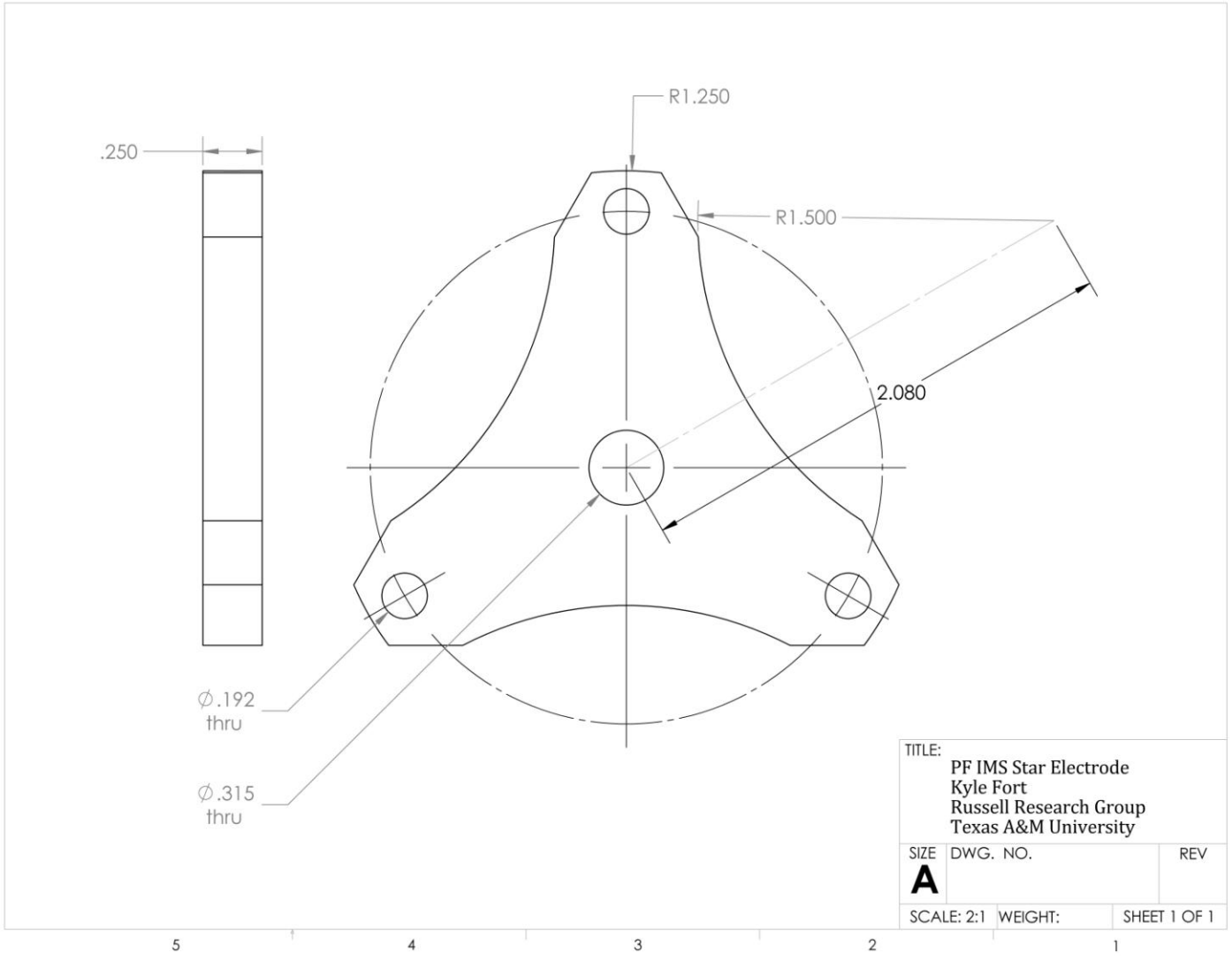
R1.250
.250
R1.500
2.080
∅.192
thru
∅.315
thru
TITLE:
PF IMS Star Electrode
Kyle Fort
Russell Research Group
Texas A&M University
SIZE
A
DWG. NO.
REV
SCALE: 2:1
WEIGHT:
SHEET 1 OF 1
5
4
3
2
1

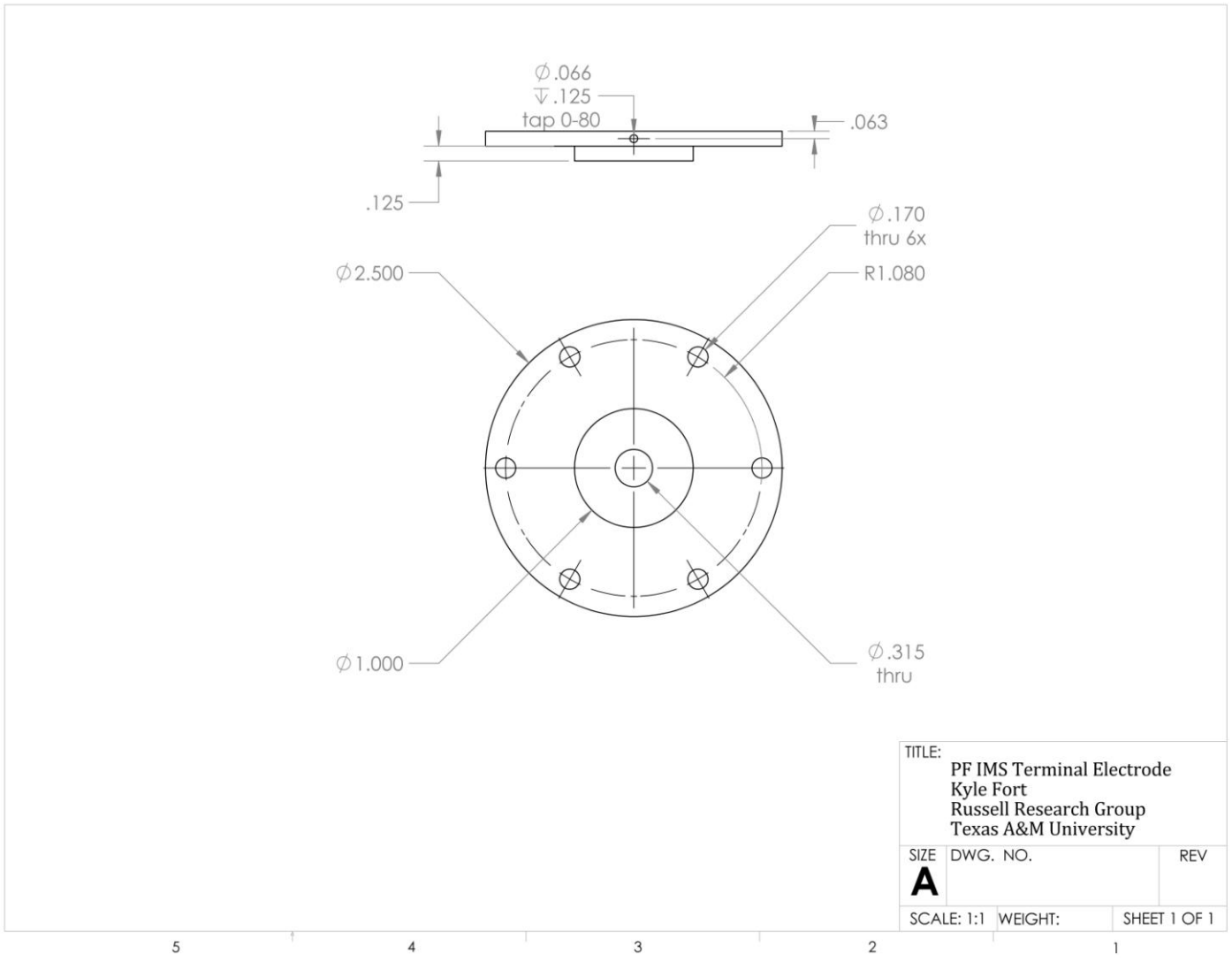
∅.066
↧.125
tap 0-80
.063
.125
∅.170
thru 6x
∅2.500
R1.080
∅1.000
∅.315
thru
TITLE:
PF IMS Terminal Electrode
Kyle Fort
Russell Research Group
Texas A&M University
SIZE
A
DWG. NO.
REV
SCALE: 1:1
WEIGHT:
SHEET 1 OF 1
5
4
3
2
1

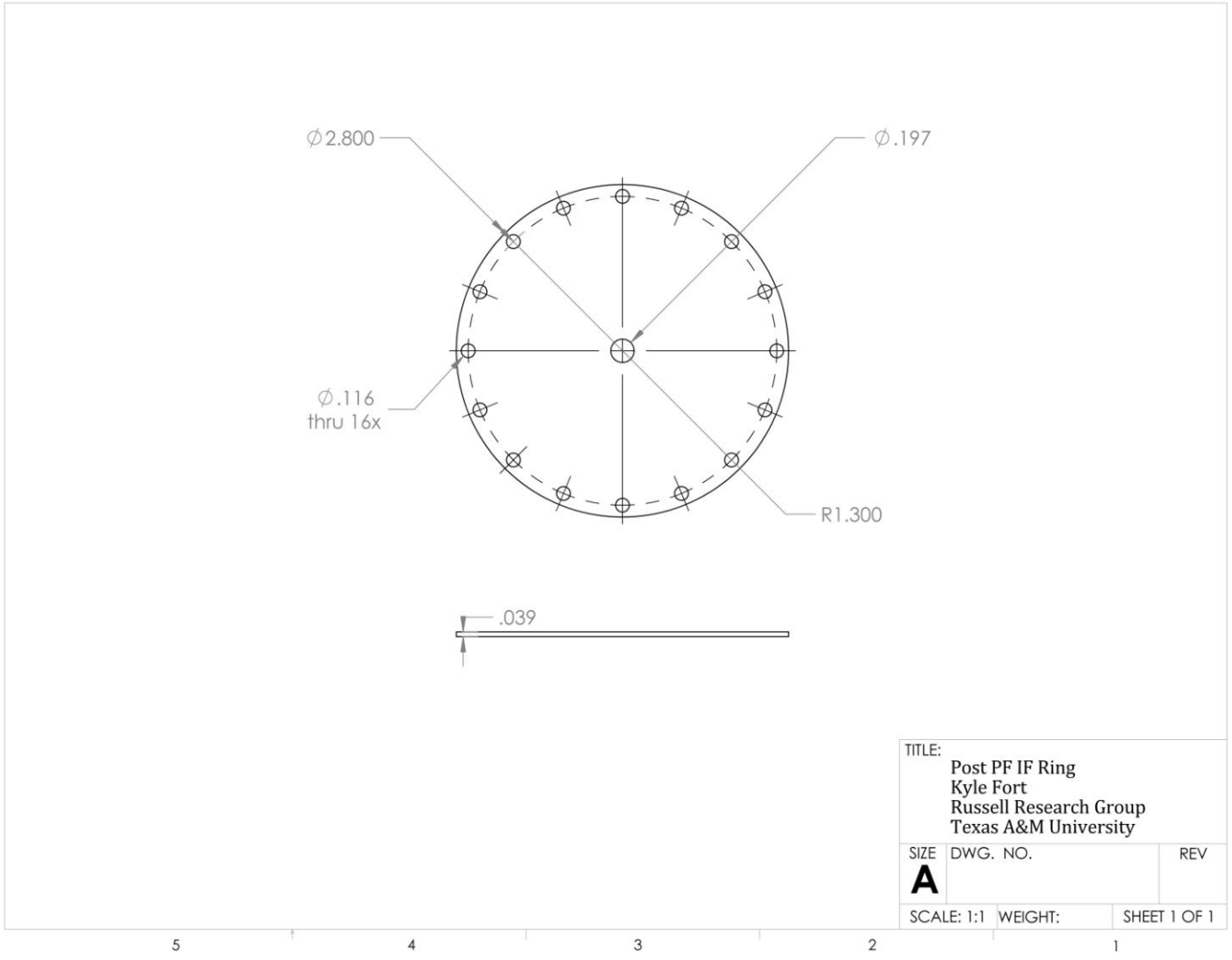
∅2.800
∅.197
∅.116
thru 16x
R1.300
.039
TITLE:
Post PF IF Ring
Kyle Fort
Russell Research Group
Texas A&M University
SIZE
A
DWG. NO.
REV
SCALE: 1:1
WEIGHT:
SHEET 1 OF 1
5
4
3
2
1

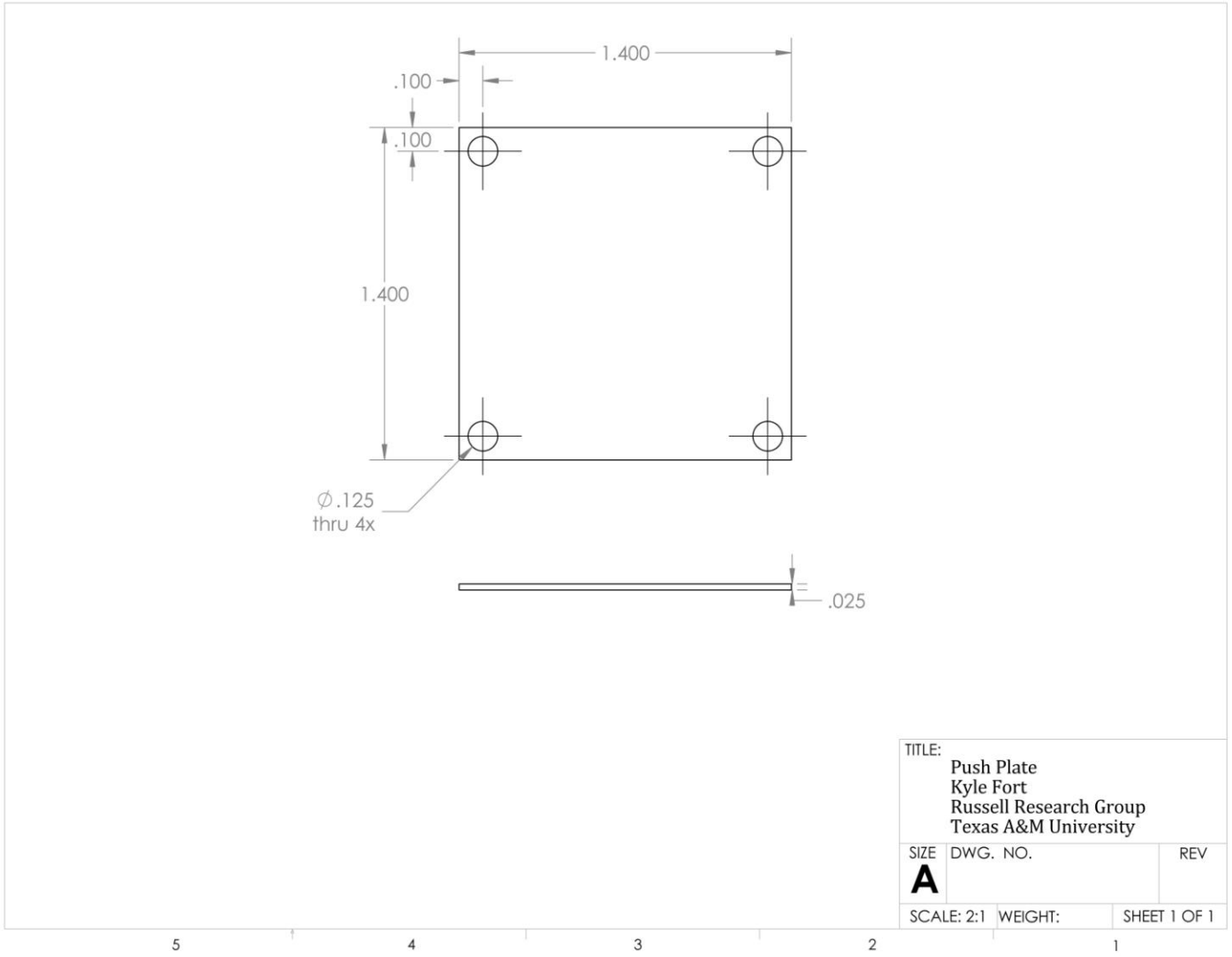
1.400
.100
.100
1.400
∅.125
thru 4x
.025
TITLE:
Push Plate
Kyle Fort
Russell Research Group
Texas A&M University
SIZE
A
DWG. NO.
REV
SCALE: 2:1
WEIGHT:
SHEET 1 OF 1
5
4
3
2
1

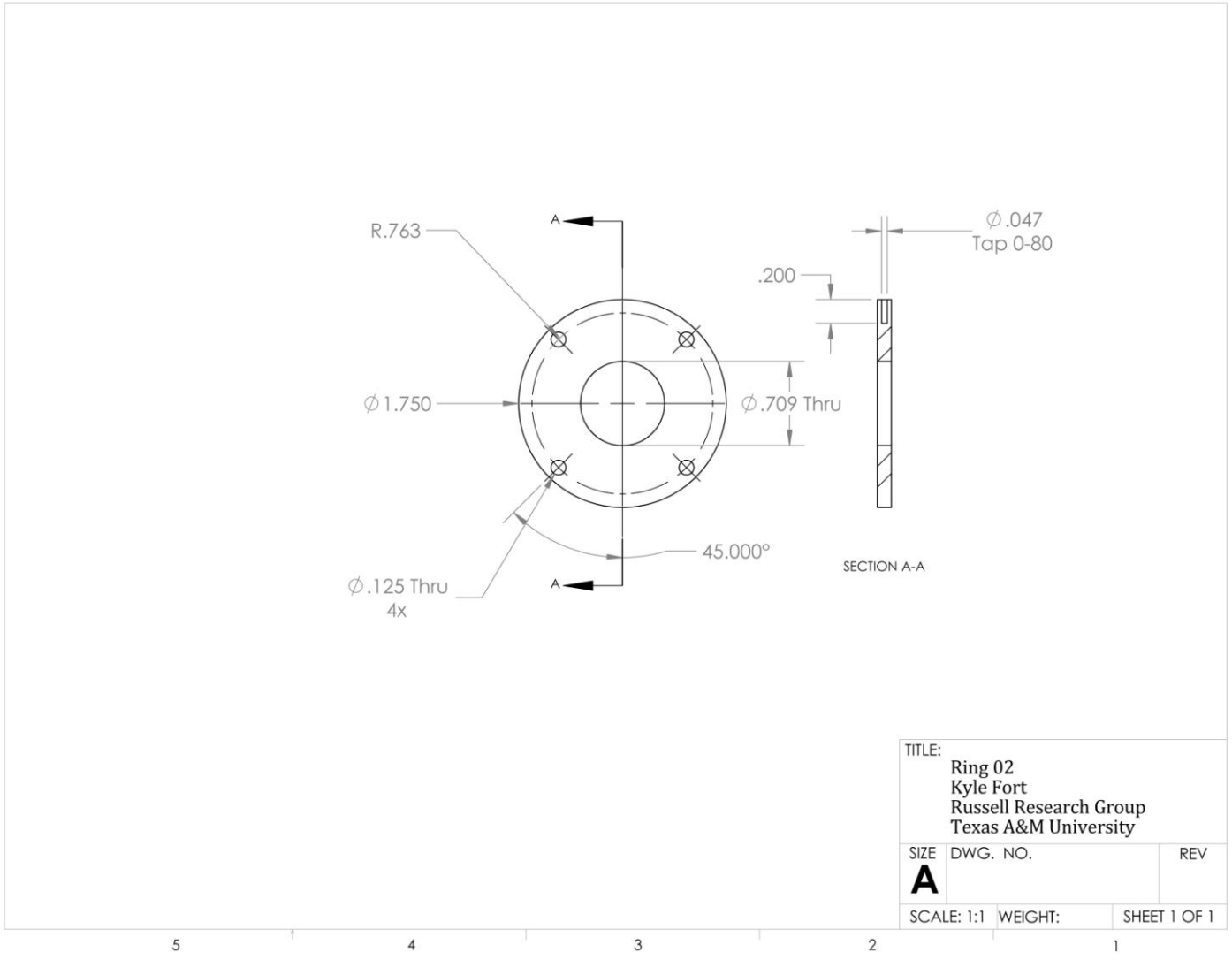
R.763
A
Ø.047
Tap 0-80
.200
Ø1.750
Ø.709 Thru
45.000°
Ø.125 Thru
4x
A
SECTION A-A
TITLE:
Ring 02
Kyle Fort
Russell Research Group
Texas A&M University
SIZE
A
DWG. NO.
REV
SCALE: 1:1
WEIGHT:
SHEET 1 OF 1
5
4
3
2
1

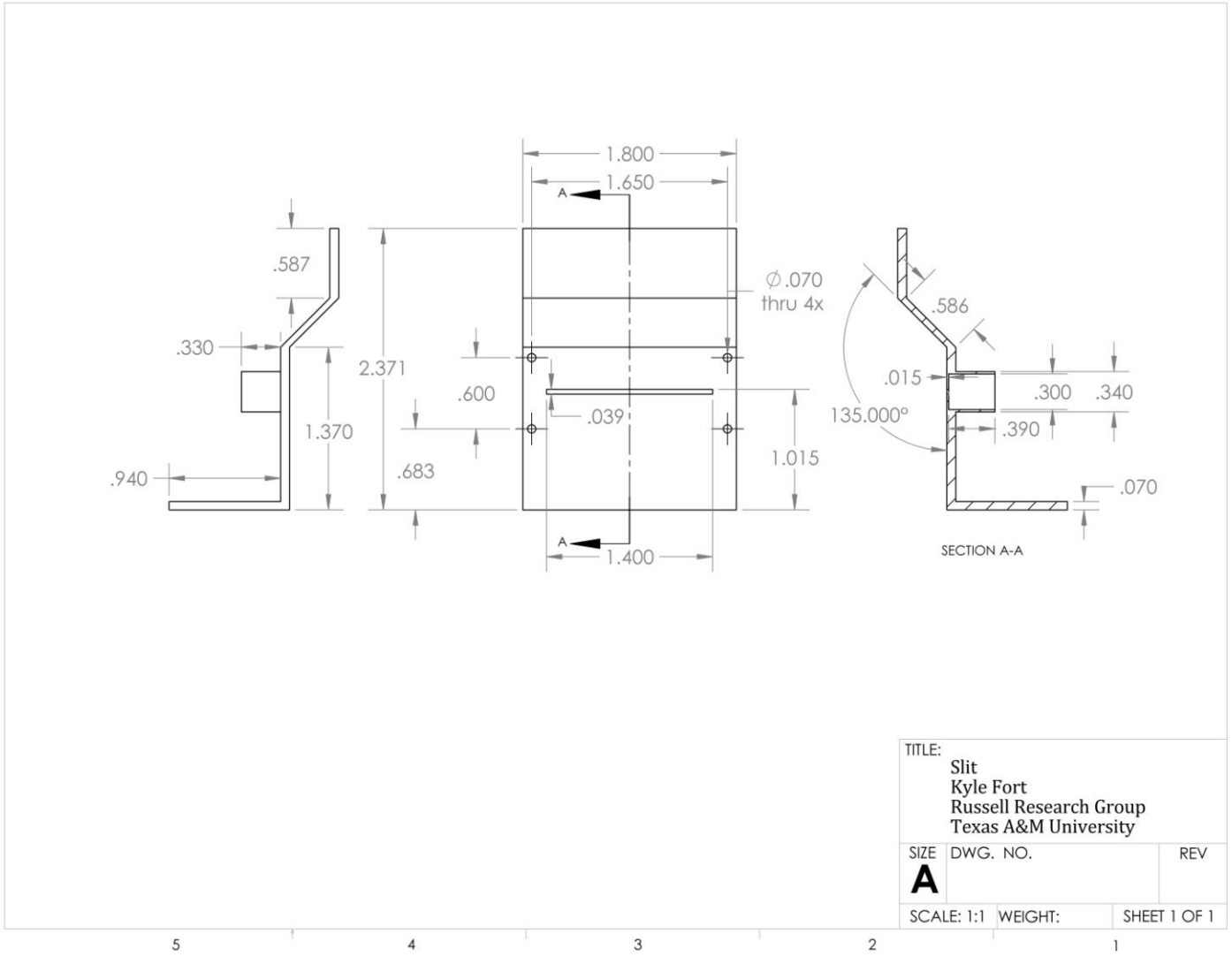
1.800
1.650
A
.587
.330
1.370
.940
2.371
.600
.683
.039
∅.070
thru 4x
1.015
A
1.400
.586
.015
.300
.340
135.000°
.390
.070
SECTION A-A
TITLE:
Slit
Kyle Fort
Russell Research Group
Texas A&M University
SIZE
A
DWG. NO.
REV
SCALE: 1:1
WEIGHT:
SHEET 1 OF 1
5
4
3
2
1

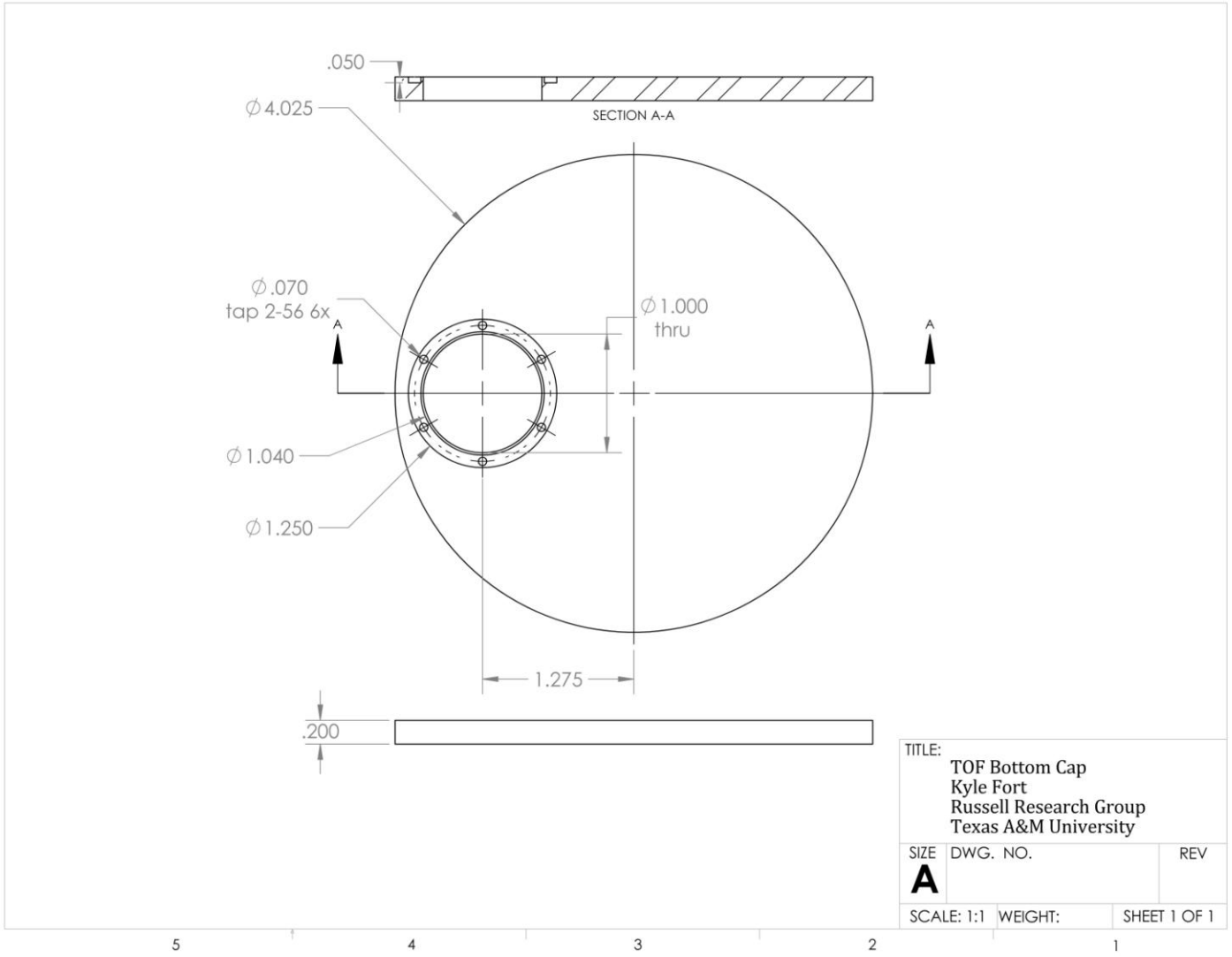
.050
SECTION A-A
∅4.025
∅.070
tap 2-56 6x
A
A
∅1.000
thru
∅1.040
∅1.250
1.275
.200
TITLE:
TOF Bottom Cap
Kyle Fort
Russell Research Group
Texas A&M University
SIZE
A
DWG. NO.
REV
SCALE: 1:1
WEIGHT:
SHEET 1 OF 1
5
4
3
2
1

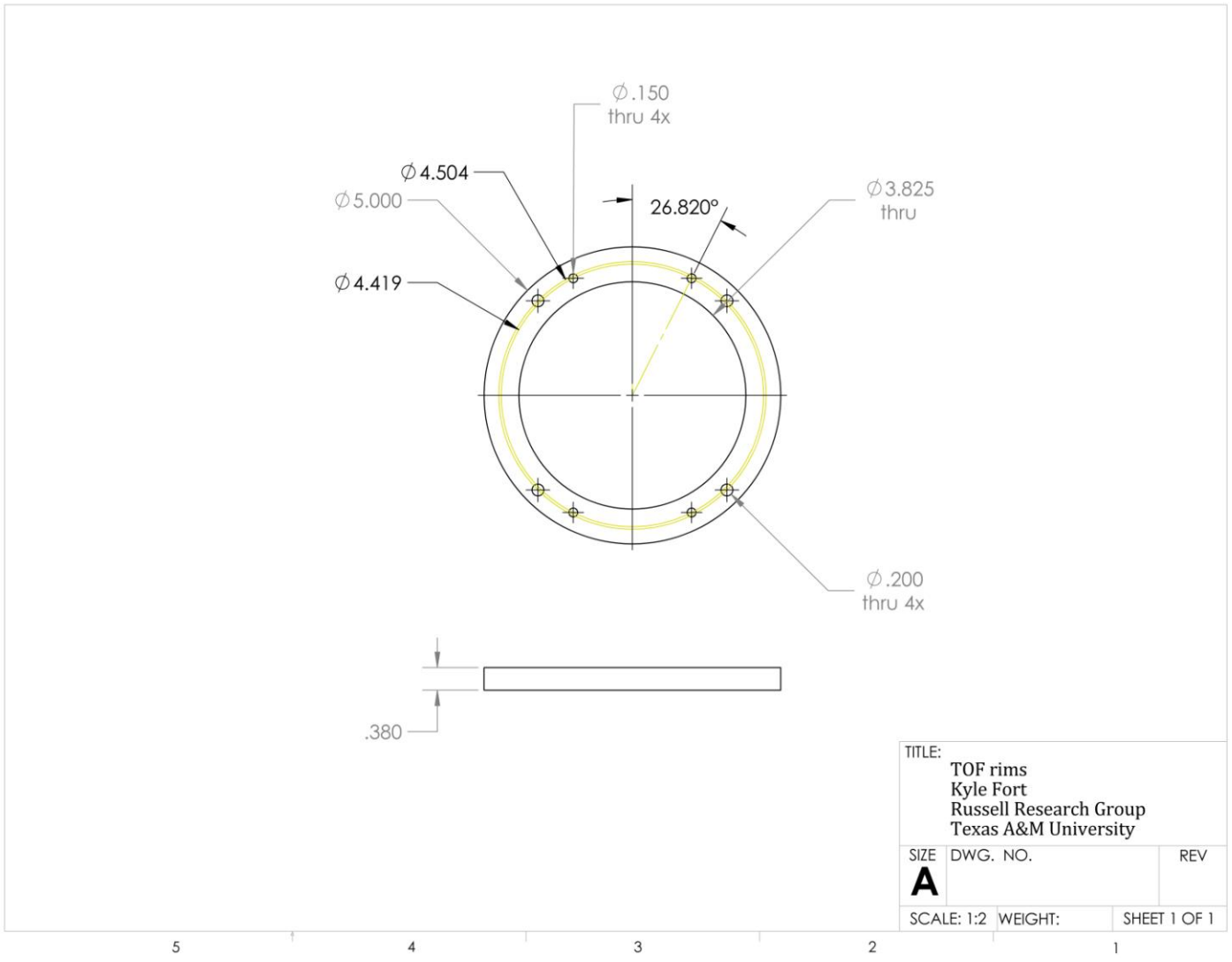
∅.150
thru 4x
∅4.504
∅5.000
26.820°
∅3.825
thru
∅4.419
∅.200
thru 4x
.380
TITLE:
TOF rims
Kyle Fort
Russell Research Group
Texas A&M University
SIZE
A
DWG. NO.
REV
SCALE: 1:2
WEIGHT:
SHEET 1 OF 1
5
4
3
2
1

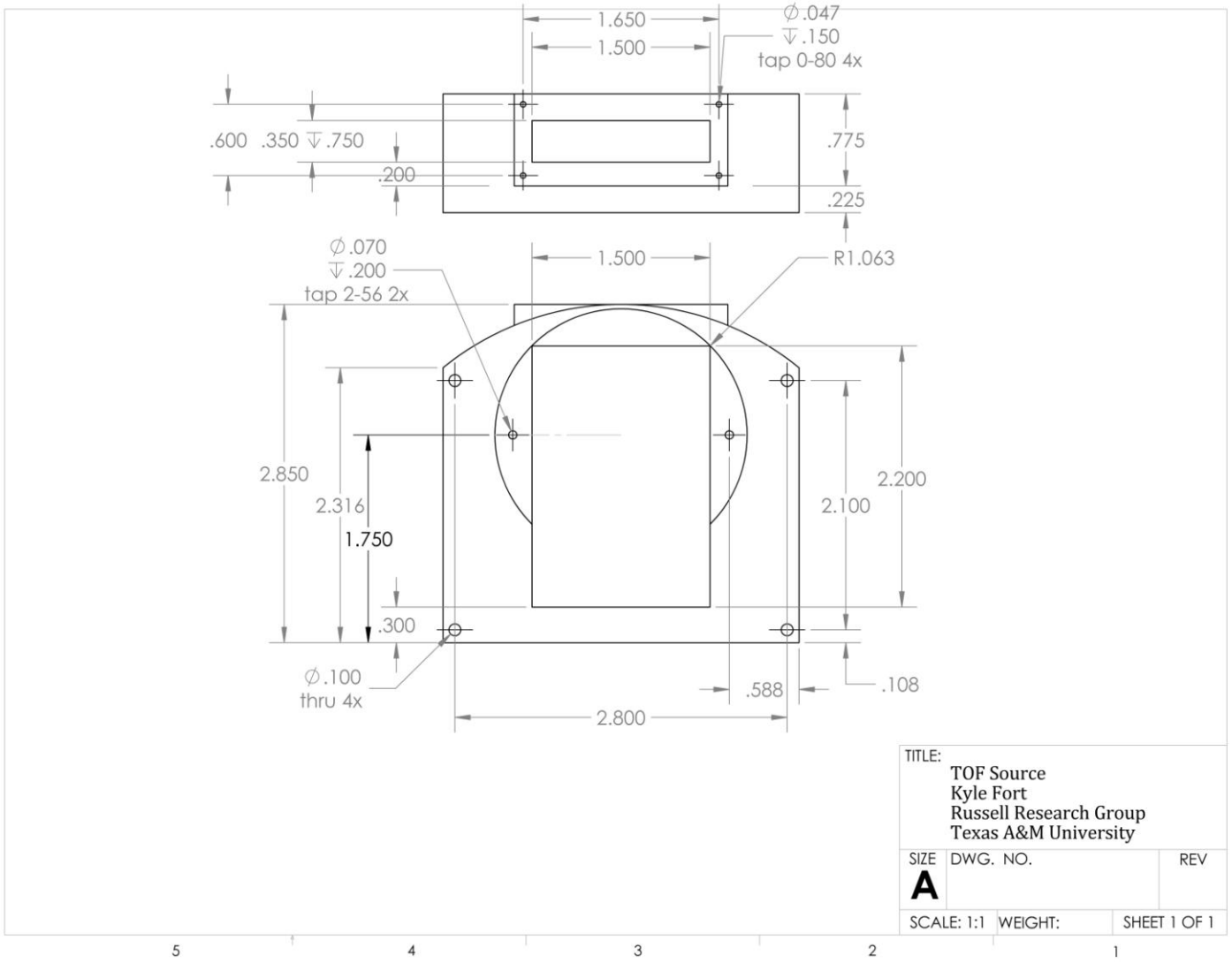
1.650
1.500
⌀.047
↧.150
tap 0-80 4x
.600
.350
↧.750
.200
.775
.225
⌀.070
↧.200
tap 2-56 2x
1.500
R1.063
2.850
2.316
1.750
2.100
2.200
.300
⌀.100
thru 4x
.588
.108
2.800
TITLE:
TOF Source
Kyle Fort
Russell Research Group
Texas A&M University
SIZE
A
DWG. NO.
REV
SCALE: 1:1
WEIGHT:
SHEET 1 OF 1
5
4
3
2
1

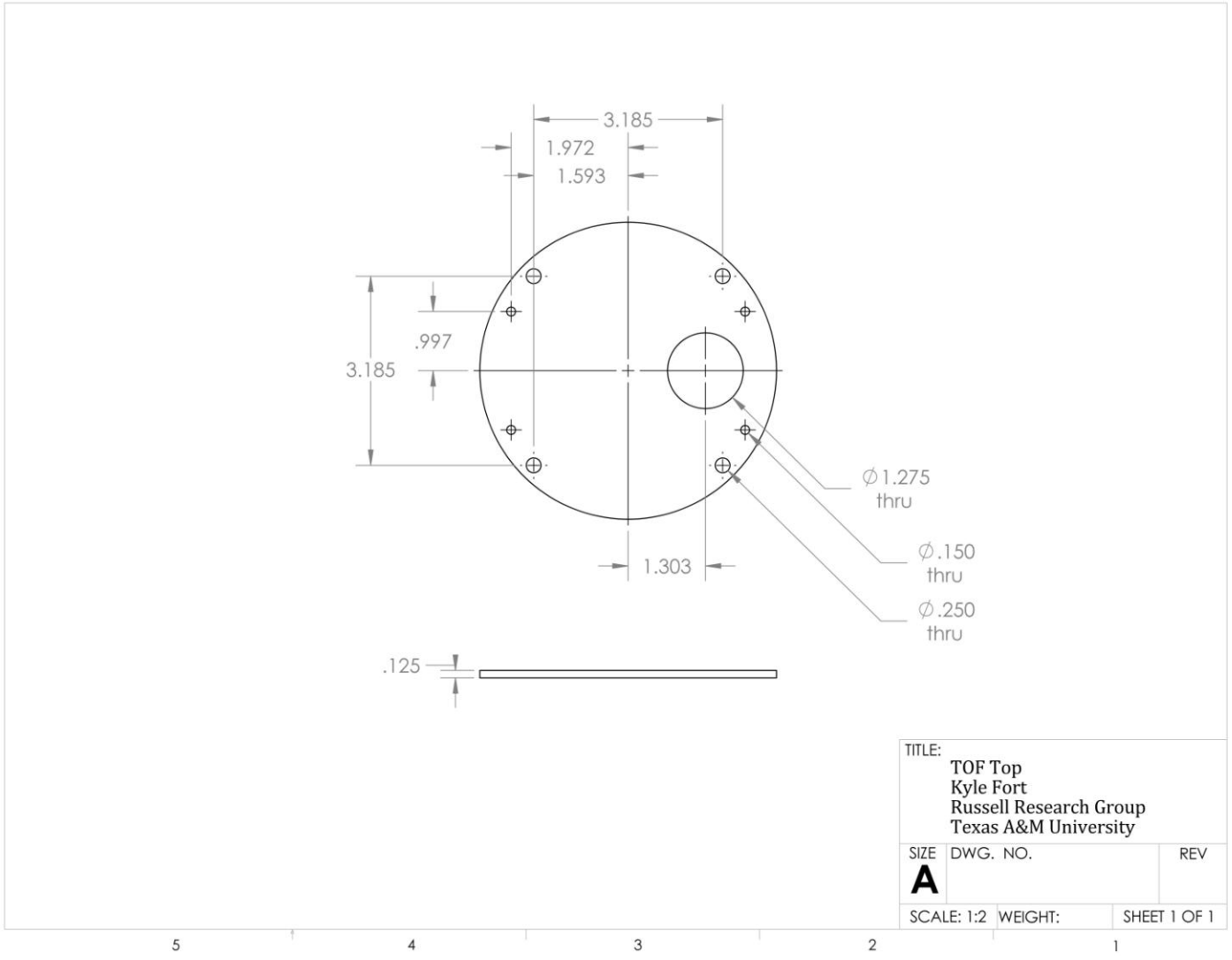
3.185
1.972
1.593
.997
3.185
∅1.275
thru
∅.150
thru
∅.250
thru
1.303
.125
TITLE:
TOF Top
Kyle Fort
Russell Research Group
Texas A&M University
SIZE
A
DWG. NO.
REV
SCALE: 1:2
WEIGHT:
SHEET 1 OF 1
5
4
3
2
1

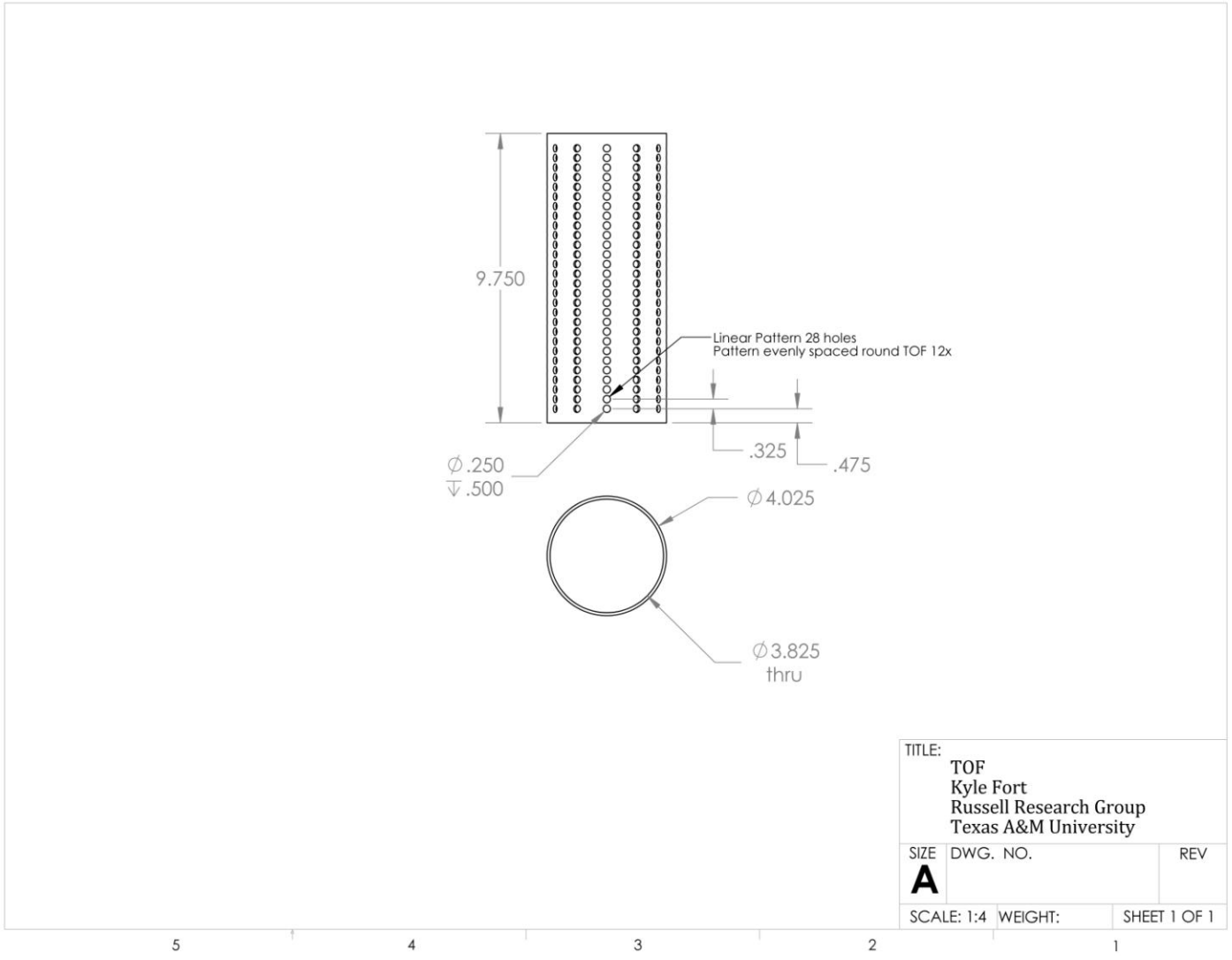
9.750
Linear Pattern 28 holes
Pattern evenly spaced round TOF 12x
.325
.475
⌀.250
↧.500
⌀4.025
⌀3.825
thru
TITLE:
TOF
Kyle Fort
Russell Research Group
Texas A&M University
SIZE
A
DWG. NO.
REV
SCALE: 1:4
WEIGHT:
SHEET 1 OF 1
5
4
3
2
1

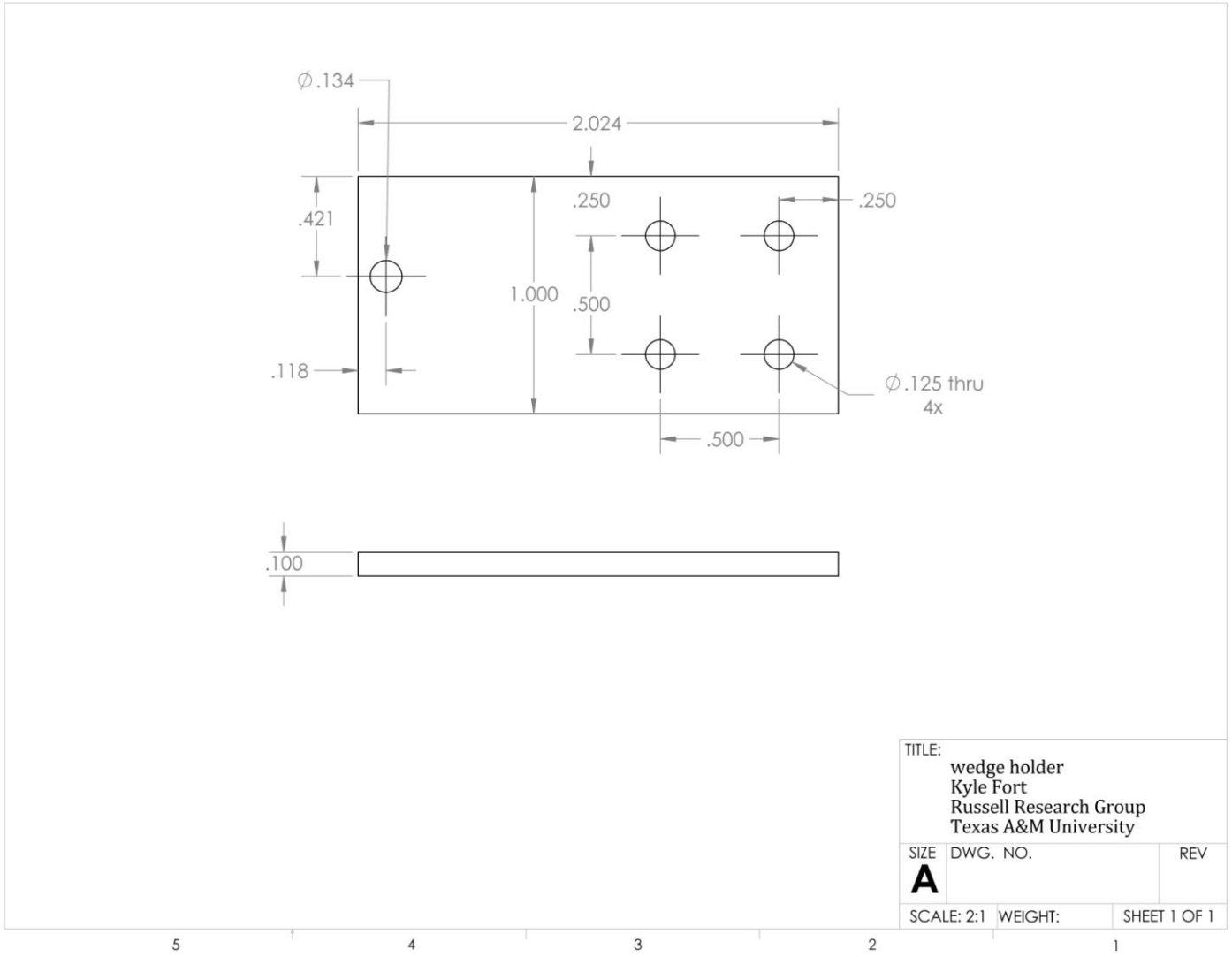
∅.134
2.024
.421
.250
.250
1.000
.500
.118
∅.125 thru
4x
.500
.100
TITLE:
wedge holder
Kyle Fort
Russell Research Group
Texas A&M University
SIZE
A
DWG. NO.
REV
SCALE: 2:1
WEIGHT:
SHEET 1 OF 1
5
4
3
2
1

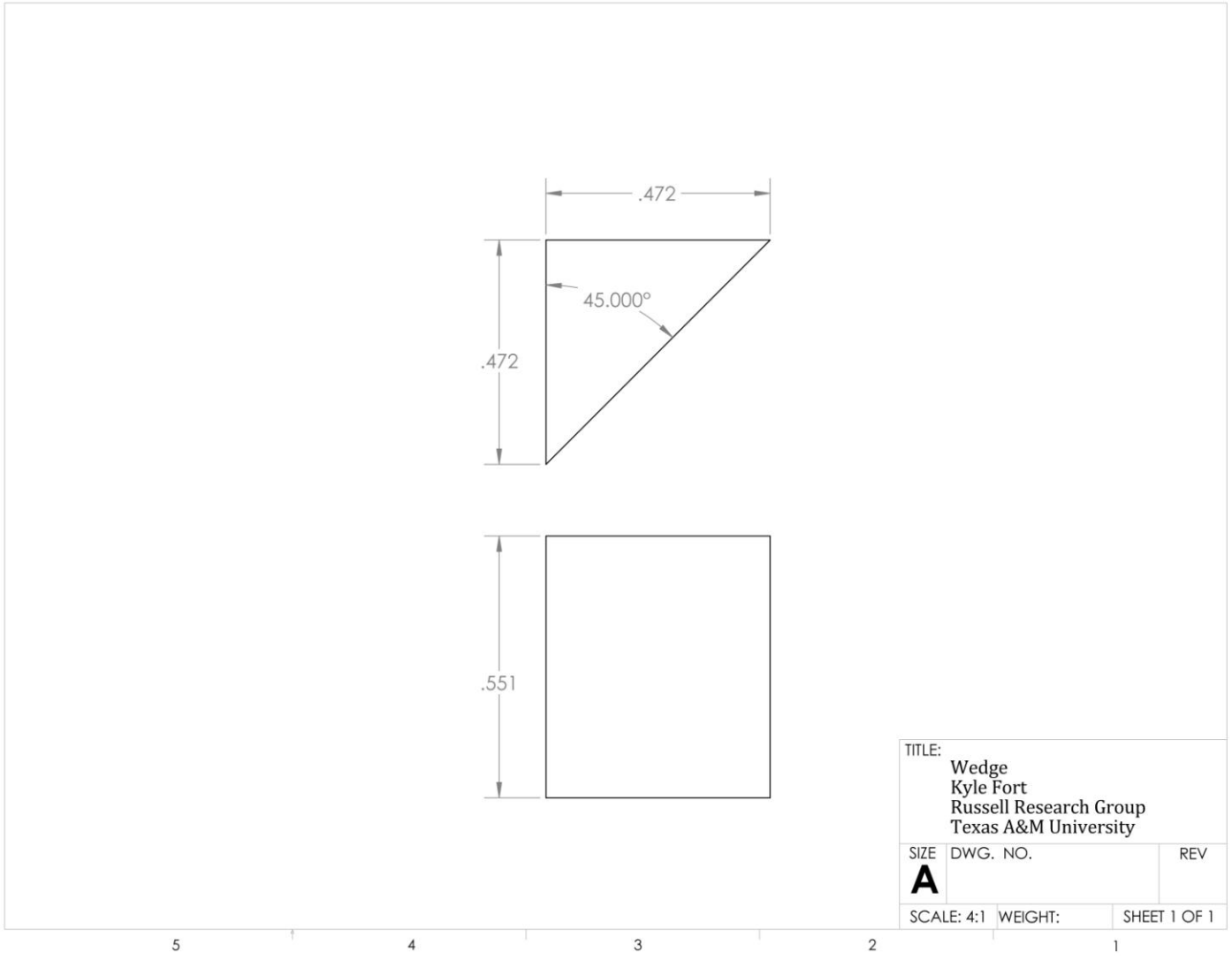
.472
45.000°
.472
.551
TITLE:
Wedge
Kyle Fort
Russell Research Group
Texas A&M University
SIZE
A
DWG. NO.
REV
SCALE: 4:1
WEIGHT:
SHEET 1 OF 1
5
4
3
2
1